Dissertation
submitted to the
Combined Faculty of Natural Sciences and Mathematics
of the Ruperto Carola University Heidelberg, Germany
for the degree of
Doctor of Natural Sciences

Presented by

M.Sc. Ruth Großeholz
born in: Mannheim-Neckarau
Oral examination: 14.09.2018

Computational Modeling of the Fast Brassinosteroid Response in the Plasma Membrane of *Arabidopsis thaliana*: From Molecules to Organ

Referees: Prof. Dr. Ursula Kummer
Prof. Dr. Karin Schumacher

Zusammenfassung

Es ist das Ziel dieser Arbeit, die Aktivierung und Regulation des schnellen Brassinosteroidsignalwegs in *Arabidopsis thaliana* und dessen Rolle bezüglich Zellelongation mithilfe computergestützter, integrativer Modellierung zu analysieren. Brassinosteroide sind pflanzliche Steroidhormone, die an einer Vielzahl von physiologischen and entwicklungsbiologischen Prozessen beteiligt sind. Einer dieser Prozesse ist Zellelongation, welche für den Großteil des Wachstums von pflanzlichen Organen verantwortlich ist.
Als sessile Organismen müssen sich Pflanzen neue Ressourcen durch Wachstum erschließen. Da Wachstum jedoch ein Prozess ist, der viel Energie benötigt, muss dies auch streng reguliert werden. Daher ist es notwending, die Aktivierung und Steuerung der schnellen Brassinosteroidantwort zu verstehen. In dieser Arbeit analysierte ich diese Aspekte der schnellen Brassinotsteroidantwort mithilfe Computer-gestützter Modellierung auf unterschiedlichen Ebenen, die vom Molekül zum Organ reichen.
Zum einen analysierte ich, wie Modelle aus gewöhnlichen Differentialgleichungen auf Änderungen in Zellform und -größe reagieren, wenn Prozesse, die meherere Kompartimente betreffen, auf unterschiedliche Weisen beschrieben sind. Diese Studie zeigt, dass es tatsächlich notwendig sein kann, die Membrane als Kompartiment im Modell zu beschreiben, um das korrekte Modellverhalten zu beobachten. Dies ist abhängig von dem modellierten System.
Des Weiteren studierte ich die Interaktionen zwischen Rezeptor, Co-Rezeptor und negativem Regulator auf Basis ihrer zytoplasmatischen Domänen. Hier zeigen die simulierten Komplexe, dass der negative Regulator präferentiell an die katalytische Domäne des Co-Rezeptors bindet und ihn so an der Teilnahme am Signalweg hindert.
Als dritten Aspekt modellierte ich den schnellen Signalweg der Brassinosteroidantwort mithilfe eines Modells aus gewöhnlichen Differentialgleichungen. Die Parameter dieses Modells wurden basierend auf dosisabhängigen Daten der Membranpotentialänderung geschätzt. Neben der Membranpotentialänderung beschreibt das Modell auch die Zunahme des Zellwandvolumes, welche ebenfalls von Brassinosteroiden stimuliert werden. Ich habe das Modell bezüglich des Verhaltens in der meristematischen Zone und in der Mutante eines negativen Regulators getestet, was durch die Kooperationspartner experimentell überprüft wurde. Aufgrund des Modellverhaltens und der Daten zur Proteinquantifikation stellen wir die Hypothese auf, dass die zelluläre Antwort der schnellen Brassinosteroidantwort von der lokalen Konzentration der H^+-ATPasen abhängt.
Als letzten Themenblock in dieser Arbeit erweiterte ich das Modell des schnellen Brassinosteroidsignalwegs aus gewöhnlichen Differentialgleichungen, sodass es auch Zellelon-

gation beschreibt. Das vorläufige Modell kann das Elongationsverhalten einer Epidermiszelle von der meristematischen Zone bis zur endgültigen Zelllänge in der Differenzierungszone beschreiben. Dieses Modell kombinierte ich mit einem agentenbasierten Modell der Wurzelspitze, was einen integrativen Einblick in Zellelongation in der Wurzel ermöglicht. Bislang beschreibt dieses Modell lediglich das Verhalten von Epidermiszellen bis zu einer Zelllänge von $25\,\mu m$. Selbst dieses reduzierte Modell zeigt aber, dass dies eine valide Herangehensweise ist um Wurzelwachstum zu modellieren.

Summary

It is the aim of this thesis to analyze the initiation and regulation of the fast brassinosteroid response pathway *Arabidopsis thaliana* and its role for cell elongation in an integrative fashion using mathematical modeling. Brassinosteroids are plant steroid hormones that mediate various physiological and developmental processes. One of these processes is cell elongation, which is the major mechanism for organ growth in plants.

As sessile organisms, plants have to rely on growth to open up new resources. However, growth is an energy consuming process that has to be tightly regulated. Therefore, it is necessary to understand the activation and regulation of the fast brassinosteroid response. The computational modeling and analysis of the fast brassinosteroid signaling focused on several different aspects.

Because of the importance of compartmentalization in biological systems, I first studied the different modeling approaches to describe multi-compartment processes in models consisting of ordinary differential equations and how these modeling approaches react to changes in cell morphology. This analysis shows that including the membrane as interaction area can be crucial to proper modeling behavior depending on the modeled system.

Second, I used molecular modeling to clarify the interactions between receptor, co-receptor and a negative regulator of the fast brassinosteroid response. Here, the simulated complexes show that the negative regulator acts by blocking the catalytic domain of the co-receptor, which is then unable to participate in propagating the signal.

Third, I used a dynamic model consisting of ordinary differential equations to simulate the fast brassinosteroid response on a cellular scale. The parameters of this model were fitted to dose-response data of the membrane potential change. Furthermore, this model includes the BR-induced increase in cell wall volume. I validated this model with respect to the behavior in the meristematic root zone and the behavior in a deletion of a negative regulator. Based on the model behavior and the quantification of model species, we hypothesize that H^+-ATPase levels in the different root zones determine the response to brassinosteroid stimulation in the fast response pathway.

Finally, I expanded the ordinary differential equation model for the fast brassinosteroid response to include the process of cell elongation. This model can describe the experimentally observed elongation behavior of an epidermis cell from the meristematic zone to the final cell length in the maturation zone. I combined this model with an agent-based representation of the root. This model provides an integrative view on cell elongation. While this multi-scale model is currently limited to one cell type and a maximal cell length of $25\,\mu m$, this shows that it is a valid approach to modeling root elongation.

Contents

List of Figures

List of Tables

1 Introduction

It is the aim of this thesis to analyze the initiation and regulation of the fast brassinosteroid (BR) respone pathway in the plasma membrane of *Arabidopsis thaliana* (*A. thaliana*) and its role in cell elongation by integrative computational modeling. Here, the computational models of the fast BR response pathway are used to analyze the properties of the system as a whole as well as the role of individual components of the pathway. BRs are plant steroid hormones that fulfill various functions in plant physiology and development [1]. In particular, BR hormone functions concern processes that range from pollen tube elongation [2] to senesence [3, 4, 5] (Fig. 2.1). Without functional BR signaling, *A. thaliana* shows a significantly reduced growth [6], highlighting the crucial role of BRs for normal plant development.

As sessile organisms, plants have to rely on growth to tap new resources or to adapt to varying environmental stimuli (such as wind or frost). Due to the central role of growth in plant development and physiology, understanding the activation and regulation of growth is crucial.

Plant organ growth is determined to a large part by cell expansion [7]. Cell division also impacts organ growth, though this effect is by determining the number of cells that elongate [7]. In order for cell growth to occur, the cell wall needs to be acidified [8, 9]. This increases the flexibility of the cell wall [10]. In the plant root, this happens in one specific region, the elongation zone. In the root, cells elongate from an initial length of about $8\,\mu m$ to a final length of up to $220\,\mu m$, depending on the cell type [11]. Cell wall loosening is achieved by enzymes called expansins, which are activated upon cell wall acidification [9, 12]. The increased proton concentration is caused by the activation of the proton pumps *Arabidopsis* H^+-ATPases 1 and 2 (AHA1 and AHA2), after hormone stimulation [13].

The fast BR response pathway [14, 15, 16], which is analyzed by computational modeling in this thesis, is one hormonal pathway that can induce cell wall acidification [17, 18, 19, 20], which results in BR-induced cell elongation [2, 17, 21].

BRs are detected on the cell surface by the receptor brassinosteroid-insensitvite 1 (BRI1) [3, 22], which then associates with the co-receptor BRI1-associated kinase (BAK1) [23, 24, 25]. The activity of both, receptor and co-receptor, is strictly regulated by a number of inhibitors: BRI1 kinase inhibitor (BKI1) [26, 27] and Botrytis-induced kinase 1 (BIK1) [28] act on the receptor BRI1, while BAK1-interacting receptor like kinase (BIR3) primarily regulates the co-receptor BAK1 [29, 30]. After a series of transphosphorylation events [31], membrane hyperpolarization and cell wall acidification are induced by activating the proton pumps AHA1 and AHA2 [14, 15, 16], which results in cell wall swelling preceding

cell elongation [14]. However, while the individual proteins are known, the dynamics of the system as a whole are not completely understood.
Here, computational modeling can provide an additional perspective on the signaling pathway. Computational modeling is a powerful tool to understand the behavior of a system as a whole as well as the emergent properties of the system. Modeling can also aid in outlining the experimental information and highlighting gaps in the available knowledge that need to be investigated.
Just as there are different scales that need to be considered in a biological system (proteins, cells, tissues and organs), there are different modeling scales that can be employed in understanding a system: Molecular modeling allows for i.e. the computation of interactions of 3D protein structures [32]. Dynamic models of signaling and metabolic pathways can provide insight into emergent properties, initiation and regulation of the particular model system [33]. Furthermore, tissue dynamics emerging based on cellular behavior can be analyzed by agent-based models (ABMs) [34]. This represents but a small sample of what is possible with computational modeling.
Notwithstanding how useful computational models are, there are currently few published plant models [33]. Among the curated biochemical models on the biomodels database [35] (last accessed: 24.05.2018), only 30 out of 699 models concern plants, with the vast majority (27) being specific to *A. thaliana*. Nonetheless, there are four published computational models of BR signaling at the time of writing this thesis. The qualitative properties of the BR signaling pathway have been examined using a logic-based model [36]. A small dynamic ODE model has aided in understanding the dynamics of an transcription factor in response to BR stimulation [37]. A steady state model links the receptor occupancy to root and hypocotyl growth [38, 39, 40]. Finally, a dynamic model of the gene-regulatory pathway explores the possible behavior patterns that can emerge based on the available experimental information [41].
It is the primary aim of this thesis to analyze the initiation and regulation of the fast BR response pathway by computational modeling. To provide a comprehensive analysis of the fast BR response, I employed several different modeling methods that range from analyzing the molecular interactions, cellular dynamics and the root as an organ.
For one, as growth influences the size of cellular compartments, I analyzed the impact of changes in cell morphology on the behavior of ODE models with different modeling approaches to describing multi-compartment processes (Chapter 4). In these cases it can actually be a necessary prerequisite to scale processes between compartments with the interaction area instead of a compartment volume. Since inducing cell elongation is one function of BR [2, 17, 21], the accurate description of the signaling pathway in the model requires the inclusion of the membrane both as interaction area for scaling and as compartment for receptor and co-receptor.
To analyze the complex formation of the receptor BRI1, the co-receptor BAK1 and the negative regulator BIR3, I used molecular modeling to compute potential complexes between the cytoplasmic domains these proteins (Chapter 5). In the case of BR signaling, the detection of the ligand by the receptor BRI1 [42, 43] as well as the interaction with

the co-receptor BAK1 has been of special interest [25, 44, 45]. After the discovery of the negative regulator BIR3 that acts on the co-receptor BAK1 [46, 30], the interaction of all three proteins needed to be defined. The interactions of the ectodomains have been characterized recently [47], but the precise mode of interaction for the cytoplasmic domains is still unclear. Computationally, this question can be addressed by the molecular docking of 3D protein structures computing either fully docked or encountered complexes [48, 49, 49, 50, 51, 52]. By sampling and clustering the potential interactions it is possible to obtain a complex that is close to the native state of interaction between the proteins of interest. The analysis of these interactions shows that the negative regulator BIR3 and the receptor BRI1 compete for the same interaction site of BAK1 and that the energetic landscape favors the interaction of BIR3 and BAK1.

Furthermore, I analyzed an ODE model that comprises the known components and steps of the fast BR signaling module. The dynamic ODE model of the fast BR response pathway yields insight into the pathway's response in the different root regions as well as the deciding factors for the model's reaction to hormone stimulation (Chapter 6). This model describes BR-induced cell wall acidification, membrane hyperpolarization and cell wall swelling, which makes processes involving more than one compartment a central aspect of this model. The analysis of this model determined the important proteins and reactions for the model's response and thereby aided in the understanding of the fast BR response in *A. thaliana*.

As BRs initiate cell elongation [2, 17, 21], the next step was to include actual cell growth in the ODE model by implicitly including pH activated elongation (Chapter 7). This elongating cell model represents the chance to analyze BR-induced cell elongation *in silico*. By linking this model to an agent-based representation of the root, this extends the scope of this project from analyzing single cell behavior to visualizing the growth of an organ. Much like ODE models show the emergent behavior of a system by considering the individual proteins and reactions, agent-based models show the tissue dynamics based on the behavior rules of the cellular agents. The modeling software of choice, EPISIM [53, 54], allows not only for the simulation of cell behavior and biomechanical aspects, but also enables the inclusion of intracellular ODE models. This allows the link between the physiological response to hormonal stimulation and the growth observed in the organ of interest, the *A. thaliana* root.

All computational models rely heavily on the availability of experimental data. For one, kinetic parameters are estimated based on experimental data. Second, model set up depends on what kind of experimental data is available. If detailed, temporally resolved data on the individual phosphorylation states are available, it is reasonable to include these species in the model individually. If such data are not available, including the different phosphorylation states would introduce a source of uncertainty in the model. Lastly, computational models are tested by comparing the model's prediction to experimental data. This is the final step in model development as it demonstrates the validity of the model.

The reliance on experimental data is also the case for the computational models presented in this thesis. Experimentally, this project was supported by the work of Dr. Friederike

Wanke and Nina Glöckner in the research group of Prof. Dr. Klaus Harter at the Center for Molecular Biology in Plants (ZMBP) at the University of Tübingen. Furthermore, I collaborated with Sarina Schulze in the research group of Dr. Birgit Kemmerling (ZMBP, University of Tübingen) to specify the role of BIR3 as negative regulator in BR signaling. Dr. Stefan Scholl in the group of Prof. Dr. Karin Schumacher (Centre for Organismal Studies (COS)) provided measurements of the proton leak for the ODE model.
For some aspects of my thesis, I worked in collaboration with colleagues or external experts for that particular field. To specify the role of BIR3 in the signaling pathway by molecular modeling, I was advised by Dr. Anna Feldman-Salit (Bioquant, COS, Heidelberg University). Here, we also consulted with Prof. Dr. Rebecca Wade and Dr. Neil Bruce at the Heidelberg Institute for Theoretical Studies (HITS) and the Interdisciplinary Center for Scientific Computing (IWR), Heidelberg University. For the analysis of multi-compartment rate laws, I collaborated with Pascal Holzheu (Bioquant, COS, Heidelberg University). Finally, the multi-scale, agent-based model of the elongating root was built in close collaboration with Erika Tsingos (research group of Prof. Dr. Joachim Wittbrodt, COS, Heidelberg University).

2 | Biological and Theoretical Background

2.1 Brassinosteroid Signaling

BRs fulfill a diverse range of functions in plants (Fig. 2.1). Notably, BRs regulate cell elongation in root and hypocotyl with an activating low concentration and an inhibiting high concentration [11]. However, the concentration at which that effect is achieved differs greatly between different tissues [11]. While a concentration around $100\,\mathrm{nM}$ has a positive effect on hypocotyl elongation, such a concentration is already in the inhibitory range for root elongation [11].

BRs are detected on the cell surface by membrane receptors [3, 22]. BR signaling occurs on two levels; the fast membrane-associated response [14, 15, 16] and the slower gene-regulatory pathway [1, 56], both of which will be introduced here. The two pathways have serveral components in common: the receptor, the co-receptor and the regulatory elements that act on both.

The receptors that detect BRs on the cell membrane belong to one family: brassinosteroid-insesitive 1 (BRI1) [3, 22] and BRI1-like receptors (BRL1-3) [57, 58]. All of these receptors follow the same basic structure; a cytoplasmic kinase domain, a transmembrane domain and extracellular leucin-rich repeats (LRRs) [57]. Within the LRR domain, there is the island domain, which is responsible for ligand binding [59]. In the absence of the ligand, this domain is very flexible and cannot be resolved structurally [42]. Upon ligand binding, the island domain stabilizes and forms a binding pocket around the hormone molecule [42, 43]. Ligand binding and the stabilization of the binding pocket then facilitate the association of the co-receptor BRI1-associated kinase 1 (BAK1) [23, 24, 60, 25, 45].

The co-receptor BAK1 is a membrane associated kinase that acts as a co-receptor in several signaling pathways. In addition to BR signaling, BAK1 is also involved in mediating cell death control [61] and plant pathogen-associated molecular pattern (PAMP)-triggered immunity, where it acts as a co-receptor for several receptors [62]. While the co-receptor occurs with a lower density than BRI1 thoughout the root [11], BAK1 is not a limiting factor [63]. In BR signaling, the existence of preformed complexes consisting of BRI1 and BAK1 has been discussed with experimental evidence supporting this hypothesis [64, 65]. Interestingly, biochemical interaction studies have shown that both the hormone and an acidic cell wall pH are necessary for the LRR domains of the receptors to interact [25, 44, 45]. Furthermore, structural biology and computational analysis have demonstrated that the ligand acts as glue between the LRR domains, stabilizing the receptor complex [66].

To prevent unspecific signaling activity in the absence of BRs, there are several nega-

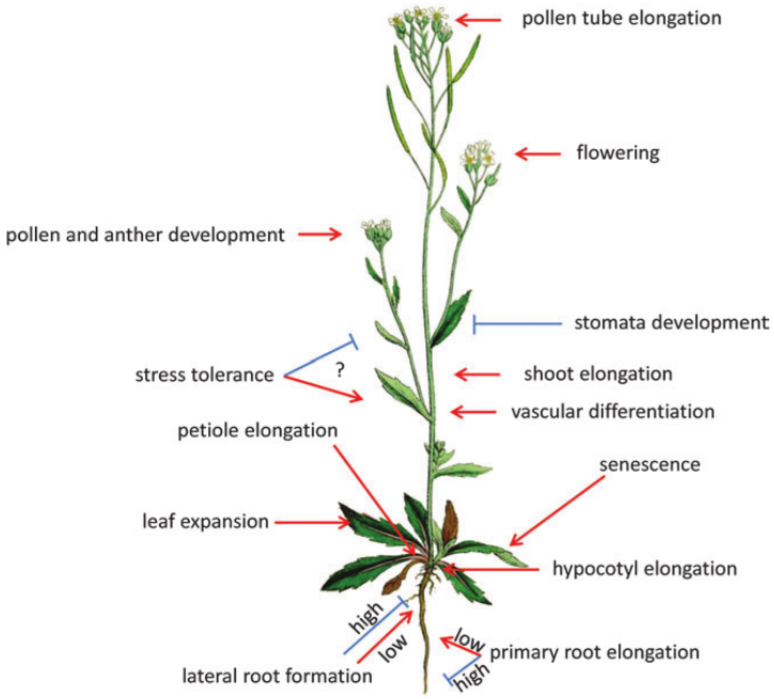

Figure 2.1: Overview of brassinosteroid functions with the respective area of effect. Red arrows indicate a stimulating effect, blue arrows denote inhibitory effects. Figure from [55]

tive regulators that fine-tune the signaling response. In particular, the interaction between BRI1 and BAK1 is regulated by the BAK1-interacting kinase (BIR3) [29, 30], which prevents the formation of an active signaling complex when the hormone is absent [47]. For one, this is achieved by the stable interaction of the ectodomains of BIR3 and BAK1, which requires BR-bound BRI1 to compete with BIR3 for the interaction with BAK1 [47]. Second, BIR3 blocks the kinase domain of BAK1 from interacting with the kinase domain of BRI1 (this thesis). In order for BRI1 and BAK1 to interact in the presence of BIR3, the hormone needs to be present and stabilize the interaction of the extracellular domains [47].
Additionally, BRI1 kinase inhibitor (BKI1) [27] and botrytis-induced kinase 1 (BIK1) [28] inhibit the activity of the receptor. Once BR binds to the receptors, both inhibitors are phosphorylated and released from the cytoplasmic domain of the receptor [28, 27], which can now transfer the signal to the fast response pathway [14, 15, 16] (see section 2.1.1) and the gene-regulatory pathway [1, 56] (see section 2.1.2).

2.1.1 Fast Response Pathway

BRs stimulate a fast, membrane-associated pathway in the plasma membrane of *A. thaliana* [14, 15, 16]. The computational analysis of the activation and regulation of this pathway as a system and the individual components is the focus of this thesis. The fast response pathway comprises the receptor Brassinosteroid-insensitive 1 (BRI1), the co-receptor BRI1 associated kinase (BAK1), the negative regulator BAK1-interacting kinase 3 (BIR3), the

inhibitor BRI1 kinase inhibitor 1 (BKI1), the inhibitor botrytis-induced kinase (BIK1) as well as the Arabidopsis H^+-ATPases 1 and 2 (AHA1/2) [14, 15, 16].

In the inactive state, as depicted in Figure 2.2 A, there is only the basal activity of the H^+-ATPases AHA1 and AHA2 counteracting a proton leak across the membrane and thus maintaining pH homeostasis. BRI1 and BAK1 form complexes with the negative regulator BIR3 [30] and there is no signaling activity.

Upon stimulation with the ligand, BR binds to the receptor BRI1. Subsequently, BRI1 autophosphorylates [67] and recruits the co-receptor BAK1 [23, 24]. BRI1 and BAK1 then phosphorylate each other [31] and then activate the H^+-ATPases AHA1 and AHA2 by an as of yet unknown mechanism (Fig. 2.2 B) [14, 15, 16]. A recent phosphoproteomics study revealed that AHA1 and AHA2 might be phosphorylated by casein kinases (CKs) in response to BR stimulation [68]. The increased activity of the H^+-ATPases then results in the acidification of the apoplast and the hyperpolarization of the plasma membrane [14]. Concomitantly, the cell wall expands [14]. This is understood to be one of the initial steps of expansive cell growth.

H^+-ATPases have been long been implicated to be involved in growth in what is typically called the acid-growth theory [13]. Not only brassinosteroids but also auxin and the peptide growth hormone PSY1 as well as phytosulfokine (PSK) can activate proton pump activity [13, 69, 70, 71].

H^+-ATPase activity is generally regulated via the C-terminal regulatory domain functioning as an autoinhibitor of pump activity [72, 73, 74]. This inhibition can be released by phosphorylation at several residues, such as threonine 948 [75, 76]. These phosphorylations induce the association of 14-3-3 proteins [75, 76] that release the inhibition by the C-terminal regulatory domain [77, 78]. However, in the case of BR signaling experiments have shown the activation of the H^+-ATPases to be independent of the threonine 948 phsophorylation [15].

Currently, signal termination is not fully characterized. BRI1 slowly autophosphorylates in the glycine-rich loop at serine 891, which inhibits BRI1 function and therefore BR signaling activity [79]. Interestingly, the time-scale of these phosphorylations is extremely slow: Upon stimulation with $100\,\mathrm{nM}$ BL the levels of pS891 increases steadily over the course of $12\,\mathrm{h}$ [79]. The dephosphorylation rate of that particular phosphorylation site is even slower. Even after $4\,\mathrm{d}$ of treatment with brassinazole (Brz), an inhibitor of BR synthesis, the phosphorylation of S891 has not yet vanished completely [79].

One potential mechanism to restore the receptor to the initial state has been identified: the serine/threonine-protein phosphatase 2A (PP2A) can interact with BRI1 *in vitro* [80]. PP2A dephosphorylates BRI1 *in vitro* [80], which might be one mechanism to reset BR signaling [81].

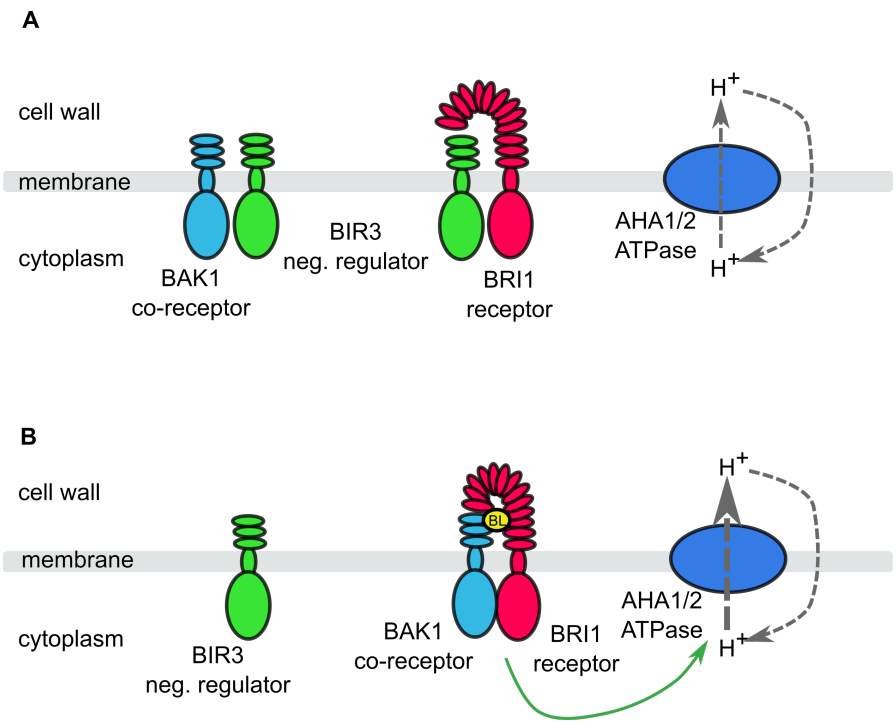

Figure 2.2: Overview of the fast BRI1 associated response pathway in the plasma membrane of *Arabidopsis thaliana*. A: Inactive state of the fast BRI1 associated response pathway in the plasma membrane. BIR3, a negative regulator of the signaling pathway interacts with both BRI1 and BAK1 to prevent signaling without the ligand. Basal activity of the proton pumps AHA1 and AHA2 ensures pH homeostasis. **B:** Active state of the fast BRI1 associated response pathway in the plasma membrane. The ligand brassinolide (BL) binds to the receptor BRI1 and induces its interaction with the co-receptor BAK1. The receptor complex then stimulates AHA1/2 pump activity to induce membrane hyperpolarization and cell wall acidification.

2.1.2 BR-Regulated Gene Expression

In addition to the fast response pathway, BRs also affect gene expression [1, 56] (Fig. 2.3). In particular, BRs control the expression of enzymes responsible for BR synthesis, the receptor BRI1, expansins and auxin response elements [82]. In the inactive state, this signaling pathway prevents the transport of transcription factors into the nucleus by phosphorylation and subsequent degradation (Fig. 2.3).
Upon stimulation with BRs, the initial steps of the signaling pathways that result in the active form of the receptor are identical to the fast response pathway. The active receptor complex then phosphorylates the brassinosteroid signaling kinases (BSKs) [83] inducing the activation of the BRI1 supression protein 1 (BSU1) [84], which in turn dephosphorylates brassinosteroid-insensitive 2 (BIN2) [85, 86]. Dephosphorylated BIN2 is no longer able to phosphorylate the transcription factors BRI1-ems-surpressor 1 (BES1) and brassinazole-resistant 1 (BZR1) [86]. BES1 and BZR1 are then dephosphorylated by serine/threonine-protein phosphatase 2A [87] and can now diffuse into the nucleus, where it affects the expression of BR-repressed and BR-induced genes [86]. Among the BR-repressed genes, there are the receptor BRI1 and enzymes for BR synthesis [82]. This means that on the long term, BR signaling inactivates on its own by reducing both receptor and hormone concentration.

2.2 Computational Modeling

Computational modeling has been a widely used approach in biology in the last decades resulting in an increasing number of models being published [33]. However, models of plant systems have been widely lacking [33]. Successful examples include the auxin model of Vernoux *et al.* [88], where the dynamics of auxin in the shoot apex of *A. thaliana* was analyzed. Another successful example is the detailed analysis of auxin transport in the *A. thaliana* root that revealed that the auxin pattern in the root requires both influx and efflux carriers to be present in order to be reproduced computationally [89].
Just like biological systems have different scales ranging from proteins to whole organisms, there are different scales in computational modeling (Fig. 2.4). While modeling an organisms is only possible in a much reduced way (e.g. pharmaco-kinetic modeling and genome-scale models), other scales can be investigated in much more detail. On a molecular level, protein structures can be modeled based on homology and potential complexes between 3D protein structures can be computed by molecular docking analysis (see p. 12). On a cellular scale, detailed models (e.g. ODE models, stochastic models, spatial models, logic-based models) of metabolic systems or signaling pathways provide insight into the emerging properties and important components of the system of interest (see p. 13). Finally, on a tissue scale, agent-based models show how tissues arise from the interactions of cellular agents (see p. 14).

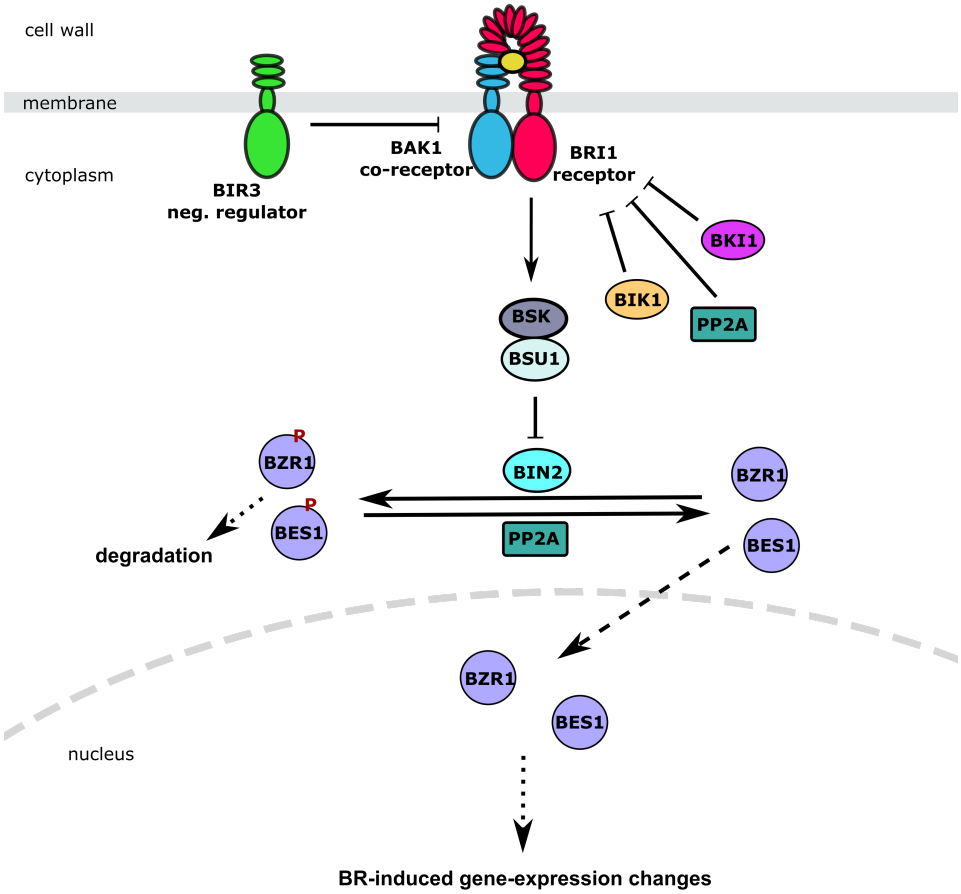

Figure 2.3: Overview of the BR gene-regulatory pathway. BR are detected in the plasma membrane by the receptor BRI1. Without the ligand, BRI1 is inhibited by BKI1, BIK1 and PP2A. Upon ligand binding BRI1 then autophosphorylates and associates with the co-receptor BAK1. After a number of transposphorylations the active form of the receptor complex is achieved, which phosphorylates BSKs. BSKs interacts with BSU1, which dephosphorylate BIN2. Unphosphorylated BIN2 can no longer phosphorylate transcription factors BES1 and BZR1. PP2A dephosphorylates BES1 and BZR1, which can now diffuse into the nucleus and affect gene expression.

.

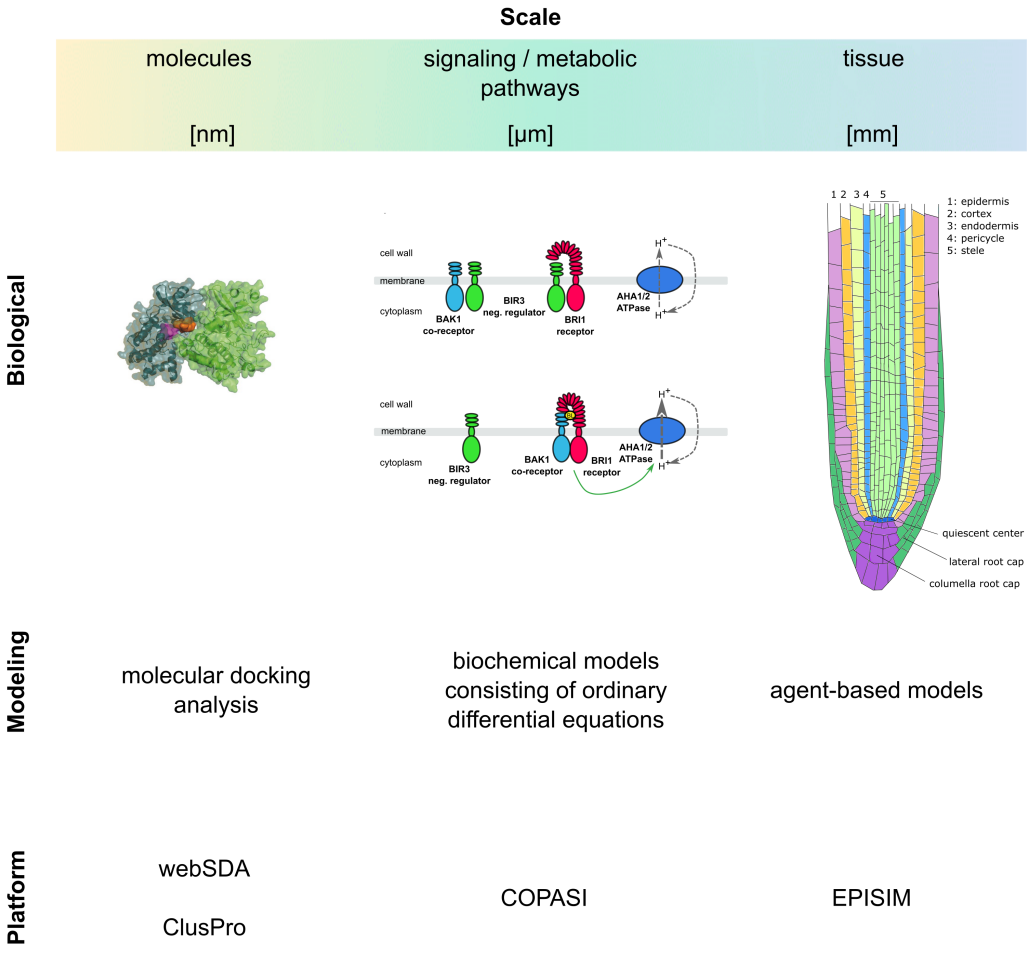

Figure 2.4: Overview of modeling approaches in this thesis. Throughout this thesis several modeling approaches were applied; molecular modeling to compute potential complexes between proteins, ODE modeling to study single-cell dynamic behavior and agent-based modeling linked with a cellular ODE model to study the behavior on organ-scale.

2.2.1 Molecular Modeling

Molecular modeling comprises various different computation methods for computing and analyzing the interactions of proteins, DNA and RNA molecules. In particular, molecular modeling allows for the modeling of protein structures based on sequence homology and the computational complex formations between proteins as well as proteins and DNA. In this case, comparative modeling and molecular docking analysis were employed to study the interactions of the receptor BRI1, the co-receptor BAK1 and the negative regulator BIR3.

As there are not always 3-dimensional structures available for the proteins of interest, a number of methods have been developed to allow for the comparative modeling of a protein, based on the experimentally determined structure of a closely related protein [90, 91]. This modeling approach is based on the fact that proteins sharing a high percentage of sequence identity also have similar structures. While a high degree of sequence identity is always favorable, proteins with as little as 35% sequence identity can provide useful structural information [92].

Furthermore, comparative modeling can also be used to fill gaps in the experimentally determined structures. In particular, flexible loops in protein structures are often a source of uncertainty and thus are represented as gaps in the experimental structures. As these gaps are often of limited length and have a defined start and end point, potential solutions of the structurally unresolved loops can be computed by comparative modeling [91].

Comparative modeling yields an ensemble of potential structures that need to be evaluated based on their quality. Here, the simplest approach is to analyze the torsion angles of the peptide bonds. Experimentally, the ranges of the torsion angles have been studied in great detail leading to the definition of favoured, allowed, generously allowed and disallowed regions for both α helices and β sheets in Ramachandran plots [93, 94]. This can be done by using i.e. the PROCHECK software [95, 96]. A more elaborate scoring mechanism such as QMEAN evaluates a number of different aspects [97, 98]. Instead of determining the torsion angle of a single amino acid bond, QMEAN evlautes the torsion angle in a three amino acid region, which yields more reliable results [97]. In addition, the solvation potential and the interaction potential between Cβ are considered [97].

Molecular modeling also allows for the computational docking of proteins. This modeling approach requires detailed protein structures and environmental conditions to define the reaction space. Potential interactions between the proteins of interest can then by computed by simulating the diffusional association by Brownian dynamics (e.g. webSDA [99, 48]) or by extensive sampling of potential conformations (e.g. ClusPro [49, 49, 50, 51, 52]). In the simulated diffusional association, the proteins start out in different spatial orientations to each other and are docked based on their electrostatic potential (Fig. 2.5). Here, one protein - typically the larger one - is stationary (blue), while the other is mobile (red) and moves around and towards the stationary protein. The potential complexes are then calculated based on the electrostatic energy, electrostatic desolvation and non-polar desolvation energy, in the case of webSDA [48]. By sampling several hundred complexes it is thereby possible to determine likely complexes between the analyzed proteins. Meth-

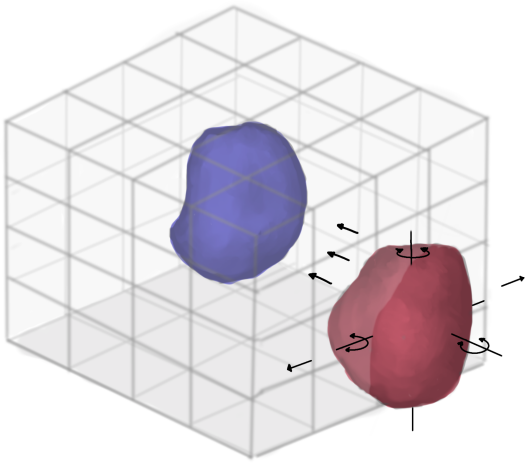

Figure 2.5: Principle of molecular docking analysis by Brownian dynamics. Potential complexes between two proteins are calculated by docking a mobile protein (red) to a stationary protein (blue) considering the elctrostatic binding, the electrostatic desolvation and the nonpolar desolvation energy.

ods that rely on sampling alone, first generate a large pool of potential interactions and filter them based on a scoring function.
There are several webServers that allow the calculation of encountered and docked complexes. In webSDA simulations, encountered complexes are calculated by rigid body docking that keeps both backbones and side chains immobile [48]. Another tool, ClusPro, allows for the computation of fully docked complexes as amino acid side chains are allowed to react to the complex formation by changing their orientation in an additional step [52].

2.2.2 ODE Modeling

Ordinary differential equation (ODE) models describe the evolution of species over one variable, typically time ($\frac{d[S]}{dt}$) or space ($\frac{d[S]}{dx}$). Models consisting of ODEs are versatile tools to understand the dynamic behavior of systems up to a certain model size. ODE models have been successfully used to study specific metabolic and signaling pathways in a myriad of organisms: human erythrocytes [100], *Sacharomyces cerevisiae* [101], *Escherichia coli* [102] and *Streptococcus pyogenes* [103] to name but a few examples.
A tool frequently used to set up and analyze ODE models is the COmplex Pathway Simulator (COPASI) [104]. COPASI provides an intuitive user-interface to construct and simulate ODE models based on biochemical reactions while taking into account the compartment information provided by the user. COPASI allows for the analysis of ODE models using, e.g. time-course simulations, sensitivity analysis, steady state analysis and metabolic control analysis.
Some model analysis methods, such as metabolic control analysis are used to analyze the steady state properties of an ODE model. This method is therefore most useful for

metabolic systems that have a meaningful steady state. Signaling pathways, however, are only in steady state if the signal is absent or when the response reaches a plateau at constant, continuous stimulation. In these cases, sensitivity analysis is instead a suitable tool to determine the important factors of the model's response to a signal.
When modeling a biological system, the ODEs are constructed based on the system's biochemical reactions. Each reaction has a corresponding rate law that defines the speed of the reaction. Ideally, these rate laws comprise detailed information on enzyme speed, reaction mechanism and regulatory elements. However, this is often limited by the lack of detailed experimental data.
Most commonly, reaction rate laws are defined using convenience kinetics [105] and the overall speed of the reactions scales with the size of the compartment, in which the reaction occurs. This is fine as long the reaction occurs in one compartment. However, if the reaction involves more compartment, scaling the speed of the reaction with a compartment volume is thermodynamically wrong [106]. Therefore, in the Systems Biology Markup Language (SBML) [107] and in COPASI [104], these reactions are not automatically scaled with an compartment volume. Instead, it is left to the user to decide the scaling of these reactions. I examine the practical implications of this for ODE models of cellular systems in Chapter 4.

2.2.3 Agent-based modeling

Agent-based models (ABMs) are computational models that allow for the analysis of tissue dynamics. Just as ODE models serve to understand a system as a whole based on the interactions of the involved proteins, an ABM provides a view on the tissue dynamics that emerge based on the cellular interactions. ABMs consist of an cell behavior model (CBM), where cells are modeled as autonomous agents, and a biochemical model that determines how the cellular agents interact with each other.
Several platforms are available to model ABMs in different organisms, using different approaches, e.g. VirtualLeaf for plant tissue [108, 109]. Here, we used EPISIM as platform for the ABM [53]. EPISIM supports both lattice-based and off-lattice simulation approaches to ABMs. The off-lattice, center-based approach to ABMs incorporates ellipsoid cell shapes and allows a more realistic representation of the mechanical interaction forces between cells [110]. In particular, this means that there is no underlying lattice and that cells are defined by their center and a set radius. EPISIM has been successfully applied to study epidermis organization [53] to the extend of barrier formation and hydration [110]. A particularity of EPISIM is the fact that it is possible to import a cellular COPASI model [54]. Typically, agent-based models in EPISIM consist of several aspects:

- The mechanical model determines the overall shape and mechanic properties of the agent-based model.

- The cell behavior model includes the different cell types and dynamics.

- The (optional) ODE model provides a detailed simulation of intracellular processes that occur on a faster time-scale.

By linking these scales it is possible to obtain a more detailed picture of the process of interest as a whole. It allows the examination of processes that occur on a much faster time-scale than the simulation step size of an agent-based model. In the context of organ growth in plants, this integrative approach is crucial as the signaling pathways that initiate growth respond within minutes [14], while noticeable growth requires several hours [7].

3 | Materials & Methods

3.1 Collaborations

The computational models presented in this thesis rely on the experimental data provided by the collaborators. To a large extend, the experiments were conducted by Friederike Wanke and Nina Glöckner in the research group of Prof. Dr. Klaus Harter at the Center for Molecular Biology of Plants (ZMBP) at the University of Tübingen. Nina Glöckner quantified the H^+-ATPase AHA2 as well as the negative regulator BIR3 in relation to the receptor BRI1 (see section 3.3.5). She also measured the pH change in response to hormonal stimulation in the different root zones using HPTS according to a protocol established recently [111] (see section 3.3.5). Dr. Friederike Wanke measured the interaction of BIR3 with both BAK1 and BRI1 using Förster Resonance Energy Transfer (FRED) - Fluoresence Lifetime Imaging Microscopy (FLIM) to validate the results of the molecular modeling (see section 3.2.5). The molecular modeling project also relied on the initial information provided by Sarina Schulze and Dr. Birgit Kemmerling (ZMBP, University of Tübingen). Furthermore, I consulted with Prof. Dr. Rebecca Wade (HITS gGmbH, IWR, Heidelberg University). Finally, Dr. Stefan Scholl in the research group of Prof. Dr. Karin Schumacher (Centre for Organismal Studies (COS), Heidelberg University) provided data for the proton leak into the cell after inhibiting the ATPases by vanadate (see section 3.3.5).
The description of experimental data in this section is meant to provide some background information to the experimental data that were used in combination with the computational modeling. Since I did not conduct the experiments myself, these descriptions are not meant to represent precise protocols but rather help with the understanding of the context.

3.2 Molecular Modeling

3.2.1 Structure / Template Selection

Special care was taken in the structure and template selection for the structural modeling. The Protein Data Bank[1] [112] was used to obtain the template structures. The completeness and overall structure quality were considered in selecting the structure for used for the docking analysis. If an apo structure of sufficient quality was available, that structure was chosen. In the case of BIR3, a template for comparative modeling was chosen based

[1] https://www.rcsb.org/

on maximal sequence identity. Several indicators were used for structure evaluation that are described in the following sections: structure comparison as well as scoring factors for structure quality and structure flexibility.

Structure Comparison

In the case where no apo structure of sufficient quality was available, the potential structures of that protein were evaluated based on similarity (conservation of structure and root mean square distance (RMSD) of the C_α atoms in the amino acid backbone), completeness, and the structure quality evaluation available as part of the protein entry in the Protein Data Bank[2] [112, 113].
The structure comparison was done using the MatchMaker and Match→Align tools in Chimera [114, 115]. In particular, in the MatchMaker tool, a structure based alignment was generated using the Needleman-Wunsch algorithm and the BLOSUM62 matrix [116]. A gap opening penalty of 12 and a gap extension penalty of 1 were applied to the alignment. In the Match→Align tool an alignment was created by superposition, where residues at a distance exceeding 5 Å were no longer considered for superposition.

QMEAN

The structures were evaluated based on the QMEAN (Qualitative Model Energy ANalysis) score [97, 98] using the QMEAN server[3]. Generally speaking, the closer the QMEAN score is to zero, the better is the evaluated structure. A QMEAN score below -4 is a sign of a low quality structure (see SWISS-MODEL documenation[4]).

B-Factor

Structures were also evaluated based on the flexibility throughout the structure. A measure for this is the B-Factor B, also called temperature or Debye-Waller factor [117]. The B-Factor represents an estimate of how much atoms oscillate from their calculated, average position [117, 118]. In protein structures it describes the the mean squared displacement u^2 of the individual atoms and calculated according to the following equation [118]:

$$B = 8\pi^2 u^2 \tag{3.1}$$

The B-factor is part of every protein structure file deposited in the Protein Data Bank and required no additional computational effort.

[2] `https://www.rcsb.org/`
[3] available at `http://swissmodel.expasy.org/qmean`
[4] `https://swissmodel.expasy.org/docs/help`, last accessed 30.05.2018

Multiple Sequence Alignment

The multiple sequence alignment of the cytoplasmic domains of BAK1, BRI1, BIR2 and BIR3 was done using the Multiple Sequence Alignment tool Clustal Omega of the European Bioinformatics Institute[5] [119, 120, 121]. The standard settings were used.

3.2.2 Comparative Modeling

Comparative modeling was used to generate a structure for BIR3 and to fill the structurally unresolved parts in the structures of BRI1. The comparative modeling was conducted with Modeller v9.16 [91]. The pdb files were downloaded from the Protein Data Bank[6] [112]. The structure of BIR3 (At1g27190) was modeled based on the structurally resolved parts of the cytoplasmic domain of BIR2 (Uniport ID Q9LSI9, PDB ID 4l68, *Arabidopsis thaliana*, expressed in *Escherichia coli*) [122]. BRI1 was modeled based on an existing structure of the BRI1 cytoplasmic domain (BRI1 - Uniprot ID O22476, PDB ID 5lpw, *Arabidopsis thaliana*, expressed in *Escherichia coli* [123]), where comparative modeling was employed to fill the gaps in the structure.
As a first step, all modified residues were removed from the templates and replaced with the respective unmodified residue. An alignment of the amino acid sequence and the structurally resolved parts was generated using the algorithm implemented in Modeller version 9.16 and the code listed in the Supplementary Information on p. 177. On the basis of these alignments and with a resolution of 2 Å, a total of 20 structures were generated for each protein (see Supplementary Information p. 179).
The structures were evaluated based on the QMEAN4 score (see p. 18). If two or more modeled structure shared the same QMEAN4 score, both structures were chosen for further modeling.

3.2.3 Docking

Electrostatic Potential

The electrostatic surface potential of the proteins was checked to determine the relevance of phosphorylated residues in the structures of BAK1, BRI1 and BIR3. To this end, a pqr file of the charge distribution at pH 7.2 was generated using the PDB2PQR server[7] [124]. This pqr file was then opened in Chimera, a visualization and analysis tool for protein structures [114, 115]. Here, the pqr file was used to generate a grid file of the charges using the ABPS (Adaptive Poisson-Boltzmann Solver) tool that accesses the ABPS server. The webserver was directly accessed using Chimera [125]. Based on the generated electrostatic potential map file, the surface was colored accordingly.

[5] https://www.ebi.ac.uk/Tools/msa/clustalo/
[6] https://www.rcsb.org/
[7] http://nbcr-222.ucsd.edu/pdb2pqr_2.1.1/

webSDA

The "Webserver for Simulation of Diffusional Association 1.0" (webSDA)[8] of the Heidelberg Institute for Theoretical Studies gGmbH [48], served as platform for running the molecular docking analysis [99, 126, 127, 128]. Using webSDA, 500 potential complexes of the gap-filled structures were computed in 500 SDA runs based on the electrostatic interaction [125, 129], electrostatic desolvation [130] and non-polar desolvation [131] at an ionic strength of 150 mM and a pH of 7.2.
The docking of BRI1 and BAK1 had an allowed center to center distance of 45 Å between the proteins to prevent the formation of complexes blocking the N- or C-termini. The docking of BAK1 and BRI1 with BIR3 was not subjected to a center-to-center constraint to get an unbiased estimate of the energetic landscape. The complexes were selected based on the criteria listed in section 3.2.4.

ClusPro

In addition to webSDA we used ClusPro to generate fully docked complexes of the proteins of interest [49, 132, 50, 51, 52]. For the docking between BIR3 and either BAK1 and BRI1, the standard settings were used and no distance criterion was imposed. The complexes were evaluated based on the scoring function describing van der Waals and electrostatic forces.
To reproduce the settings of webSDA for the docking of BAK1 and BRI1, I included a constraint in the form of JSON (JavaScript Object Notation). This constraint limits the distance between the residues at the centers of the structures to a maximum of 45 Å. The JSON constraints were generated using the web tool, which is available as part of ClusPro[9] and are included in the supplementary information (see Supplementary Information B.2.1 p. 180). As the scoring function based on van der Waals and electrostatic forces consistently yielded no feasible complexes within the criteria, the balanced scoring function was used instead to evaluate this docking run.

3.2.4 Complex Selection

Not all of the complexes computed by docking analysis were biologically feasible. To select the biologically relevant complexes a series of criteria was developed. The failure to meet one of the criteria resulted in the exclusion of a complex from further analysis.

- All structures used during the docking analysis are truncated at both N- and C-termini. Therefore, the following constraints were added:
  - Neither N- nor C-terminus was allowed to be part of the interaction surface. To specify this criterion I introduced the "minimal distance criterion" below.

[8] available at `http://mcm.h-its.org/webSDA`
[9] `https://cluspro.org/generate_restraints.html`

  - The C-terminus **was not allowed** to extend to where the membrane would be. If the C-terminus was as close or closer to the approximate location of the membrane than the N-termini of both proteins, this was considered to be a clash (Fig. 3.1).
  - The N-terminus **had to be allowed** to extend to where the membrane would be.

- Assuming that the extracellular or transmembrane domains are also involved in the interaction between proteins, the N-termini of the proteins have to be oriented in approximately the same direction. Therefore, proteins were not allowed to interact by C-terminal and N-terminal (membrane proximate) domains or by their C-terminal domains along the longitudinal axis.

To specify the first criterion a "minimal distance" was introduced, more precisely a minimal distance for the N- and C-terminus of one protein from the surface of other protein in the complex. This minimal distance was defined by sampling the complexes computed for the proteins interest at the interaction surface and measuring the distance between amino acid backbones in Pymol [133] (sample size $n = 100$). The resulting distribution approximately follows a normal distribution (Fig. 3.2). Using a threshold of $x + 2\sigma$, where x is the mean and σ is the standard deviation of the sample, we expect to cover $97.8\,\%$ of potential clashes. Different thresholds were applied for ClusPro complexes and for webSDA complexes since one yields docked complexes and the other yields encountered complexes. The distribution of distances between proteins for complexes computed by webSDA (Fig. 3.2 A) yielded a mean distance of $x = 9.403$ and a standard deviation of $\sigma = 1.733$, which results in a threshold of 11.136 Å. In comparison, the distribution of complexes computed by ClusPro (Fig. 3.2 B) has a mean of $x = 6.447$ and a standard deviation of $\sigma = 1.478$, which results in a threshold of 9.403 Å. The complexes were rendered in Chimera [114]. As the number n_K of complexes within a cluster K is an indicator for the energetic landscape of the observed cluster [52], the complexes were evaluated based on the relative cluster size. The relative cluster size f was defined as

$$f = n_K / N_{total\,observed\,complexes} \quad , \tag{3.2}$$

where the number of complexes in a cluster n_K is scaled with the total number of observed complexes $N_{total\,observed\,complexes}$ in that docking run. This was done to allow for the comparison of webSDA and ClusPro results, as the two methods record and cluster a different number of complexes per docking run.

3.2.5 FRET-FLIM Measurements

To validate the result of the molecular docking analysis, Friederike Wanke conducted a FRET-FLIM experiment and measured the occurrence of the complexes between BIR3, BAK1 and BRI1. To this end, C-terminal fusions of GFP (BIR3) and mCherry (BAK1

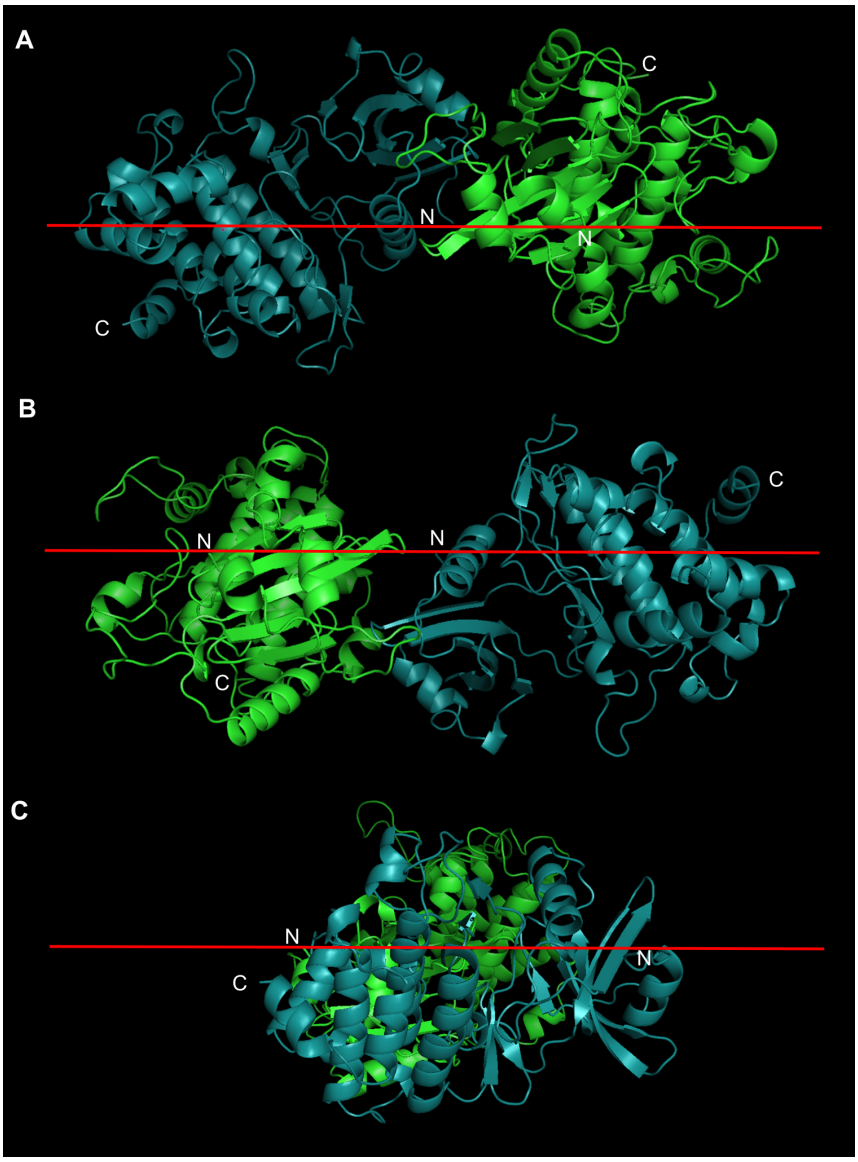

Figure 3.1: Definition of a membrane clash in potential complexes. A, B: The C-terminus of one protein in the complex clashes with the membrane. A clash occurs if the C-terminus is as close or closer to the membrane than the line defined by both N-termini and if the C-terminus continues in the direction of where the membrane would be. A & B show different orientations for the same complex. **C:** Example of a complex that is close to be considered a membrane clash but is considered feasible according the the analysis parameters.

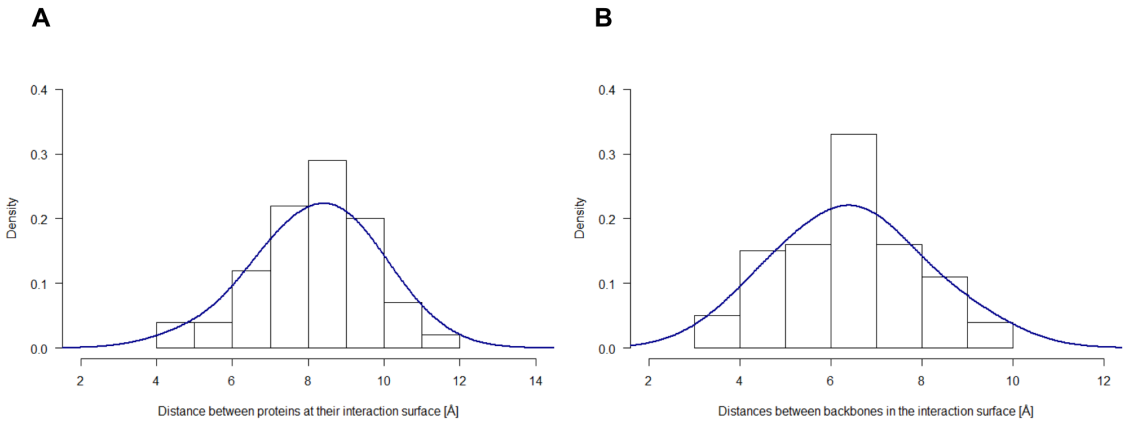

Figure 3.2: Density of sampled distances between amino acid back bones in protein complexes. A: Distribution of distances in complexes computed by webSDA. **B:** Distribution of distances in complexes computed by ClusPro. Sampled were the distances between amino acid backbones in protein complexes at the interaction surface between the proteins ($n = 100$).

and BRI1) [134, 135] were expressed in combination with a gene silencing suppressor, transformed into *Agrobacterium tumefaciens* strain GV3101 and infiltrated into *Nicotiana benthamiana* leaves.

The FRET-FLIM measurements were performed 2 days after infiltration. The lifetime τ [ns] was measured with a pulsed laser as excitation light source of $470\,\mathrm{nm}$ and a repetition rate $40\,\mathrm{MHz}$. The lifetime τ of the donor only serves as control for the measurements. All measurements were repeated for three different biological replicates consisting of at least seven cells. The GFP fluoresence lifetime was determined by data processing using the SymPhoTime software and bi-exponential curve fitting, while correcting for the instrument response function (IRF) and using a fitting range from channel 90 to channel 1400.

To ensure the statistical significance of the results, Nina Glöckner ran a Steel-Dwass test on the FRET-FLIM data using JMP version 13.1 (SAS Institute Inc., Cary, NC, 1989-2007). As the samples displayed significantly different variances, the application of an analysis of variance (ANOVA) test was not possible.

3.3 ODE Modeling of the Fast BR Response

3.3.1 Model Setup

The model was built in the COmplex PAthway SImulator (COPASI) version 4.23 build 184 [104] running on WINDOWS 8. COPASI allows for the definition of multiple compartments, species, global quantities and events to model a system based on biochemical reactions that are used to construct an ODE model. The ODEs are generated automatically using the rate laws of the individual reactions.

Units The units of the model were chosen such that the units of volume and area compartments were compatible: dm^3 (l) for volumes and dm^2 for areas. The model time was measured in s and the concentrations in nmol.

Compartments COPASI build 184 is the first version that allows for two-dimensional compartments. Therefore, the membrane was actually included as an area instead of using a three-dimensional compartment and treating it as if it were two-dimensional. Cell wall and cytosol were defined as three-dimensional compartments.

Reactions The model reactions were defined by indicating substrate and product. The reversibility of the reaction was indicated by the symbol, $\rightarrow$ for an irreversible reaction and $=$ for a reversible reaction.

Rate Laws The velocity v_i of reaction r_i was defined in the rate law. Since most of the reactions between the signaling components concern processes occurring within a protein complex, there can be no saturation. Therefore, these reactions were described by mass action kinetics:

$$v_i = k_i \cdot [substrate] \tag{3.3}$$

Here, the reaction rate is defined by k_1 and $[substrate]$ is the transient substrate concentration. Reactions occurring between proteins, which were not in a complex, were described by a simple saturation kinetics:

$$v_i = \frac{V_{max} \cdot [substrate]}{[substrate] + K_m} \quad , \tag{3.4}$$

where V_{max} is the maximum reaction velocity and K_m defines the substrate concentration where $\frac{1}{2}V_{max}$ is reached. More precise, V_{max} is defined as the product of the enzyme concentration $[E]$ and the enzyme's turnover number k_{cat}.
For the reactions with known regulators, the appropriate term was included in the respective rate law. Based on the currently available experimental knowledge, only inhibitors are known to act on the fast BR response. Here, the denominator of the rate law was multiplied with $(1 + \frac{[inhibitor]}{K_i})$ indicating a non-competitive inhibitory mechanism [105].

3.3.2 Parameter Estimation

Not all parameters of the model are experimentally determined and, therefore, had to be estimated. This is achieved by minimizing the least-squares function, which is a measure for the difference between model behavior and experimental data:

$$E(P) = \sum_{i,j} w_j (x_{i,j} - y_{i,j}(P))^2 \quad , \tag{3.5}$$

where $E(P)$ is the difference function for the parameter set P, w_j is the weighting factor of the data set, $x_{i,j}$ are the data points i of the data set j and $y_{i,j}(P)$ is the model value corresponding to the data point $x_{i,j}$ for the parameter set P. The weighting factor w_j is used to scale between different orders of magnitude of individual parameter sets. Since w_j is not squared automatically, any weight applied needs to be squared by the user.
For this project, different strategies were applied to parameter estimation. The initial parameter estimation was done by switching between particle swarm [136], a global optimization method, and Hooke-Jeeve's algorithm [137], a local optimization method, all as implemented in COPASI. To explore the parameter space, 50 parameter estimations with randomized starting values were set up on the computing cluster with the particle swarm algorithm.
Wherever possible, experimental data were used to define the allowed range for parameters during parameter estimation. If no data were available at all the range was set to 10^{-6} and 10^{6}.

Local Methods

Local parameter estimation methods generally utilize the gradient of the objective function. Here, the Hooke-Jeeves algorithm was used, which has a slightly different approach to determining the new parameter values: Instead of merely using the gradient, it checks for patterns in the development of the objective functions and follows these until the (local) minimum is reached [137].

Global Methods

Global parameter estimation methods take a different approach to optimization. For one, several parameter sets are evaluated per function evaluation, thus spanning a wide range of the parameter space. It is therefore more unlikely for global optimization methods to become stuck in a local minimum. Some global parameters also contain a stochastic element. For example, both the genetic algorithm [138, 139, 140, 141] and the particle swarm algorithm [136] can introduce changes in a parameter set ("mutations").
The ODE models in this thesis have been fitted using the particle swarm algorithm. For the fits running on the computing cluster, $15,000$ generations with a population of 100 parameter sets and the random number generation turned on. Local fits were run switching between particle swarm (100 generations, 100 parameter sets, random number generation on) and Hooke-Jeeves (see previous paragraph) to speed up the estimation process.

3.3.3 Model Simulation

Time-Course Simulations

For this model, time-courses were simulated deterministically using the LSODA solver as implemented in COPASI. The LSODA solver switches automatically between integration methods for stiff and non-stiff systems [142].

Sensitivity Analysis

To determine the importance of the individual model parameters, the scaled sensitivities were calculated as defined in COPASI build 184. Generally speaking, sensitivites are defined as the change of a model quantity X resulting from a change in model paramter P :

$$sensitivity = \frac{\delta X}{\delta P} \tag{3.6}$$

These unscaled sensitivities have the drawback that even within one model it is impossible to compare the numerical values of the sensitivities due to different parameter values. Thus, the scaled sensitivities were used here:

$$scaled\ sensitivity = \frac{\delta X}{\delta P} \cdot \frac{P}{X} = \frac{\delta ln(X)}{\delta ln(P)} \tag{3.7}$$

Scaled sensitivities are normalized with the actual paramter values of X and P allowing a comparison of sensitivity values within one model.

Parameter Scan

To determine the dose-response of the model to the negative regulator BIR3, a parameter scan was set up of time-course simulations for the factor describing the BIR3 expression level. By scanning the factor from 0 to 100 in 99 non-logarithmic intervals, the responsiveness of the model after $30\,\mathrm{min}$ was characterized from the *bir3* deletion to the overexpression level assumed for the 35S promotor in the overexpression experiments done by Imkampe *et al.* (2017) [30].

3.3.4 Visualization

Plotting The simulation results of the ODE models in this thesis were visualized by plotting in R [10] [143].

Movies To illustrate the results of the elongating cell model, I combined the plots of the cellular dimensions into a movie using ImageJ [144].

[10] `https://r-project.org`

3.3.5 Experimental Data

Membrane Potential Change

Caesar *et al.* (2011) measured the membrane potential change in response to 10, 50 and $100\,\mathrm{nM}$ BL and showed that a fluorescence lifetime change in BRI1-GFP (FLT) can serve as a readout for this change [14]. As I knew that the response to BL exceeds the $20\,\mathrm{min}$ and that the FLT changes by $-0.007\,\mathrm{ns\,min^{-1}}$ for $30\,\mathrm{min}$ after stimulation with BL (Prof. Dr. Klaus Harter, personal communication), I extrapolated the membrane potential change for the BL response to up to $30\,\mathrm{min}$. Here, I increased the range of the extrapolated BL response according to the standard deviation originally measured at $20\,\mathrm{min}$. Based on the standard deviations from the mean membrane potential change, I reconstructed three time series for each dose of BL.
To ensure that the model also shows the correct dynamics for the resting membrane potential, I included several data points of the resting membrane potential at different time points up to model stimulation. The data used for fitting are included in the supplementary information (see Section C.4 p. 187).

Protein Quantification

To increase the amount of experimental data in the model, the proteins AHA2 and BIR3 were quantified in relation to the receptor BIR1, which has been quantified experimentally in great detail by van Esse *et al.* (2011) [11]. This was done by both Western blotting of the whole root and fluoresence microscopy of single roots.

Batch Experiments For the protein quantification by the Western blotting, four plates of seedlings were prepared for each of the following transgenic lines: Col-0, pBRI1::BRI1-GFP, pBIR3::BIR3-GFP and pAHA2::AHA2-GFP. Shoot and root were separated before protein extraction. After gel electrophoresis and transfer, BIR3-GFP, AHA2-GFP and BRI1-GFP were detected in Western Blotting by an anti-GFP antibody.

Single Plants Nina Glöckner further quantified the negative regulator BIR3 and and the H^+-ATPase AHA2 by fluoresence microscopy. The following plants were used for the analyis: Col-0 pBRI1::BRI1-GFP, pBIR3::BIR3-GFP and pAHA2::AHA2-GFP. The quantification was done my measuring and adding up the fluorescence in a $50\,\mu\mathrm{m}$ times $50\,\mu\mathrm{m}$ area. The BIR3-GFP and AHA2-GFP were then quantified in relation to BRI1-GFP after subtracting the background and the signal by free GFP.

Microelectrode Ion Flux Estimation (MIFE)

Microelectrode Ion Flux Estimation (MIFE) is a non-invasive method that uses a microelectrode to measure the ion movement at the root surface. By measuring the voltage of the solution in comparison to the liquid ion exchanger in the electrode tip at two different

distances from the cell surface, it is possible to determine the direction of ion flux. Let U_1 be the current closer to the root and U_2 the current further away from the root. Then, if $\Delta U > 0$ there is a net influx, and if $\Delta U < 0$ there is net extrusion of ions from the root. The MIFE experiments were conducted with Col-0 and *bri301* plants at different distances from the root tip with 10 nM brassinolide and with DMSO serving as control.

pH Measurements

The pH measurements were done using the water-soluble dye 8-Hydroxypyrene-1,3,6-trisulfonic acid trisodium salt (HPTS). HPTS has recently been applied to measure auxin induced pH changes in the root [111]. The protonated and unprotonated forms of HPTS occur in a pH-dependent manner and have different absorption and emission spectra. To measure the extracellular pH, 4 day old seedlings were transferred to solid growth medium with 1 mM HPTS and imaged after incubation using a Zeiss 710 confocal microscope with a 405 nm and a 458 nm laser. The ratiometric image is calculated by dividing the signal intensities of the two channels.

Proton Leak Measurements

An estimate of the proton leak was provided by Dr. Stefan Scholl (research group of Prof. Dr. Karin Schumacher, COS, Heidelberg University) by measuring the pH change in the cell wall after treatment with vanadate, which inhibits P-type ATPases but not V-type ATPases. The seedlings stably expressed SYP122-pHusion. SYP122 is located in the cell membrane [145], with the pHusion molecule being located in the cell wall. pHusion is a combination of mRFP and eGFP, the latter of which is pH sensitive [146]. The ratio of the fluorescent signal after excitation at $488\,\mathrm{nm}$ and $561\,\mathrm{nm}$ yields quantitative data of the pH between 4.8 and 7. The plants were treated with $500\,\mu\mathrm{M}$ ortho-vanadate and the pH was measured after $30\,\mathrm{min}$ and $60\,\mathrm{min}$ based on the fluorescent ratio of mRFP and eGFP in the elongation zone. The measurements were conduted for $n = 30$ seedlings. Plants treated with normal medium were taken as control. The calculations are listed in the Supplementary Information (p. 181).

3.4 Agent-Based Modeling

The agent-based modeling was done using the platform EPISIM [53] running on Windows 8. The ABM consisted of a biochmechamical model (see section 3.4.1), a cell behavior model (see section 3.4.2) and a cellular ODE model (see section 3.4.3).

3.4.1 Biomechanical Model

The biomechanical model describes both biomechanical forces and initial settings for the ABM, which are encoded in java and loaded into the cell behavior model. The underlying biomechanics in this agent-based model are based on a center-based 2D approach. As basis for the root biomechanical model, Erika Tsingos adapted an existing center-based 2D model in the EPISIM code [53] to the root tip. This means that pressure and adhesive force act between the centers of two neighbouring cells a and b, which are at a distance of $d(a,b)$ (according to [110]):

$$F(a,b) = F_{pr}(a,b) + F_{adh}(a,b) \tag{3.8}$$

Here, the pressure force F_{pr} scales with the degree of overlap between the cells. As long as the overlap is between 15% and 50% a linear dependency of the pressure force and the degree of overlap is assumed to follow a spring like dynamic. Exceeding that threshold of 50% the pressure force becomes exponential.
The adhesive forces between cells are also modeled by spring dynamics that correlate with the interaction area between cells a and b. However, adhesion only occurs if cells are within $1.3 \cdot d_{opt}(a,b)$. The optimal distance $d_{opt}(a,b)$ is calculated depending on the centers of the cells a and b.
Erika Tsingos and I adapted an existing center-based 2D model, which was part of the EPISIM simulator code, to account for particularities in the root tip. Notably, cell division does not occur in all direction equally, but rather in a transverse direction such that the new cells are placed along the longitudinal axis [147]. Instead of generating a completely new position for the daughter cell, the position along the x-axis was inherited from the mother cell. The details of all changes are explained in the corresponding results section.

3.4.2 Cell Behavior Model

The cell behavior model (CBM) of the agent-based model was setup using the EPISIM Modeller, which is part of the EPISIM platform [53]. The network describing the behavioral rules of the CBM were defined using sub-models, transitions, states and edges as pre-defined in EPISIM [53] (Fig. 3.3). Global parameters were introduced to describe division rate and cell height. The division rate was adjusted from the experimentally observed values (in $\mathrm{cell}^{-1}\,\mathrm{h}^{-1}$) [7] to the time step of the cell behavior model (in $\mathrm{cell}^{-1}\,10\,\mathrm{min}^{-1}$) [7].

3.4.3 Cellular ODE Model

The cellular ODE model was constructed in COPASI v4.23 (build 184). To prepare the model for integration in EPISIM, the model was simulated for $24\,\mathrm{h}$ to allow for the complex formation between BIR3, BAK1 and BRI1 and to update the species concentrations. The dose of BL was set to $10\,\mathrm{nM}$ BL and the model was exported in SBML. This SBML model was then loaded in the CBM and linked by referring to the sbml entities as loaded by

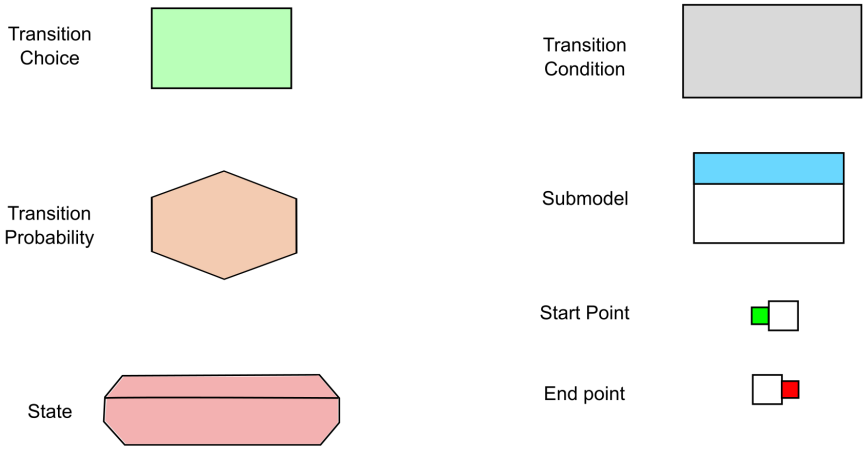

Figure 3.3: Components of the cell behavior model. A cell behavior model in EPISIM [53] consists of transition choiches (green), transition probabilities (orange), state changes (red), transition conditions (grey), submodels (blue) as well as a start and end point of the simulations.

EPISIM. The ratio of simulation steps was determined by trial and error: One simulations step in the CBM is equivalent 2100 simulation steps in the ODE model. Thus, the scale was set accordingly. Notably, EPISIM simulates one instance of the ODE model per cell simulated in the cell behavior model.

3.4.4 Model Simulations

Model simulations were run using the EPISIM Simulator [53]. One simulation step represents a duration of 600 seconds. During the simulations, one snapshot was taken per simulation step. These snapshots were later converted into a movie using ImageJ [144].

4 | Multi-Compartment Rate Laws

BRs affect cell morphology in a number of different ways. For one, BRs induce cell swelling by hydration [14], which is preceded by cell wall acidification [17, 18, 19, 20]. Second, BR signaling is involved for cell elongation [2, 17, 21]. Both processes change the cellular dimensions, which in turn is crucial for the choice of modeling approach.

In ODE models it is generally assumed that all species exist in well mixed containers, the compartments. By assuming a uniform distribution of species within a compartment, it is possible to ignore the spatial aspect to reactions and instead analyze the purely temporal dynamics of species. Based on this assumption, the speed of reactions is generally scaled with the volume of the compartment, where the reaction occurs. This is not the case for reactions that span more than one compartment, as these scale with the area between compartments [106]. Here, it is wrong to scale the rate laws of these reactions with the volume of a compartment. Some software still scale the rates of these reactions with the compartment volume (e.g. PottersWheel [148]). However, both COPASI [104] and SBML [107] do not presume any automatic scaling. Instead, it is the responsibility of the user to define the reaction rates correctly.

As long as neither cell shape nor cell size change throughout the course of a simulation, it is possible to create an equivalent model using a volume-scaling or one compartment model. It does, however, require careful treatment of the parameter values and information content. As soon as the model is transferred to a different setting (different cell shape or size) all parameters of multi-compartment reactions need to be readjusted.

Differences in cell shape can indeed have an impact on how a system reacts to certain stimuli. For example, signal-modulated negative regulators have different dynamics depending on the cell shape in a spatial partial differential equation (PDE) model of the β-adrenergic receptor response [149]. Experimentally, the controlling influence of cell shape and morphology is well documented [150, 151, 152, 153]. For computational models, the general impact of cell shape and size had been demonstrated for spatial PDE models [154, 155].

Here, I examine how different approaches to model multi-compartment processes in ODE models react to changes in cell morphology. As BR signaling affects both cell size and cell shape, it was crucial that I analyzed the impact of this in order to describe all multi-compartment reactions correctly. The inclusion of two-dimensional compartments is not common in ODE models. If the membrane is included as compartment in the ODE model [156, 149, 157], this model often serves as basis for constructing a PDE model, where the spatial impact is analyzed [149, 157].

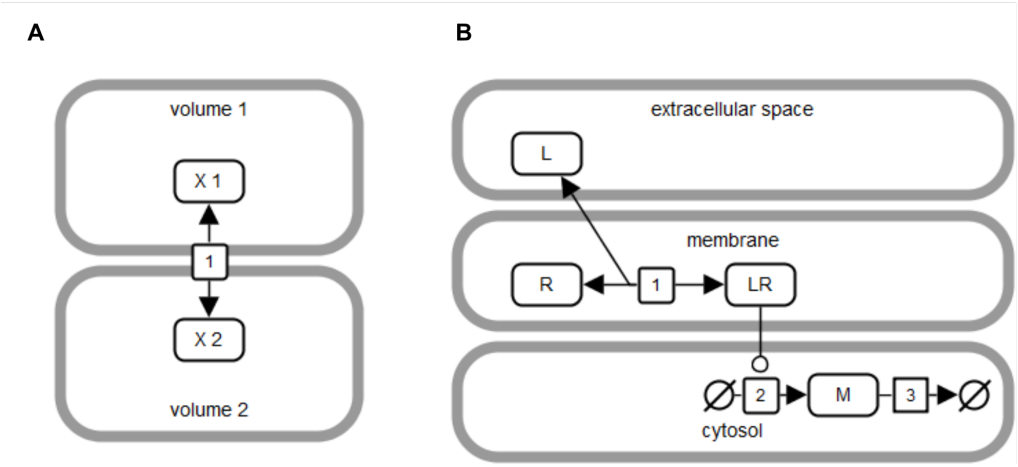

Figure 4.1: Toy models used to analyze the importance of multi-compartment rate laws. **A:** Transport model. **B:** Receptor model. The reaction numbers are indicated in the reaction icon. This scheme was created using VANTED [158] according to the SBGN standard [159].

To analyze the impact of cell shape and morphology in ODE models, I will examine the practical aspects of the following modeling approaches - multiple compartments with interaction area, multiple compartments without an interaction area (COPASI default) and one universal compartment. In the last approach, species that normally exist in different compartments are instead differentiated by name (i.e. cytosolic calcium ions Ca^{2+}_{cyt} and endoplasmic calcium ions Ca^{2+}_{ER}).
I examined the impact of the different modeling approaches in two ways. For one, I analyzed the behavior of simple toy models to determine the effect of the different modeling approaches on model behavior. Here, I also determined the information content of the parameters that describe the reactions between multiple compartments. Next, I collaborated with Pascal Holzheu (research group of Prof. U. Kummer, Bioqant, Heidelberg University) to check the behavior of published biochemical models.

4.1 Toy Models

Starting with the analysis of the toy models allows a first, simplified view into how the different modeling approaches impact model behavior and the information content of the individual parameters. To this end, I studied two models - a transport model (Fig. 4.1 A) and a simple receptor model (Fig. 4.1 B) - to ascertain the informational content of individual parameters in each model. The scenarios examined for the toy models were chosen to represent a physiologically relevant situation.
To determine how much the modeling strategy can impact the model response depending on the choice of model structure, I chose different spatial conformations to model that represent relevant biological scenarios (Fig. 4.2). As cell sizes differ greatly between the different root zones [11], the first set of simulations concerns the transport of a substance from the cell wall into an epidermis cell in each root zone. Here, I considered an epidermis

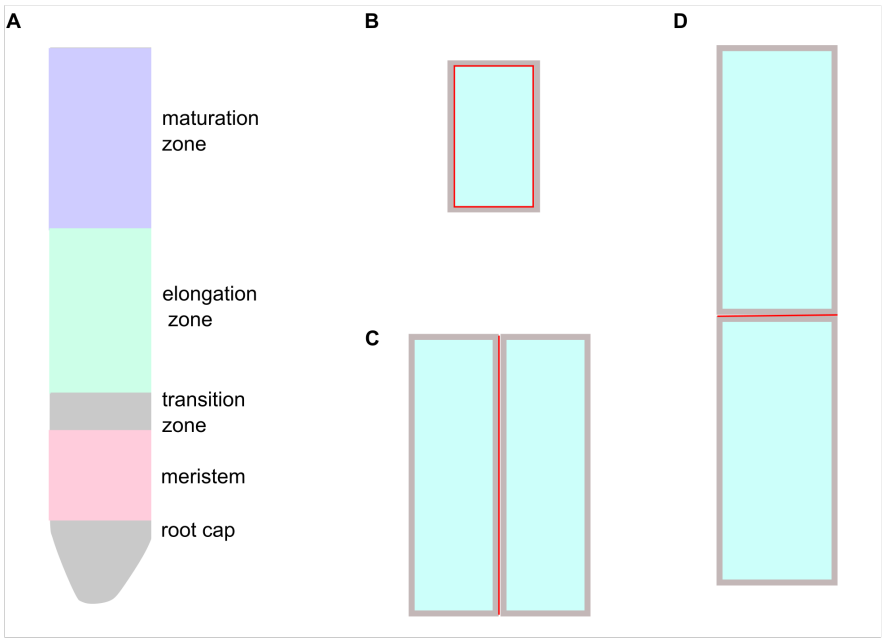

Figure 4.2: Overview of modeled situations for the transport and receptor toy models. **A.** Represented root regions highlighted in color. Rosa: meristematic zone; green: elongation zone; blue: maturation zone. Cell dimensions were taken from a representative epidermis cell of that region [11]. **B-D:** Modeled scenarios with the interaction area highlighted in red. **B:** Transport into a cell from the cell wall. **C:** Horizontal transport between two cells. **D:** Vertical transport between two cells. C & D concern cells of identical cell type in the same root region.

cell in the meristematic zone, in the elongation zone and in the maturation zone (Fig. 4.2 B).

Furthermore, I considered directional transport both horizontally (Fig. 4.2 C) and vertically (Fig. 4.2 D) between two cells of the same cell type and root region. Using these spatial conformations, I analyzed the behavior of the transport model for all modeling approaches.

4.1.1 Transport Model

The transport model only comprises the reversible transport of the model species, X_1, from compartment V_1 into another compartment V_2, where it is denoted as X_2. Thus, the whole system is described in one reversible reaction:

$$X_1 \underset{v_{-1}}{\overset{v_1}{\rightleftharpoons}} X_2 \quad , \tag{4.1}$$

where v_1 and v_{-1} describe the transport rate of X_1 and X_2, respectively. To address a biologically relevant situation, I used the information on plant epidermis cells across the different root regions [11] and looked at how the transport across the membrane might change (Tab. 4.1). In particular in plant roots, transport patterns of auxin have been analyzed and shown to have a deciding impact on root growth and development [89]. Therefore, I also checked the horizontal and vertical transport between cells of the same cell type and root region. To determine the impact of the different modeling approaches on model behav-

Table 4.1: Overview of compartment sizes used in the toy model simulations. * Cell wall volume was calculated according to membrane area and the experimentally determined cell wall thickness [11].

Root Zone	**Cell Wall*** V_1 [µm^3]	**Membrane** A [µm^2]	**Cytosol** V_2 [µm^3]
meristem	302.965	767	847
elongation	2082.835	5273	5803
maturation	5054.025	12 795	16 367

ior in changing spatial conformations, I modeled the different transport model structures without adjusting the parameters in between as described earlier. One adjustment was made to allow for an easier comparison of the different model approaches: In the model consisting of only one compartment, the initial particle number of X_1 was adjusted to be the same as in the other two modeling approaches. By having the identical number of particles at the beginning of the simulation, the time-scales can be compared more easily.

Multi-Compartment, with Area-Scaling

The transport between two three-dimensional compartments scales with the interaction area between these compartments. Therefore, the mathematical description of inter-compartment transport should read like the following equation:

$$\frac{d([X_1] \cdot V_1)}{dt} = -\frac{d([X_2] \cdot V_2)}{dt} = A_{interaction} \cdot (-k_1 \cdot [X_1] + k_{-1} \cdot [X_2]) \quad , \tag{4.2}$$

where the change of X_1 and X_2 in the different compartments depends on the interaction area, $A_{interaction}$, and the transport rate constants, k_1 and k_{-1}. A larger interaction area between the compartments or a more permeable membrane result in a faster equilibrium between the compartments V_1 and V_2.
The distinction between membrane and interaction area is intentional, as transport can occur with a set direction that limits the interaction area to a subset of the membrane area, e.g. during the directional transport of auxin between cells in the *A. thaliana* root [160]. Here, the parameters k_1 and k_{-1} have the units $\mathrm{dm\,s^{-1}}$ and describe the translocation rate constants of X_1 and X_2 across the membrane.

Multi-Compartment, without Area-Scaling

In this modeling approach, reactions involving multiple compartments are not scaled with any volume or area. This means that this information is implicitly contained in the respective reaction parameters. As this approach does not presume any automatic scaling, this is the approach used by both COPASI [104] and SBML [107].
By omitting the membrane in the model, this changes Equation 4.2 to the following ODE:

$$\frac{d([X_1] \cdot V_1)}{dt} = -\frac{d([X_2] \cdot V_2)}{dt} = -k_1 \cdot [X_1] + k_{-1} \cdot [X_2] \tag{4.3}$$

Here, it is assumed that the parameters k_1 and k_{-1} already contain the information of the interaction surface between the two volumes, over which X_1 and X_2 diffuse. This means that the apparent values of k_1 and k_{-1} (in $\mathsf{dm}^3\,\mathsf{s}^{-1}$) are the product of the actual permeability parameters p_1 and p_{-1} (in $\mathsf{dm}\,\mathsf{s}^{-1}$) and the interaction surface (in dm^2). Accordingly, the parameters k_1 and k_{-1} are only valid for one specific interaction area. Any change in cell shape or growth that results in a changed interaction area, necessitates an adjustment of the parameters k_1 and k_{-1}. Therefore, this kind of model is only valid for one specific set up regarding cell shape and size.

One Compartment

In some cases, one universal compartment is used to model multi-compartment processes. Here, species are distinguished by their names instead of the allocated compartment. In the transport model, using only one compartment changes equation 4.2 to:

$$\frac{d([X_1]\cdot V)}{dt} = -\frac{d([X_2]\cdot V)}{dt} = V\cdot(-k_1\cdot[X_1] + k_{-1}\cdot[X_2]) \tag{4.4}$$

The omission of one of the compartments means that the species can only be distinguished by different names, X_1 and X_2 in this case. It also means that the information about the interaction area and potential differences in compartment sizes need to be included in the kinetic parameters k_1 and k_{-1}. This kind of model is therefore only valid for one unique setting. Any change in compartment volume or interaction area requires the careful adjustment of the kinetic parameters.

Model Behavior

To analyze the impact of cell size and shape in the different ODE modeling approaches, I looked at the transport of a species X_1 from the cell wall into the cytoplasm (Fig. 4.3 A). The test case here was to follow transport across different root regions for an epidermis cell. To determine the effect of not adjusting the parameters between settings, I determined the correct parameters for the meristematic zone and kept them unchanged for the simulations in the elongation and maturation zones (Tab. A.1 on p. 173). It is noteworthy that the divergence of cell surface and cell membrane does not have a strong effect on the steady state concentrations since plant cells gain volume mostly by taking up water into the vacuole [161]. Therefore, the cytoplasm changes on a slightly different scale than the cell surface [11].
In this context, it is not surprising that the dynamics of X_1 and X_2 do not change much in the different root zones in the multi-compartment model with area-scaling (Fig. 4.3 B). While the speed remains constant between the different root zones, the model reaches a different equilibrium in the maturation zone (Fig. 4.3 B, blue and light blue).
In contrast to this, the multi-compartment model without area-scaling shows noticeable differences in transport speed (Fig. 4.3 C). Here, the equilibrium is reached at a later time

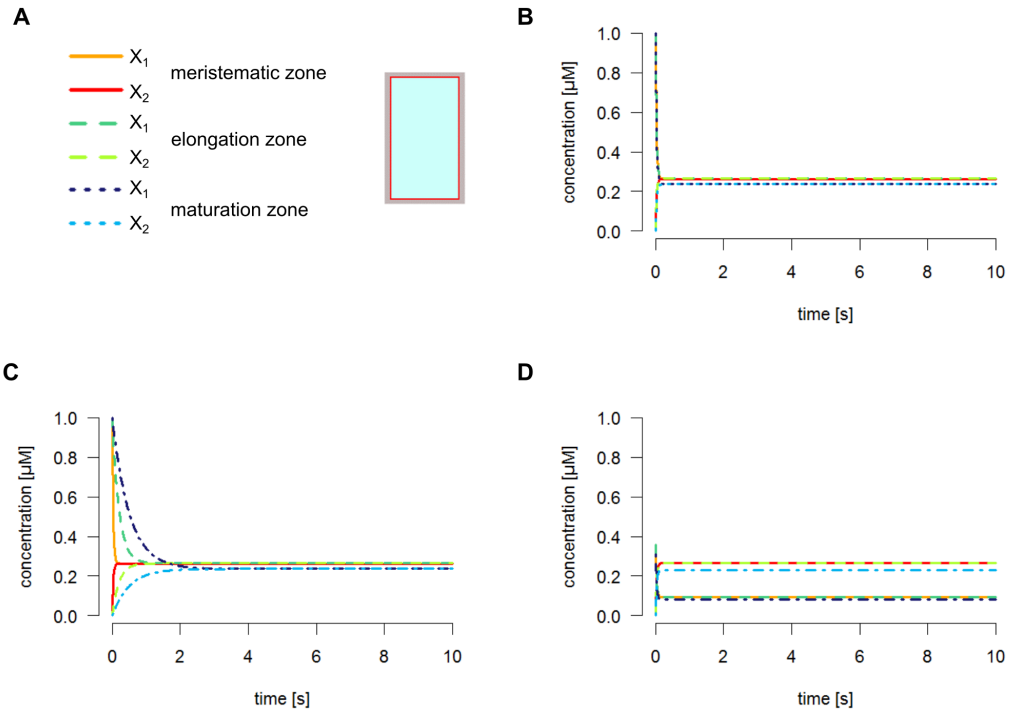

Figure 4.3: Overview of the transport model behavior with varying compartment volumes. A: The exchange of the species X_1 was modeled from the cell wall into an epidermis cell in the different root zone. **B:** Behavior of the area-scaling model. **C:** Behavior of the multi-compartment model without area-scaling. **D:** Behavior of the one compartment model. Red and orange: meristematic zone, light green and dark green: elongation zone; light blue and dark blue: maturation zone.

in the elongation zone (green) and the maturation zone (blue). Nonetheless, the correct equilibrium is reached.

Finally, there is the one compartment model to be considered. To have the same particle numbers in each model, the initial number of X_1 was adjusted to be the same as the models presented in Fig. 4.3 A and B. As the one compartment model consists only of the compartment, V_2 (here: cytoplasm), the apparent concentration of X_1 is lower than the one observed for the other models. Besides this adjustment, this model behaves much like the area-scaling model. The reason for this lies in the fact that plants mainly increase their cell volume by water uptake into the vacuole instead of increasing the cytoplasm [161]. Therefore, the ratio between cell surface and cell compartment does not change as much as it would in another model organism.

Since directed transport plays a crucial role in organ development in plants [160], looking at vertical and horizontal transport is equally important as looking at the different root regions. Here, I looked at the transport between cells of identical cell type and root region and simulated both vertical (Fig. 4.4) and horizontal (Fig. 4.5) transport. The precise interaction areas for the vertical and horizontal transport in the different root zones are listed in the Supplementary Information Table A.2, p. 173.

Figure 4.4 summarizes the simulation results of the vertical transport. Considering that plant cells mostly increase in length during growth, the vertical interaction area between two cells only changes to a small degree. Nonetheless, the cytoplasmic volume does increase. Therefore, more particles need to be transported across the membrane while the interaction area remains almost unchanged. This explains why the area-scaling multi-compartment model reaches the equilibrium at a later time in the elongation and maturation zones compared to the meristematic zone (Fig. 4.4 B).

This effect is even more pronounced in the multi-compartment model without area scaling. Here, the modest increase in interaction area is not represented by the model, resulting in much slower transport rate constants for the elongation and maturation zones (Fig. 4.4 C).

Finally, the different settings have no impact at all on the ODE model comprising only one compartment (Fig. 4.4 D). Here, the time-course simulations of the different root zones are identical. While the amount of X_1 increases from meristematic to maturation zone, so does the volume that is used to scale the rate law. Therefore, all time-courses look identical irrespective of the precise setting.

As a final situation for the transport model, I analyzed the behavior of the toy model during horizontal transport between cells of the same root zone (Fig. 4.5 A). In this case, cell growth has a greater impact as cells mostly grow along the longitudinal axis. This becomes evident in the time-course simulations of the multi-compartment model with area-scaling (Fig. 4.5 B). The transport in the meristematic zone is slowest (orange/red), while the transport in elongation zone (green) and maturation zone (blue) occur at a faster rate.

The multi-compartment model without area-scaling behaves in the completely opposite way (Fig. 4.5 C). Here, the exchange between cells in the meristematic zone is the fastest (orange/red). The transport in the elongation (green) and in the maturation zones (blue) is

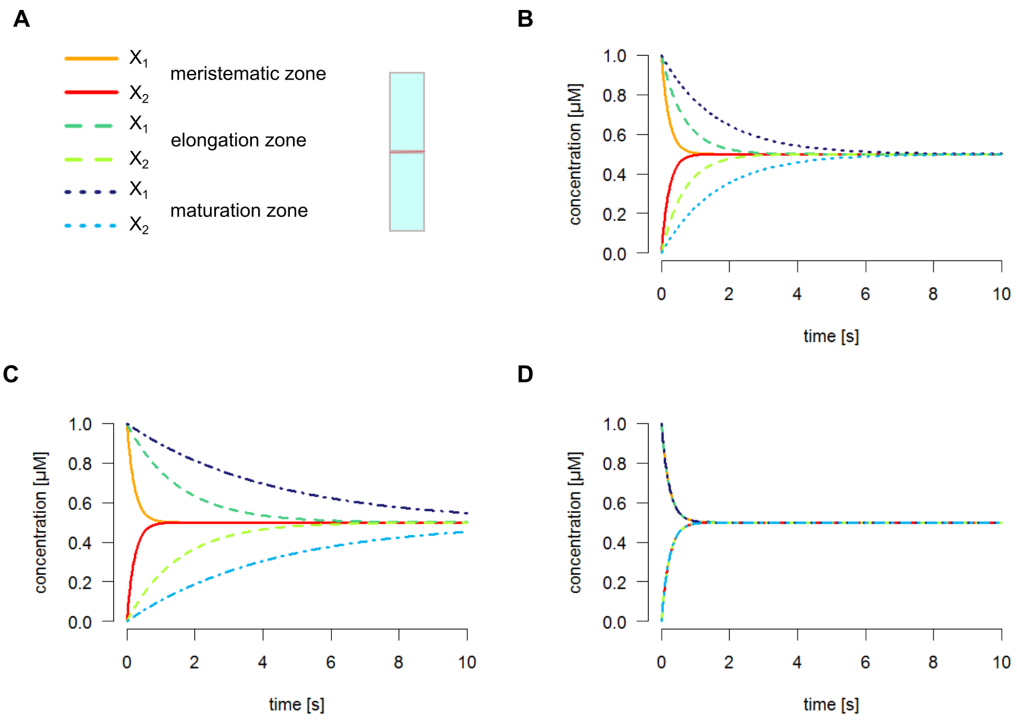

Figure 4.4: Vertical transport between root cells A: Legend and model setting. **B:** Horizontal transport between root cells in the area-scaling multi-compartment model. **C:** Behavior of the multi-compartment model without area-scaling. **D:** One compartment model. Red and orange: meristematic zone, light green and dark green: elongation zone; light blue and dark blue: maturation zone.

progressively slower as more particles diffuse according to a constantly small rate.
Lastly, the one compartment model does not change its behavior throughout the different root zones considered here (Fig. 4.5 D). Instead the time-course simulations of elongation (green) and maturation zones (blue) resemble the simulations of the meristematic zone (orange/red), which fits the behavior of this model for the vertical transport (Fig. 4.4 D).

4.1.2 Receptor Model

In addition to the transport model, I looked at the behavior of a simple receptor model. This model comprises three reactions: the reversible association of the ligand L to the receptor R

$$L + R \underset{v_{-1}}{\overset{v_1}{\rightleftharpoons}} LR \quad , \tag{4.5}$$

the production of the intracellular messenger M

$$\overset{v_2}{\longrightarrow} M \; ; LR \quad , \tag{4.6}$$

and the degradation of the intracellular messenger

$$M \overset{v_3}{\longrightarrow} \quad . \tag{4.7}$$

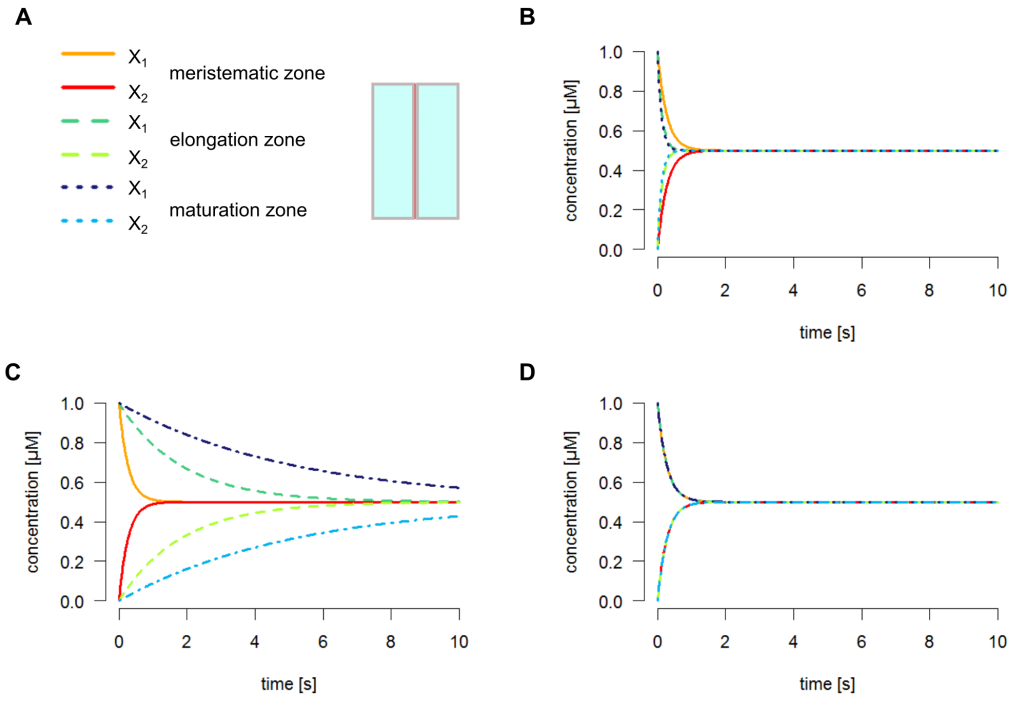

Figure 4.5: Horizontal transport between root cells. A: Legend and model setting. **B:** Horizontal transport between root cells in the area-scaling multi-compartment model. **C:** Behavior of the multi-compartment model without area-scaling. **D:** One compartment model. Red and orange: meristematic zone, light green and dark green: elongation zone; light blue and dark blue: maturation zone.

The reversible association and dissociation of the ligand L to the receptor R occurs with the rates v_1 and v_{-1} and the rate constants k_1 and k_{-1}, respectively. To keep this model as simple as possible, I used mass action kinetics for all reactions. The second messenger M is produced by the ligand-receptor complex LR at the rate v_2 and a rate constant of k_2. The final reaction concerns the degradation of the second messenger M, which is formulated as a mass action kinetics with a rate of v_3 and a rate constant of k_3.
The multi-compartment versions of this model comprise three different compartments: extracellular space, membrane area and cytosol. The extracellular space is defined as the cell wall volume in this case.

Mutli-Compartment, with Area-Scaling

In the version of the receptor model with area-scaling, there are two reactions that scale with the membrane - the ligand-receptor interaction and the production of the second messenger M that depends on the amount of ligand-receptor complex LR.

$$\begin{aligned}
\frac{d([L] \cdot V_{extracellular})}{dt} &= \\
\frac{d([R] \cdot A_{membrane})}{dt} &= \\
-\frac{d([LR] \cdot A_{membrane})}{dt} &= -A_{membrane} \cdot (k_1 \cdot [L] \cdot [R] - k_{-1} \cdot [LR]) \\
\\
\frac{d([M] \cdot V_{cytosol})}{dt} &= A_{membrane} \cdot k_2 \cdot [LR] - V_{cytosol} \cdot k_3 \cdot [M]
\end{aligned}$$

The degradation of the second messenger M is the only reaction that scales with the cellular volume $V_{cytosol}$. This model here is not specific to one spatial configuration. Since the kinetic parameters are independent of cell volume or cell surface, different cell morphologies can be modeled without adjusting the parameters.

Multi-Compartment, without Area-Scaling

As with the transport model, this modeling approach does not scale the reaction rate laws spanning multiple compartments either with a volume or with an area but rather considers

them as particle fluxes:

$$\begin{aligned}
\frac{d([L] \cdot V_{outside})}{dt} &= \\
\frac{d([R] \cdot A_{membrane})}{dt} &= \\
-\frac{d([LR] \cdot A_{membrane})}{dt} &= -k_1 \cdot [L] \cdot [R] + k_{-1} \cdot [LR] \\
\\
\frac{d([M] \cdot V_{cytosol})}{dt} &= \quad k_2 \cdot [LR] - V_{cytosol} \cdot k_3 \cdot [M]
\end{aligned}$$

All reactions that are recognized as involving multiple compartments do not scale with a compartment automatically. Here, the user has to include that information in the kinetic parameters k_1, k_{-1} and k_2, which are the product of the actual permeability parameters and the interaction area. This means that this kind of model is specific to one spatial configuration. If the model is transferred to another cell type or cell morphology, the parameters for multi-compartment reaction need to be adjusted.

One Compartment

In many signaling models, the receptor and often also the ligand are placed in the cytoplasm to avoid complicating the model by using several different compartments, i.e. Kholodenko *et al.* (1999) [162] and Brown *et al.* (2004) [163]. In this case, the set of ODEs look like the following set of equations:

$$\begin{aligned}
\frac{d([L] \cdot V_{cytosol})}{dt} &= \\
\frac{d([R] \cdot V_{cytosol})}{dt} &= \\
-\frac{d([LR] \cdot V_{cytosol})}{dt} &= -V_{cytosol} \cdot (k_1 \cdot [L] \cdot [R] + k_{-1} \cdot [LR]) \\
\\
\frac{d([M] \cdot V_{cytosol})}{dt} &= \quad V_{cytosol} \cdot (k_2 \cdot [LR] - \cdot k_3 \cdot [M])
\end{aligned}$$

In this model there are several simplifications from what would be a realistic representation. For one, both receptor and receptor-ligand-complex exist within a volume instead of a surface. Hence, the units of these species are different than they are in reality: mol per volume instead of mol per area. Depending on the model units and the sizes of the compartments the nominal concentrations can be very different, even if the particle number is identical. This makes the concentrations of membrane proteins in this model

meaningless.
Further differences concern the informational content of the parameters k_1 and k_{-1}. These parameters now also contain the ratio of the cell surface $A_{membrane}$ to the extracellular volume $V_{extracellular}$ and the cytosolic volume $V_{cytosol}$, respectively. Furthermore, depending on the ratio of extracellular to cellular volume, the concentration of the ligand $[L]_{t=0}$ will have to be adjusted to ensure an identical initial amount of particles in both the model and the experimental setting. Otherwise, a different steady state receptor occupancy level would be reached.
The parameter k_2 can be kept constant compared to the model with area-scaling, since the production of messenger molecules scales with the number of occupied receptors LR. While the ligand-receptor complexes are located in the membrane, the modeler has assigned them to the cytoplasm making the standard approach of scaling this ODE with the cell volume mathematically correct as long as the correct amount of particles was included in the initial settings.

Model Behavior

To analyze the impact of cell morphology and modeling approach on a signaling model, I simulated the receptor model for an epidermis cell located in different root regions. The compartment sizes were chosen as listed in Table 4.1. To facilitate the comparison between the modeling approaches, the initial particle numbers for ligand and receptor were chosen to be identical in all modeling approaches: $10,000$ ligand particles L_0 and $100,000$ receptor particles R_0. The parameters were chosen such that all models show identical behavior in the meristematic zone (Tab. A.3). No parameters were adjusted for the simulations in the elongation or maturation zone to show the effects of the different modeling approaches.
Figure 4.6 illustrates the simulation results for all modeling approaches regarding the messenger particle numbers. In the meristematic zone (Fig. 4.6 A) all models respond identically to the stimulation with the ligand. The simulations of the elongation and maturation zone show that in these cases the one compartment model deviates less from the multi-compartment model with the membrane compared to the one without the membrane. The discernible differences are a slightly faster response in both elongation and maturation zone (Fig. 4.6 B,C) and a slightly higher steady state concentration of the second messenger in the maturation zone (Fig. 4.6 C). In comparison to this, the multi-compartment model without the membrane shows great differences in in steady state messenger levels in both root zones (Fig. 4.6 B, C) and a delayed response in the maturation zone (Fig. 4.6 C).

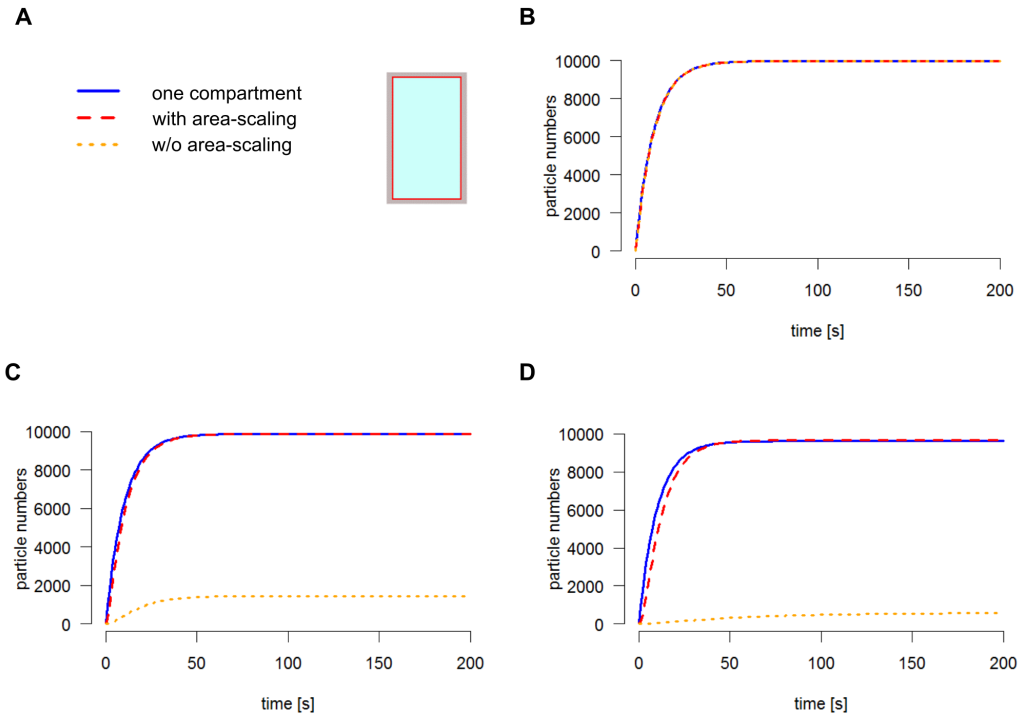

Figure 4.6: Overview of the receptor toy model behavior in different settings. A: Modeling setup. **B-D:** Signaling output as determined by the messenger concentration in the cytoplasm according to modeling approach in an epidermis cell of different root regions. **B:** Meristematic zone. **C:** Elongation zone. **D:** Maturation zone. Blue: One compartment model; red: multi-compartment model with area scaling; yellow: multi-compartment model without area scaling. The behavior of the other species is shown in the Supplementary Information A.2 on p. 175.

4.2 Example Models

While the behavior of the toy models can help to get an idea of the importance of multi-compartment rate-laws, the toy models are not as complex as models of biological systems and, therefore, yield only a simplified picture. Therefore, together with Pascal Holzheu, I also analyzed published biological models. First, we categorized the curated models in the biomodels database [35] (`https://wwwdev.ebi.ac.uk/biomodels/`, last accessed: 24.05.2018) into several subcategories:

1. models comprising only one compartment
2. multi-compartment models
   (a) compartments have an arbitrary volume of $1\,\mathrm{l}$ (or $1\,\mathrm{ml}$)
   (b) model compartment volumes describe the ratio between the biological compartment volumes
   (c) compartments are of realistic volumes
   (d) compartment volumes do not matter since the ODEs are written in a way that the volumes cancel out
   (e) pharmaco-kinetic or organ-scale models

We considered only those models as examples, where the model comprises multiple compartments with realistic size and where the formulation of the ODEs does not cancel out the compartments. We further limited our selection to models that describe cellular processes instead of pharmacokinetic or organ-scale models.
This leaves only a few of the curated models listed in the biomodels database [35]: Out of the 699 curated models 474 are one compartment models. Of the 225 multi-compartment models, 147 have arbitrary volumes in the range of $1\,\mathrm{l}$ or $1\,\mathrm{ml}$ per cell. A further 32 contain the ratio between compartments while having a compartment volume in the range of liters. This kind of model is only valid for one specific cell size and morphology as any change in either of these would require careful adjustment of the model paramters. Only 22 models have several compartments with realistic volumes (Tab. 4.2). Of these, only three also contain the plasma membrane as a compartment and interaction area [156, 149, 157]. Neves *et al.* even considered the impact of cell size and shape on the signaling behavior, though this analysis was limited to PDE model [149]. One particular model by Fridlyand *et al.* considers the membrane implicitly by defining a total membrane capacitance to calculate the membrane potential [164]. Another model defines the plasma membrane as interaction volume instead of an interaction area [165]. Finally, five models were built using the VirtualCell software that allows for PDE simulations [166] and an additional seven were organ-scale or pharmacokinetic models.

All of the models in Table 4.2 comprise multiple compartments that have realistic compartment sizes according to the cell or organelle size. Only three include the membrane as reaction compartment [156, 149, 157]. However, the aim of these models was to represent a basis for spatial PDE modeling. Here in this chapter, it is the aim to analyze the impact

Table 4.2: Curated multi-compartment models in the biomodels database. Listed are only those models with realistic compartment sizes with biomodel number (#) [35] (`https://wwwdev.ebi.ac.uk/biomodels/`, last accessed: 24.05.2018). The chosen example model is highlighted in bold font. Models built in Virtual Cell [166] are marked by VC.

#	Description	Reference
16	Circadian oscillations in the *drosophila* period protein (PER)	[167]
19	Dynamics of the MAP kinase cascade activated by surface and internalized EGF receptors	[168]
59	Ca^{2+} flux in pancreatic beta-cells: role of the plasma membrane and intracellular stores	[164]
122, 123	NFAT and NFκB activation in T lymphocytes	[169]
161 (VC)	Compartment-specific feedback loop and regulated trafficking can result in sustained activation of Ras at the Golgi	[170]
162 (VC)	Modeling and analysis of calcium signaling events leading to long-term depression in cerebellar Purkinje cells.	[157]
173	Smad nucleocytoplasmic shuttling as a dynamic signal-interpreting system	[171]
192	Ran-driven cargo transport and the RanGTPase system	[101]
182 (VC)	Cell shape and negative links in regulatory motifs together control spatial information flow in signaling networks.	[149]
250	Ligand-specific c-Fos expression	[172]
342	Transient and sustained transforming growth factor-β signaling	[173]
399	Thermodynamically consistent model calibration in chemical kinetics	[174]
407	Heterogeneity reduces sensitivity of cell death for TNF-stimuli	[175]
474	Regulation of insulin signaling by oxidative stress	[176]
505, 506	Fatty acid β-oxidation	[177]
547	Arsenic transport, distribution and detoxification in yeast	[178]
557	Pseudophosphatase STYX modulates cell-fate decision and cell migration	[179]
638	Yeast GPCR signaling reflects the fraction of occupied receptors	[165]
699, 702	Regulation of Tem1 by the GAP complex in Spindle Position Checkpoint	[180]

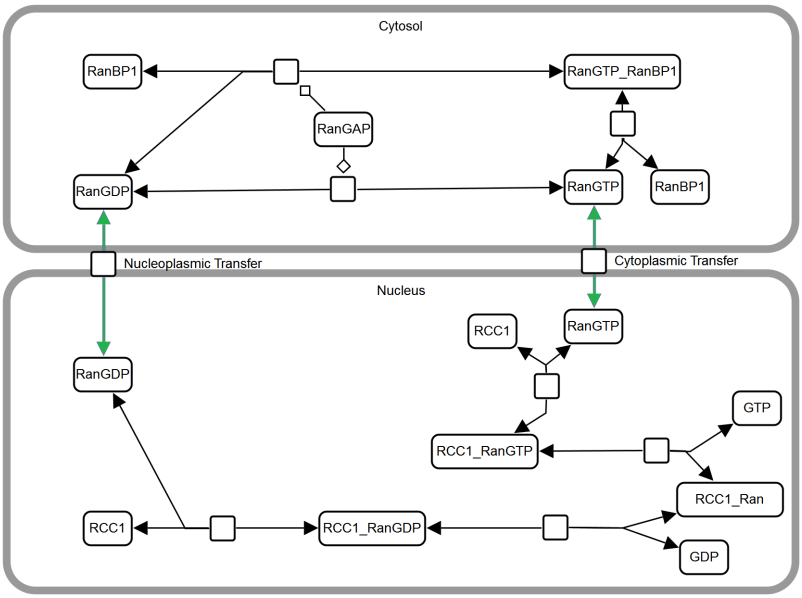

Figure 4.7: Schematic representation of the RanGDP/GTP shuttling model. The reactions were depicted according to the model file on the biomodels data base. Reactions involving more than one compartment are indicated in green. The model scheme was rendered using VANTED [158] according to the Systems Biology Graphical Notation (SBGN) standard [159].

of cell size and morphology in ODE models. Therefore, I selected one of the remaining ODE models in Table 4.2 for this section.

4.2.1 RanGTP Transport

The model of RanGTP nuclear shuttling by Görlich *et al.* (2003) serves as the example for situation, where area-scaling can be crucial for the correct model behavior [101]. This model describes RanGDP/GTP transport cycle between nucleus and cytosol (Fig. 4.7). Of the nine reactions in the model, two involve more than one compartment: nucleoplasmic and cytoplasmic transfer of RanGDP and RanGTP, respectively (as highlighted by the green arrows in Fig. 4.7).

In the original model, the transport reactions between nucleus and cytosol scale with the nuclear volume. In reality, these reactions scale with the area of the nuclear envelope or - more precisely - with the number of nuclear pores. Assuming an uniform distribution of nuclear pores this number can be approximated by the nuclear envelope area. Thus, these reactions were rewritten to include the nuclear surface as approximated by assuming a spherical nucleus. To reproduce the behavior of the original model (Fig. 4.8 A), I adjusted the permeability parameters by calculating the area-scaling transport rate k_{area} based on the volume-scaling transport rate k_{vol}, the nuclear volume $V_{nucleus}$ and the nuclear area $A_{nucleus}$ (Tab. 4.3):

$$k_{area} = k_{vol} \cdot \frac{V_{nucleus}}{A_{nucleus}} \tag{4.8}$$

Table 4.3: Parameter overview of the RanGTP example model. Shown are the parameters of the multi-compartment reactions concerning cytosolic and nuclear transfer. *Volume-scaling models.

	Cytosolic Transfer	**Nuclear Transfer**
original model*	$0.03\,\mathrm{s}^{-1}$	$0.12\,\mathrm{s}^{-1}$
area-scaling	$1.429 \times 10^{-6}\,\mathrm{dm\,s}^{-1}$	$5.714 \times 10^{-6}\,\mathrm{dm\,s}^{-1}$
wild-type*	$0.483\,002\,\mathrm{s}^{-1}$	$1.932\,01\,\mathrm{s}^{-1}$
sch9 -/-*	$0.575\,887\,\mathrm{s}^{-1}$	$2.303\,55\,\mathrm{s}^{-1}$

Figure 4.8 A illustrates that the same behavior can be simulated with different modeling approaches. The only changes concern the parameter values and units of the kinetic parameters for the reactions that involve more than one compartment (i.e. nucleoplasmic and cytoplasmic transfer).

Model Behavior

To illustrate the relevance of area-scaling I considered the RanGTP transport model by Görlich *et al.* (2003) [101]. Interestingly, *Saccharomyces cerevisiae* (*S. cerevisiae*) has a near constant volume ratio of nucleus to cytosol at $7\,\%$ independent of the genotype [181]. To analyze how this might effect RanGTP transport, I transferred the model from the HeLa cell, which is the original setting [101], to *S. cerevisiae*. First, I reproduced the behavior of the volume-scaling model with the area-scaling model (Fig. 4.8 A). Both of these models are then changed from representing a HeLa cell to *S. cerevisiae* (Fig. 4.8 B). The simulation results of these models illustrate the importance of adjusting the model parameters. In this case, this is a rather trivial situation: As the model organisms are different between Figure 4.8 A and B, adjusting the parameters is a reasonable step.
Finally, I also simulated the behavior of a *S. cerevisiae* mutant (Fig. 4.8 C). The protein sch9 is a serine-threonine kinase involved in growth regulation [182]. In *sch9-/-* cells, the cellular volume is approximately $60\,\%$ of the wild-type volume. Here, I simulated three different versions of the model. For one, I modeled the behavior of the area-scaling model (light blue). Second, I simulated the model with the adjusted parameters representing the wild-type of Figure 4.8 B. Finally, I adjusted the parameters of the volume scaling model to represent the setting of the *sch9* mutant. For all of these parameter sets, there is only a small difference between the area-scaling model and the volume-scaling models (Fig. 4.8 C). This demonstrates that it may not be necessary to use the area-scaling modeling approach in every situation.

4.3 Summary

It was the aim of this chapter to provide insight into how the description of processes spanning multiple compartments processes can affect simulation results in ODE models. Both the toy models as well as the analysis of the example model demonstrate that the choice

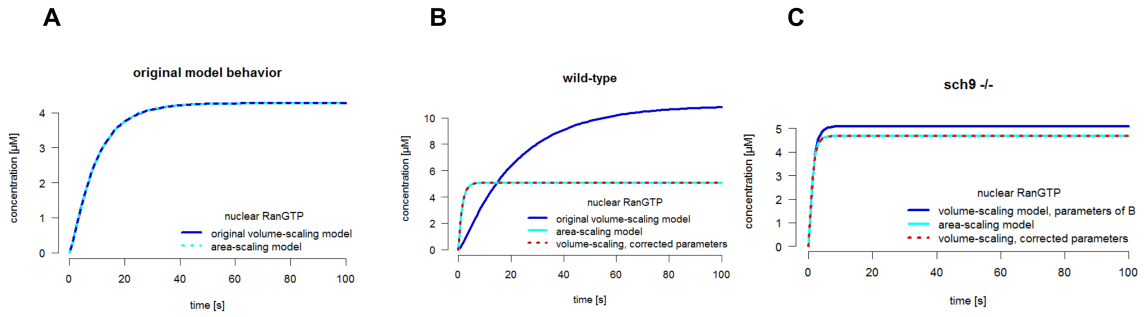

Figure 4.8: Transferring the example RanGTP transport model from HeLa cells to *S. cerevisiae*. A: The original model behavior can be reproduced using the area-scaling model that includes the nuclear envelope. **B:** Dynamics of the *S. cervisiae* wild-type. **C:** Dynamics of the *S. cervisiae* sch9 deletion mutant. Blue: volume-scaling model before parameter adjustment. Light blue: area-scaling model. Red: volume-scaling model with corrected parameters.

of modeling approach very much depends on the modeling question. In plant cells, where cells can elongate from an initial length of 8 µm to a final length of up to 220 µm, the correct scaling with the membrane area can be crucial for the correct model behavior. Even if the model is only simulated in the different root regions, the parameter adjustment alone is a easy source for error. If, however, cell growth is included in some form in such a model, it is a necessary prerequisite for correct simulation results.

The example model, which I analyzed in this chapter, however, demonstrates that small changes in cell volume do not necessarily require a change in model structure or even parameter adjustment. Here, the volume-scaling model with the parameterization of the *S.cerevisiae* wild-type behaves similar to the area-scaling model in *S.cerevisiae sch9-/-*.

The elongating cell model that I present in chapter 7 falls into the first category, where area-scaling is crucial. As I simulate an epidermis cell from the meristematic zone to the elongation zone, the compartments change constantly which would require a constant adjustment of the parameters throughout the simulation. As this is overly complicated and would require the abundant use of assignments and global quantities in COPASI, using an area-scaling approach is the most practical one.

5 | Specifying the role of BIR3

BIR3 is a negative regulator of BR signaling that acts by interacting with the co-receptor BAK1 [29, 30]. Extensive experimental studies have revealed several aspects to the role of BIR3. For one, BIR3 interacts with both the receptor BRI1 and the co-receptor BAK1 [30]. Overexpressing BIR3 inhibits BR signaling to the point, where the plants resemble *bri1 -/-* mutants [30]. The additional overexpression of BRI1 restores BR signaling so that the plants look like the wild type Col-0 in terms of growth [30]. Lastly, there is evidence for a constitutive interaction of BAK1 and BRI1 [14, 64, 65].
Furthermore, Imkampe *et al.* (2017) used a bridge yeast two hybrid assay [183] to test a potential tripartite interaction [30]. In particular, they used both BIR3 and BAK1 as bridge between bait- and prey-constructs. Both scenarios yielded weak *S. cerevisiae* growth indicating that if a trimeric complex exists, it is likely due to independent interaction sites.
Recently, Hohmann and colleagues investigated the interactions of the ectodomains of BIR3, BAK1 and BRI1 [47]. This study demonstrated that the ectodomains of BAK1 and BIR3 interact with a high affinity and that BL-bound BRI1 is required to compete with BIR3 for the interaction with BAK1 [47]. However, this study did not show evidence of BIR3 and BRI1 interacting based on the respective ectodomains [47], suggesting that cytoplasmic and transmembrane domains play a role in the experimentally observed interactions of the full length proteins [30] (and section 5.2.2). At the very least, the cytoplasmic domains have to interact transiently in order for transphosphorylation events to occur [31].
To specify the role of BIR3 in BR signaling even further, I employed molecular modeling to test the complex formation between the cytoplasmic domains of BAK1, BRI1 and BIR3 computationally. For this part of my thesis, I was advised by Dr. Anna Feldman-Salit (research group of Prof. Dr. Ursula Kummer, BioQuant, Centre for Organismal Studies (COS), Heidelberg University). At a later stage of this project, we consulted with Prof. Dr. Rebecca Wade and Dr. Neil Bruce (Heidelberg Institute for Theoretical Studies (HITS gGmbH), Interdisciplinary Center for Scientific Computing (IWR), Heidelberg).
As it was the aim of this project to specify the role of BIR3, the first step was to define the state of the interaction between BAK1 and BRI1 without BIR3 (see section 5.2.1) before looking at the interactions of BAK1 and BIR3 as well as BRI1 and BIR3 (see section 5.2.2). Finally, I investigated a potential trimeric complex based on the results of the previous sections (see section 5.2.3). To validate the computational results our collaborators Friederike Wanke and Nina Glöckner (research group Prof. Dr. Klaus Harter, Centre for Molecular Biology of Plants (ZMBP), Tübingen University) analyzed the interactions of BIR3 with BAK1 and BRI1 *via* FRET-FLIM (see section 5.2.2).

5.1 Obtaining the Structures for Docking Analysis

Before potential complexes could be computed by docking analysis, I had to obtain suitable structures for BAK1, BRI1 and BIR3. Wherever possible, I used a experimentally determined structure from the Protein Data Bank[1] [112, 113]. As these structures sometimes contain gaps due to flexible loop regions, these gaps were filled by comparative modeling. If no crystal structure was available for a protein, I used the structure of a closely related protein as a template for comparative modeling (see section 5.1.1).

5.1.1 Structure Selection

In general, the protein template structures were selected according to their completeness and quality. If it was possible within this set of criteria, an *apo* structure was selected.
In the case of BAK1 and BRI1, there were several structures available for the cytoplasmic domains of each protein. In particular, for BRI1 there was a monomeric *apo* structure of good quality: *A. thaliana* BRI1, structure ID 5lpw, expressed in *Escherichia coli* [123] (Fig. 5.2 A and Tab. 5.1). This structure has three gaps that need to be filled by comparative modeling (Tab. 5.1, Fig 5.2, sequence alignment Fig. B.1 on p. 178).
The structure selection for BAK1 was more complicated: three structures with resolutions between 2.2 Å and 2.6 Å were available: 3ulz [184], 3uim [184] and 3tl8 [185]. The apo structure 3ulz and the related structure 3uim crystallized with an ATP derivate, have very bad wwPDB metrics [113]: 10.8 and $16\,\%$ Ramachandran outliers, 11.8 and $26.4\,\%$ side chain outliers and a high clash score of 47 and 81. The final structure of cytoplasmic BAK1, 3tl8, shows better metrics but was crystallized with the inhibitor AvrPtoB [185]). AvrPtoB (uniprot ID Q8R9Y1) is a viral inhibitor that impacts plant immunity signaling [186].
To check if 3tl8 is a suitable structure for BAK1, I first compared all three structures of BAK1 by aligning them in Chimera [114] using the MatchMaker and Match→Align tools [115]. The most notable difference is the fact that the gap in 3ulz and 3uim is resolved in 3tl8 (residues E322 to G326) (Fig. 5.3 A, B, gap highlighted by an arrow).
The structure of 3tl8 was co-crystallized with an inhibitor. The binding site of the inhibitor is easily recognizable in the rendering of the B-factor of 3tl8 (Fig. 5.3 C). The B-factor represents a measure of how much atoms fluctuate around their average position [117]. The binding of the inhibitor AvrPtoB has a stabilizing effect on the respective residues (blue). Figures 5.3 E and F illustrate that the differences between the structures are in the N-terminal helix and in loops that have a higher flexibility as indicated by the higher B-Factor (orange, red). This means that the differences at those positions can be explained by the increased flexibility.
To further ensure the suitability of 3tl8 as template, I evaluated the structures based on their QMEAN scores (Fig. 5.3 G, H). Here, both 3uim and 3ulz have bad QMEAN scores of -8.09 and -6.75, respectively (Fig. 5.3 H). In comparison to this the four chains of

[1] `http://www.rcsb.org`

the 3tl8 structure show QMEAN scores in the range of -0.74 to -1.5 (Fig. 5.3 G). The closer the QMEAN score is to zero the better is the evaluated structure. Furthermore, by computing the QMEAN score, the structures of interest are also automatically compared to the QMEAN scores of a non-redundant set of reference PDB structures (Fig. 5.3 I).
As a final check, I analyzed the crystal structures of BIR2 (Fig. 5.2 B) and BRI1 (Fig. 5.2 A) to check if the $alpha$-helix in 3tl8 residues E322 to G326 is potentially an artifact of the crystallization with the inhibitor AvrPtoB. BRI1 and BAK1 belong to the same group of protein kinases and share $36.11\,\%$ sequence identity as evident in the sequence identity matrix computed by Clustal Omega[2] [119, 120, 121] (for the multiple sequence alignment see Supplementary Information p. 178):

	$BAK1$	$BRI1$	$BIR2$	$BIR3$
$BAK1$	–	40.96	36.22	36.11
$BRI1$	40.96	–	43.02	42.66
$BIR2$	36.22	43.01	–	66.06
$BIR3$	36.11	42.66	66.06	–

Therefore, it also stands to reason that the structures are quite similar [92]. In the structures of BIR2 and BRI1, it becomes apparent that the α-helix is not necessarily an artifact of BAK1 binding the inhibitor AvrPtoB. Therefore, 3tl8 was chosen as template and the chain with the best QMEAN score was used for docking analysis (chain A).
There was no experimentally determined structure for BIR3, specificially. However, there was a structure for a closely related protein that shares 66 % sequence identity with BIR3 (see Fig. 5.1 and Tab. 5.1) - *A. thaliana* BAK1-interacting receptor-like protein 2 (BIR2) [122] (Uniprot ID Q9SLI9, PDB ID 4l68, expressed in *Escherichia coli*). In this case, comparative modeling had to be employed to get a structure for BIR3 (see subsection 5.1.1). In the crystal cell of the 4l68 structure, there were two different chains that showed a very different structural conformation for the residues G467 to Y479. To check, which one of these chains was suitable as a template, I analyzed the structures of related proteins. Notably, BIR2, BIR3, BAK1 and BRI1 all share at least $36\,\%$ sequence identity with each other (see identity matrix above). Therefore, it is reasonable that the structures are also similar [92]. As apparent in the structural alignment in Fig. 5.2 part (B) of 4l68 (chain A) with BAK1 (3tl8, chain D), the loop in question in chain A resembles the spatial orientation of the corresponding region in BAK1 (3tl8, chain D). This means that the conformation of chain A is the more likely one and was therefore used for the subsequent docking analysis.

Comparative Modeling

We used molecular modeling to generate a structure for BIR3 based on the template structure of BIR2 (4l68) [122] and to fill the gaps in the BRI1 structure selected for docking analysis (5lpw) [123]. To account for the uncertainty introduced by the gaps in both

[2] `https://www.ebi.ac.uk/Tools/msa/clustalo/`

Table 5.1: Characteristics of the protein crystal structures from the Protein Data Bank [112] used during this analysis. Listed are the protein name, the UniProt identifier, the sequence segment expressed for crystallography, the PDB ID, the structurally resolved residues, the resolution (Res.) and the crystallographic unit.

Protein	UniProt	Sequence	PDB ID	Residues	Res.	Unit
BRI1	O22476	865-1160	5lpw [123]	867-871, 873-973, 975-1086, 1095-1160	2.43 Å	monomer
BAK1	Q94F62	250-590	3tl8 [185]	273-576	2.5 Å	hetero-dimer
BIR2	Q9LSI9	266-605	4l68 [122]	272-456, 568-509, 515-600	2 Å	monomer

```
position          280       290       300       310       320       330
BIR2        GLAQRLRSHKLTQVSLFQKPLVKVKLGDLMAATNNFNSENIIVSTRTGTTYKALLPDGSALAVKH
BIR3        DWIGLLRSHKLVQVTLFQKPIVKIKLGDLMAATNNFSSGNIDVSSRTGVSYKADLPDGSALAVKR
conserved        ****** ** ***** ** ************ * ** ** ***  *** **********

position     340       350       360       370       380       390
BIR2        LSTCKLGEREFRYEMNQLWELRHSNLAPLLGFCVVEEEKFLVYKYMSNGTLHSLLDSNR---GEL
BIR3        LSACGFGEKQFRSEMNKLGELRHPNLVPLLGYCVVEDERLLVYKHMVNGTLFSQLHNGGLCDAVL
conserved   ** *  **  ** *** * **** ** **** **** *  **** * **** * *         *

position    400       410       420       430       440       450       460
BIR2        DWSTRFRIGLGAARGLAWLHHGCRPPILHQNICSSVILIDEDFDARIIDSGLARLMVP-------
BIR3        DWPTRRAIGVGAAKGLAWLHHGCQPPYLHQFISSNVILLDDDFDARITDYGLAKLVGSRDSNDSS
conserved   ** **  ** *** ********* ** *** * * *** * ****** * *** *

position         470       480       490       500       510           520
BIR2        ----DLGEFGYVAPEYSTTMLASLKGDVYGLGVVLLELATGLKAVG---------GSLVDWVKQL
BIR3        FNNGDLGELGYVAPEYSSTMVASLKGDVYGFGIVLLELVTGQKPLSVINGVEGFKGSLVDWVSQY
conserved       **** ******** ** ********* * ***** ** *            ******* *

position        530       540       550       560       570       580
BIR2        ESSGRIAETFDENIRGKGHDEEISKFVEIALNCVSSRPKERWSMFQAYQSLKAIAEKQGYSFSEQ
BIR3        LGTGRSKDAIDRSICDKGHDEEILQFLKIACSCVVSRPKERPTMIQVYESLKNMADKHG--VSEH
conserved      **     *  *  *******  *  **  ** ******  * * * ***  * * *   **

position   590       600
BIR2         DDDFPLIFDTQ
BIR3         YDEFPLVFNKQ
conserved     * *** *  *
```

Figure 5.1: Sequence alignment of BIR3 with the structurally resolved parts of BIR2. The template has two gaps of 11 and 6 residues, starting at residue 457 and at residue 513, respectively. The three residue mismatch between BIR3 and BIR3 at residue 396 as well as the three starting from 510 are caused by an insertion in BIR3. Overall, the sequence identity of BIR3 with BIR2 in the region of interest is 62.25 %.

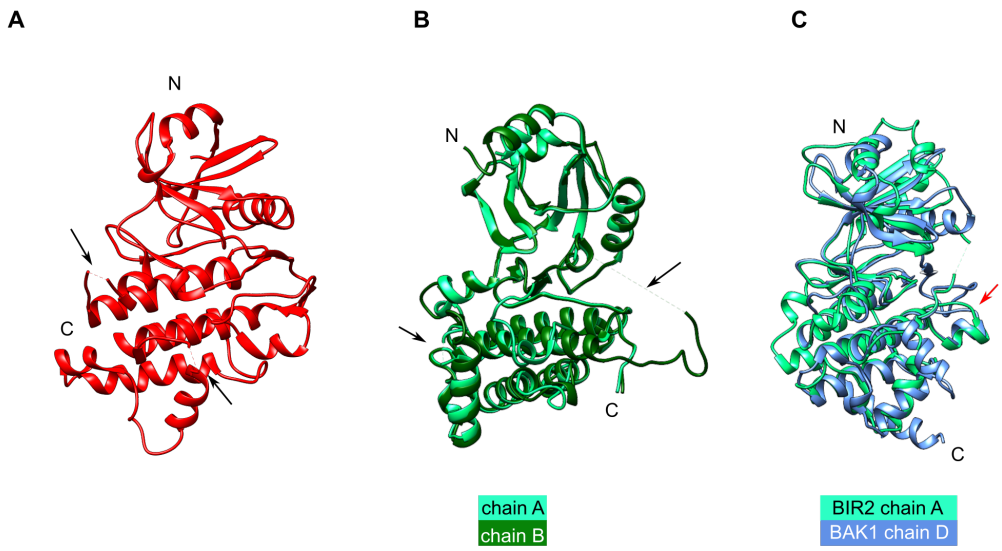

Figure 5.2: Template structures for BIR3 and BRI1. A: Template structure for BRI1: *A. thaliana* BRI1 - 5lpw [123]. **B:** Template structure of BIR3: *A. thaliana* BIR2 - 4l68 [122] chains A (bright green) and B (dark green). **C:** Alignment of BIR2 chain A and BAK1 structure 3tl8 chain D.

structures, we generated a set of 20 individual structures using the Modeller tool v. 9.16 [91]. Modeller uses the backbone of the template structure to map the sequence of the protein of interest. In the case of gaps, Modeller computes possible solutions of these loops. To validate the computed structures, I used the QMEAN4 score, which is a more reliable measure than using torsion angles [97, 98].
Comparative modeling yielded two structures with equally good QMEAN4 scores with different solutions of the structurally unresolved loops in the template structure (Fig. 5.4). As it requires little computational power to compute additional complexes, both structures were used for the docking analysis by webSDA and ClusPro.

Phosphorylated Residues

The experimentally determined structures of BAK1 [185] and BRI1 [123] were phosphorylated at several residues (see Tab. 5.2). To assess if these phosphorylations are relevant for the docking analysis, I investigated both the structural information and the available experimental data.
Experimental studies have shown that threonine phosphorylations are greatly dependent on stimulation with the hormone in the case of BRI1 [187]. For BAK1, phosphorylations depend on both the hormone and BRI1 [187]. Accordingly, the authors found no or almost no residual phosphorylations for BAK1 and BRI1 in the absence of brassinolide (BL), respectively [187]. Furthermore, extensive substitution studies were conducted for BAK1 that showed that substituting T446, T449 and T450 at the same time does not change the interaction with BRI1 [188]. Some experimental evidence even suggests that BAK1 and

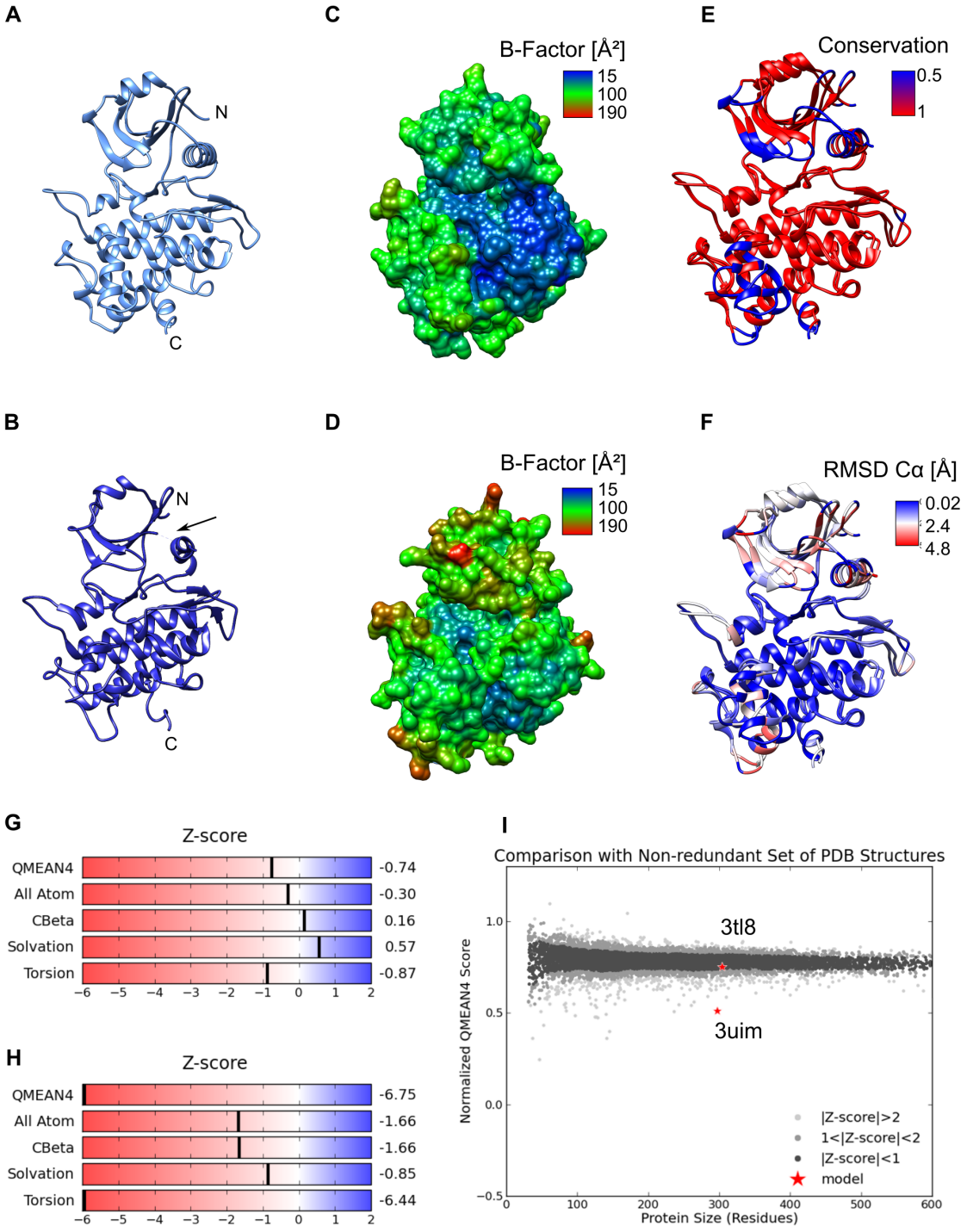

Figure 5.3: Structure comparison of BAK1 cytosolic domains of 3tl8 and 3uim. A: Chain A of 3tl8 [185]. **B: D:** Structure of 3uim [184]. Gap from E322 to G326 is highligted by the arrow. **C:** B-factor of 3tl8, chain A. **D:** B-Factor of 3uim. **E:** Conserved structural orientation between 3tl8 (chain A) and 3uim. **F:** Mean displacement of the $C\alpha$ atoms between 3tl8 (chain A) and 3uim. **G,H:** QMEAN4 Z-scores. Shown is both the overall score (QMEAN4) as well as the individual components that are used to calculate the QMEAN4 score. **G:** QMEAN4 scores of 3tl8 (chain A). **H:** QMEAN4 scores of 3uim. **I:** Comparison of the QMEAN4 score with the score of other non-redundant structures as computed by the web server. G-I were generated as part of the QMEAN4 output. I is a combination of the results for 3uim and 3tl8.

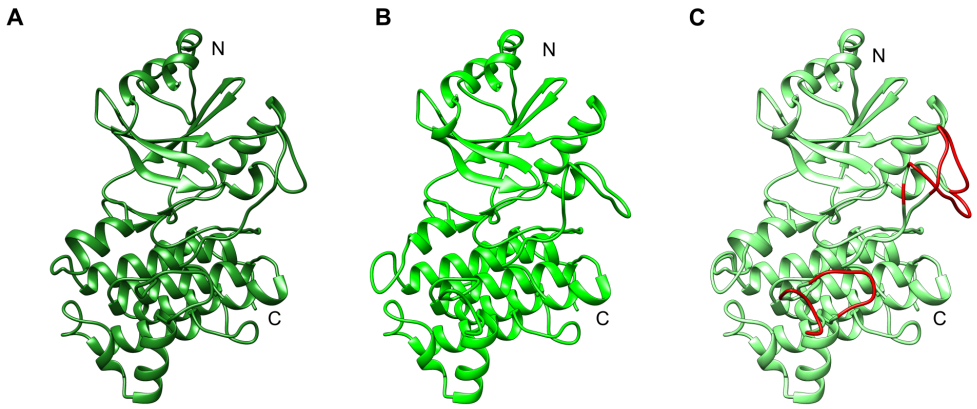

Figure 5.4: Modeled structures of BIR3 based on the template of BIR2 [122]. **A:** First structure computed for BIR3 by comparative modeling. **B:** Second structure computed for BIR3 by comparative modeling. **C:** Alignment of both structures. Residues that are not conserved between the structure are highlighted in red. The structure alignment was generated with the Match→Align tool in Chimera [114, 115].

Table 5.2: Phosphorylated residues in the template structures for BAK1 and BRI1. Listed are the phosphorylated residues for BRI1 (5lpw [123]) and BAK1 (3tl8 [185]) along with the experimental information and reference.

Protein	Residue	Experimental Information	Reference
BRI1	T1039	dependent on hormone stimulation	[187]
	S1042	transphosphorylation target by BAK1	[189]
	S1044	required for BRI1 activation	[187]
	S1060	not a known phosphorylation site	
BAK1	T324	not a known phosphorylation site *in vivo* or *in vivo*	
	T446	substitution with A does not change interaction	[188]
		substitution has no effect on plant phenotype	[31]
	T449	substitution with A does not change interaction	[188]
		substitution has no effect on plant phenotype	[31]
	T450	substitution with A does not change interaction	[188]
		substitution has a small effect on plant phenotype	[31]

BRI1 phosphorylations are completely dependent on each other [188].

While the experimental information suggests that the phosphorylations are not the deciding factor for the interaction between BAK1 and BRI1, I inspected the surface electrostatic potential of all relevant structures, nonetheless. In the case that there are regions with a strong positive charge these can be impacted by phosphorylations. Here, I used the ABPS tool in Chimera [125, 114] to calculate the electrostatic map based on the charged protein state at pH 7.2 (see Fig. 5.5).

Figure 5.5 shows that the cytoplasmic domain of BRI1 is the only structure with large region of strong positive potential. However, this region does not overlap with the region of interest that inlcudes the catalytic domain and the activation loop. Furthermore, the N- and C-terminus of the structure are in that region. As all structures in this analysis are trun-

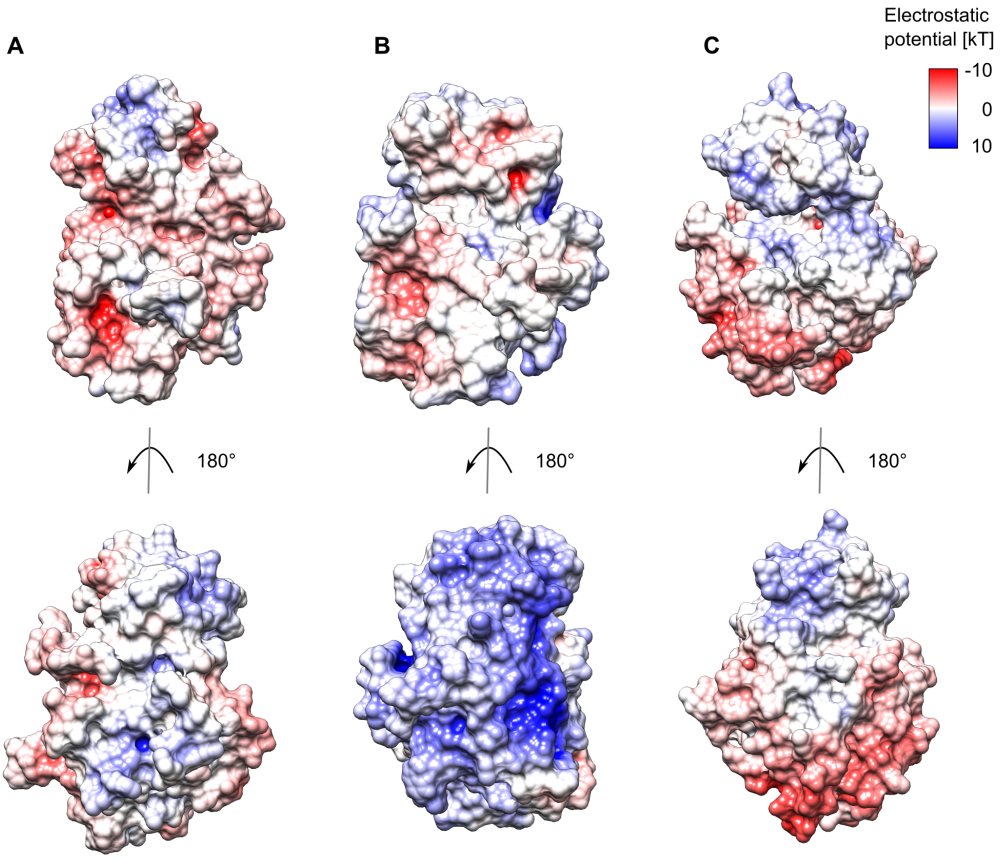

Figure 5.5: Electrostatic surface potential of the structures of BAK1, BRI1 and BIR3. **A:** Electrostatic potential of BIR3 (structure modeled based on BIR2 - PDB ID 4l68 [122]). **B:** Electrostatic potential of BRI1 (PDB ID 5lpw [123]). **C:** Electrostatic potential of BAK1 (PDB ID 3tl8 [185]). Shown are front and back of the proteins with the N-terminus being at the top of the structure. The electrostatic sufrace potential was calculated using PDB2PQR as integrated in webSDA at a pH of 7.2.

cated at N- and C-termini, any complex docking at this position will cause a clash between the artificial ends of the protein structures and will be excluded from the list of feasible complexes (see Materials & Methods, section 3.2.4 on the criteria for complex selection, p. 20).

5.2 Docking Analysis

5.2.1 Interaction of BAK1 and BRI1

Before I could specify the role of the negative regulator BIR3 in the early events of BR signaling, I had to determine how the cytoplasmic domains of the receptor BRI1 and the co-receptor BAK1 interact. Furthermore, it is also a question if the cytoplasmic domains of BRI1 and BAK1 can interact at all without the hormone inducing the interaction of the extracellular domains first.

Therefore, I used both webSDA to calculate a possible complex of the two cytoplasmic domains. To substantiate the results of webSDA analysis, I used ClusPro for futher validation. Both webSDA and ClusPro calculate potential complexes between the two proteins by sampling the interaction space and clustering the results. In general, docking methods yield either encountered complexes, which were computed by rigid body docking, or docked complexes, which have an additional step of flexible side chain adjustment. webSDA uses rigid body Brownian dynamics to calculate encountered complexes between the proteins [99, 48]. This way, the actual process of diffusional association is approximated computationally. The 500 encountered complexes with the lowest complex energies are stored and clustered into a predefined number of clusters [99, 48]. For each cluster, a representative complex is selected. The representative complex is the complex, which has the least RMSD from all other complexes in the cluster [99].

In contrast to this, ClusPro uses extensive sampling by first creating 70 000 potential interactions [132, 49, 52, 51]. Of these, only the 1000 complexes with the lowest scoring energies are considered for further structure refinement and clustering. Unlike webSDA, ClusPro has an additional computational step, where the amino acid residues are allowed to adjust their orientation in the complex. Therefore, in summary both proteins are closer to each other in the resulting complex than any complex obtained from webSDA based on the sampled distances of the amino acid backbones (see Materials & Methods section 3.2.4). Similar to webSDA, the cluster representative is the complex with the lowest RMSD to the other complexes in the cluster [52].

As the docking simulations allow more degrees of freedom than the actual membrane-associated receptor and co-receptor, I used a number of constraints to filter the results after docking. For one, all of the structures I analyzed for this chapter have structurally unresolved residues at N- and C-termini. Therefore, neither N- nor C-terminus of either protein is allowed to be part of the interaction surface between the proteins. For this criterion, I introduced a "minimal distance criterion" that serves as a threshold for the allowed distance between N- and C-terminus and the other protein. Furthermore, the N-terminus of both proteins have to be allowed to extend towards the membrane, while the C-terminus

is not allowed to clash with the membrane.
The complexes that pass all of these criteria, I evaluated based on the number of complexes in the cluster instead of the average cluster energy. The number of complexes per cluster is a measure of the energetic landscape for each cluster [52]. A cluster with a favorable energetic landscape will therefore have a high number of recorded complexes per cluster. As every method uses different ways of calculating the cluster energy, comparing these values is not a trivial issue. Furthermore, Kozakov *et al.* (2017) show that the probability of encountering a cluster P_k is proportional to the number of complexes N_k within a cluster. Therefore, I used the relative number of complexes per cluster $f = N_k / N_{total\,recorded\,complexes}$ as criterion to evaluate the computed complexes.
For the cytoplasmic domain of BAK1 and BRI1 (Fig. 5.6 A, B), the docking analysis was additionally limited by a center to center distance of 45 Å to prevent complexes from blocking either N- or C-termini of the proteins. Here, webSDA analysis yielded one potential complex (Fig. 5.6 C). Based on the number of complexes in this cluster $N_{BAK1\,BRI1} = 4$ out of a total of 500 recorded complexes ($f_{BAK1\,BRI1} = 0.008$), this particular interaction has an unfavorable energetic landscape. In this complex, BAK1 and BRI1 interact with their catalytic domains and activation loops facing each other. Therefor, this complex carries the risk of unwanted transposphorylation events between the cytoplasmic domains of BAK1 and BRI1, which normally occur after the stimulation with BR [31].
This complex fits into the current understanding of the interaction between the cytoplasmic domains of BAK1 and BRI1. Bojar *et al.* have shown that the inhibitor BKI1 binds to BRI1 at a region that involves D1139 (Fig. 5.6 C, highlighted in cyan) [123]. Furthermore, the authors showed that BKI1 binding prevents BRI1 from interacting with BAK1 [123] meaning that this region is involved in the interaction with BAK1. A mutation at D1139N is the underlying cause of the BRI1 missense allele *bri1-117* [190] highlighting the importance of that region.
The corresponding ClusPro docking results, yields a similar complex (Fig. 5.6 D). Notably, this complex was not observed for the complexes based on the scoring function of van der Waals and electrostatic forces, but rather with the balanced scoring function that also uses Decoys As the Reference State (DARS) [191]. Here, structural compatibility is also weighted into the scoring function, which yields near native docking results but shows poor discrimination of complexes for proteins other than enzyme-inhibitor and antigen-antibody complexes [191].
In summary, the docking of the cytoplasmic domains of BAK1 and BRI1 shows that, though energetically unfavorable, the cytoplasmic domains can interact. This interaction includes the activation loops and catalytic domains of both proteins. Therefore, this complex carries the risk of phosphorylation events in the absence of the hormonal ligand.

5.2.2 Interaction of BIR3 with BAK1 and BRI1

I further investigated the interactions of the cytoplasmic domain of BIR3 with both BAK1 and BRI1. Here, I addressed the question of how BIR3 can impact BAK1 activity. First,

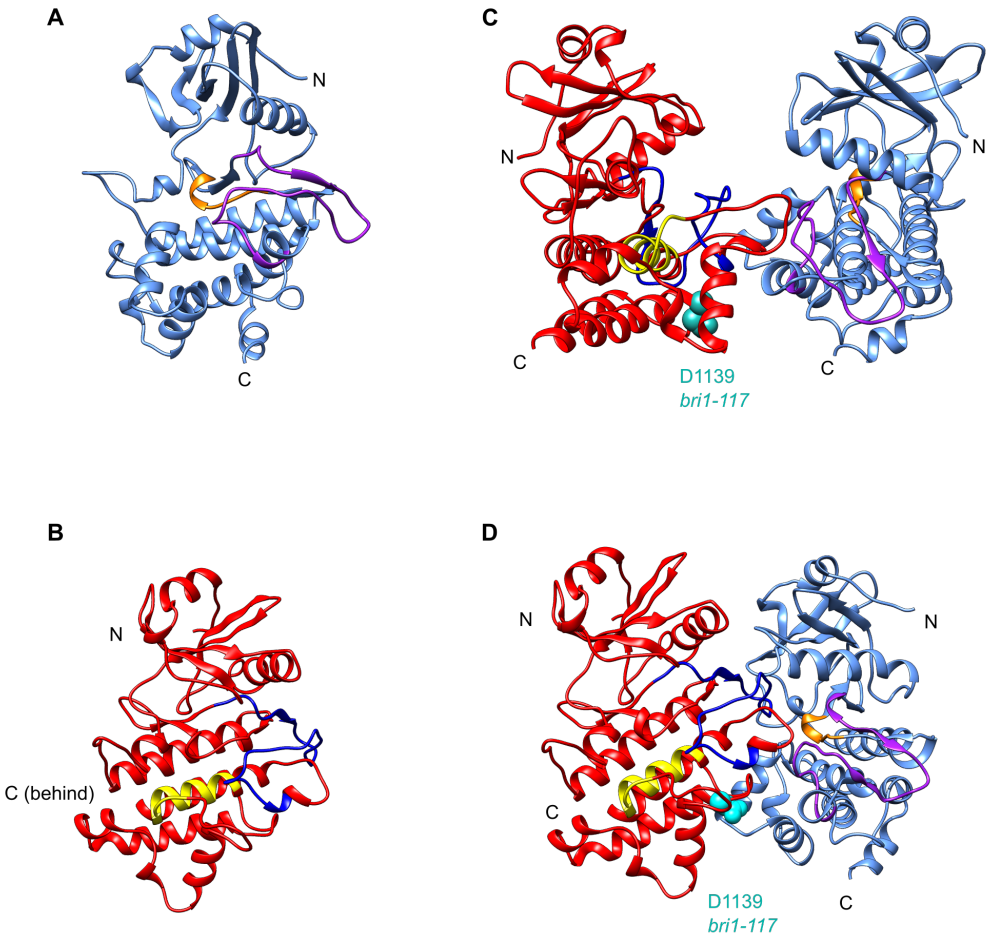

Figure 5.6: Modeling complexes between the cytoplasmic domains of BAK1 and BRI1. **A:** Cytoplasmic domain of BAK1 (3tl8, chain A). The catalytic loop (orange) and activation loop (purple) were annotated according to Yan *et al.* (2012) [184]. **B:** Gap-filled structure of BRI1 based on the template structure 5lpw [123]. The catalytic loop (yellow) and activation loop (blue) were annotated according to Bojar *et al.* (2014) [123]. **C:** Encountered complex between the cytoplasmic domains of BAK1 and BRI1 as calculated by webSDA. BAK1 and BRI1 are color coded according to parts A and B. D1139 on BRI1 is highlighted in light blue. **D:** Docked complex bewteen the cytoplasmic domains of BAK1 and BRI1 as calculated by ClusPro. Color code as before.

I computed potential complexes between the cytoplasmic domains of BIR3 and BAK1 by webSDA and ClusPro. To allow for a later comparison of the docking results of the different docking methods, I did not impose a distance criterion on the modeled complexes. Furthermore, I evaluated the ClusPro results based on the scoring function for van der Waals and electrostatic forces as this scoring function is closest to the scoring used by webSDA [125, 129, 130, 131]. I then evaluted the complexes based on the criteria listed in the section Materials & Methods (p. 20).
For the docking of BAK1 and BIR3, these complexes revealed that BIR3 preferentially binds to the catalytic domain and the activation loop of BAK1. This in turn means that these domains are not accessible for the substrates. Therefore, BAK1 cannot phosphorylate any substrate (other than possibly BIR3).
The precise orientation of the cytoplasmic domains of both BAK1 and BIR3 varies to a small degree between the individual complexes (Fig. 5.7). However, both webSDA and ClusPro are sampling processes that filter computed complexes based on a scoring function and combine them into clusters based on RMSD. Both structures select the representative complex for each cluster by the lowest RMSD to the other complexes in the cluster. In combination, this explains some variations between the precise complex orientation.
I further tested the interaction between the cytoplasmic domains of BRI1 and BIR3 (Fig. 5.8). Here, there are feasible complexes for both BIR3 structures though these complexes vary more in orientation than the ones observed for BIR3 and BAK1. Furthermore, the complexes in Figure 5.8 occur with a notably lower frequency than the ones observed in the corresponding docking analysis betwen BIR3 and BAK1 (Fig. 5.7). In general, the complex of BIR3 interacting with BAK1 is 1.8 to 3.8-times more frequent compared to the complex of BIR3 interacting with BRI1. This is based on the fact that the number of complexes per cluster correlates with the probability of encountering an complex [52].

Analysis of Interaction Sites of BIR3

To ensure that the results of docking BAK1 and BIR3 are consistent between the docking methods webSDA and ClusPro, I analyzed the interaction sites on BIR3 and BAK1 (Fig. 5.9). Therefore, I aligned the favored complexes computed by webSDA and by ClusPro to BAK1 (to study the interaction site of BAK1) and to BIR3 (to study the interaction site of BIR3). Here, I used the Match$\rightarrow$Align tool in Chimera to generate the alignments to BAK1 and BIR3, respectively [114, 115].
Figure Fig. 5.9 illustrates that the domains, which are involved in the interaction between BAK1 and BIR1 in the different docking methods, overlap to a high degree. There is some variation in the precise orientation of the cluster representative. However, this can be attributed to the fact that both ClusPro and webSDA are sampling methods that rely on clustering the computed complexes into representative clusters. The respective cluster representative is chosen to be the complex with the least RMSD to all other complexes in the cluster. Therefore, some variation in the orientation of representative complexes is to be expected. Nonetheless, Figure 5.9 highlights the fact that the binding sites are

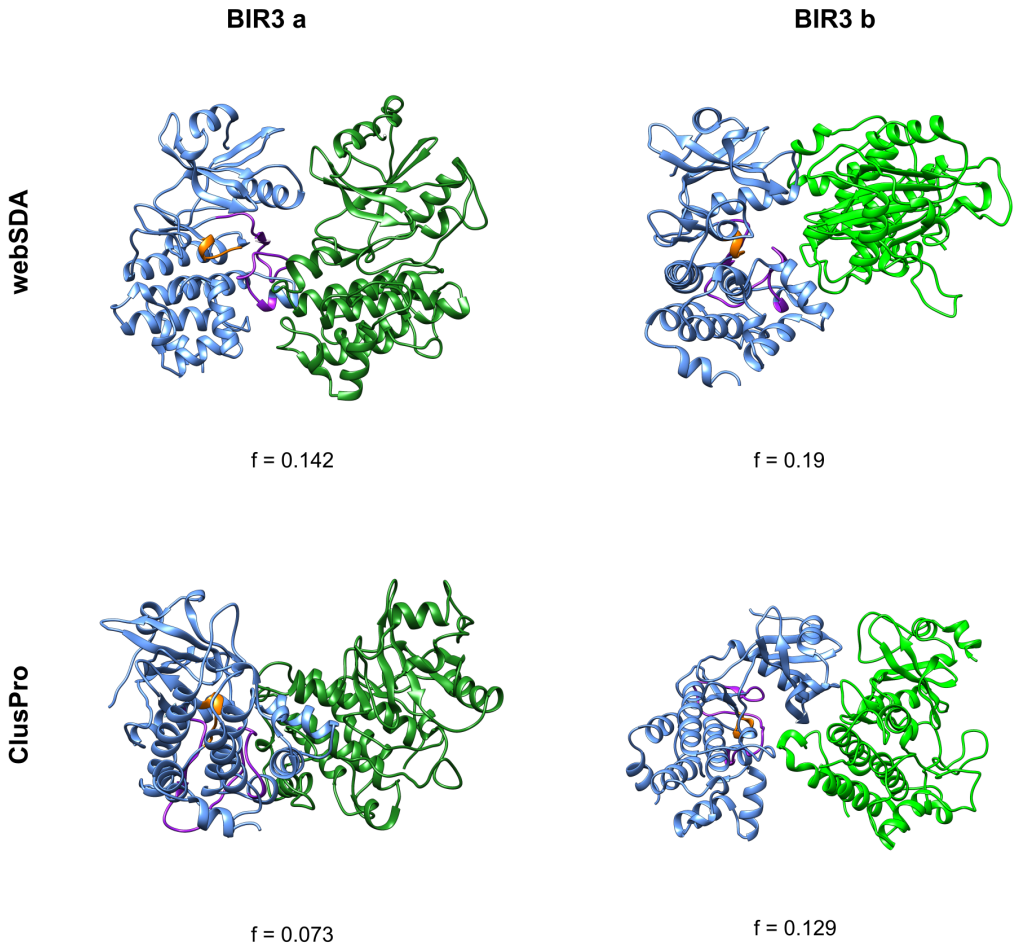

Figure 5.7: Modeled complexes between the cytoplasmic domains of BIR3 and BAK1. The results of both BIR3 structures and both docking methods, webSDA and ClusRro show high agreement with respects to the computed complexes. The relative size of the clusters is inidcated for each computed cluster.

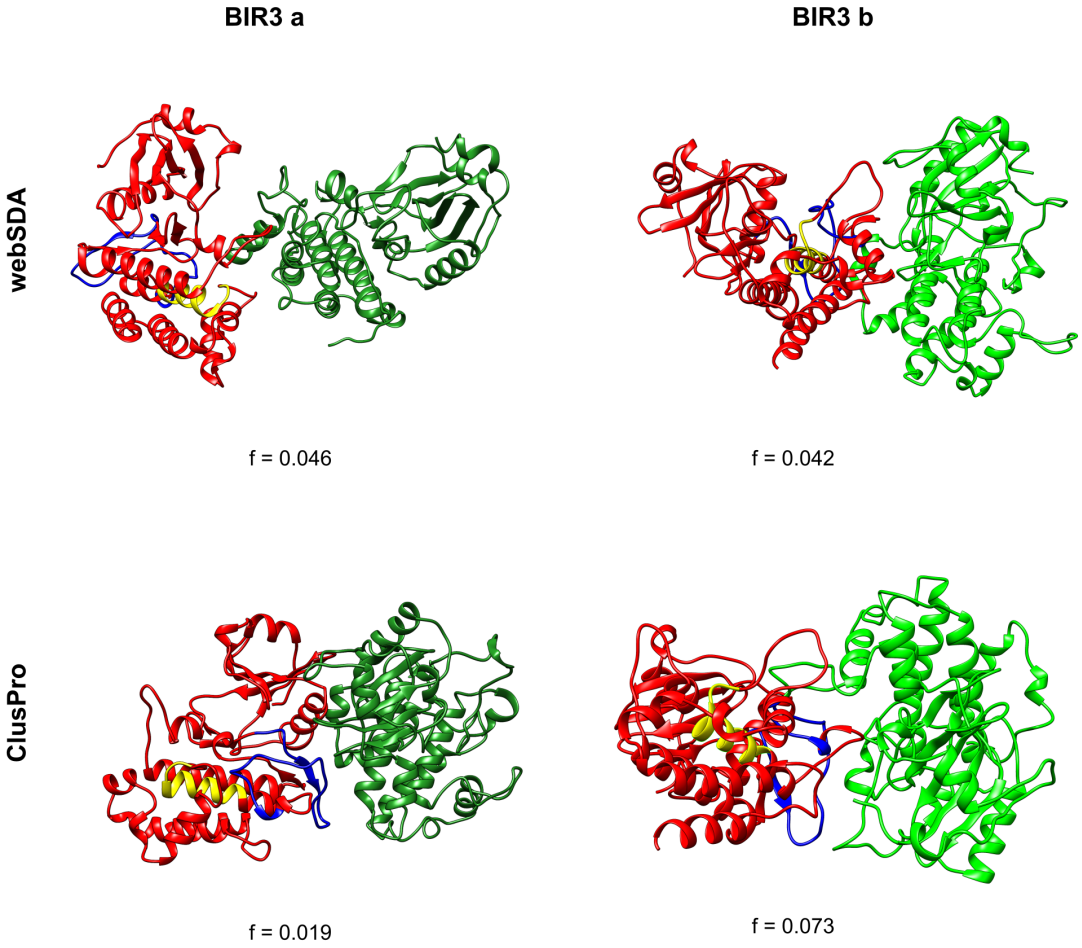

Figure 5.8: Modeled complexes between the cytoplasmic domains of BIR3 and BRI1. Shown are the results of both BIR3 structures and both docking methods, webSDA and ClusRro. The relative size of the clusters is inidcated for each computed cluster.

consistent between docking methods, which substantiates our computational results.

Experimental Validation by FRET-FLIM

To validate the results of the docking analysis regarding the complexes of BIR3 with BAK1 and BRI1, Friederike Wanke measured the interaction of the proteins of interest *in planta* by Förster Resonance Energy Transfer (FRET) Fluorescence Lifetime Imaging Microscopy (FLIM) (see Materials & Methods p. 21). By measuring the decrease in fluorescence lifetime τ (FLT) it is possible to get a measure of the degree of interaction between the proteins. A more prominent decrease in τ does not indicate a stronger interaction but rather a larger frequency of encountering an interaction. It is therefore, much like the number of docked complexes per cluster, a measure of the energetic landscape and how favorable the interaction is.
Here, full length BIR3-GFP was expressed in *Nicotiana benthamiana* either alone or in combination with BRI1-mCherry or BAK1-mCherry (Fig. 5.10 A). The measurements of BIR3-GFP alone served as control. When expressed in combination with BRI1-mCherry, the FLT of BIR3-GFP decreases significantly indicating that the proteins interact to some degree (Fig. 5.10 B). In comparison, the decrease in FLT is more pronounced in the the plants expressing both BIR3-GFP and BAK1-mCherry (Fig. 5.10 B). The observed $\Delta\tau$ is significantly lower than both the control and the FLT observed for BIR3-GFP and BRI1-mCherry. This indicates that BIR3 is more often in a complex with BAK1 than with BRI1, which fits the results of the computational modeling.

5.2.3 BRI1 can interact with BIR3-complexed BAK1

Finally, I checked if BRI1 can still interact with BIR3-complexed BAK1. Several experiments have indicated that there might be a trimeric complex consisting of all three proteins [30] and that BRI1 and BAK1 might exist in preformed, albeit inactive complexes in the *A. thaliana* membrane [14, 64, 65]. As the extracellular domains of BAK1 and BRI1 only interact in an acidic environment as long as the hormone is present [60, 44, 25, 64, 192], this interaction has to be due to the transmembrane or cytoplasmic domains of BAK1 and BRI1 [44].
Therefore, I tested if the cytoplasmic domain of BRI1 can bind to the BIR3-complexed BAK1 by ClusPro analysis. Here, webSDA analysis was not possible as the PDB2PQR server [124], which is used to compute the charged states of the proteins, could not process dimeric structures. This created an error during webSDA analysis. Therefore, I relied on ClusPro alone to run the trimeric docking. Nonetheless, I included the complexes between BIR3 and BAK1 that had been computed by webSDA in this analysis to have a larger sample size.
This docking analysis reveals that BRI1 can indeed interact with BAK1 while the co-receptor is in complex with BRI1 (Fig. 5.11). Here, BRI1 binds to the back of BAK1, which is on the opposite site of the catalytic domain and the activation loop. Therefore,

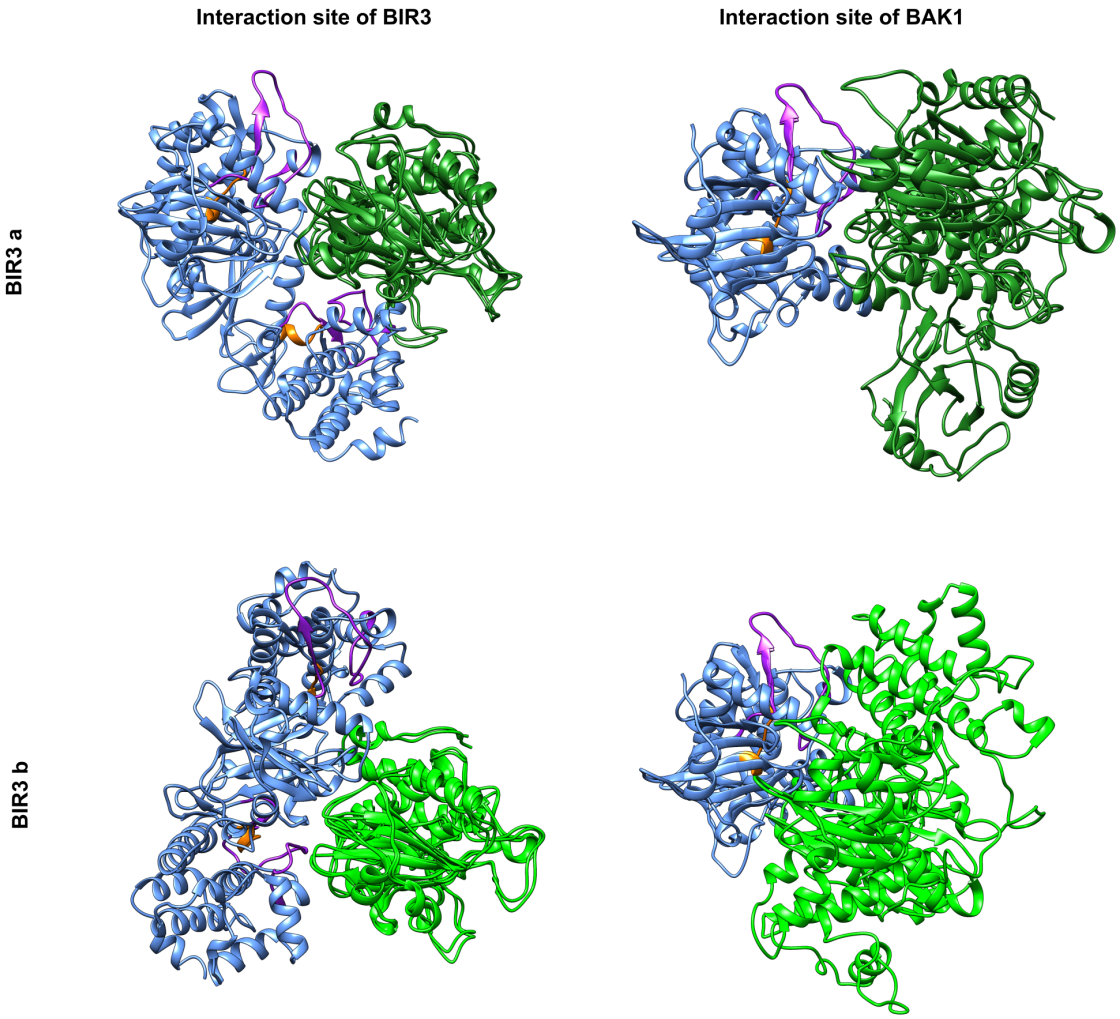

Figure 5.9: Comparison of interaction sites between BIR3 and BAK1. Figures were generated by alternately aligning the complexes computed for BAK1 and the different BIR3 structures to either BIR3 or BAK1 using the Match→Align tool in Chimera [114, 115]. The alignment consists of the favored complex computed by webSDA and by ClusPro.

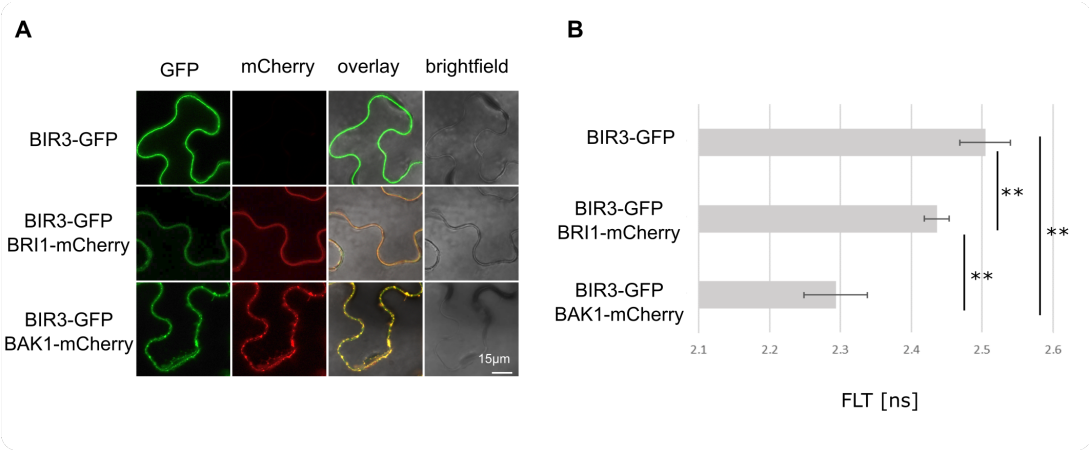

Figure 5.10: Experimental validation of the structural modeling results by FRET-FLIM. BIR3 interacts with BAK1 and BRI1 in the plasma membrane of *Nicotiana benthamiana*. **A:** The indicated fusion constructs of conding sequence and fluoresence dye were transiently expressed in tobacco epidermal leaf cells and collocalized in the membrane. **B:** Fluorescence lifetime (FLT in ns) of BIR3-GFP alone (control) and in combination with BAK1-mCherry and BRI1-mCherry. The values are the $mean \pm SD$ of three biological replicates with at minimum 7 cells. The statistical significance was tested by the Steel-Dwass-Test. (**) p-value < 0.01. Figures A and B were kindly provided by Friederike Wanke. The statistical analysis of the data in Fig. B was done by Nina Glöckner.

this complex carries no risk for unintentional phosphorylation events between receptor and co-receptor in the absence of the hormone. Also, the observed frequency of these complexes is quite low ranging from 0.03 to 0.04 indicating an unfavorable energetic landscape for this interaction.

Only the docking analysis of the second BIR3 structure in complex with BAK1 (originally computed by ClusPro) did not yield a feasible trimeric complex within the criteria set for complex selection. Here, either it was not possible for all N-termini of the proteins to continue to the membrane or a clash between a N- or C-terminus and another protein structure occurred. This shows that the occurrence of a trimeric complex is indeed quite unfavorable based on the energetic landscape.

5.2.4 Assessing the Implications of Unresolved Residues in the Template Structures

In the first step of this analysis, I selected structures from the Protein Data Bank [112, 113] to serve for the molecular docking analysis. For BAK1 there was a structure of the cytoplasmic domain without any gaps (3tl8 [185]). In contrast to this, the available structures for the receptor BRI1 contain gaps, where flexible loops could not be resolved structurally (5lpw [123]). While I was able to compute potential solutions for these gaps by comparative modeling, they represent a source of uncertainty. This is mitigated to some degree as I have employed the QMEAN4 score to evalute the qualities of the structures, which combines several different criteria for structure validation [97, 98]. I further used ClusPro

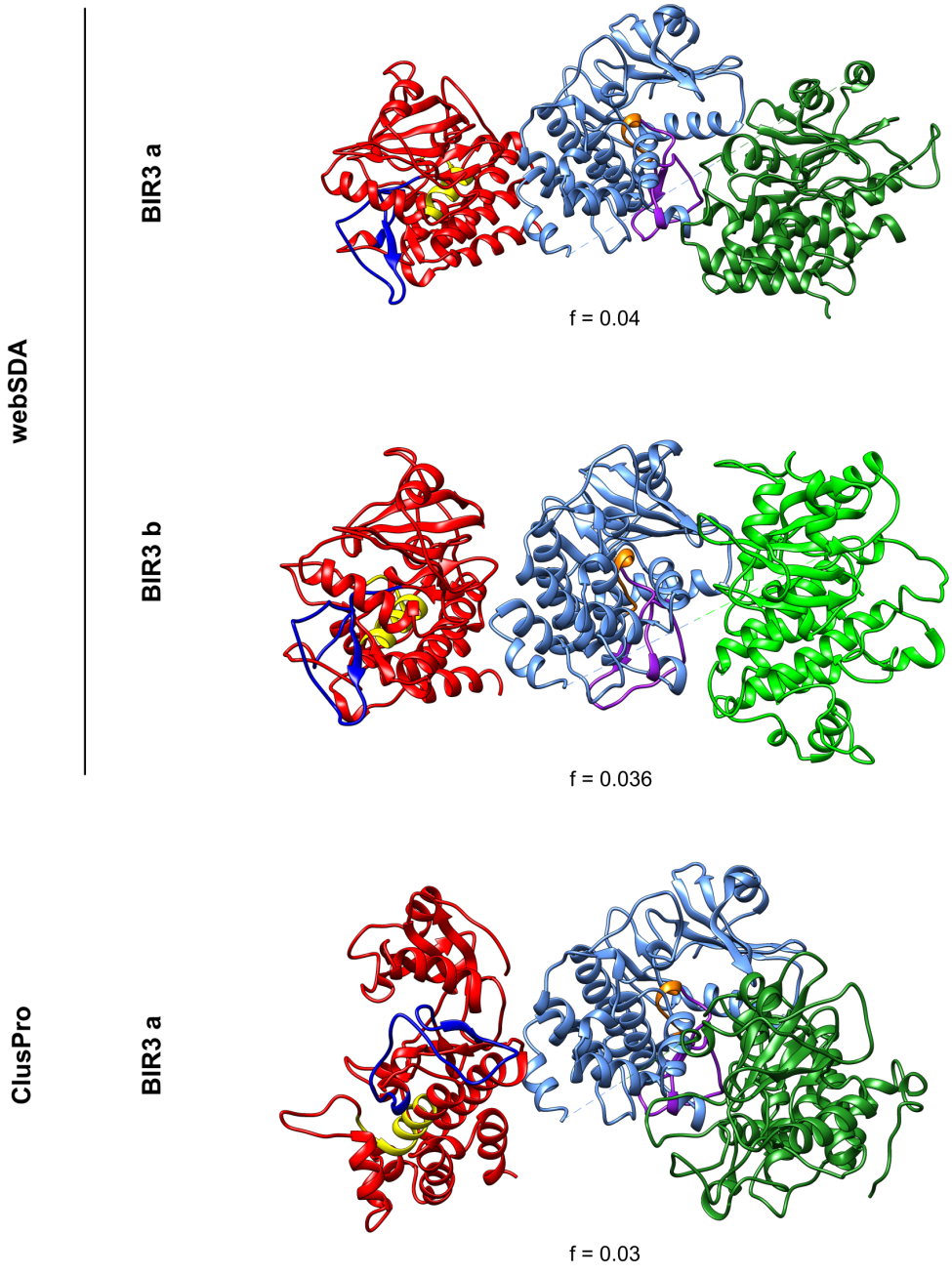

Figure 5.11: Putative trimeric complexes consisting of the cytoplasmic domains of BRI1, BAK1 and BIR3. The potential complexes were computed by ClusPro based on the complexes between BIR3 and BAK1 of the ClusPro and webSDA docking runs. The relative size of the clusters is inidcated for each computed cluster.

to substantiate the results of the webSDA analyses. Unlike webSDA, ClusPro includes an additional step, where amino acid side chains can adjust to complex binding [52].
Furthermore, the negative regulator BIR3 has not been resolved structurally at this time. Here, I used the structure of a closely related protein, BIR2 (4l68 [122]), to model a structure for BIR3. This is at all possible as proteins with high sequence identity also share a high degree of structural similarity [92]. With more than $60\,\%$ of sequence identity to BIR3, BIR2 is a suitable template for BIR3. Interestingly, the subsequent evaluation of the structures based on their quality by the QMEAN score yielded two BIR3 structures of equal quality. As it takes little effort to compute the additional interactions of the second BIR3 structure, both were used for the docking analysis, which also aids in substantiating the results of the computational analysis.
Therefore, I considered the position of the modeled segments in the protein structures for BRI1 and BIR3:

- In the complexes computed between BRI1 and BAK1 (Fig. 5.12 A) as well as the BIR3 structures with BAK1 (Fig. 5.12 B,C), the modeled segments are at the periphery of the interactions surface - if they are part of the interaction surface at all. Only in Figure 5.12 B, the small modeled segment of three amino acids is part of the interaction surface.

- In the complexes computed between BRI1 and BIR3 the position of the modeled segments is more varied. They can be apart from the interactions surface (Fig. 5.12 F) to at the periphery of the interaction surface (Fig. 5.12 D, E) to interacting directly (Fig. 5.12 G).

- In the computed trimeric complexes, BRI1 does not dock to BAK1 by its modeled segments, which are facing away from the interaction surface between BRI1 and BAK1 (Fig. 5.12 H-J).

This shows that for the most part, the modeled segments are not central to the interaction surface. Even if they are, longer and shorter segments need to be treated differently: Modeled segments are defined by their start, their end and their length. A short modeled segment like the three amino acid gaps in BRI1 and BIR3 are therefore well defined and only a minor source of uncertainty in the complexes. Longer modeled segments like the remaining ones of BRI1 and BIR1 are a more uncertain as these loops have more impact on the overall protein shape. However, I mitigated this in two different ways: For one, I used the QMEAN4 score, which is a reliable measure for 3D structure quality [97, 98]. Second, I used ClusPro in combination with webSDA to compute the complexes between the receptor BRI1, the co-receptor BAK1 and the negative regulator BIR3. ClusPro has an additional computational step, where amino acid residues adjust to the complex formation to remove steric clashes that occurred during rigid docking [52].

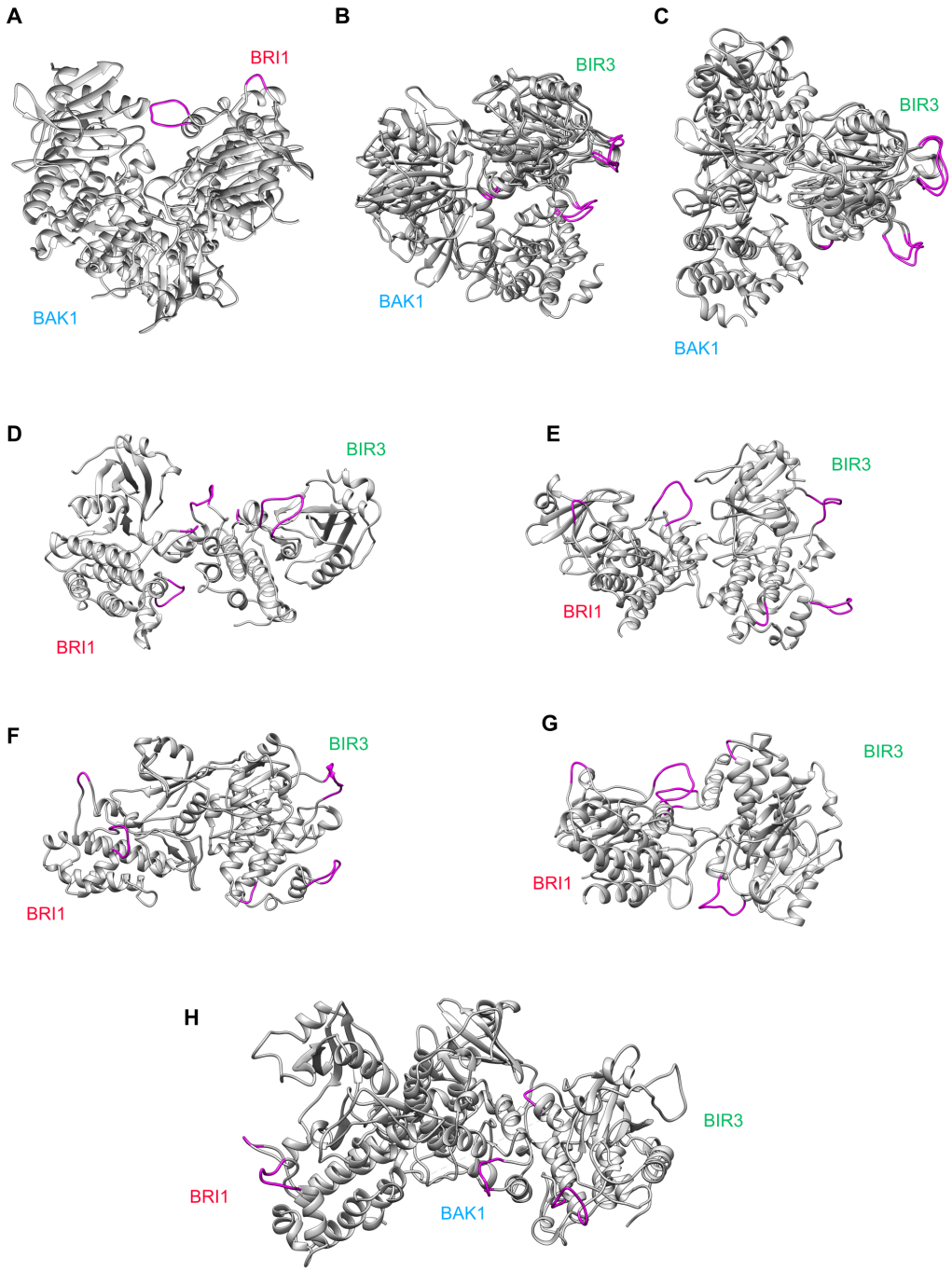

Figure 5.12a: Location of modeled segments due to unresolved loops in the template structures. Modeled segments where the respective template structures contained sturcturally unresolved amino acids are highlighted in magenta. **A:** Computed complexes between BAK1 and BRI1 are aligned according to the position of BRI1 in the complex. **B:** Complexes between the first BIR3 structure and BAK1. **C:** Complexes between the second BIR3 structure and BAK1. **D:** Complex between BRI1 and the first BIR3 structure as calculated by webSDA. **E:** Complex between BRI1 and the second BIR3 structure as calculated by webSDA. **F:** Complex between BRI1 and the first BIR3 structure as calculated by ClusPro. **G:** Complex between BRI1 and the second BIR3 structure as calculated by Cluspro. **H:** Putative trimeric complex calculated by docking BRI1 to BIR3-complexed BAK1.

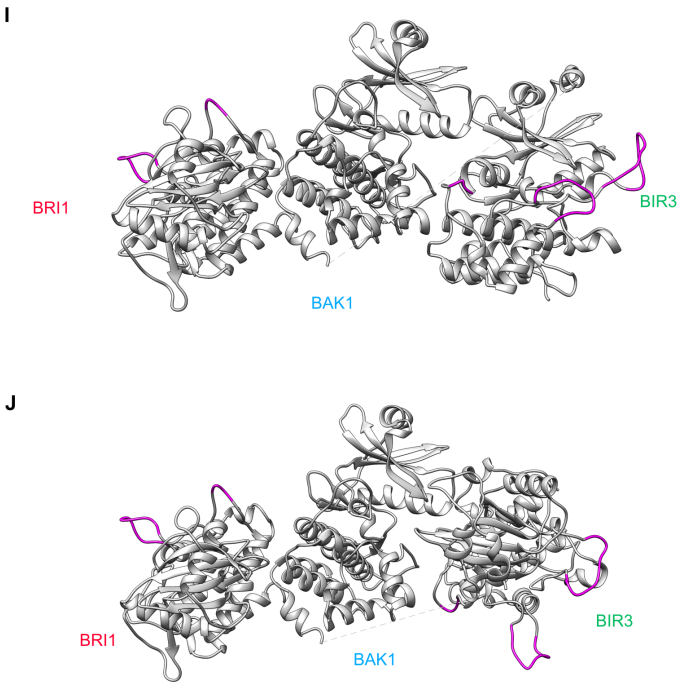

Figure 5.12b: Location of modeled segments due to unresolved loops in the template structures (continued). Modeled segments where the respective template structures contained sturcturally unresolved amino acids are highlighted in magenta. **I:** Putative trimeric complex calculated by docking BRI1 to BIR3-complexed BAK1. **J:** Putative trimeric complex calculated by docking BRI1 to BIR3-complexed BAK1.

5.3 Summary

The structural analysis of the cytoplasmic domains of the receptor BRI1, the co-receptor BAK1 and the negative regulator BIR3 provided insight into the interactions between these proteins. Based on the computational results, BIR3 preferentially binds to BAK1 at its catalytic domain and activation loop. BAK1 is therefore unable to interact with its substrates and to phosphorylate them. BIR3 can also form a complex with BRI1 based on my computational modeling. However, this interaction appears to be less favorable than the one between BAK1 and BRI1. This result was validated experimentally *in planta* by Friederike Wanke. Finally, I show that based on the computational results, a trimeric complex consisting of BRI1 - BAK1 - BIR3 is theoretically possible but has a unfavorable energetic landscape based on the number of complexes in that cluster.

6 | Modeling the fast BR response

This chapter comprises my work on analyzing the fast BR response pathway focusing on initiation and control of the signaling pathway using ODE models. The model comprises the known components and steps of the fast BR response and describes the physiologically observed responses of membrane hyperpolarization and cell wall acidification (see Introduction section 2.1.1 on p. 6). Furthermore, the ODE model also includes the BR-induced cell wall expansion by hydration [14]. I used this model to analyze the dynamics of the proteins in the fast BR response pathway and which model components control the response to BR stimulation.
To analyze the fast BR response pathway computationally, I fitted the model parameters to dose-response data of the change in membrane potential E_m to stimulation with brassinolide (BL) and the qualitative overexpression behavior of BIR3 and BIR3&BRI1 plants (section 6.2). To address parameter non-identifiability, I generated an ensemble of 50 models that describe the data equally well (section 6.2.3). After analyzing the impact of the different model parameters on the membrane potential change by sensitivity analysis (section 6.2.4), I predicted the model's behavior in the meristematic zone and in a *bir3* mutant. This behavior was validated experimentally (section 6.3).
The experimental data shown in this chapter are the results of experiments done by our collaborators in the research group of Klaus Harter at the Center for Plant Molecular Biology (ZMBP) at the University of Tübingen. In particular, Nina Glöckner quantified the negative regulator BIR3 and the ATPase AHA2 in relation to the receptor BRI1 (for the experimental procedure see Materials & Methods 3.3.5). She also validated the model experimentally by measuring the proton flux at the root surface by non-invasive MIFE and pH measurements using HPTS (see section 6.3.1).

6.1 Model Structure

In this section I describe the model structure including the involved compartments, species, reactions, global quantities and events. The model was built in COPASI version 4.23 build 184 running on Windows 8.

Table 6.1: Compartments of the ODE model in the different root zones. Values were taken from van Esse *et al.* (2011). (*) The cell wall volume listed here is only the initial cell wall volume as the model includes cell wall swelling. The initial cell wall volume was calculated based on the cell membrane area and the cell wall thickness [11].

Root zone	Compartment	Size
Meristematic zone	cytosol	$8.47 \times 10^{-13}\,\mathrm{dm}^{-3}$
	membrane	$7.67 \times 10^{-8}\,\mathrm{dm}^{2}$
	cell wall*	$3.03 \times 10^{-13}\,\mathrm{dm}^{3}$
Elongation zone	cytosol	$5.8 \times 10^{-12}\,\mathrm{dm}^{3}$
	membrane	$5.27 \times 10^{-7}\,\mathrm{dm}^{3}$
	cell wall*	$2.08 \times 10^{-12}\,\mathrm{dm}^{3}$

6.1.1 Compartments

The proteins involved in the fast BR response pathway are predominantly located in the plasma membrane of *A. thaliana*. Furthermore, the fast BR response affects cell wall volume by initiating cell wall hydration [14]. As multi-compartment rate laws are very important in such cases (see Chapter 4), I took special care to consider the information on cell morphology for the signaling pathway in the computational model. Therefore, I modeled three compartments - cell wall, plasma membrane and cytoplasm. The information on the size of the compartments was taken from van Esse *et al.* [11], who measured cell dimensions across the different root zones.

The ODE model includes the cell wall swelling, which is one of the steps preceding cell elongation [8, 9]. Therefore, the initial cell wall volume $V_{cell\,wall}$ is defined by the cell surface $A_{cell\,surface}$ and cell wall thickness $cell\,wall\,thickness(t)$. The latter is defined to be variable allowing the description of experimentally observed cell wall swelling [14].

$$V_{cell\,wall}(t) = A_{cell\,surface} \cdot cell\,wall\,thickness(t) \tag{6.1}$$

6.1.2 Species

The ODE model comprises the known components of the fast BR response pathway (see section 2.1.1). Wherever experimental data were available, I used this information to define the initial concentration of the species. If no experimental information was available, I made an effort to have a realistic estimate. As the model starts in the inactive state of the signaling pathway, the initial concentration of all phosphorylated species is $0\,\mathrm{nmol\,dm}^{-2}$ or $0\,\mathrm{nmol\,dm}^{-3}$, respectively.

BRI1 The receptor BRI1 has been quantified in detail by van Esse *et al.* (2011). In an epidermis cell in the elongation zone there are an average of 11 receptor molecules per $\mu\mathrm{m}^2$. As this concentration changes in the different root zones and cell types [11], I used a number of global quantities to define the initial receptor concentration $BRI1\,concentration$ based on the number of receptor molecules per $\mu\mathrm{m}^2$ (see section 6.1.4). The initial species con-

Table 6.2: Overview of species in the ODE model with the appropriate identifiers. Proteins are specfied by their UniProt identfier [193] and gene identifier and chemicals are specified by the ChEBI (Chemical Entities of Biological Interest) identifier [194]

Name	Model Name	ID	Gene ID
Brassinolide	BL	28277	
Proton	H^+	24636	
Brassinosteroid insensitive 1	$BRI1$	O22474	At4g39400
BRI1-associated kinase 1	$BAK1$	Q94762	At4g33430
BRI1 kinase inhibitor 1	$BKI1$	Q9FMZ0	At5g42750
Botrytis-induced kinase 1	$BIK1$	O48814	AT2g39660
BAK1-interacting receptor-like kinase 3	$BIR3$		At1g27190
P-type Arabidopsis H^+-ATPase 1	$AHA1$	P20649	At3g18960
P-type Arabidospis H^+-ATPase 2	$AHA2$	P19654	At4g30196

centration of the receptor is then defined by multiplying the calculated initial concentration and an expression factor:

$$[BRI1]_{t=0} = BRI1\,concentration \cdot expression\,factor \tag{6.2}$$

The expression factor was used to change the expression level of the receptor for the overexpression data (see section 6.2.2).

AHA1 and AHA2 Thanks to the work done by Nina Glöckner on quantifying important model species, I was able to define the initial concentrations for BIR3 and AHA2 using experimental data in the model. Based on the quantification of BRI1 by van Esse *et al.* [11] (Fig. 6.1 D), she measured the abundance of BIR3-GFP and AHA2-GFP in relation to BRI1-GFP using both microscopy and Western blotting.
The Western blotting experiments revealed that ATPase levels are 2 to 5-times the concentration of BRI1 throughout the whole root (Nina Glöckner, personal communication) (an exemplary result of the Western blot protein quantification is shown in Fig. C.1, p. 181). The fluorsecence microscopy data support the higher concentration at 5-times the amount of BRI1 (Fig. 6.1 A). As the receptor has a concentration of 2 proteins per µm^2 [11], this translates into an overall concentration of 10 proteins per µm^2 (Fig. 6.1 D). Microscopical analysis further showed that H^+ ATPase pumps have far lower concentrations of around 2 to 4 proteins per µm^2 in the meristematic zone (Fig. 6.1 B). Interestingly, the images have also shown that ATPase levels increase as cells start to elongate (Fig. 6.1 C, blue arrows). Cells that elongate at a later time have lower ATPase levels (Fig. 6.1 C, yellow arrow).
In the model, the amount of AHA2 is defined by the following equation:

$$[AHA2]_{t=0} = BRI1\,concentration \cdot ratio_{AHA2:BRI1} \quad , \tag{6.3}$$

which comprises the global quantities $BRI1\,concentration$ and $ratio_{AHA2:BRI1}$.
The H^+-ATPase AHA2 is not the only ATPase in the root. Rather AHA2 acts in concert with the H^+- ATPases AHA1 [68]. Here, there were no protein quantification data available. In-

stead, I relied on the RNA expression data on the eFP server[1] [195]. Assuming that AHA1 and AHA2 are translated at the same rate and have similar turnover rates, I approximated AHA1 protein levels based on the expression ratio of AHA1 and AHA2 according to the eFP server. In the elongation zone epidermis, AHA1 is expressed at approximately 1.1-times the amount of AHA2.
As there is no knowledge about a differential role of AHA1 and AHA2 in the fast BR signaling pathway at the time of writing this thesis, AHA1 and AHA2 are combined into one species in the model. The initial concentration of $[AHA]_{t=0}$ is simply the sum of AHA1 and AHA2 concentrations. The same holds true for the initial concentration of the AHA C-terminus.

BIR3 In contrast to the H^+ ATPases, the BIR3 concentration does not change as much throughout the root. Here, both fluorescence microscopy (Fig. 6.1 B) and Western blotting (Nina Glöckner, personal communication) have shown the BIR3 concentration to be around 1.3 to 1.4-times the amount of BRI1. The initial concentration of BIR3 is defined by the global quantity $BRI1\,concentration$ that is multiplied with the $ratio\,BIR3 : BRI1$ and the expression factor $factor_{BIR3}$. The latter was used to model the overexpression behavior (see section 6.2.2).

BAK1 Finally, van Esse *et al.* (2011) also quantified the co-receptor BAK1. Here the experiments have shown that BAK1 has around 5 proteins per μm^2 [11]. Despite the low concentration of the co-receptor, experiments have shown that is not rate limiting [63].

pH In addition to the quantification of protein species in the model, there exist some information on the initial proton concentrations in the cytoplasm and in the cell wall. For one, the intracellular pH is very stable around pH 7.2 [196, 197] and was fixed in the model. In the elongation zone, the extracellular pH starts out at pH 5.4 [111].

BL The model is stimulated by brassinolide (BL), which is the biologically most active form of brassinosteroids. The dose was defined according to the experimental setup for measuring the membrane potential change [14].

BKI1 and BIK1 For the final species in the model, BKI1 and BIK1, I had to estimate the initial concentrations. As both proteins act as inhibitors of the receptor BRI1 [26, 27, 28] and silencing or deletion has a positive effect on the response to BR stimulation [26, 28], I estimated their concentrations to be slightly higher than the initial concentration of the receptor. To be precise, I set the initial concentrations of $[BKI1]_{t=0}$ and $[BIK1]_{t=0}$ to be

[1] `http://bar.utoronto.ca/efp/cgi-bin/efpWeb.cgi`

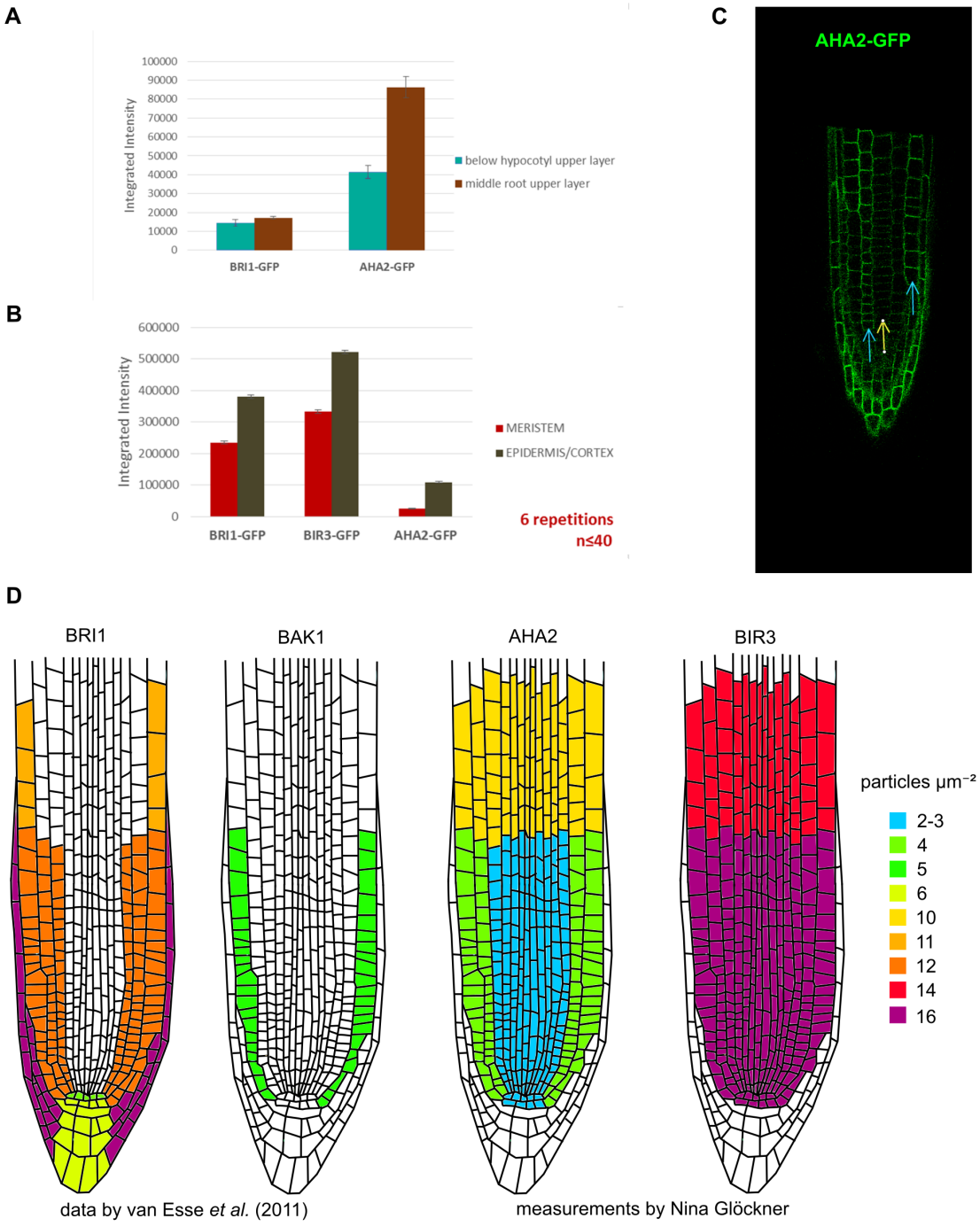

Figure 6.1: Experimental quantification of important model species. A: Quantification of AHA2-GFP in the root and below the hypocotyl by fluoresence microscopy. **B:** Quantification of BIR3-GFP and AHA2-GFP in relation to BRI1-GFP in the meristematic zone. **C:** Example image of AHA2-GFP expressing seedlings in the meristematic zone (cortex). Cell collumns with higher ATPase concentration (blue arrows) start to elongate earlier than cell collumns with lower concentration (yellow arrow). **D:** Concentrations of the receptor BRI1, the co-receptor BAK1, the ATPase AHA2 and the negative regulator BIR3 in the different root zone based on the experimental data by van Esse *et al.* (2011) [11] and the measurements by Nina Glöckner. Figures A-C were kindly provided by Nina Glöckner (University of Tübingen). The colors of panel A were adjusted for easier understanding.

$1.2 \cdot BRI1\,concentration.$

6.1.3 Reactions

In this section I describe the processes taking place without the hormone, the signal transduction and the dephosphorylation and dissociation processes of the fast BR response (see Fig. 6.2). The actual ODEs of the model species can be found in the supplementary material for this chapter (see section C.3 on p. 183). Wherever possible, I used experimentally determined data ranges for the model parameters or for the parameter ranges for the fitting process (see Supplementary Information Tab. C.5, p. 189).
COPASI automatically generates the ODEs of the species based on the chemical reactions that are part of the model. If a reaction involves only one compartment, the speed of that reaction is scaled with the respective compartment volume. In case of multi-compartment rate laws, the scaling of the reactions has to be defined by the user. In the model described here, this was the case for reactions occurring between the membrane and the neighboring compartments (r_{01}, r_{02}, r_5, r_6, r_{d1}, r_{d2}, r_{d3}, r_{d4}, r_{d5}).

BR-Independent Processes

The model is formulated such that an equilibrium is reached in the absence of the hormone. This is not a physiological situation that would occur in a living cell as proteins are constantly produced and degraded, which is currently not a part of the model. Furthermore, the model does not comprise metabolism nor is the ATP consumption by the H^+-ATPases AHA1 and AHA2 included in the model. As the model is a closed system without the hormone (r_{s1} and r_{s2} in Fig. 6.2) and only consists of for reactions (r_{01} to r_{04}), the system can only reach a zero-flux state, an equilibrium. I specifically designed the model to reach this equilibrium as to allow the model to adjust to the *in silico* overexpression BIR3 and BIR3 & BRI1 before stimulation with the hormone (see section 6.2.2).
In this state, only some of the reactions of the model take place; the P-type ATPase pump activity (r_{01}), the proton leak (r_{02}), the interaction of BIR3 and BAK1 (r_{03}) and the interaction of BIR3 and BRI1 (r_{04}). The basal pump activity of the P-type ATPases AHA1 and AHA2 is modeled by an expanded mass action rate law. This was possible, as the intracellular proton concentration $[H^+_{in}]$ is fixed at a pH of 7.2.
Experimental studies have demonstrated that ATPase activity is regulated by the C-terminus [72, 73, 74]. Furthermore, detailed expression studies in yeast revealed that removing the C-terminus of AHA2 increases the activity by a factor of up to 7.78 [73]. A phenomenological describtion of this inhibition is included in the rate laws by including the following term:

$$\cdot \left(\frac{[AHA]}{[AHA] + inhibition_{AHA\,C\,terminus} \cdot [AHA_{C\,terminus}]} \right) \tag{6.4}$$

In the beginning of the simulation, none of the AHA C-termini is phosphorylated and the inhibition is in full effect. The strength of the inhibition is described by the factor

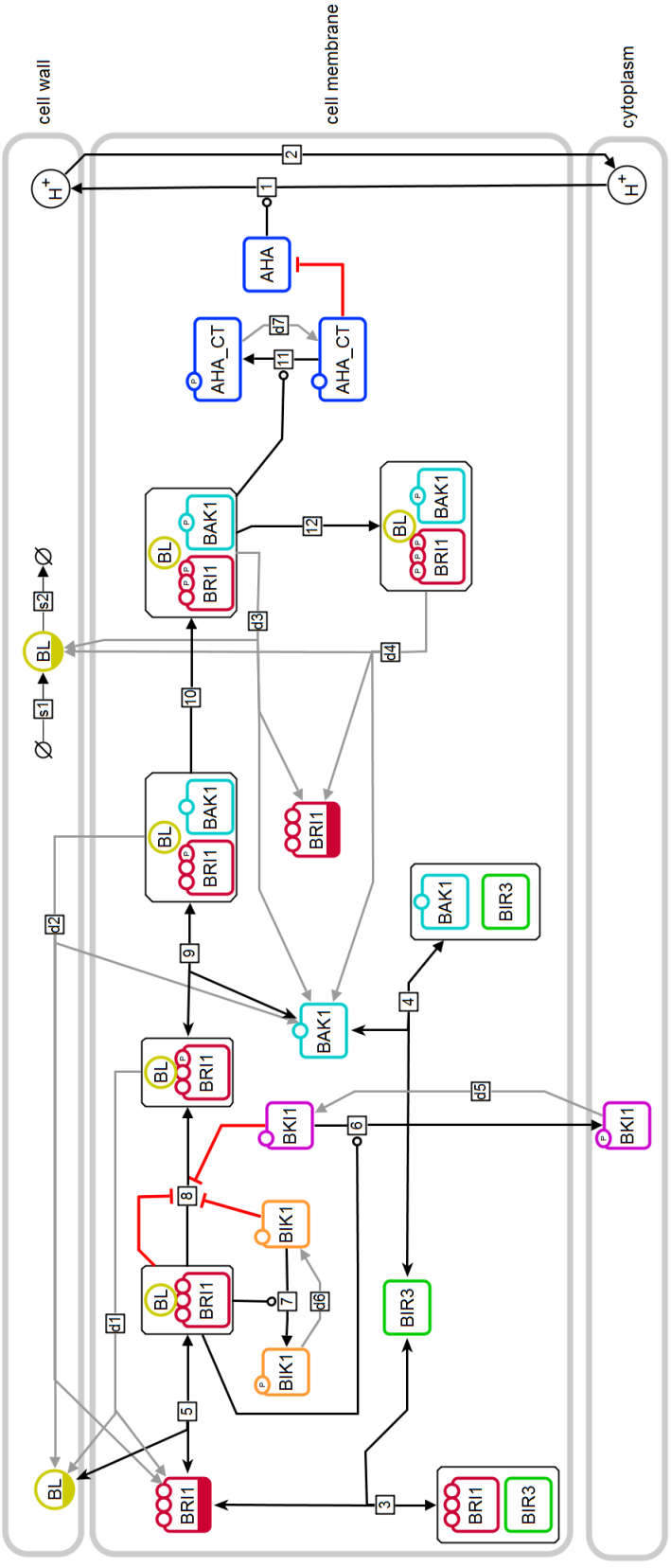

Figure 6.2: Model scheme including all species, compartments and reactions. The model's compartments rae indicated by grey boxes: cell wall, cell membrane and cytoplasm. Reactions are depicted by arrows. Black arrows signify reactions occurring without the hormone and upon hormone stimulation. Dephosphorylation and dissociation reactions are indicated by grey arrows. The reaction number is indicated by the small icon in the arrow. Inhibitory effects are represented by red arrows. Species that occur more than once in the scheme are indicated by a bar at the bottom of the icon. The figure was rendered using VANTED [158] according to the SBGN standard [159].

$inhibition_{AHA,C\,terminus}$, which was defined as a global quantitiy in the ODE model. The strength of the inhibition by the C-terminus was fitted within the minimal and maximal effect found in that study [73]. If every single C-terminus in the model is phosphorylated, this term becomes 1, which releases the inhibition.
The ATPase pump activity counters the proton leak into the cell (r_{02} in Fig. 6.2). While biological membranes represent a barrier to most substances, protons can diffuse over the membrane. Therefore, I have formulated the proton leak reaction to scale with the mebrane area. Thanks to the experimental measurements by Stefan Scholl (research group of Prof. Dr. Karin Schumacher (COS)), I was able to estimate the time scale of the proton leak rate. The calculations are included in the supplementary material for this chapter (see section C.1.2 on p. 181).
The last two reactions that occur without the hormone being present are the interactions of BIR3 with BAK1 (r_{03}) and BRI1 (r_{04}). Both of these reactions use the respective K_d and the association rate k to define the dissociation rate k_{off}. Based on the communications with Dr. Birgit Kemmerling and Sarina Schulze and my own work (Chapter 5 on p. 49), I knew that the interaction between BIR3 and BAK1 is more favorable than the one between BIR3 and BRI1. I integrated this information in the model by setting the parameter ranges for the respective K_d correspondingly (see Supplementary Information Tab. C.5, p. 189).

Signal Transduction

The signal transduction is initialized by hormone stimulation in both the model and in the plant cell. In the model, hormone stimulation is triggered by an event (see p. 83). This event enables two reaction, which were not allowed to occur previously (Fig. 6.2):

- ligand binding r_{05}
- hormone influx r_{s1} (see p. 79)

The process of ligand binding has been well studied experimentally using both biochemical studies and structural assays [1, 59, 198, 25, 44, 45]. In particular, the affinity of the receptor BRI1 to the ligand BL has been characterized by several different groups and ranges from 7.4 nM to 55 nM [1, 59, 198, 45]. Recently, a study by Hohmann *et al.* (2018) reaffirmed these values by measuring a K_D value of 11.0 nM [45]. In addition, this study also includes a measured association rate of the ligand to the receptor k_a [45]. All of this information was used in the rate law for this reaction. Since the receptor BRI1 is membrane-associated, this reaction scales with the membrane area.
The ligand bound receptor $BL\,BRI1$ now catalyzes of several reactions, the phosphorylation of BKI1 r_{06}, the phosphorylation of BIK1 r_{07} and the receptor itself r_{08} (Fig. 6.2). All of these reactions are inhibited by the unphosphorylated species $BKI1$, $BIK1$ and $BL\,BRI1$, which was modeled using a non-competitive inhibition mechanism. The reactions r_{07} and r_{08} occur within the membrane and do not involve other compartments. In contrast, reaction r_{06} involves not only the membrane but also the cytosol, as the phosphorylated form of $BKI1pY211$ is released from the membrane. Nonetheless, all three

reactions are scaled with the membrane area.
Once the inhibition by BKI1, BIK1 and the BRI1 C-terminus is released, the receptor BRI1 associates with the co-receptor BAK1 (r_{09}). In reaction r_{10}, BRI1 and BAK1 transphosphorylate each other resulting in the active form of the receptor complex $BAK1p\,BRI1pp\,BL$. Since no experimental data for the individual phosphorylations were available, all transphosphorylation events between BAK1 and BRI1 were lumped into one reaction. In this state the receptor can activate the P-type ATPases by releasing the inhibition of the C-terminus by phosphorylation (r_{11}).
Finally, the active receptor complex autophosphorylates at S891 (r_{12}) at a slow rate [79]. This phosphorylation inactivates the receptor [79] and represents the only mechanism of signal termination in this model version.

Dephosphorylation Reactions

All phosphorylated species in the model also have a reaction describing the dephosphorylation of the species. This ensures that the model can return to a steady state after the hormone is removed from the system. For the receptor species, the dephosphorylation also includes the dissociation of the ligand from the receptor.
Wherever possible, I used experimental data to estimate the dephosphorylation rate. The speed for the dephosphorylation rate of $BL\,BRI1p$ is the same as the dissociation rate of the ligand from the receptor in reaction r_{05}. Hohmann *et al.* (2018) have measured the dissociation rate of the ligand from the receptor [45]. I used this information as the upper bound for the reactions r_{d2} and r_{d3}, where BL dissociates from the receptor/co-receptor complex. Similarly, I defined the upper and lower bounds for reaction r_{d4} based on the fact that residual phosphorylations remain after five days of inhibiting BR [79].

Reactions for BL Stimulation

Due to the fact that the cell wall volume is not constant in the model, special care had to be taken to ensure a constant concentration of BL. If the concentration of BL was simply fixed in the model, there would be a steady dilution of the hormone due to the cell wall swelling. Thus, I introduced to reactions producing and consuming BL, where the ratio of these reactions defines the dose of BL in the model:

$$\xrightarrow{r_{s1}} BL \xrightarrow{r_{s2}} \tag{6.5}$$

BL is produced by a constant flux in reaction r_{s1} that only occurs if the event for BL stimulation has been triggered. The flux through this reaction is defined by a production flux and the dose of BL. To avoid an accumulation of BL exceeding the target dose, BL is re-

Table 6.3: Overview of reactions and available experimental data. Listed are reaction ID, the biochemical reaction, the rate law as well as the parameters with available experimental data (including the source). Abbreviations: MA - mass action kinetics; MM - Michaelis-Menten kinetics; CF - constant flux. The ordinary differential equations are listed in the Supplementary Informaiton section C.3, p. 183.

ID	Reaction	Rate Law	Parameter	Value	Source
r_{01}	$H^+_{in} \rightarrow H^+_{out}$	modified MA	K_i	up to 7.7 fold	[73]
r_{02}	$H^+_{out} \rightarrow H^+_{in}$	modified MA	k	0.84×10^{-9} dm s^{-1} to 1.25×10^{-9} dm s^{-1}	Dr. Stefan Scholl personal communication
r_{03}	$BIR3 + BAK1 \leftrightarrow BIR3\,BAK1$	MA			
r_{04}	$BIR3 + BRI1 \leftrightarrow BIR3\,BRI1$	MA			
r_{05}	$BL + BRI1 \leftrightarrow BL\,BRI1$	modified MA	K_d	7.4 nM to 55 nM	[1, 45, 59, 198]
			k_{on}	9.49×10^{-4} nMol^{-1} s^{-1}	[45]
r_{06}	$BKI1 \rightarrow BKI1\,pY211$	modified MM	k	0.97 s^{-1}	[199]
r_{07}	$BIK1 \rightarrow BIK1p$	modified MM			
r_{08}	$BL\,BRI1 \rightarrow BL\,BRI1p$	modified MA			
r_{09}	$BRI1p\,BL + BAK1 \leftrightarrow BAK1\,BRI1p\,BL$	MA			
r_{10}	$BAK1\,BRI1p\,BL \rightarrow BAK1p\,BRI1pp\,BL$	MA			
r_{11}	$AHA_{C\,terminus} \rightarrow AHA_{C\,terminus}p$	MM			
r_{12}	$BAK1p\,BRI1pp\,BL \rightarrow BAK1p\,BRI1pppS891\,BL$	MA	$time\ scale$	slow increase over 12 h	[79]
r_{d1}	$BRI1p\,BL \rightarrow BRI1 + BL$	MA			
r_{d2}	$BAK1\,BRI1p\,BL \rightarrow BAK1 + BRI1 + BL$	MA	max. k_d	1.05×10^{-2} s^{-1}	[45]
r_{d3}	$BAK1p\,BRI1pp\,BL \rightarrow BAK1 + BRI1 + BL$	MA	max. k_d	1.05×10^{-2} s^{-1}	[45]
r_{d4}	$BAK1p\,BRI1pppS981\,BL \rightarrow BAK1 + BRI1 + BL$	MA	$time\ scale$	residual P_i after 5 d	[79]
r_{d5}	$BKI1\,pY211 \rightarrow BKI1$	MA			
r_{d6}	$BKI1p \rightarrow BKI1$	MA			
r_{d7}	$AHA_{C\,terminus}p \rightarrow AHA_{C\,terminus}$	MA			
r_{s1}	$\rightarrow BL$	CF	$dose$	0 nM, 10 nM,50 nM, 100 nM	[14]
r_{s2}	$BL \rightarrow$	MA			

moved from the system in reaction r_{s2}. The parameters for the reactions r_{s1} and r_{s2} were chosen such that the effective dose of BL is described in the model. Furthermore, I set the production and consumption rate constants such that they are fast enough to ensure that BL levels remain approximately constant throughout the simulations.

6.1.4 Global Quantities

In addition to the biochemical reactions I used several global quantities to define some of the signaling components, such as the amount of transported charges across the membrane and the membrane potential itself. I used further global quantities to calculate the amount of BRI1 based on the numbers of receptor per µm and to define reaction parameters that were used by more than one reaction.

Calculating Protein Concentrations

Several model species are defined in relation to the concentration of the receptor BRI1. The concentration of the receptor itself, $BRI1\,concentration$ (in nmol dm^{-2}), is calculated based on the number of receptor molecules per µm^2, scaling factors from µm^2 to dm^2 (10^{10}) and from mol to nmol (10^9) as well as the Avogadro constant:

$$BRI1\,concentration = \frac{molecules\,per\,m^2 \cdot 10^{10} \cdot 10^9}{Avogadro\,constant} \tag{6.6}$$

The resulting receptor concentration is then used in combination with protein expression ratios to determine the amount of AHA2, BIR3, BKI1 and BIK1 by calculating the product of $ratio_{protein:BRI1}$ and $BRI1\,concentration$. Indirectly, it is also used to define the amount of AHA1 in the model as AHA1 is expressed in relation of AHA2.

Expression Factors

As some of the experimental information used for parameter estimation concerns the overexpression behavior of the negative regulator BIR3 and the receptor BRI1 [30], I included expression factors that allow for an easier parameter estimation. Therefore, the initial species concentration is defined as the product of the $normal\,concentration$ and the $expression\,factor$. I introduced the factors for BIR3 and BRI1 as these are the ones that were overexpressed by Imkampe *et al.* (2017) [30].

Transported Charges

This global quantity calculates the net charges transported across the membrane. In the current version of the model, only protons are transported across the membrane in the pump activity of the ATPase r_{01} and in the proton leak reaction r_{02}.

$$netto\,charge\,change = (Flux_{r_{02}\,proton\,leak} - Flux_{r_{01}\,ATPase\,pump\,activity}) \cdot \overbrace{96485.3365}^{\text{Faraday constant}} \cdot \underbrace{10^{-9}}_{\text{mol to nmol}} \quad (6.7)$$

Membrane Potential

The membrane potential change is calculated based on the transported charges, the membrane area and the specific membrane capacitance. This means that, since different cell sizes are modeled throughout the root, the membrane potential for those cell sizes differs even if the cell wall pH and all other parameters are identical.
According to the experimental data, the initial membrane potential was set to $-121\,\text{mV}$ in the elongation zone [14]. The data for the initial membrane potential was included in the parameter estimation at $0\,\text{nM}$.

$$membrane\,potential\,change = \frac{netto\,charge\,change}{specific\,membrane\,cpacitance \cdot surface \cdot scaling\,factor} \quad (6.8)$$

The specific membrane capacitance of *A. thaliana* is $8.1\,\text{mF}\,\text{m}^{-2}$ [200]. To scale between the specific capacitance of the membrane (in $\text{mF}\,\text{m}^{-2}$) and the $surface$ (in dm^2), I included the $scaling\,factor$.

Stimulation

The hormonal stimulation is mediated by an event in this model (see sectoin 6.1.5). Therefore, I defined this global quantity to enable reactions depending on the hormonal stimulation. The initial value of the global quantity $stimulation$ is 0. Once the event is triggered, the transient value is overwritten with a value of 1, which switches on the reactions for hormonal signal transduction and allows processes like cell wall expansion to occur.

Proton Readout

The cell wall instability is described depending on the extracellular pH. To have a description of the cell wall instability that depends on the model itself, I included the global quantity of the extracellular proton concentration at the time of BR stimulation.

Cell Wall Thickness

As BR signaling induces cell wall swelling, the thickness of the cell wall is not constant. Instead, I used an ODE to describe the change in volume. The membrane potential changes

according to the cell wall instability and the current cell wall thickness:

$$\frac{d\,(cell\,wall\,thickness)}{d\,t} = cell\,wall\,instability \cdot cell\,wall\,thickness(t) \tag{6.9}$$

Cell Wall Instability

To ensure that the cell wall volume does not increase indefinitely, I used a combination of two logistic functions: The first describes the activating effect of cell wall pH on cell wall swelling. The second logistic function comprises the inhibiting effect of the cell wall width getting closer to the maximal thickness.
Logistic functions are sigmoid curves defined by the steepness k and the midpoint x_0 of the curve:

$$f(x) = \frac{L}{1 + e^{-k(x-x_0)}}, \tag{6.10}$$

Here, L is the maximal value the function can assume and x is the independent variable. The parameters k, L and x_0 were chosen such that the the maximal thickness of the cell wall was at double the initial thickness:

$$\begin{aligned} cell\,wall\,instability = 20 \;\cdot\; & stimulation \\ & \cdot \left(\frac{1}{1 + e^{-0.001 \cdot ([H_{out}] - 4 \cdot proton\,readout)}} \right. \\ & \left. - \frac{1}{1 + e^{-5{,}000{,}000 \cdot (cell\,wall\,thickness - 6.525\,10^{-6})}} \right) \end{aligned}$$

To prevent the cell wall from expanding while the model reaches an equilibrium, the cell wall instability is only allowed to occur after hormone stimulation. I achieved this by including the global quantity $stimulation$ in the description of cell wall instability.

Kinetic Parameters

Finally, I defined kinetic parameters that were used by more than one reaction by introducing global quantities. For one, this concerns the inhibitory constants K_i for BKI1, BIK1 and the BRI1 C-terminus. As all three inhibitors affect any reaction that phosphorylates one of these inhibitors (r_{06}, r_{07}, r_{08}), the same K_i is used for each inhibitor in these reactions.
Furthermore, the dissociation constants K_D for the the ligand BL from BRI1, BAK1 from BRI1, BAK1 from BIR3 and BRI1 from BIR3 are defined by global quantities. The K_D of BL is also used to define the dissociation rate k_{off} by multiplying the association rate k_{on} in r_{05} with the K_D.

6.1.5 Events

The stimulation with the hormonal ligand BL is mediated by an event. This was done to allow the model to reach a steady state in the respective *in silico* overexpressions before

triggering the actual signaling pathway. Otherwise, the observed behavior would represent a combination of signaling activity and the model reacting to the different protein concentrations. In particular in the case of simulating overexpressions, the event is necessary to allow the model to adjust to the changed initial conditions.
Here, the model was simulated for one day ($86\,400\,\mathrm{s}$), before the stimulation is triggered by changing the value of the global quantity $stimulation$ from 0 to 1. This allows the reactions for BL influx and ligand association to proceed. Also, the cell wall becomes susceptible to the extracellular pH allowing the swelling of the cell wall to occur.

6.2 Model Behavior

Even though there are experimental information for several of the model components and reaction parameters available (see section 6.3), a number of parameters had to be estimated. Here, I used the available dose-response behavior [14] and the information on the behavior of the overexpression of BIR3 and BIR3 in combination with BRI1 to estimate the remaining parameters (Sarina Schulze, research group Dr. Birgit Kemmerling, ZMBP Tübingen) [30].
As the behavior of some model species could not be fitted to experimental data (e.g. all phosphorylated receptor species), there is a non-negligible issue of parameter identifiability (see section 6.2.3 for further detail). Therefore, I generated an ensemble of 50 independent parameter sets and analyzed the behavior and predictions for the whole ensemble [201].
Since some of the data used to fit the model concerned overexpression data, I simulated the model for $24\,\mathrm{h}$ before triggering the stimulation with BR by an event. Most importantly, the complex formation between BIR3, BAK1 and BRI1 had to be in an equilibrium. Otherwise, the complexes of BIR3 with BAK1 and BRI1 would start with a concentration of $0\,\mathrm{nmol\,dm^{-2}}$ and the observed model behavior would arise from too much free receptor and co-receptor (see Discussion 6.10, p. 92). Therefore, I checked that all of the models in the ensemble are in a chemical equilibrium before the stimulation with BR (Fig. 6.3 and Fig. C.3, p. 191).The time-course of all BIR3-related species in the model clearly shows that all of these species are in an equilibrium before the model is stimulated with BL. The precise amount of the individual complexes varies between parameter sets but the qualitative behavior is clear: BIR3 interacts more frequently with BAK1 compared to BRI1, which fits the experimental observations [30].

6.2.1 Dose-Response Behavior

First, I fitted the model to dose-response data of the membrane potential for 10, 50 and $100\,\mathrm{nM}$ BL of wild-type *A. thaliana* [14] (see Materials&Methods 3.3.5). Figure 6.4 summarizes the behavior of all 50 model parameterizations for the different doses of BL. The range of the experimental data is indicated by the colored area, while each model of the

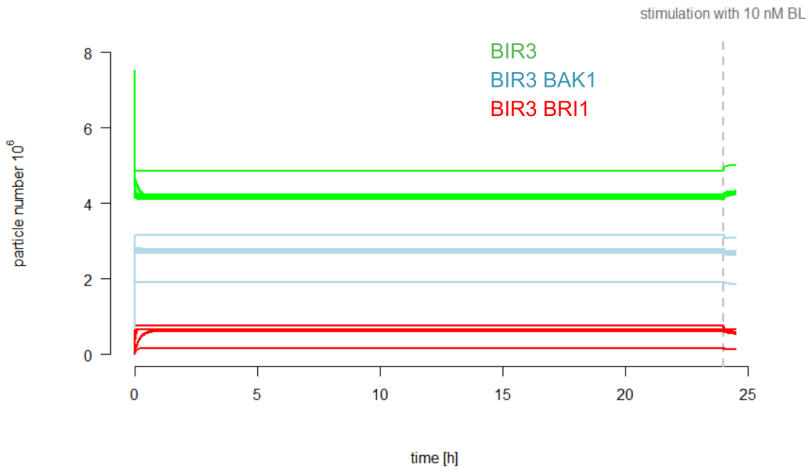

Figure 6.3: Model behavior before stimulation with 10 nM **BL after 24h.** Green: Particle numbers of $BIR3$. Blue: Particle numbers of $BIR3\,BAK1$. Red: Particle numbers of $BIR3\,BRI1$.

model ensemble is represented by a line in the plot.

First, Figure 6.4 illustrates how consistent the model behavior is for all parameter sets. Furthermore, the fitted time-courses describe the membrane potential change of 10 and 100 nM very well (Fig 6.4 A, C). For 50 nM BL, the model overestimates the response to BL stimulation slightly. Considering the fact that the experimentally determined average change in membrane potential at 50 nM BL is identical to the one observed at 10 nM BL, this not surprising.

Interestingly, the time-course particle numbers of $BAK1p\,BRI1pp\,BL$ vary between the different model parameterizations (Fig. 6.5 A) at 10 nM BL. While most models show a particle number around either 500 or 800, at least one model is in the range of 1000 active receptor molecules. This shows that the different parameterizations are in fact not identical but are different parameter combinations describing the final output of the change in membrane potential equally well.

Finally, Figure 6.5 B summarizes the behavior of the cell wall volume at 10 nM BL. During the simulated 30 min the cell wall shows a modest increase in size that falls slightly below the range of the experimentally observed cell wall hydration [14]. Experimentally, an average expansion of $35 \pm 10\,\%$ has been observed for the cell wall in response to 10 nM BL [14]. The definition of cell wall expansion in the model represents a compromise between describing the experimentally observed expansion rates and an artificially fast dilution of the extracellular proton concentration $[H^+_{out}]$.

6.2.2 *in silico* BIR3 Overexpression

I knew from my communications with Sarina Schulze in the research group of Dr. Birgit Kemmerling at the University of Tübingen that the overexpression of BIR3 reduces BR signaling to such an extend that the plants resemble *bri1-/-* mutants [30]. Furthermore,

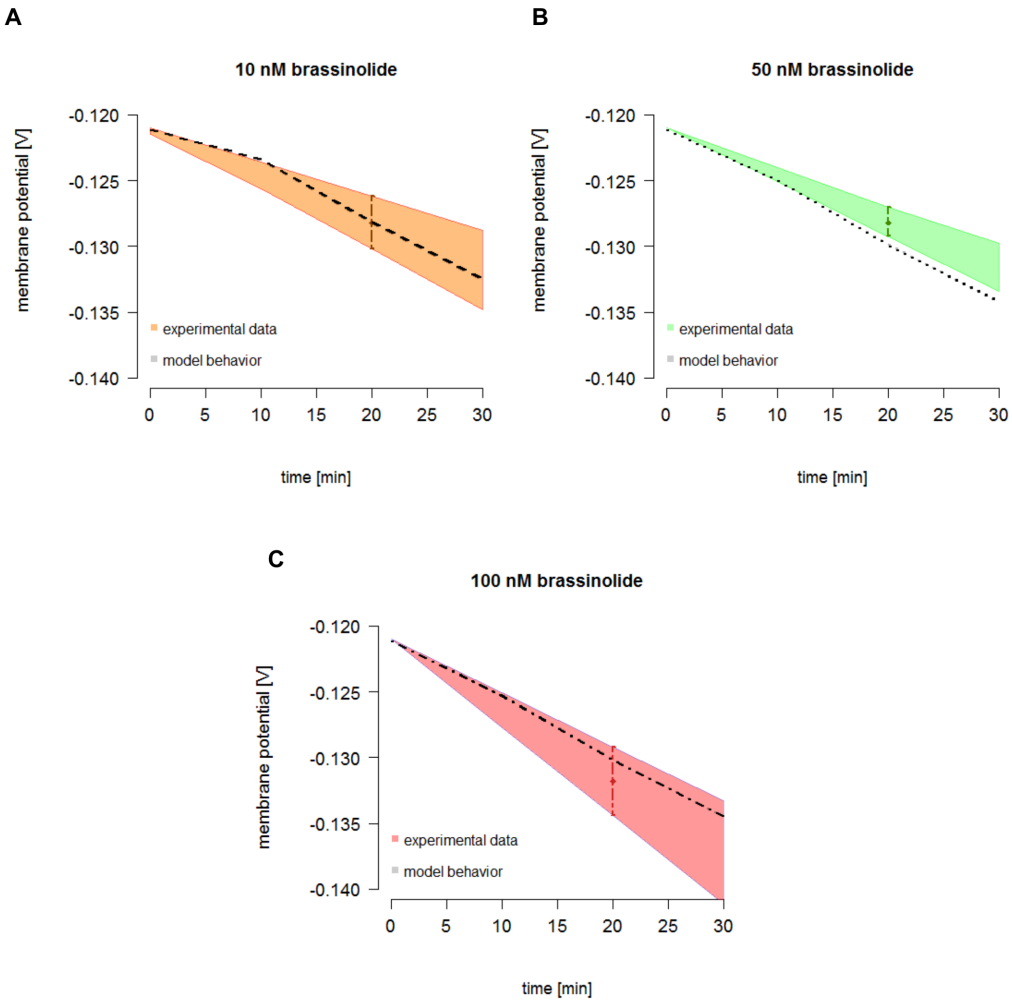

Figure 6.4: Fitted dose-response behavior of the membrane potential change. A: 10 nM BL. **B:** 50 nM BL. **C:** 100 nM BL. Shown are the ranges for the experimental data, with the measurements by Caesar *et al.* (2011) indicated by the points with standard deviation. The plots summarize the behavior of all 50 models of the model ensemble.

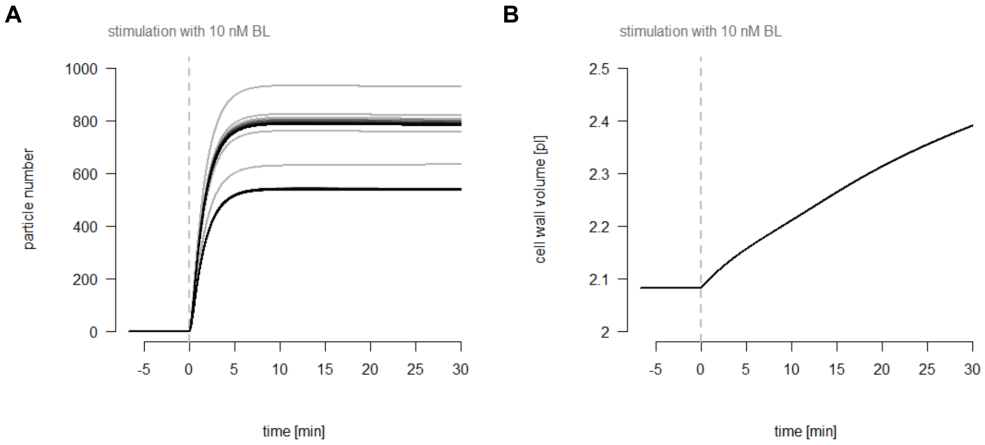

Figure 6.5: Time course simulations of active receptor molecules and cell wall volume. **A:** Time course of active receptor molecules $BAK1p\,BRI1pp\,BL$ for all 50 models. **B:** Time course of the cell wall volume for all 50 models.

the additional overexpression of BRI1 restores the activity of BR signaling such that the plants resemble wild-type Col-0 Arapdiopsis plants in terms of growth (Fig. 6.7 B).
I used this information in addition to the dose-response data to fit the parameters of the ODE model. To this end, I translated the qualitative information of the overexpression behavior into information that could be utilized to fit parameters of the ODE model. This means that stimulating the model with BL in the BIR3 overexpressing model should result in no membrane potential change. Also, the model overexpressing both BIR3 and BRI1 should show a response close to the wild-type levels after $20\,\mathrm{min}$ of stimulation with $10\,\mathrm{nM}$ BL.
Imkampe *et al.* overexpressed BIR3 and BIR3&BRI1 using the 35S promotor [30], which has a high activity. Consequently, both proteins should be overexpressed to the same level in the BIR3&BRI1 overexpressing plants. Therefore, I estimated an overexpression factor of 100 for BIR3 and 130 for BRI1. As the normal concentration of BIR3 is 1.3 times the amount of BRI1, this ensures that BRI1 is overexpressed to the same amount (not the same factor) as BIR3.
To test if this level of overexpression exceeds the available surface area of the cell, I estimated the occupied membrane area by all membrane proteins for each genotype. Here, I used the structural information of the proteins in this signaling pathway: I downloaded the structures from the Protein Data Bank [112] and approximated the protein diameter in the membrane using PyMOL [133]. Assuming a circular shape of the proteins (Fig. 6.6), I then calculated the occupied membrane area for the wild-type, the BIR3 overexpressing plants and the BRI3&BRI1 overexpressing plants (Tab. 6.4). The resulting percentages of the overexpression lines show that the signaling pathway occupies at most $8.2\,\%$ of the available cell surface area. While this is a relatively high degree, the overexpression using the 35S promotor is very strong.
In fact, Imkampe and colleagues checked the expression levels of BIR3 of two independent 35S-BIR3 overexpressing lines by quantitative and showed that the relative BIR3

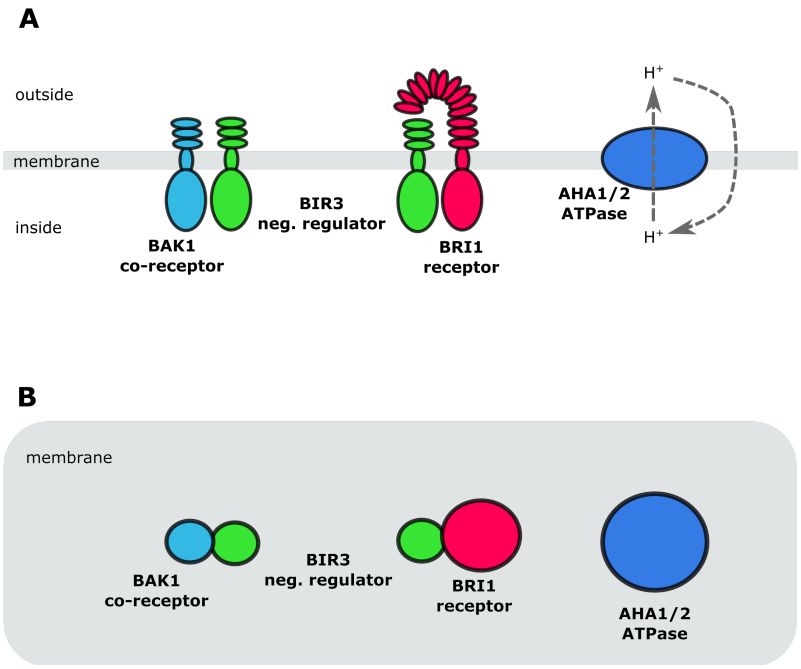

Figure 6.6: Estimating the membrane area occupied by the proteins of the signaling pathway. A: Scheme of the involved proteins. **B:** Projection of the occupied space onto the membrane.

expression is at least 100-times higher than the wild-type levels (Supplenental Figure 4 in [30]). The average BIR3 overexpression is in fact 150-times higher compared to the wild type. Since this quantification is based on the mRNA levels, this only approximates the actual protein concentration, as translation still has to occur.

I have previously examined the role of BIR3 in the fast BR response by molecular modeling. Here, I provide more context to the dynamics of the interactions by analyzing the behavior of the ODE model. The model behavior shows that all 50 models can describe the qualitative BIR3 and BIR3&BRI1 overexpression behavior (Fig. 6.7 A). Here, the model shows only a minute change in the membrane potential in the BIR3 overexpressing model. In turn, the additional overexpression of BIR3 restores the model response to the level of the wild-type.

The behavior of BIR3 as well as BIR3&BRI1 overexpression plants can be explained by the principle of Le Chatelier. The principle of Le Chatelier states that a system in steady state will react to a perturbation such that the effects of that perturbation are reduced. In the case of the BIR3 as well as BIR3&BRI1 overexpression plants this results in the observed growth phenotypes [30].

In wild-type plants, BIR3 will interact and form complexes with both BRI1 and BAK1 (Fig. 6.8 A). The addition of the hormone, perturbs that system by inducing the interaction between BAK1 and BRI1.

The strong overexpression of BIR3 under the control of a 35S promotor shifts the equilibrium of these reactions towards the formation of the complexes consisting of BAK1, BRI1 and BIR3 (Fig. 6.8 B). In this case, the addition of the hormone to the system is not

Table 6.4: Esitamed membrane area occupied by the proteins of the signaling pathway. Molecule counts were based on an epidermis cell in the elongation zone as measured by van Esse *et al.* (2011) and Nina Glöckner. Note: $1\mu m^2 = 1,000,000nm^2$, the surface area occupied by each protein was approximated by using a circular shape - in the case of the extracellular domain of BRI1 this results in an overestimation of the occupied surface area. * BIR3 was approximated based on the cytoplasmic structure of BIR2 [122].

Protein	**PDB ID**	molecules µm^{-2}	area per protein nm^2	**Col-0**	**BIR3**	**BIR3 & BRI1**
BIR3*	4l68 [122]	14	13.8	192.2	19 320	19 320
BRI1	4m7e [25]	11	43	473	473	61 490
BAK1	3tl8 [185]	5	13.8	69.5	69.5	69.5
AHA1	5ksd [202]	11	38.5	434	434	434
AHA2	5ksd [202]	10	38.5	385	385	385
total				1553.7 0.16 %	20 681.5 2.1 %	81 698.6 8.2 %

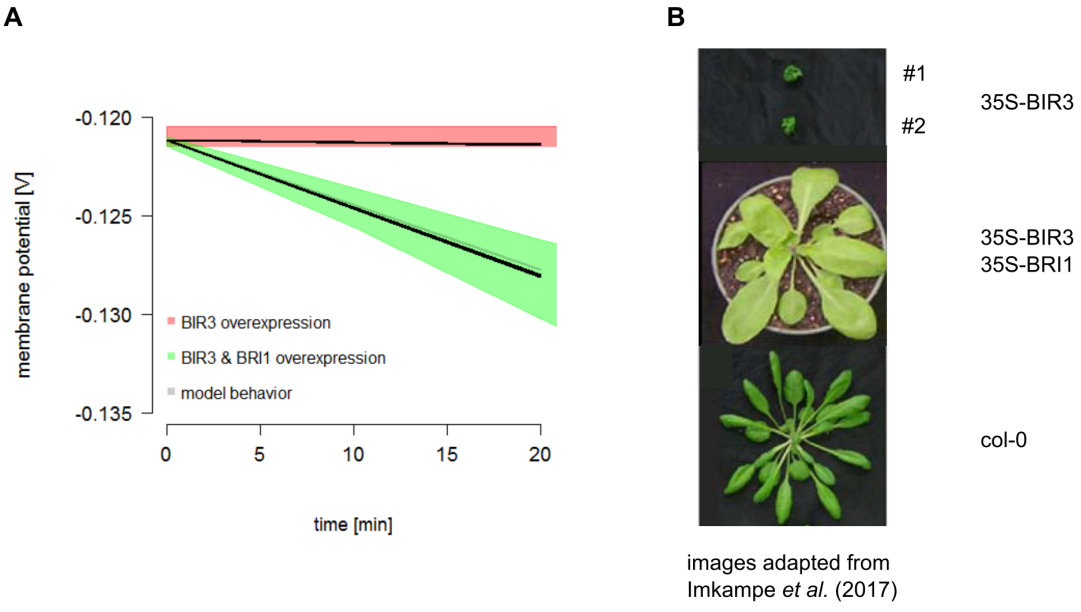

Figure 6.7: Behavior of the *in silico* overexpression of BIR3 as well as BIR3 & BRI1. **A:** Modeled behavior. **B:** Plant phenotypes. Two independent 35S-BIR3 overexpression lines (top) show a much reduced growth. The additional overexpression of BRI1 (middle) restores growth to the point that plants are close to the wild-type Col-0 (bottom) in this aspect. Plant pictures adapted from [30].

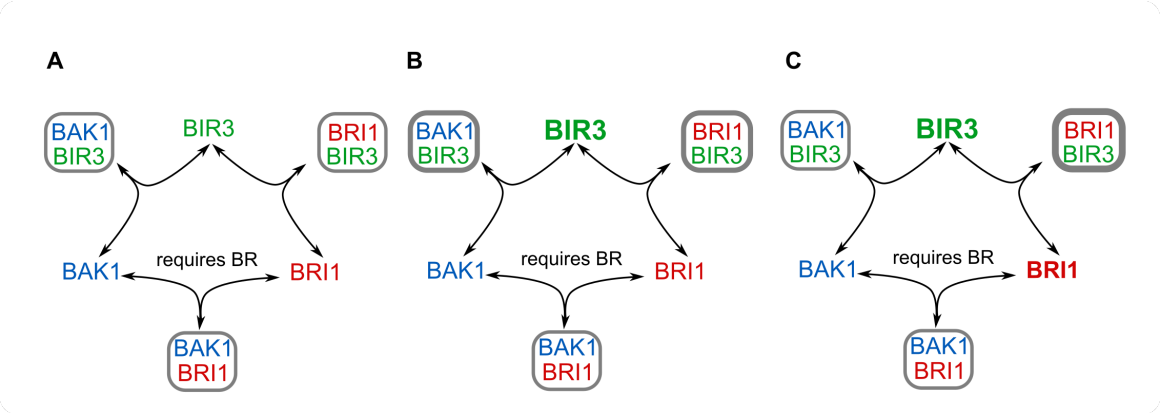

Figure 6.8: Mechanism behind BIR3 overexpression behavior. A: Reactions betweeen receptor and co-receptors in wild-type plants. **B:** Overexpressing BIR3 shifts the reactions towards the formation of $BAK1\,BIR3$ and $BRI1\,BIR3$ complexes. **C:** The additional overexpressiong of BRI1 shifts the reactions strongly towards the complex consisting of BRI1 and BIR1, therefore "freeing" BAK1 to interact with BRI1.

enough to overcome the strong overexpression of BIR3 as neither BAK1 or BRI1 are free to interact with each other and induce downstream signaling. This explains the growth phenotype of the BIR3 overexpression plant that resemble *bri1-/-* mutants.
The additional overexpression of BRI1 shifts the system again, this time towards the formation of the complex consisting of BRI1 and BIR3 (Fig. 6.8 C). In turn, BIR3 interacts less with BAK1. If the hormone is added to the system in this state, BAK1 is free to interact with BRI1. BAK1 and BRI1 can now activate downstream signaling, which restores growth to near normal levels, as the respective plants resemble the wild type [30].

6.2.3 Parameter Space

To explore the parameter space I did not limit the parameter estimation to a single run. Instead, I conducted 50 parameter estimations with randomized start values for all parameters that needed to be fitted. Wherever possible, I used experimental information to limit the range of allowed parameter values (see Tab. C.5 on p. 189).
What becomes evident when analyzing the distribution of the parameters is that only some parameters are identifiable (see Fig. 6.9). For example, while there was no experimental information of the proton pump activity, this parameter is well defined due to the measurements of the proton leak (Supplementary Information p. 181).
I have tried to remove as many structural non-identifiablities in the model as possible. For one, once it was clear that there would be no detailed phosphorylation data on either receptor or co-receptor, I lumped all phosphorylation events between the two proteins into one reaction. Furthermore, as the intracellular proton concentration in the model is fixed, I was able to describe the ATPase pump activity by a modified mass action kinetics instead of a saturation kinetics.
Still, several other parameters such as most of the dephosphorylation reactions show a

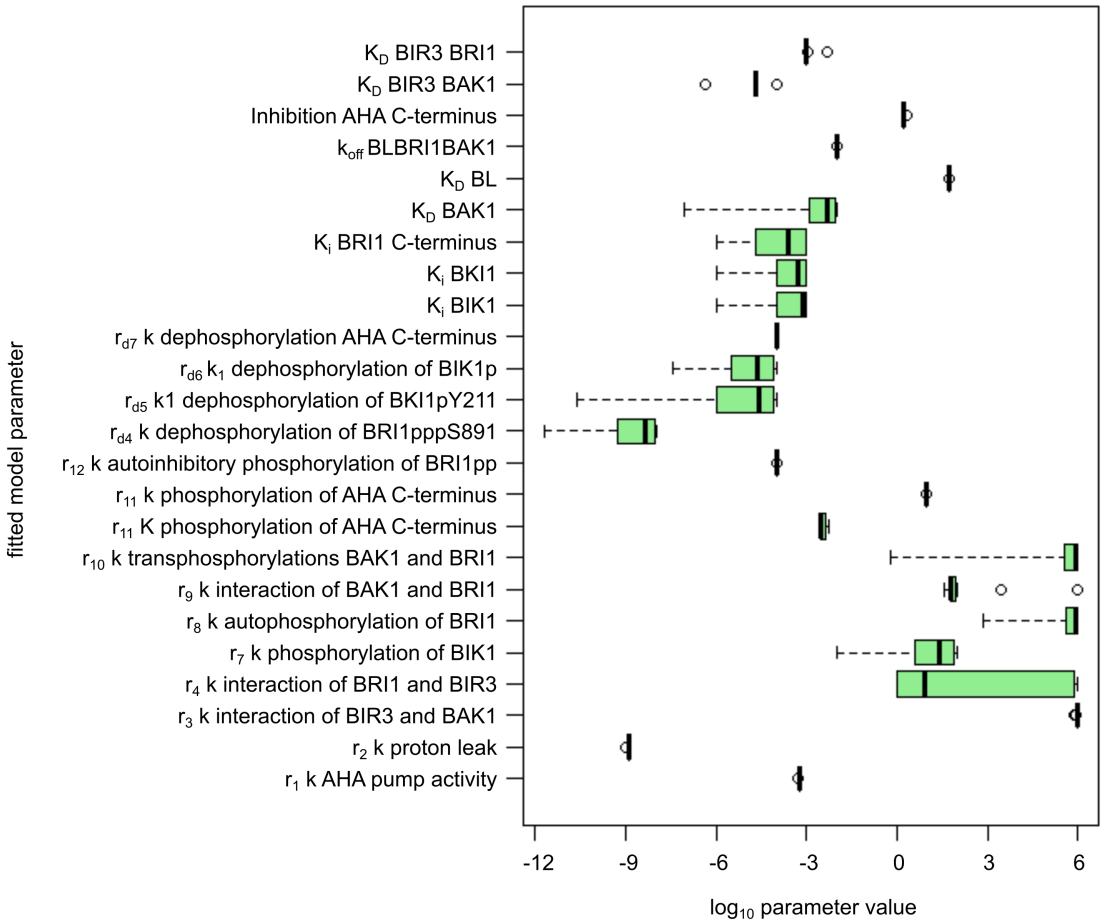

Figure 6.9: Overview of the model parameter values. Shown are the parameter values of all 50 models. The box represents upper and lower quartile, with the median indicated by the line. The extreme values are indicated by the outer lines with outliers represented by points.

broader range in parameter values (see Fig. 6.9). Here, several aspects come together: For one, there is no quantitative information on any phosphorylated species currently available. Second, the information on the inactivation of the signaling pathway is sparse. This facts results in less identifiable model parameters regarding all dephosphorylation reactions.

Furthermore, the strength of the inhibition by the BRI1 C-terminus, BKI1 and BIK1 varies between parameter sets. Similarly, the phosphorylations rates for BIK1 and the receptor vary by four orders of magnitude.

After a first set of parameter estimations, I observed a number of models, where the model behavior described a situation completely beyond what is physiologically feasible. For example, if the parameters for the AHA C-terminus phosphorylation were left unconstrained (with an interval between $1 \times 10^{-6}\,s^{-1}$ to $1 \times 10^{6}\,s^{-1}$), I obtained a good fit of the membrane potential change with less than 50 active receptor complexes (Fig. 6.10 A, B). While another computational model has suggested that even at signaling saturation

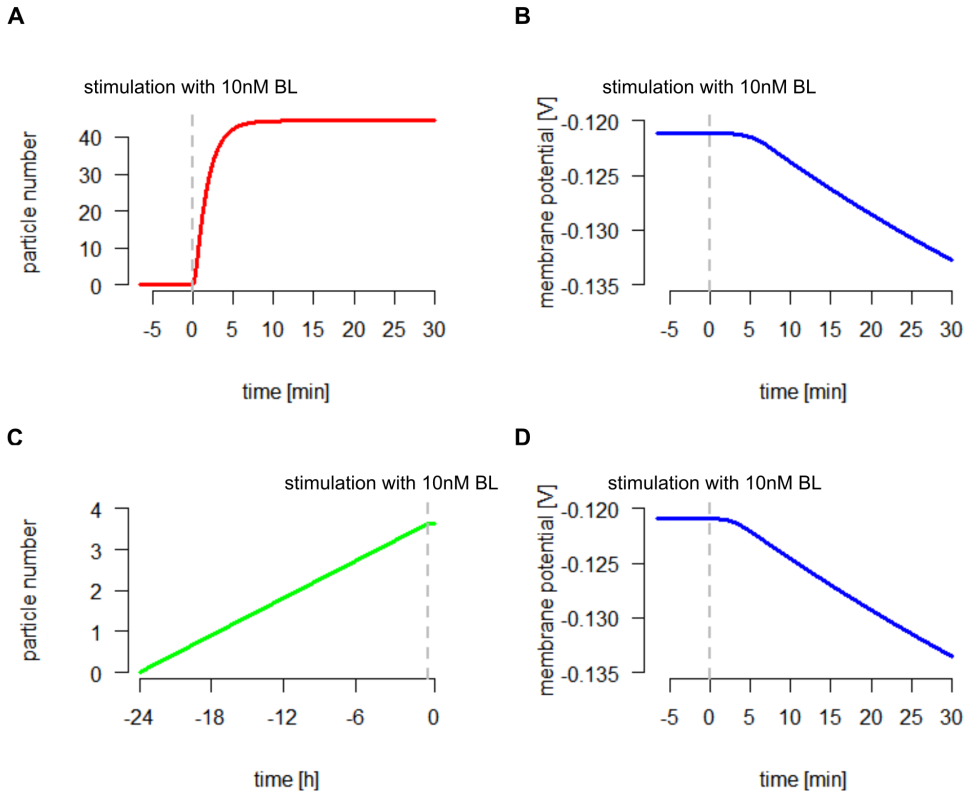

Figure 6.10: Parameter fit with low active receptor numbers in response to 10 nM BL. **A,B:** Model with the low number of active receptors. **A:** Particle numbers of the complex $BIR3\,BAK1$. **B:** Membrane potential change over 30 min of the same model parameterization as A. **C,D:** Model with slow association of BIR3 and BAK1. **C:** Active receptor numbers. **D:** Membrane potential change over 30 min in response to $10\,\mathrm{nM}$. The model has the same parameters to the model in C.

less than 15 % of the receptor BRI1 is active [38, 39, 40], observing the experimentally measured membrane hyperpolarization with less than 50 receptors is highly unlikely. It becomes even more unlikely when considering the fact that there are over $55,000$ receptors in the membrane of an epidermis cell [11]. Therefore, by limiting the speed of the phosphorylation of the AHA C-terminus by the active receptor complex $BAK1p\,BRI1pp\,BL$, the parameter estimation results in more realistic receptor numbers. The bounds for the affinity K_m and the rate of the reaction k were chosen such that approximately 500 (around 1%) of the receptor BRI1 is active when the model is stimulated with 10 nM BL.

An additional issue arose with the complex formation between BAK1 and BIR3. Originally, the speed of association between the two proteins was left completely open between $1 \times 10^{-6}\,\mathrm{dm^2\,nmol^{-1}\,s^{-1}}$ to $1 \times 10^{6}\,\mathrm{dm^2\,nmol^{-1}\,s^{-1}}$. For some parameter estimation results, this yielded a very slow association of BAK1 and BIR3 so that the model was not in an equilibrium state before stimulation with BR (Fig 6.10 C,D). Therefore, I set the boundaries for the association rates of BIR3 to both BAK1 and BRI1 to 1 and $1 \times 10^{6}\,\mathrm{dm^2\,nmol^{-1}s^{-1}}$. This ensures that the complex formation for both sets of proteins is fast enough that the model is in an equilibrium state before stimulation with BL (see $24\,\mathrm{h}$ simulations before BL

stimulation Fig. 6.3, p. 85).
The issue of parameter non-identifiability will be examined in more detail in the discussion (p. 129). I have included an exemplary parameter set in the Supplementary Information (p. 190). A summary of all parameter estimation results is further provided on the attached CD.

6.2.4 Sensitivities

To determine the model components that share control over the model output, I calculated the scaled sensitivities of the membrane potential with respect to the model parameters. By analyzing not only one parameter set but a whole model ensemble of independent parameter sets, this yields some insight into which model species or parameter contributes to the model's response.
Figure 6.11 summarizes the sensitivities for all parameter sets. The color code of the figure is scaled in such a way that blue represents a positive impact on membrane hyperpolarization and red a negative impact. White means that the model parameter has no impact on membrane hyperpolarization in that specific parameter set.
In particular, there are some model parameters and quantities that are crucial for the membrane potential change in any model parameterization. The highest control over the models' response is shared by the rate of the proton leak and the AHA pump activity. Furthermore, the receptor concentration as well as the amount of AHA1 and AHA2 have a positive impact on membrane hyperpolarization. The inhibition of the AHA pump activity by the AHA C-terminus has a lesser degree of influence on the membrane potential change. Similarly, the affinity of the active receptor for the AHA C-terminus as well as the dephosphorylation rate of the C-terminus have a negative impact on the model's response.
Here, it is worth mentioning that while the number of receptor molecules per μm^2 have a positive impact on the model response, the expression factor of BRI1 has no or very little control over the membrane hyperpolarizaton. The reason for this lies in the fact that several other model species are defined based on their ratio to the receptor and the global quantity $BRI1\,concentration$. As the latter is calculated based on the receptor density, it stands to reason that this model quantity has a large control over the overall model response.
In contrast to this, the expression factor of BRI1 is only used to adjust the initial concentration of the receptor alone. Therefore, this quantity describes the actual impact of the receptor levels on the model response. In light of the general dynamics of the signaling pathway, this is unsurprising. Even though the signaling pathway is almost saturated at a response of $10\,nM$, there are only 500 to 1000 active receptor molecules. With a total of over $50,000$ BRI1 molecules, it stands to reason that small changes of the initial concentration of BRI1 will have little effect on the actual number of active receptors and therefore the model response.
Finally, some model quantities that are not directly involved in the transport of protons

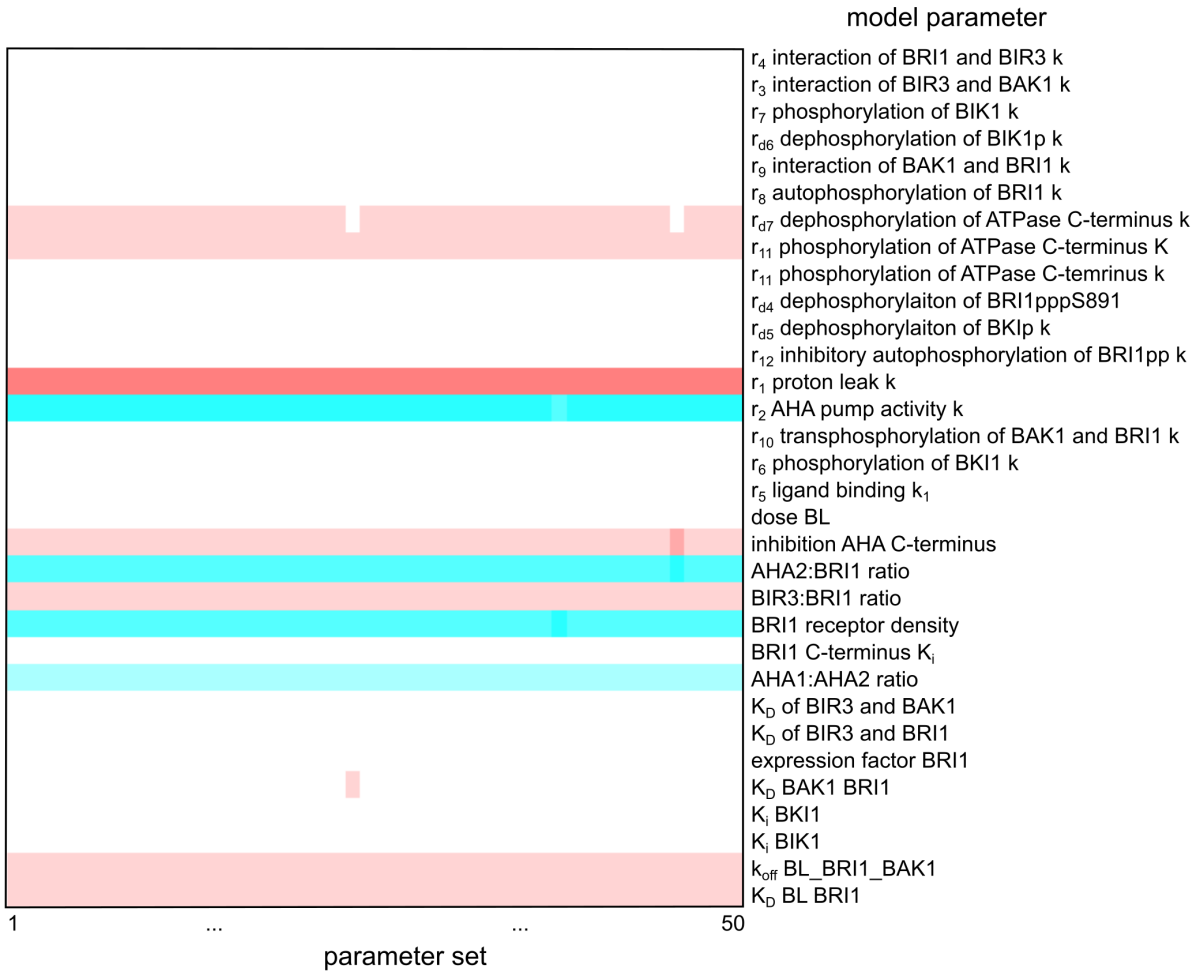

Figure 6.11: Sensitivities of the membrane potential change to parameter changes. Color code is scaled such that values close to 0 are indicated in white, red represents a negative impact and blue a positive impact of the model parameter on the membrane potential change.

across the membrane have an impact on the model response. The affinity of the receptor for BL as well as the rate of dissociation of the ligand-receptor-co-receptor complex have some control over the membrane hyperpolarization. Both of these parameters impact the amount of active receptor molecules in the system. Last, the amount of the negative co-receptor BIR3 has a negative impact on the membrane potential change.

Taken together, this shows that model quantities that are directly or indirectly involved in the transport of protons across the membrane have the highest impact on the membrane potential change. It also illustrates that the qualitative behavior of the sensitivities is consistent, even though not all model parameters are equally important in the different parameter sets. Furthermore, this demonstrates that even though not all parameters are identifiable in the given model structure, a prediction regarding the model behavior is possible.

6.3 Model Validation

To test the validity of the model, I made several predictions regarding the model behavior in different scenarios. For one, based on the sensitivity analysis the ATPases AHA1 and AHA2 seem to play a crucial role in the models response to hormonal stimulation. As the protein quantification has shown that the concentration of the ATPases increases from the younger tissue to the older tissue (Fig. 6.1), we decided to test the model behavior in the meristematic zone of the root. Furthermore, I predicted the behavior of the model with respect to a *bir3* deletion.

6.3.1 Model Response in the Meristematic Zone

Based on gene expression data (Arabidopsis eFP server[2] [195]) and the protein quantification by Nina Glöckner, I knew that the ATPase levels change along the root axis. Based on this and the sensitivity of the membrane potential to ATPase concentration, I used the model to predict the behavior of the fast BR response in the meristematic zone.
Figure 6.13 A shows the behavior of all 50 parameterized models in the meristematic zone. The time-course behavior of the models shows that for one the membrane potential before hormonal stimulation changes from $-0.121\,\mathrm{V}$ to $-0.11\,\mathrm{V}$ due to the lower ATPase concentration and the changed cell surface area. After stimulation with 10 nM BL the model reacts to the presence of the hormone by membrane hyperpolarization but not as strongly as the model in the elongation zone. This supports the role of the ATPase in the process of cell elongation as meristematic cells, which express the ATPases at a much reduced level, show only a basal rate of elongation [7].
Nina Glöckner tested this prediction experimentally using two different methods. First, she measured the ion flux at the root surface by MIFE experiments (Fig. 6.13 B). In the wild-type col-0 there is a notable difference in the average net ion flux between the meristematic zone and the elongation zone. This means that proton influx is more dominant in the young tissue and that proton extrusion increases along the root axis. This fits the model prediction, where the elongation zone reacts more strongly to the stimulation with BL than the meristematic zone.
Furthermore, the response to BL stimulation was also tested by measuring the extracellular pH *via* the pH sensitive salt HPTS. Figure 6.13 B shows the response to $10\,\mathrm{nM}$ BL in the elongation zone with Fusicoccin as positive control (Fig. 6.13 A) and DMSO as negative control (Fig. 6.13 C). These fluoresence microscopy images show that BL strongly induced the acidification of the cell wall.
The more extensive measurements along the root axis at lower BL concentrations shows that the response to the hormone indeed changes: In the younger tissue the cell wall pH is less acidic than in the tissue including the elongating cells (Fig. 6.13 D-F).

[2] `http://bar.utoronto.ca/efp/cgi-bin/efpWeb.cgi`

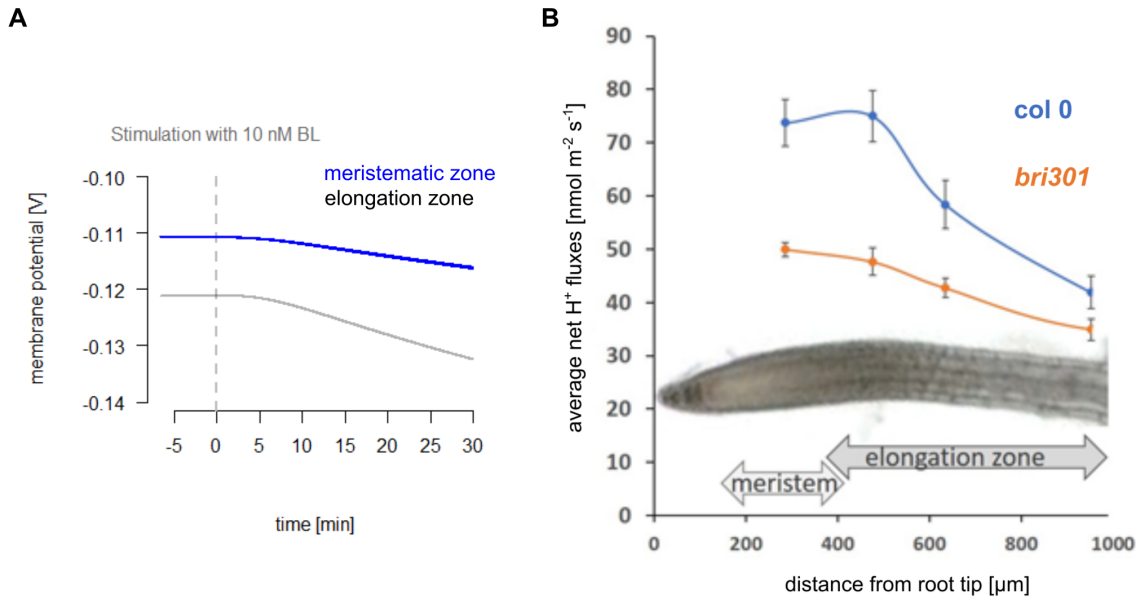

Figure 6.12: Validation of the fast BR response pathway in the meristematic zone. The net ion flux at the root surface was measured by MIFE at different positions from the root tip for the wild type Col-0 and the *bri301* mutant. The figure was provided by Nina Glöckner (University of Tübingen) and adapted for easier understanding.

6.3.2 *bir3* Deletion

I further tested the model by predicting the behavior of a *bir3* inactive mutant. Here, the model behavior shows a minor change as it responds a bit faster than the model representing the wild type. After that, the slope of the membrane potential change is identical between wild type (black) and *bir3* deletion (red) (Fig. 6.14 A). This is reflected in the phenotype of the *bir3-1* and *bir3-2* plants that resemble the wild type Col-0 (Fig. 6.14 B). The slight increase in membrane hyperpolarization also fits the experimental observations as *bir3* mutants show a slight hypersensitivity to BR stimulation [30].

To investigate the model behavior in response to changes in BIR3 concentrations further, I scanned the membrane potential change after 30 min depending on the amount of BIR3 in the system. Here, I scanned the BIR3 concentration from the *bir3* deletion to the modeled overexpression concentration for all 50 model parameterization. The results of this scan are summarized in Figure 6.15. The normal model concentration of BIR3 is highlighted in red. Figure 6.15 illustrates that the normal BIR3 concentration is in the range where changing the BIR3 concentration impacts the change in membrane potential. This shows that BIR3 does indeed exert a controlling influence of BR signaling in the model.

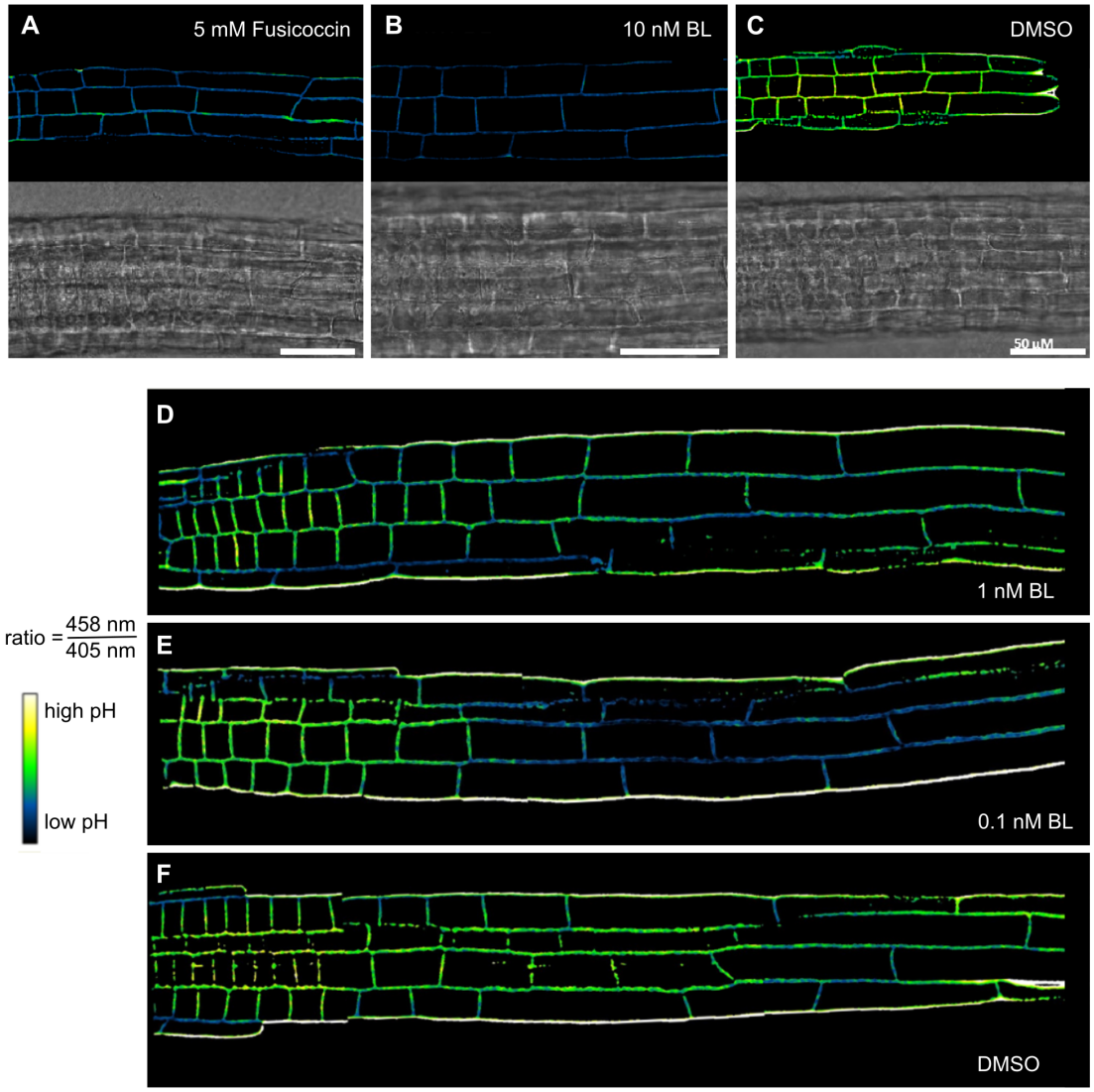

Figure 6.13: Validation of the fast BR response pathway in the meristematic zone by pH measurements in the cell wall. HPTS was used to dye the roots and fluoresence microscopy was used to measure the cell wall pH. **A-C:** Extracellular pH measurements after 1 h for 10 nM BL including positive (Fusicoccin) and negative (DMSO) control. **A:** Positive control using 5 mM Fusicoccin. **B:** 10 nM BL. **C:** Negative control using DMSO. **D-F:** pH measurements along the root axis after 30 min prestaining and 1 h incubation with BL. **D:** 1 nM BL. **E:** 0.1 nM BL. **F:** Negative control using DMSO. The images were kindly provided by Nina Glöckner (University of Tübingen).

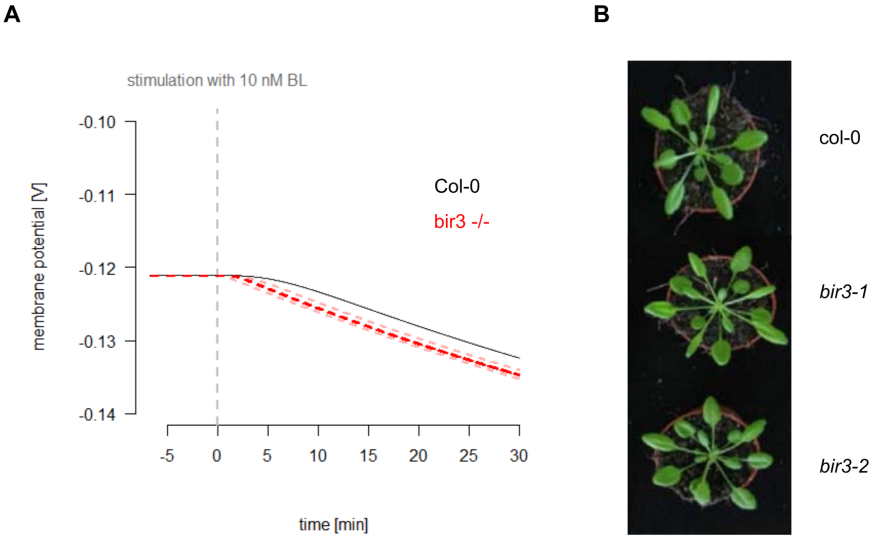

Figure 6.14: Validation of the *bir3* overexpression behavior. A: Model prediction. The behavior of the wild-type is indicated in black. The behavior of the *bir3* deletions of all 50 model parameterizations is plotted in red. **B:** Experimentally determined behavior. Plant pictures: [30].

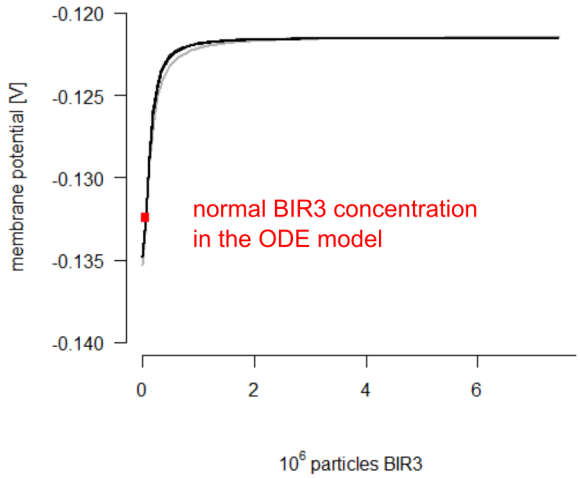

Figure 6.15: Scan of the membrane potential at different BIR3 concentrations. The BIR3 concentration was scanned from 0 to the 100-fold concentration of BIR3 used for the overexpression scenario. The normal BIR3 concentration is indicated by the red dot.

6.4 Summary

The ODE model of the fast BR response pathway that I presented in this chapter comprises the known components and steps of this pathway. This model can describe the experimentally observed dose-response behavior and the overexpression behavior of BIR3. Furthermore, I included the response of cell wall swelling in the model. I validated the model behavior with respect to the behavior of the signaling pathway in the meristematic zone and in a *bir3* mutant, which was tested experimentally by the collaborators.
An exploration of the parameter space has shown that while some parameters are not identifiable, the model behavior is consistent. This holds true not only with respect to the response to BL stimulation, but also the qualitative aspects analyzed by sensitivity analysis and the model predictions.
A detailed model analysis of the model behavior suggests a fine-tuning role of BIR3 in the system. Furthermore, it seems that the response to BR stimulation in the fast response pathway is determined to a large part by the expression of the H^+-ATPases AHA1 and AHA2.
The current version of the model contains only sparse information on the inactivation of the signaling pathway. This is reflected in the parameters of dephosphorylation and dissociation reactions, which are not well determined. To address this, longer measurements of the extracellular pH in response to different BL concentrations are planned.

7 | Modeling Root Elongation

In the previous chapter, I introduced an ODE model that describes the more immediate effects of BR signaling concerning membrane hyperpolarizatoin as well as cell wall acidification and swelling on a cellular level. Ultimately, the activation of BR signaling results in cell elongation [2, 17, 21]. Therefore, I expanded the ODE model to include BR-induced cell elongation and combined it with an agent-based representation of the root to analyze cell elongation on an organ-scale. The resulting multi-scale model links the observed behavior of root elongation to the physiological effects of hormone stimulation. The current model version comprises only the behavior of one cell type but serves as proof of concept nonetheless.
Generally speaking, this multi-scale model consists of several different scales that need to be modeled individually and linked within the agent-based modeling (ABM) software. These scales are:

- the biomechanical model describing the interaction forces of the cells as well as the initial settings of the agent-based model (see pp. 102),
- the cell behavior model (CBM) describing the actions of the cellular agents like cell division (see pp. 103),
- the ODE model describing intracellular processes such as the physiological effects of BR stimulation (see pp. 108).

In this chapter, I describe both the cell-behavior and the biomechanical model. Furthermore, I list the changes made to the ODE model and show that the experimental data can still be described by the adapted ODE model. Finally, I show the behavior of the multi-scale model, which links the ABM framework of the root tip to the cellular processes of the ODE model.
For this project, I worked in close collaboration with Erika Tsingos (research group of Prof. Dr. Wittbrot, Centre for Organismal Studies (COS)). We used the agent-based modeling software EPISIM [53] as framework to build the biomechanical model of the root tip. This project was further supported by Dr. Frank Bergmann (research group of Prof. Dr. Kummer, BioQuant (COS)), who updated the software links between EPISIM and COPASI. Furthermore, he provided a special version of COPASI that allowed the correct export of the ODE model in the SBML (Systems Biology Markup Language) [107] format before the release of COPASI build 184.

7.1 Biomechanical Model

In EPISIM, the biomechanical model fulfills three roles: For one, it contains the description of the interactive forces for the cellular agents. Second, it is also the place where the initial settings of the ABM are defined. Last, a number of general parameters for the visualization and simulation are defined in the biomechanical model, the size of the simulation space, the length of one simulation step as well as general characteristics of the root tip (such as root height and width). Due to this fact, the biomechanical model is part of the EPISIM simulator code. A compiled version of the biomechanical model is further loaded into the cell behavior model to allow the link between the two different models.

Initial Settings

The initial settings described in the biomechanical model include the placement of the first set of cells that are modeled in the ABM. Erika Tsingos and I chose this placement such that the cells follow the morphology of the root cap: In total, there are 14 columns of cells in the root. To reproduce the root cap, the number of cells is reduced by one on each side per row resulting in the scheme depicted in Figure 7.1. The corresponding code is listed in the Supplementary Information, section D.1.1 on p. 193). The initial dimensions of the cells are defined in the cell behavioral model in the quantities $width_{default}$ and $height_{default}$, which are accessed by the EPISIM simulator while placing the first set of cells in the simulation space. At the beginning, all cells share the default cell type. In the first simulation step, cell types are defined based on the positioning of the cells along the longitudinal y-axis (see Fig. 7.3 in subsection 7.2).

Biomechancis

In general, the biomechanical parameters were taken form a previously published agent-based center-based 2D model constructed in EPISIM [110]. Thus, only a brief description of these parameters is included in the Materials & Methods section. Here, I present a description of the changes in the definition of cell division.
The biomechanical model was changed to account for the direction of cell divisions. Previously, cell division was modeled such that the direction of cell divisions is random. In the root, cell division occurs in a transverse manner so that the new cells are placed along the longitudinal axis [147]. Therefore, we changed the definition of the daughter cell to inherit the position along the x-axis of the mother cell.
To allow for an easier adjustment of the parameters for cell division we introduced global parameters in the cell-behavior model that are used by the biomechanical model to calculate the position of the daughter cell. The initial position of the daughter cell along the y-axis is calculated by adding a small offset to the position of the mother cell for both x- and y-axis: $bias_x$ and $bias_y$. The respective code is listed in the Supplementary Information, section D.1.2 on p. 194. The new cell is generated in the cell behavior model but does

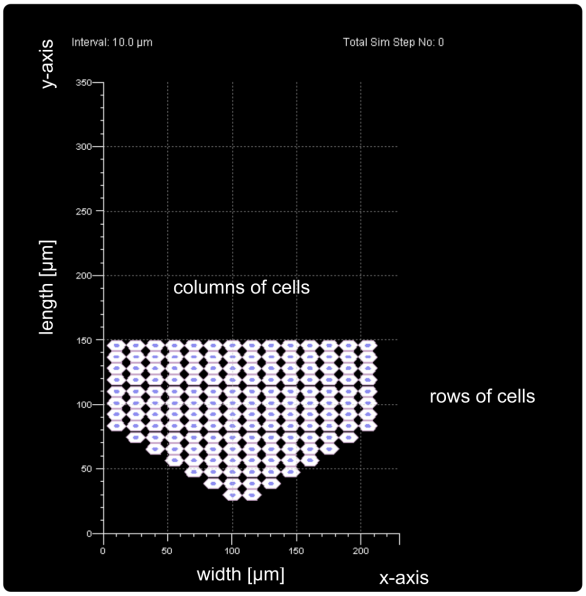

Figure 7.1: Scheme of the initial cell placement in the agent-based model. Cells are placed in 14 columns and 14 rows. The number of cells per row is decreased by two per row towards the tip to represent root morphology. The corresponding code is listed in the Supplementary Information, section D.1.1 on p. 193.

not participate the calculations in that time step. Instead, it undergoes the calculations of the biomechanical model before being included in the simulations of the cell behavior model. Therefore, a small offset along the y-axis is sufficient to place a new cell in the agent-based model and to avoid an extremely high overlap between mother and daughter cell in the simulations.

General Parameters

The general simulation parameters are also defined in the biomechanical model. This means that the simulation space and time step size need to be defined before starting the simulations. Furthermore, the EPISIM simulator needs to be restarted after changing any of these parameters.
For the initial simulations, the simulation space was set to be $230\,\mu m$ wide and $350\,\mu m$ high. The time steps were limited to $10\,min$ to constrain the amount of cell elongation per time step.

7.2 Cell Behavior Model

The CBM describes the actions of cells within the root tip. This model contains several submodels describing the definition of cell types, cell division, cell elongation, cell death and the color code for the simulations. The sequence of submodels is defined in the top hierarchical model.

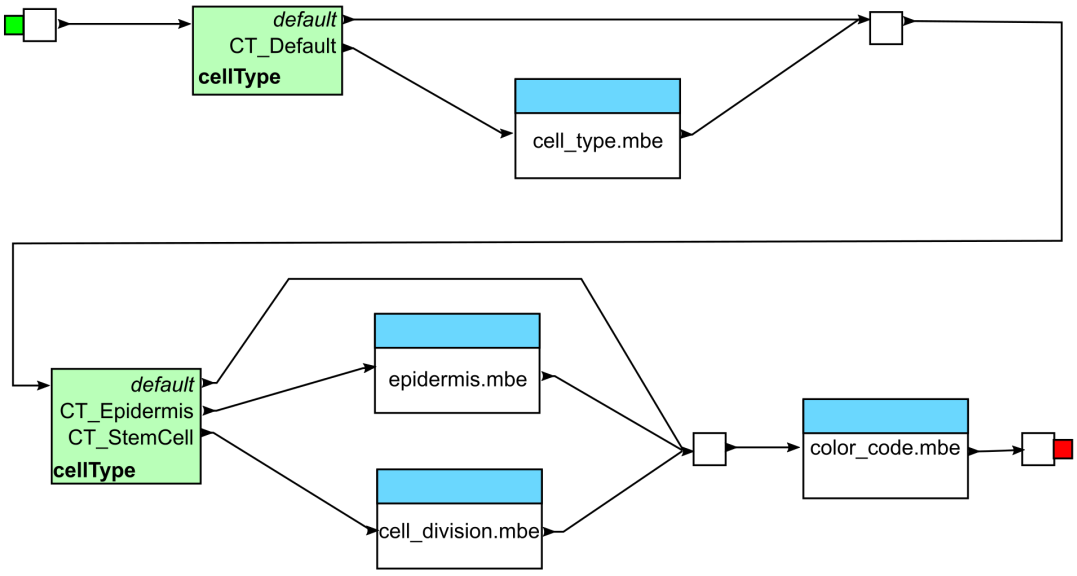

Figure 7.2: Top submodel in the cell behavior model that defines the sequence of the other submodels. Green boxes signify filters with the filtered model entity indicated in bold font. White boxes with a blue bar signify submodels.

As mentioned in the previous section, all cells have the default cell type at the initiation of the model. Therefore, the first step in the CBM is the definition of cell types (Fig. 7.3). This submodel is only active in the first simulation step, as the default cell types exists only in the initial conditions. After this submodel is cleared, the actual processes of cell elongation (Fig. 7.4) and cell division (Fig. 7.5) are considered. Last, the color code is defined for cell types, membrane potential and elongation rate (Fig. 7.6).

Cell Type Submodel

The cell type submodel (Fig. 7.3) is used to assign cell types to the cells in the initial setup as defined by the biomechanical model. This model currently only plays a role in the first simulation step of the cell behavior model, since the default cell types is unique to the initial stage.

Cell types are defined depending on the cells' location along the y-axis. A y-coordinate lower than the lower bound codes for a columella cell. In this CBM, columella cells have no function beyond the fact of providing a more complete picture of the root tip. Cells with y-coordinates between the two bounds are classified as cells that divide and supply the rest of the tissue. Above the upper bound, cells are assigned to the epidermis cell type.

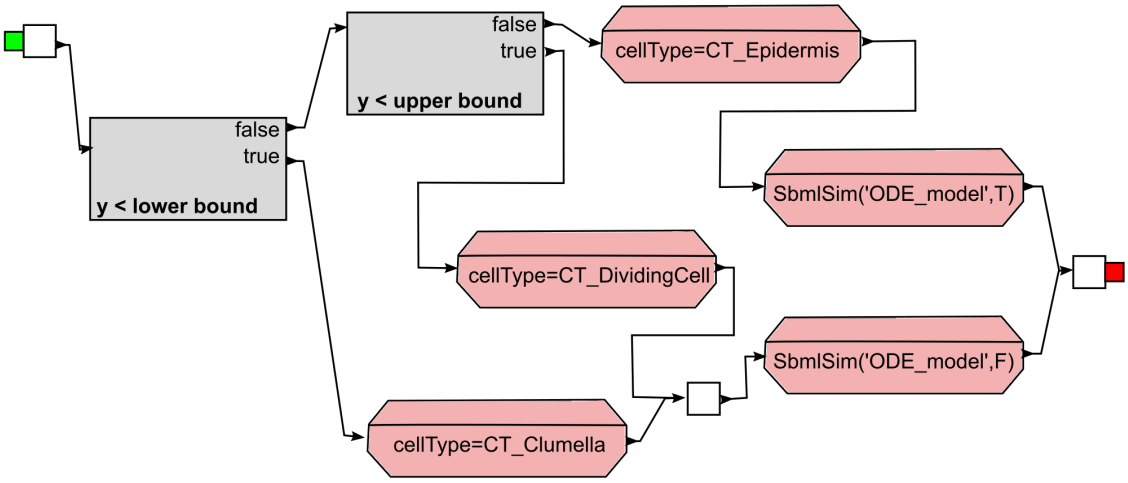

Figure 7.3: Submodel to specify cell types in the CBM. Cell types are assigned based on the cells' position along the y-axis. All cells with a y-coordinate lower than the lower bound are assigned to the cell type "columella cell". Cells with y-coordinates between the bounds are defined as dividing cells that are the only kind of cell with cell division activities. The SBML model for these cell types is turned off. All cells with a y-coordinate above the upper bound are classified to the "epidermis cell" type. Here, The SBML model is simulated. Grey boxes are conditions with the condition string indicated in bold fond. Red octagons indicate state changes of model entities.

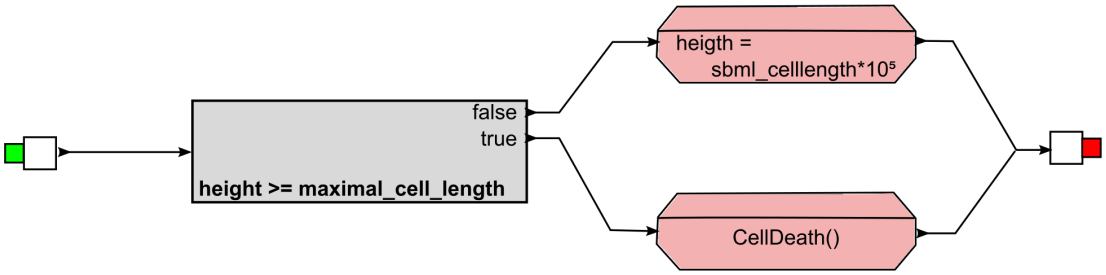

Figure 7.4: Submodel describing cell elongation in epidermis cells. As long as cells are no longer than a set maximal cell length, the cell height in the cell behavior model is updated according to the cell length modeled by the SBML model. If the maximal cell length is reached, cells die to limit the total numbers of cells simulated by the agent-based model and to optimize computing time. Grey boxes are conditions with the condition string indicated in bold fond. Red octagons indicate state changes of model entities.

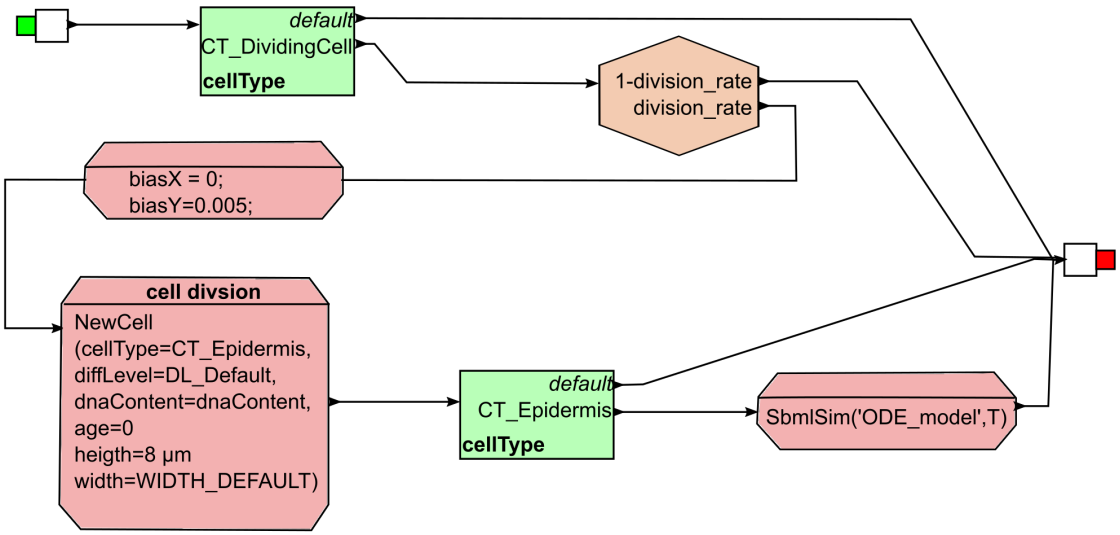

Figure 7.5: Submodel describing cell division in the stem cells. Stem cells have a probability initiating cell division in each simulation step. Once cell division is initiated, a new cell is placed in the simulation area. In the current simulation step, this is a placeholder cell that will only participate in the cell-behavior model in the next simulation step after the biomechanical model updates the cell position. Green boxes are filters with the condition string indicated in bold fond. Red octagons indicate state changes of model entities. Orange hexagons represent probabilities.

Epidermis Submodel

This submodel describes the cell elongation of epidermis cells (Fig. 7.4). Currently, epidermis cells are the only cell type explicitly represented in both cell behavior model and ODE model. Cell elongation occurs until the maximal cell length is reached. To this end, the cell height in the ABM is updated according to the simulated cell length in the ODE model, here denoted by $sbml\_cell\,length$. Since the cell length is defined in dm in the ODE model, the value has to be scaled to $\mu\mathrm{m}$ by multiplying with a factor of 10^5.
Once cells exceed the maximal cell length, cells die to limit the total number of simulated cells, which reduces the computation time. For the proof of concept, the maximal cell length was set to $25\,\mu\mathrm{m}$ to prevent long simulation times. A second reason for the limitation is the fact that the fast elongation rates beyond this point cause strong repulsive forces between the cells. Without a stabilizing framework by placeholder dummy cells this would cause a deterioration of the root shape.

Cell Division Submodel

This submodel describes cell division in the stem cells (Fig. 7.5). To ensure that this only occurs in the correct cells, a filter is applied at the beginning of the submodel. Any other cell type but the stem cell proceeds directly to the end of the submodel. Every stem cell has a chance of initiating cell division in every simulation step that is defined by the divi-

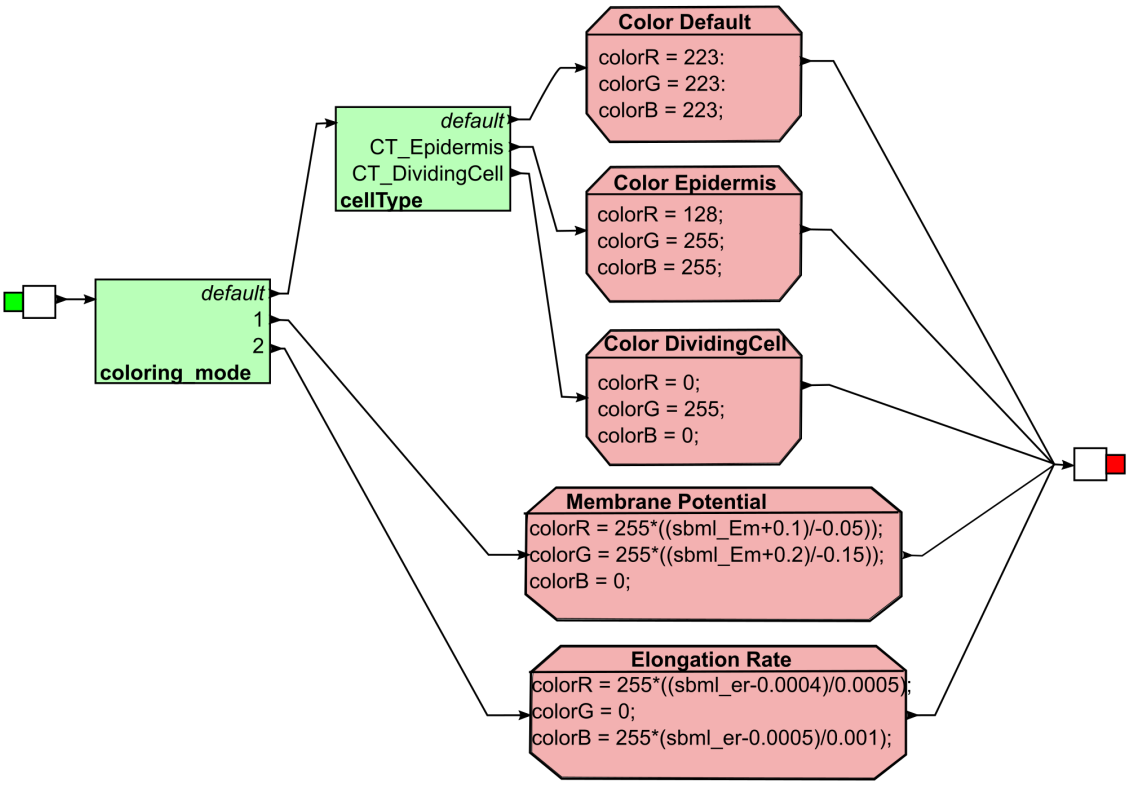

Figure 7.6: Submodel for color coding the agent-based model during simulations. Three color codes are enabled: *default* - cell types, *1* - membrane potential $sbml\_E_m$, *2* - elongation rate $sbml\_er$. Green boxes are filters with the condition string indicated in bold fond. Red octagons indicate state changes of model entities.

sion rate. The cell division rate was set according to the experimentally measured value [7]. I adjusted the measured rate of $0.04\,\text{cell}^{-1}\,\text{h}^{-1}$ to the simulation step of $10\,\text{min}$ in the agent-based model, which results in a cell division rate of $0.0066\,\text{cell}^{-1}\,10\,\text{min}^{-1}$.
Once cell division is triggered in the cell behavior model, a new epidermis is initiated with an initial height of $8\,\mu\text{m}$. The cell is initially placed just $0.005\,\mu\text{m}$ above the mother cell. This cell is at first not simulated in the cell behavior model. Only in the next simulation step of the cell behavior model, when the cell location has been calculated in the biomechanical model. As the new cell is an epidermis cell, the simulation of the ODE model is switched on and one instance of the ODE model is simulated for this cell.

Color Code Submodel

In this submodel, the color code for the simulations in the EPISIM simulator are defined (Fig. 7.6). Currently, three coloring modes are enabled. In the *default* mode, cell types are color coded with the columella cells in grey, the dividing cells in green and the epidermis cells in blue. Coloring mode *1* encodes the membrane potential, here $sbml\_Em$. Finally, the elongation rate ($sbml\_er$) is coded in mode *2*.

7.3 Elongating Cell ODE Model

To describe the intracellular processes that occur on a faster time-scale than the processes of the CBM, I created an ODE model that describes the BR-induced cell elongation. In this section, I enumerate the changes to the ODE model and show that this model still follows the behavior of the model presented in the previous chapter.

7.3.1 Changes in the ODE Model Structure

The elongating cell model is based on the model introduced in the previous chapter. Several changes had to be made to facilitate the modeling of cell elongation. All of these changes, I will list and explain in the following sections.

Compartments

In contrast to the model introduced in the previous chapter, all compartments in the elongating cell model are variable necessitating a change in compartment definition. The cytosol is now defined as a fraction of the space enclosed by the cellular dimensions. In approximation, a factor of 0.35 was used to account for the presence of the vacuole:

$$V_{cytoplasm} = 0.35 \cdot cell\,width^2 \cdot\ cell\,length \tag{7.1}$$

This simplification was possible as only two model species occur in the cytosol; the phosphorylated form of the inhibitor $BKI1p$ and protons H^+_{in}, the latter of which is kept constant.
Similarly, the definition of the membrane area is now defined by cell width and length. Again, this is not quite a realistic representation but rather an approximation as cells are not of a perfect cuboid shape.

$$A_{membrane} = 2 \cdot cell\,width^2 + 4 \cdot cell\,width \cdot cell\,length \tag{7.2}$$

Species

There are some species in the model, where the concentrations change along the root axis. The most notable one here is the ATPase, which changes from an average of $4\,\text{molecules per}\,\mu\text{m}^2$ to $10\,\text{molecules per}\,\mu\text{m}^2$ (see Fig. 6.1, p. 75). I integrated this concentration change for both the initial concentration and the synthesis rate of the ATPase and of the ATPase C-terminus in the model presented here.
Other species show only a small change in concentration at least when transitioning from meristematic to transtition to elongation zone. Here, the receptor density changes from $12\,\text{molecules per}\,\mu\text{m}^2$ to $11\,\text{molecules per}\,\mu\text{m}^2$. The ratio of the negative regulator BIR3 in relation to the receptor BRI1 changes from 1.4 to 1.3 and the ratio of AHA1 to AHA2 changes from 1.4 to 1.1. Currently, these smaller concentration changes are not included

in the model. As the model parameters are fitted in the elongation zone, I used the protein concentrations of that root zone.

P-type ATPases AHA1&2 The experimental data of our collaborators show that the ATPase expression changes along the root axis. In the meristematic zone, there are approximately 4 molecules of AHA2 per µm^2. In the root overall, there are 10 molecules per µm^2 as Nina Glöckner measured by both microscopy and Western blotting (see Fig. 6.1, p. 75).
For the elongating cell model, this means that the initial amount of ATPases has to be adapted to the different root zones. Here, I used a logistic function to describe the ratio of AHA2 to BRI1 along the root axis:

$$ratio_{AHA2:BRI1} = 0.9 \cdot \frac{1}{1 + e^{-8800 \cdot (cell\,length[dm] - 0.00016\,dm)}} \tag{7.3}$$

This ratio is used to describe both the initial level and the expression rate of the H^+ P-type ATPase AHA2 along the root axis. The parameters were chosen such that the experimentally determined expression level of AHA2 in the meristematic zone is matched. Starting at a cell length of 10 µm, the AHA2 concentration increases throughout the transition zone and continues to rise in the elongation zone that starts at 35 µm cell length (Fig. 7.7 A). The maximal initial concentration is reached at approximately 75 to 85 µm, towards the end of the elongation zone at 100 µm and the beginning of the maturation zone. The concentration of AHA1 is still defined in relation to AHA2. Furthermore, the initial concentration of the AHA C-terminus is defined in the same way. This results in the following description of AHA as well as AHA C-terminus expression levels:

$$[AHA]_{t=0} = (1 + ratio_{AHA1:AHA2}) \cdot BRI1\,concentration \cdot ratio_{AHA2:BRI1} \tag{7.4}$$

It is the purpose of this model to represent cell elongation. Therefore, proteins also have to be produced to avoid dilution during time-course simulations. The production rate of the ATPases and the ATPase C-terminus is currently described in an almost identical way as the initial concentration (Eq. 7.3):

$$translation\,rate\,AHA = (1 + ratio_{AHA1:AHA2}) \cdot BRI1[molecules\,\mu m^{-2}] \cdot ratio_{AHA2:BRI1} \tag{7.5}$$

When simulating this model for an epidermis cell from the meristematic zone to the maturation zone in the presence of 10 nM BL, this results in the concentration profile illustrated in Figure 7.7 B. As the "old" tissue with the lower ATPase concentration is inherited from the previous time step, this results in an underestimation of ATPase levels throughout the root.

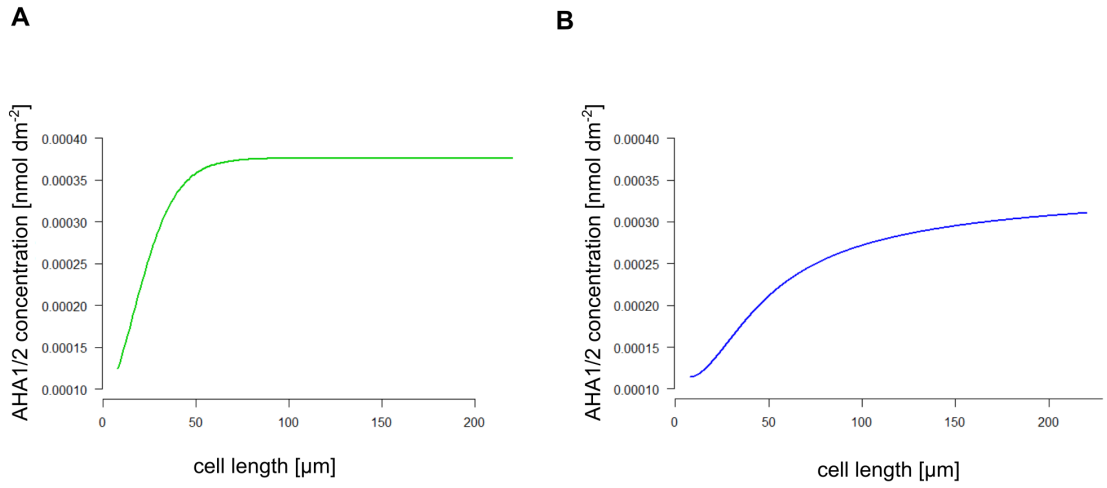

Figure 7.7: Description of AHA expression along the root. A: Initial AHA1/2 concentration along the root axis (green). **B:** Transient concentration of AHA1/2 along the root axis (blue). The model was simulated for 24 h with 10 nM BL.

Reactions

Protein Synthesis To prevent the dilution of model species by the increasing cell volume and membrane area, I had to introduce synthesis reactions producing the ATPase, ATPase C-terminus, BRI1, BAK1, BIR3, BKI1 and BIK1. All of these reactions follow the same rate law:

$$v = scaling\ factor \cdot molecules\ per\ \mu m^2 \tag{7.6}$$

The $scaling\ factor$ is calculated based on the membrane expansion rate as described in Equation 7.9. It describes the conversion from proteins per µm^2 to nmol per dm^2.

Constant Intracellular pH Similar to the situation with the hormonal ligand BL in the previous ODE model, I had to ensure that the intracellular proton concentration was not diluted due to the cell expansion. This would have caused an artificially high gradient across the membrane and, thus, a distortion in model behavior. Here, the intracellular proton concentration is not defined as constant but is rather produced and consumed such that the intracellular concentration remains constant:

$$\xrightarrow{v} H^+_{in} \xrightarrow{k_1} \tag{7.7}$$

I chose the parameters v and k_1 such that the ratio of the two results in a steady state concentration of intracellular protons $[H_{in}]$ at $63\,nM$, where $v = 6300\,nmol\,l^{-1}\,s^{-1}$ and $k_1 = 100\,s^{-1}$. The inclusion of this reaction means that this model reaches a steady state while the hormone is absent unlike the ODE model presented in the previous chapter, which reaches an equilibrium state (see section 6.1.3, p. 76).

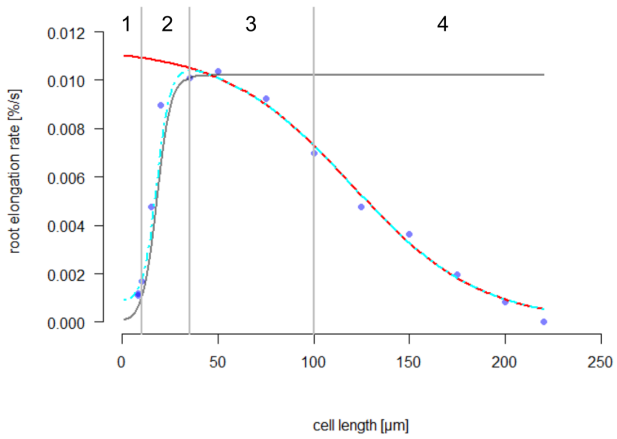

Figure 7.8: Mathematical description of the experimentally observed expansion rates. Experimental data are indicated by the blue dots. The inhibitory function is indicated in red, the activating function in grey. The combined elongation rate of inhibitory and activating function is shown in cyan. 1: meristematic zone; 2: transition zone; 3: elongation zone; 4: maturation zone.

Global Quantities

Cell Length To describe the cell elongation I changed the definition of the cell length to an ODE that follows the experimentally determined expansion rates [7]. The elongation rates were measured depending on the cells position along the root axis. Using the information on the size of the different root zones and cell sizes [11], I translated these data to elongation rates depending on cell size (specific for an epidermis cell) (Fig. 7.8). These data can be described nicely by combining two logistic functions - one for the activating effect of extracellular pH (grey) and one for the inhibitory effect of approaching the maximal cell length (red).

The activating term of the cell length ODE describes the dependence of cell elongation on the cell wall pH. It is well documented that there are enzymes in the cell wall called expansins that are activated by acidic cell wall pH [9, 12]. These expansins make the cell wall flexible enough for cell turgor driven cell expansion [203]. The inhibitory term of the cell length ODE describes the negative feedback by the cell wall and long-term activation of BR signaling to reduce the cellular response [82]. This ensures that the model does not exceed the maximum cell length observed in experiments. I combined all of these terms

into one equation:

$$\frac{d\,(cell\,length)}{d\,t} = stimulation \cdot 0.01 \cdot cell\,length \cdot \left(\underbrace{0.00112}_{\text{basal elongation rate}} + \underbrace{\frac{0.0102}{1+e^{-0.07\cdot([H^+_{out}]-3100)}}}_{\text{activating term}} - \underbrace{\frac{0.01132}{1+e^{-3000\cdot(cell\,length-0.0012)}}}_{\text{inhibition by cell length}} \right) \quad (7.8)$$

Scaling from Proteins per µm^2 to Concentrations To describe the protein synthesis properly, I required a measure of the actual expansion rate of the membrane. For this model I assumed a cuboid cellular shape. Since the cell width remains constant, this simplifies the description of the membrane expansion rate. I then used this expansion rate to define the scaling factor for the protein synthesis from molecules per µm^2 to nmol per dm^2:

$$scaling\,factor = \frac{\overbrace{4 \cdot rate_{cell\,length} \cdot cell\,width}^{\text{expansion of the membrane area}} \cdot \overbrace{10^9}^{\text{mol to nmol}} \cdot \overbrace{10^{10}}^{\mu m^2 \text{ to } dm^2}}{\underbrace{6.023 \cdot 10^{23}}_{\text{Avogadro number}} \cdot A_{membrane}} \quad (7.9)$$

Elongation Rate Readout In order to directly compare the elongation rate in the model with the experimentally observed rates [7], I introduced the readout of the elongation rate as global quantity in the ODE model:

$$elongation\,rate\,readout = \frac{rate_{cell\,length}}{cell\,length} \cdot 100 \quad (7.10)$$

This quantity describes the elongation rate in % s^{-1}, which allows for an easy comparison to the data measured by Beemster and Basking in 1998 [7].

7.3.2 Model Behavior

To ensure that the changes introduced in the ODE model did not change the qualitative behavior of the model, I checked that model predictions still fit the experimentally validated behavior. This means, that at a initial cell length of 75 µm the model describes the dose-response data by Caesar *et al.* (2011) [14] (Fig. 7.9 A). Furthermore, the qualitative behavior of BIR3 and BIR3 and BRI1 overexpressions is still the same as with the model described in the previous chapter (Fig. 7.9 B). At the moment, I have only determined the model behavior for one parameter set. The parameter values are listed in the Supplementary Information D.3 on p. 197.

Finally, I tested if the model's predictions regarding the behavior in the meristematic zone and *bir3 -/-* deletion still hold. As Figure 7.10 illustrates, the model still shows the shift towards higher membrane potential in the meristematic zone (Fig. 7.10 B) compared to the elongation zone (Fig. 7.10 A) as well as the reduced response to hormone stimulation. Furthermore, the *bir3* deletion model shows a slightly faster response in the change of

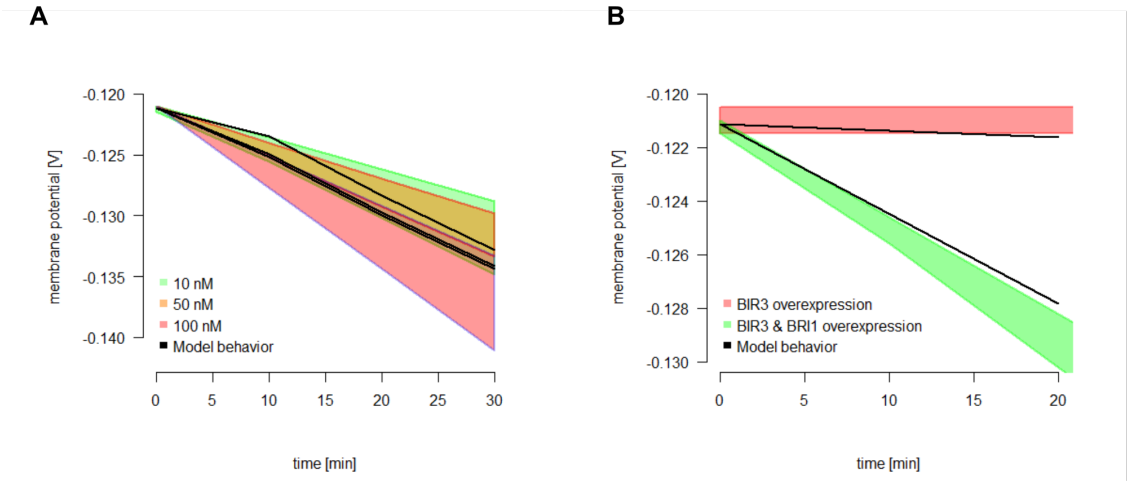

Figure 7.9: Fitted time-course behavior of the elongating cell model. A: Dose-response behavior to the data of [14]. **B:** Overexpression behavior of BIR3 and BIR3&BRI1 overexpressing lines.

membrane potential but overall the response is close to the one of the wild type (Fig. 7.10 A, C). This shows that the elongating cell model still has the same characteristics as the ODE model presented in the previous chapter.

Cell Elongation

Using the phenomenological description of the cell elongation rate on p. 111, I modeled the behavior of the ODE model in different root zones. The first simulations were limited to a window of $30\,\mathrm{min}$ as this is the range of the experimental data used for parameter estimation. The model parameters were fitted to the same experimental data as the ODE model presented in the previous chapter at an initial cell length of $75\,\mu\mathrm{m}$.
As Figure 7.11 B illustrates, the model shows a fast but decreasing elongation rate for the elongation zone (green), while still showing the correct response of membrane potential (Fig. 7.11 A). Correspondingly, in the meristematic zone, the model shows a much reduced response in membrane hyperpolarization (Fig. 7.11 C). Here, only the basal rate of cell elongation occurs (Fig. 7.11 D, highlighted by the arrow).
Cell elongation is a process that takes several hours [7]. Therefore, I decided to test the elongating cell model and run simulations for several hours to see if the model was able to show i) the proper cell elongation behavior over several hours and ii) the correct transition behavior between root zones. To this end, I started the simulations in the meristematic zone ($cell\,length_{t=0} = 8\mu m^2$) and simulated for $24\,\mathrm{h}$. Here, I simulated the model first without the hormone and repeated the simulations with $10\,\mathrm{nM}$ BL. Finally, I performed an *in silico* rescue experiment by adding the hormone after $12\,\mathrm{h}$ of simulations.
Figure 7.12 A shows that the elongation depends on the presence of the hormone. Without BL to induce the acidification of the cell wall, the transition from the basal elongation

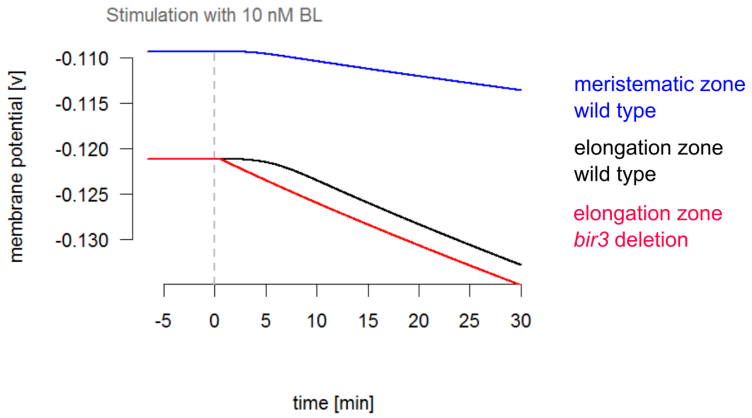

Figure 7.10: Validation of the elongating cell model. The behavior of a wild type epidermis cell in the elongation zone is indicated in red. The behavior of the same model parameterization in the meristematic zone is indicated in blue. Finally, the behavior of the *bir3* deletion model in the epidermis cell is represented in red.

rate to the faster elongation rates does not occur within the simulated time-course of 24 h. If the hormone is applied, the cells instead elongate according to the experimentally observed elongation rate [7] (Fig. 7.12 B).

To illustrate this, I also plotted the cell dimensions of the epidermis throughout the simulations (Fig. 7.13). This figure also shows the change in membrane potential (inner line) and the pH in the apoplast (outer line) throughout the course of the 24 h of simulation.

Figure 7.13 A shows that the absence of the hormone means that extracellular pH and membrane potential show almost no change. It also demonstrates that the hormone-induced acidification of the cell wall is necessary to induce cell elongation.

Next, the simulations with 10 nM BL (Fig. 7.13 B) shows that the hormone-induced change in membrane potential E_m and in the extracellular pH induces cell elongation. Notably, in the first 6 h almost no cell elongation occurs. Rather, the time window between 12 and 18 h contains the largest amount of cell elongation. During the last 6 h, cell elongation has already started to decrease as the cell approaches the maximal cell length [11, 7].

As a final test for the role of BR regarding cell elongation in the model, I performed an *in silico* rescue experiment. Here, I set the initial dose of BL to 0 nM and let the event for hormone stimulation occur normally. The event for hormone stimulation sets the global quantity $stimulation$ to 1, which allow processes like cell elongation and cell wall swelling to occur. In addition, I defined a second event that sets the dose of BL to 10 nM and that is triggered 12 h after the first event. The simulation results are summarized in Figure 7.13 C. Here, the model behavior resembles the simulation results of the model without the hormone (Fig. 7.13 A). After the addition of BL after 12 h, the cell wall starts to acidify (18 h) and elongates quickly during the last 6 h of simulation (24 h). The elongation behavior after the delayed addition of the hormone is not identical to the simulations, where 10 nM of BL is present from the beginning. This shows that the elongation at the basal rate, which

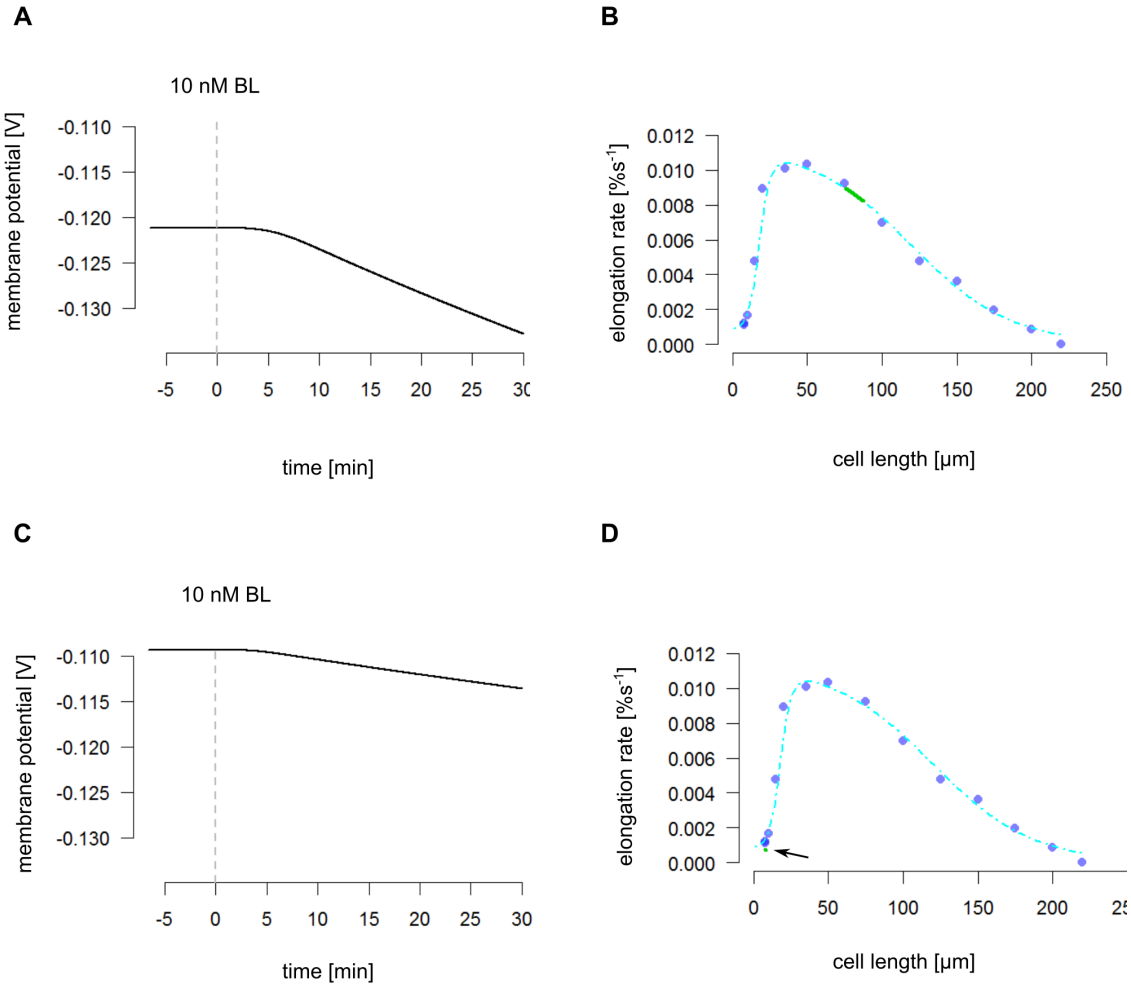

Figure 7.11: Behavior of the elongating model in meristematic and elongation zone. A, B: Elongation Zone. **A:** Membrane potential change. **B:** Elongation rate during the simulated 30 min (green). **C, D:** Meristematic zone. **C:** Membrane potential change. **D:** Elongation rate during the simulated 30 min (green). Experimentally measured elongation rates are indicated by blue points, the extrapolated elongation rate depending on cell length in cyan. The models were simulated for 30 min with 10 nM BL.

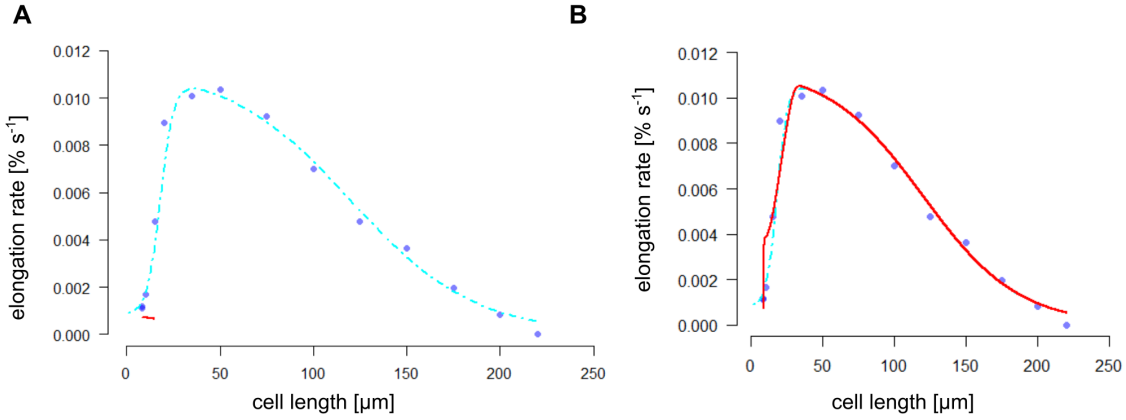

Figure 7.12: Modelled cell elongation in the ODE model. A: No cell elongation occurs in the model without brassinolide. **B:** Model behavior with 10 nM BL. The modeled cell elongation behavior of the ODE model fits the experimentally reported behavior in the different root zones.

occurs during the first 12 h of simulation, is sufficient to impact the model behavior once the hormone is added.

7.4 Simulating the Agent-based Model

To represent the elongation of the root tip, the ODE model described in the previous section was combined with an agent-based model of the root tip creating a multi-scale model of root elongation. The ABM contains the description of processes that concern the cellular agents, while the ODE model describes the intracellular response to hormone stimulation. The multi-scale model presented in this chapter is not a finalized representation of the root. Rather, this simplified representation of the root is meant to show that this approach to modeling root elongation is possible.

As the ABM currently lacks a stabilizing framework for the root cells, I applied a maximal cell length. Therefore, all cells exceeding a length of 25 µm die. I further limited the timeframe of the simulations to 8 h to 10 h to avoid a complete rearrangement of the root cells due to elongation and cell division. This means that currently only the lower rates of cell elongation can be observed. The very fast cell expansion in the elongation zone is not within the scope of the model at the moment.

Figure 7.14 shows the results of the ABM, where cells are colored according to their cell type in the ABM. This simplified model currently contains three cell types that I assigned based on the cell's position along the longitudinal axis: root columella cells (grey) that have no particular function beyond representing the shape of the root tip, dividing cells (green) that divide stochastically and epidermis cells (blue) that elongate according to the rate determined by the ODE model. During the 8 h of simulations cells elongate from an initial length of 8 µm to approximately 17 µm. In this particular simulation there is only one

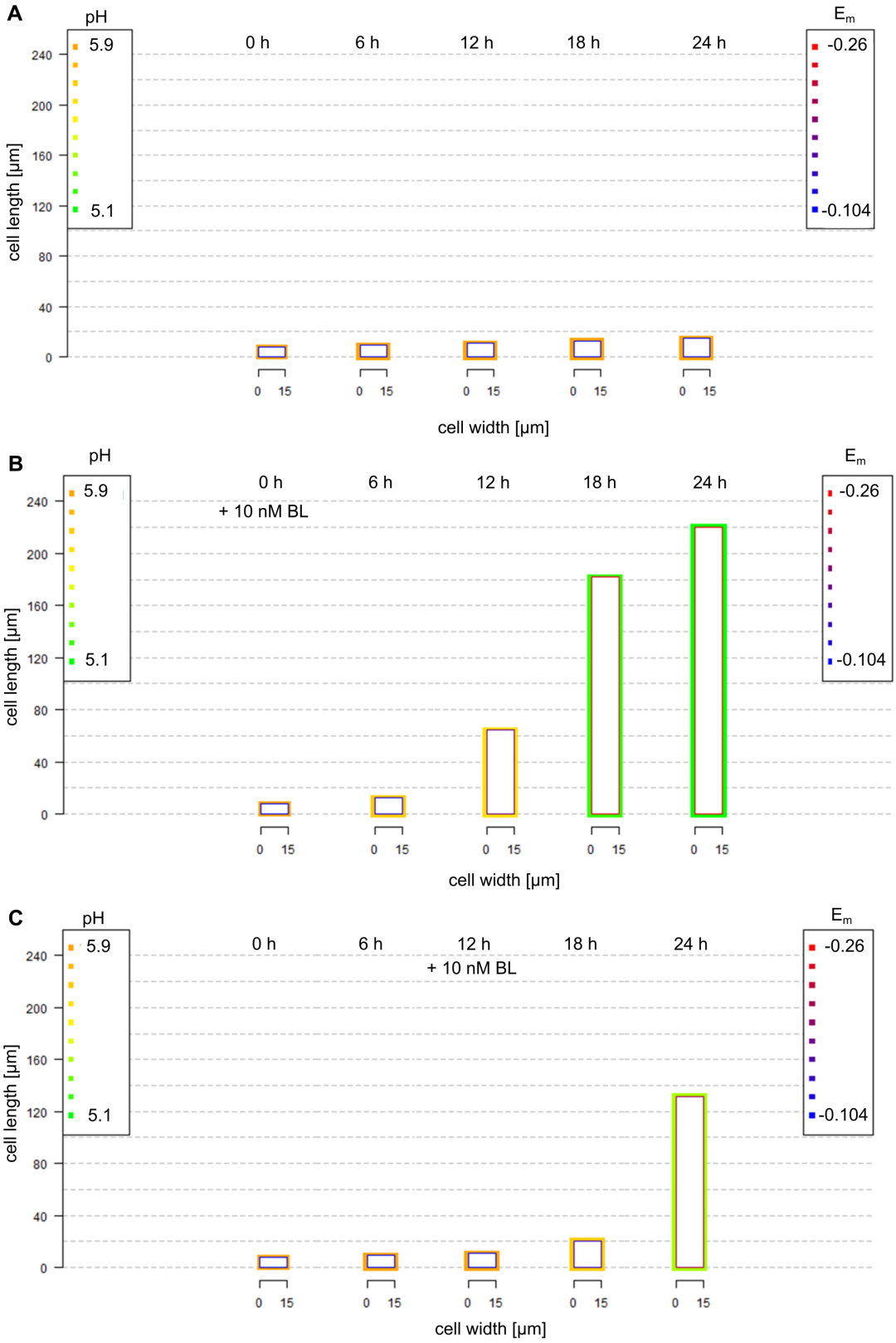

Figure 7.13: BL induced elongation in the expanded ODE model. A: Without BL. **B:** With 10 nM BL. **C:** Simulaitons are started without BL. 10 nM BL is added after 12 h. One parameter set was used for both simulations, the only difference being the BL concentrations. The cells start out with a cell length of 8 m and are simulated for 24 h. The cell wall pH is indicated by the outer line; orange: high pH; green: low pH. The membrane potential E_m is depicted by the inner line; blue: high E_m; red: low E_m.

cell division event occurring between 3 and 4 h of the simulation in cell column number 2. Since cell division is simulated stochastically, the actual number of cell division events varies between simulations of the same model (Fig. 7.15 A,B).
I further repeated the simulations with color code for the membrane potential (Fig. 7.15 A) and for the elongation rate (Fig. 7.15 B). Since only one color code can be recorded at a time, Figures 7.14 and 7.15 A and B stem from different simulations of the same model and therefore show different numbers of cell division events.
Figure 7.15 A shows that all cells are colored according to the initial membrane potential value (-0.109 V). However, only the elongating cells with the active ODE model change color according to the hormone induced membrane hyperpolarization. The change in membrane potential is depicted by the cell color shifting from a dark red to a brighter red. The simulation also demonstrates that cells, which are created during the simulations by cell division, start out with the initial membrane potential value of -0.109 V (Fig. 7.15 A, cell column 4).
Furthermore, Figure 7.15 B shows the elongation rate at different times throughout the simulation. As with the color code of the membrane potential, all cells are initially colored by the initial value of the elongation rate (purple). During the first hours of simulation, cells elongate according to the basal elongation rate. The snapshot at 10 h shows that the cells, which were present at the beginning of the simulation, start to show accelerated elongation (blue). The cells that were created by cell division later in the simulation show a lower elongation rate.

7.5 Summary

In this chapter of my thesis I show that not only can growth processes be described by an ODE model, but also that a multi-scale model of the elongating root tip is feasible. While the model presented here is by no means a finalized representation of the root, it gives first insight into what can be analyzed with such a model.
This simplified model also shows the aspects that need to be addressed for this model to become a realistic representation of the root. For one, other cell types than the epidermis need to be included in both the AMB and in the ODE model. This, in turn, requires the careful adjustment of elongation parameters for each cell type since they show different final cell lengths [11].
Currently, the model is not able to describe the fast elongation rates observed in the elongation zone. Even now at these comparatively slow elongation rates, the cells overlap to a high degree. This means that the number of time steps of the biomechanical model needs to be increased for cells to reach a steady state of repulsive and adhesive forces between simulation steps of the cell behavior model.

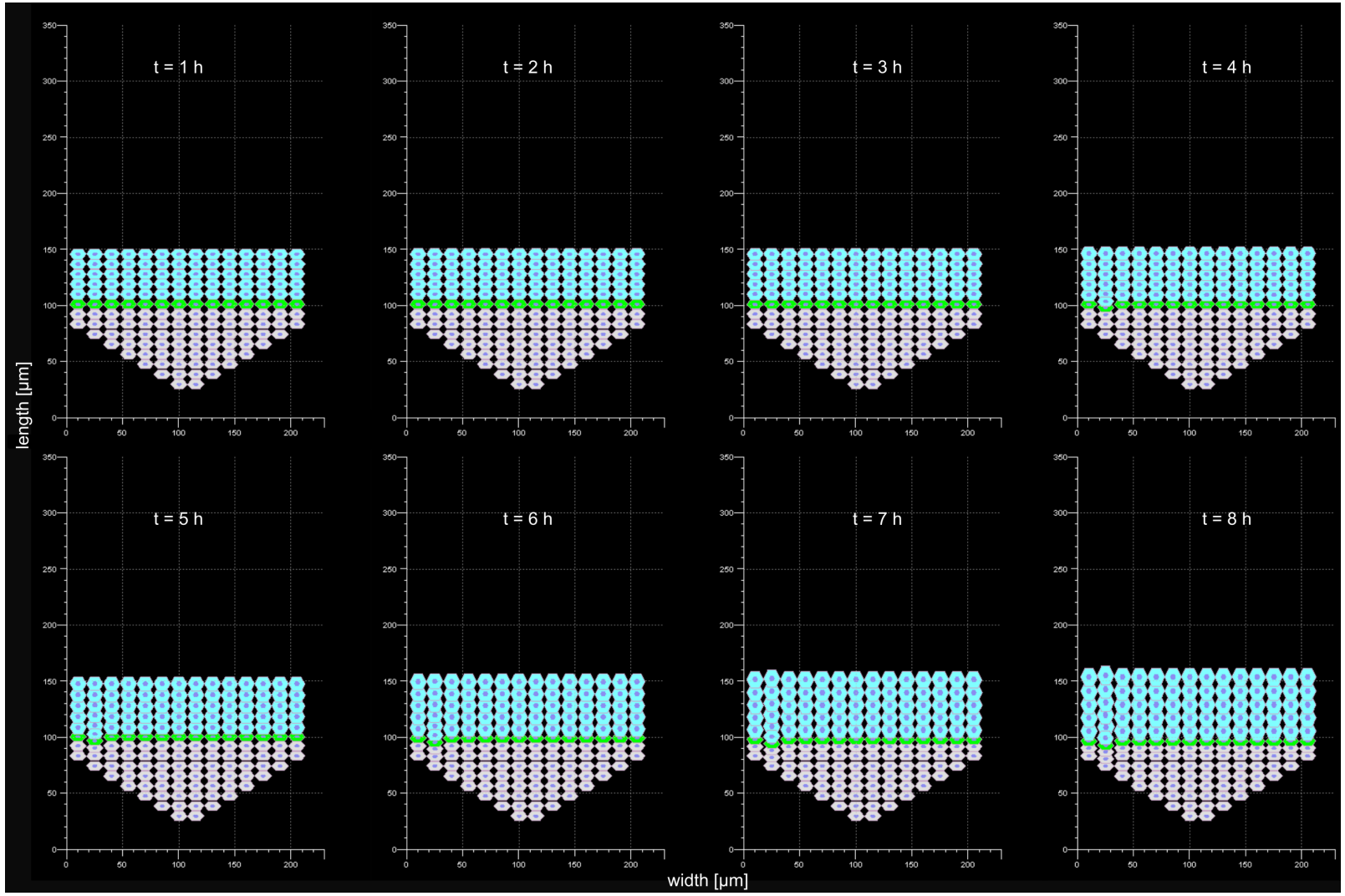

Figure 7.14: Simulation results of the agent-based model. Three types of cells are simulated in the model: columella cells to represent the root shape (light grey), dividing cells (green) and elongating cells (blue). Cell division is modeled as a stochastic process. The new cell is first represented by a placeholder (white) and has to undergo the biomechanical model before taking part in the cell behavior model. Cell elongation was modeled by the ODE model and linked to the agent-based model via the cell behavior model.

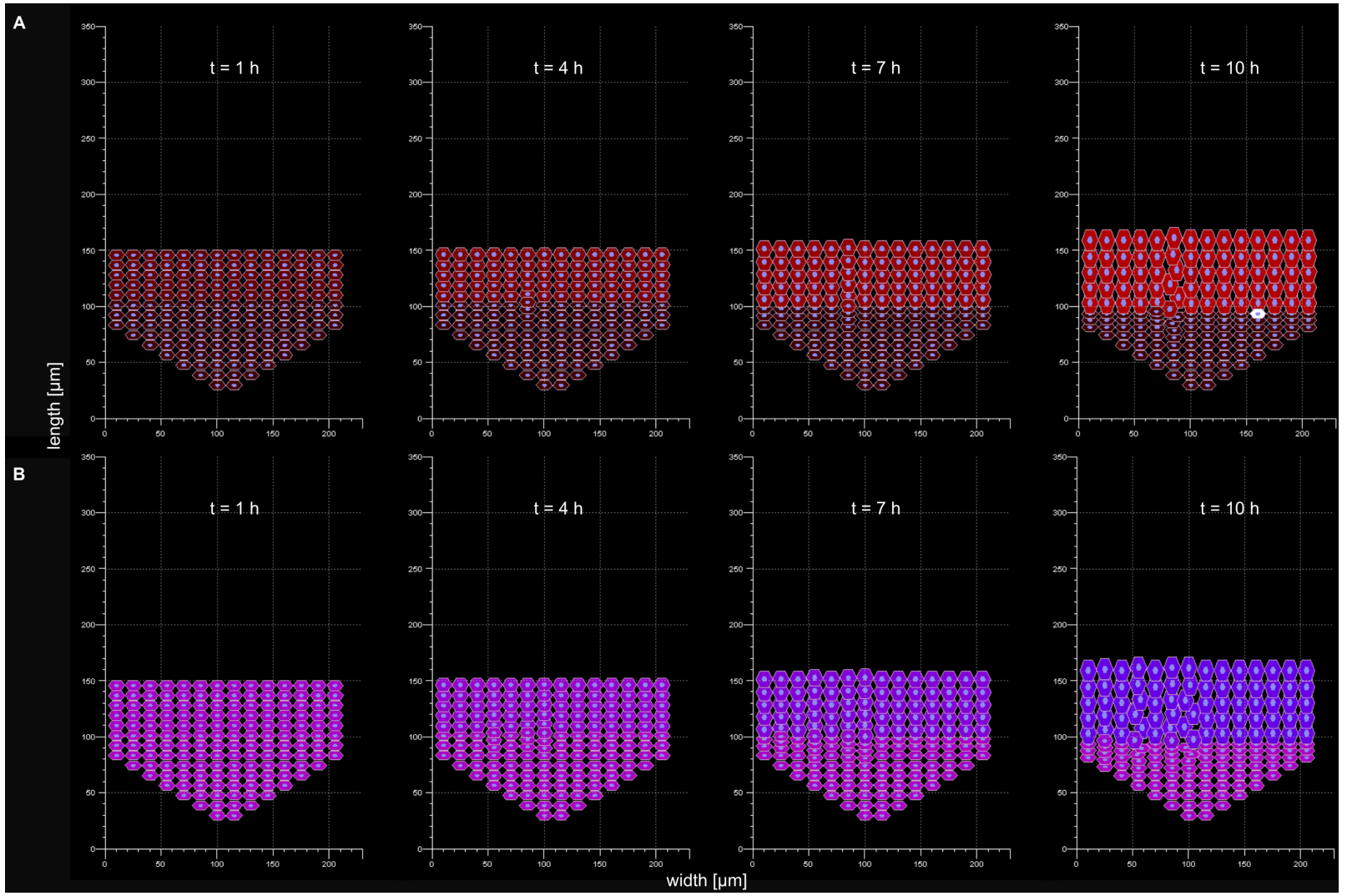

Figure 7.15: Simulation results of the agent-based model. A Instead of the default color code, color code 1 was used to show the membrane potential. Dark red: high membrane potential. Bright red: hyperpolarization the membrane. **B:** Instead of the default color code, color code 2 was used to show the elongation rate of the individual cells. Green: basal elongation rate. Purple - blue: higher elongation rates.

8 | Disscusion

BRs play a crucial role in plant growth, development and environmental adaptation [1]. Therefore, understanding the dynamics and regulation of BR signaling is an important aspect towards understanding these processes. Throughout this thesis, I analyzed the initiation and regulation of the fast BR response pathway on different scales, ranging from the interactions of proteins towards building an agent-based representation of the root.
As BRs affect cell morphology by initiating cell wall expansion and cell elongation [14, 2, 17, 21], I analyzed how changes of cell morphology can affect the model behavior in ODE models with different ways of handling compartments (Chapter 4, pp. 31). The results of this analysis served as theoretical basis for including cell wall swelling and later also cell elongation in the ODE models of the fast BR response in this thesis.
By molecular modeling I specified the role of the negative regulator BIR3 (Chapter 5, pp. 49). Here, the computational docking of the cytoplasmic domains of BIR3 with the receptor BRI1 and the co-recepotor BAK1 shows that the interaction between BIR3 and BAK1 is the one with the more favorable energetic landscape. As the interaction surface of this complex includes the catalytic domain and the activation loop of BAK1, BIR3 prevents BAK1 from participating in active BR signaling.
I further analyzed the dynamics and regulation of the fast BR response pathway by constructing an ODE model that comprises the known proteins and reactions (Chapter 6, pp. 71). After estimating the parameters based on dose-response data and the behavior during BIR3 and BIR3&BRI1 overexpression, I analyzed the impact of the different model components on the membrane potential change by sensitivity analysis. As the H^+-ATPase concentration and pump activity played a central role in the response in the elongation zone, one target for the validation of the model was the behavior in the meristematic zone. Here, the concentrations of both H^+-ATPases, AHA1 and AHA2, are much lower, which reflects in the reduced response by the model. This was substantiated by the measurements of the extracellular pH and the net H^+ flux by the experimental collaborators.
Finally, I expanded the ODE model of the fast BR response to include cell elongation. This necessitated some changes in the definitions of compartments and protein concentrations. Nonetheless, the model can still describe the dose-response data as well as the predictions regarding the behavior in the meristematic zone and in the *bir3* deletion. By combining this model with agent-based model of the root tip, I created a first multi-scale model of BR-induced root elongation (Chapter 7, pp. 101). This model currently only describes the behavior of one cell type, an epidermis cell, but represents an important step towards modeling root elongation on the scale of an organ.

8.1 Multi-Compartment Rate Laws

The analysis of the importance of multi-compartment rate laws was motivated by the fact that most of the components of the fast BR response are located in the plasma membrane. Furthermore, the response to BR stimulation comprises both cell wall swelling [14] and cell elongation [2, 17, 21], both of which change the size of cellular compartments and cellular morphology.

In 2008 Hofmeyr correctly stated that processes spanning mutliple compartments should be scaled with the respective interaction area [106]. However, an analysis of the curated models on the biomodels database[1] [35] showed that the majority of models comprise only one compartment. Out of the models that do comprise multiple compartments, most have arbitrary compartment sizes or only consider the ratio of compartments. Merely 22 models have compartments with realistic compartment volumes - of these, only three actually comprise the membrane as 2D compartment [156, 149, 157]. Considering the fact that compartments and their specific reaction environments are a key characteristic to eukaryotic metabolism, this is surprising.

While the curated models on the biomodels database represent but a sample of all available biochemical models, it already highlights the different modeling approaches to modeling a cellular system: Often one universal compartment is used to model processes that involve multiple compartments (e.g. [162, 163]). If different compartments are defined in the model, they most often do not consider the membrane as individual compartment or scaling factor. Notably, if the membrane is included in a model, it is often because the ODE model serves as a basis for a spatio-temporal PDE model [149, 157]. All of the above mentioned modeling approaches can describe the experimentally observed behavior, but all but area-scaling models are limited to one unique cell shape.

The effects of cell morphology have so far only been analyzed in the case of spatial PDE models [154, 153]. To determine the impact of changes in cell morphology on the behavior of models that comprise different ways of describing multi-compartment processes, I analyzed different biologically relevant examples. For one, I looked at the behavior of an epidermis cell in different root zones along the *A. thaliana* root. Here, I analyzed not only the diffusion from the cell wall into the cytoplasm but also vertical and horizontal transport between epidermis cells. Second, I used a simple receptor model to study the signal transduction to a second messenger in the cytoplasm. Finally, I analyzed an example model from the biomodels database.

Interestingly, it is not always necessary to include the membrane in the model. Depending on the modeled system, changing the compartment sizes actually does not affect the model behavior to a point where notable differences between the area-scaling model and the other models can be observed. For example, the analysis of the simple receptor toy model showed that using one compartment can actually yield a behavior that is closer to

[1] `https://wwwdev.ebi.ac.uk/biomodels/`, last accessed: 24.05.2018

the area-scaling model compared to the behavior of the multi-compartment model without area scaling. Furthermore, the analysis the example model demonstrated that small changes in compartment volumes can have little impact on the time-course simulations at least in this particular model of RanGTP shuttling [101].
I observed the most notable differences between the different modeling approaches in the analysis of the diffusional transport model (see pp. 35). Here, for the vertical and horizontal transport the speed of diffusion between the compartments changes a lot in the area-scaling model. In contrast to this, the multi-compartment model without area-scaling underestimates the transport rate in both the elongation zone and in the maturation zone, while the one compartment model does not react at all to changes in the modeled setting. This highlights that including the interaction area can be crucial to the correct model behavior at least when modeling the behavior of an epidermis cell along the root axis, where the cells undergo large changes in cell morphology [11].
This is the case for the ODE model of the fast BR response that I presented in Chapter 6. Here, predicting the behavior of the meristematic zone would have been impossible if the area had not been explicitly included in the model. Without the required adjustment of the permeability parameters, the rate of proton leak would have been highly overestimated resulting an even greater depolarizing shift in the membrane potential and an unrealistic prediction.
It is worth mentioning that COPASI [104], which is a widely used modeling software[2], has only recently started to support 2D compartments with build 184. While it was possible to model 2D compartments before by simply treating a 3D compartment as if comprised only two dimensions, it was quite challenging to keep track of the deviating model parameter units and protein concentrations. With COPASI now supporting 2D compartments, the number of models that include the membrane as compartment might increase.

8.2 Specifying the Role of BIR3

The motivation for the molecular modeling was to specify the role and mechanism of the negative regulator BIR3 in BR signaling by analyzing the role of the cytoplasmic domains in the interactions. BIR3 is a inactive receptor kinase that interacts with both BRI1 and BAK1 [30]. Extensive interaction studies have demonstrated that the interaction between BIR3 and BAK1 is the more favorable one [30, 47]. In that particular interaction, the ectodomains play a central role [47]. Furthermore, the ectodomains of BIR3 and BRI1 do not appear to interact [47]. Interestingly, this study by Hohmann and colleagues [47] did not show the interaction of the kinase domains of BAK1 and BIR3, which has been previously measured [30]. However, both the experiments done by our collaborators (see section 5.2.2, p. 63) and by Imkampe *et al.* (2017) have shown the interaction of the full length proteins. As the cytoplasmic domains have to interact at least on a transient level in order for transphosphorylation to occur, the interactions of the cytoplasmic domains are

[2] http://copasi.org/Research/Map/

still of interest. Furthermore, the observation of the interaction between full length proteins suggests that transmembrane and cytoplasmic domains contribute to these interactions.

8.2.1 Docking Methods

For this part of my thesis, I used two different docking methods to compute the potential interactions of the cytoplasmic domains of BIR3, BAK1 and BRI1. First and foremost, I employed webSDA to compute potential complexes between proteins by rigid body docking [48, 99]. I substantiated the results of the webSDA analyses by repeating the computations with ClusPro [49, 49, 50, 51, 52].
Docking analyses by webSDA yield only encountered complexes as side chains do not adjust to the complex formation [48, 99]. webSDA uses Brownian Dynamics to simulate the diffusional association between the proteins of interest [99]. This sampling process is limited by the fact that protein structures are not allowed to overlap during diffusional association. webSDA allows the specification of physiological parameters such as pH and ionic strength of the solvent. By further using Brownian dynamics to compute potential compelxes, webSDA does not need as large a sample as other methods. Here, only 500 complexes are sufficient to gain a good impression on the complex association and the energetic landscape. Nonetheless, there are variations between SDA runs as this method is based on Brownian dynamics.
In contrast to this, ClusPro uses extensive sampling of the interaction space by first computing an initial number of 70000 and reducing this to 1000 complexes based on a scoring function. Here, there are different options available that are optimized for enzyme-inhibitor or anitgen-antibody interactions. As we were interested in the energetic landscape, we primarily used the scoring function that describes electrostatic interactions as well as van der Waals forces. Additionally, I did not impose any constraints on the docking runs between BIR3 with BAK1 and BRI1 to avoid introducing a bias in the selection process.
The situation was different for the docking of BRI1 and BAK1. Here, the unconstrained docking does not yield any feasible complex within the selection criteria. As a first step, I constrained the docking runs in webSDA and ClusPro to a center-to-center distance of 45 Å. This did yield a feasible complex by the computations run with webSDA. However, the ClusPro analyses did not yield a feasible complex based on the scoring function describing electrostatic interactions as well as van der Waals forces. Here, I had to resort to the balanced scoring function, which also considers the "Decoys as a Reference State" (DARS) [191]. This scoring function is specifically optimized for enzyme-inhibitor and antibody-antigen complexes that show a high degree of complementary structures [191]. As a consequence for other protein interactions, while this scoring function will yield close to native complexes, the discrimination between those complexes is poor [191]. Therefore, while the complex shown for the ClusPro docking between BAK1 and BRI1 is the one with the largest cluster population and therefore still likely close to the native complex [52], this result does not yield as much information on the shape of the energetic landscape as the webSDA results.

Unlike webSDA, ClusPro first allows some degree of steric clashes between the docked protein structures. These clashes are removed in an additional computational step, where flexible side chains adjust to the complex formation. Therefore, ClusPro calculates docked complexes instead of encountered complexes like webSDA. Due to this fact and the large number of initially sampled complexes, the docking results are very consistent between ClusPro runs.
In addition to different ways of computing potential interactions, ClusPro and webSDA employ different approaches to clustering. In webSDA, all recorded complexes start out as their own cluster [99]. Then the clusters with the least RMSD from each other are identified an merged. This process is repeated until the designated number of clusters remains. Here, I set the number of clusters to the maximal value of 10.
In contrast to this, ClusPro identifies the complex with the highest number of neighboring complexes within 9 Å interface root mean square distance (IRMSD) and assigns them to the first cluster [52]. Then, the next complex with the highest number of neighboring complexes among the unclustered interactions is identified. This process is repeated until up to 30 clusters have been identified.
Considering that the two docking methods use different approaches to computing potential complexes and different ways of clustering the observed clusters, the fact that the results of both methods are so consistent underlines the validity of this approach and our computational results. However, this does not replace the need to verify the computational results by experimental validation, as a number of assumptions have been made throughout this analysis.

8.2.2 Assessing the Criteria for Cluster Selection

The docking of cytoplasmic domains of proteins that in reality also have ectodomains and transmembrane domains raises several issues in filtering the results of the docking analyses. In reality, the cytoplasmic domains of these proteins are greatly limited in their association due to the anchor to the plasma membrane. Therefore, the cytoplasmic domains of transmembrane proteins have less degrees of freedom in reality than they have in computational docking analysis. I introduced a number of selection criteria for the computed complexes to account for this fact (see Materials&Methods p. 20).
For one, all structures used for the analyses here in this thesis are truncated at N- and C-termini. Therefore, N- and C-termini are not allowed to participate in the interaction surface between the proteins. To have a clear threshold for what is considered to be an interaction, I introduced a "minimal distance criterion". Once a N- or C-terminus has a distance greater than this distance criterion it is not considered part of the interaction surface. As the "minimal distance criterion" was defined by sampling the distances between computed complexes of BAK1, BIR3 and BRI1 in both webSDA and ClusPro, the actual threshold value is specific to these structures. Furthermore, as webSDA only computes encountered complexes and ClusPro allows for the adjustment of amino acid residues, the criterion is also specific to the computational method. These limitations need to be kept in

mind when using this criterion.
An additional consequence of the structures being truncated at N- and C-termini affects the orientation of the proteins in the complexes: The N-termini of both proteins have to be able to extend towards the membrane, while the C-termini are not allowed to clash with the membrane. Finally, I could not exclude the fact that transmembrane and extracellular domains of the proteins can and do play a role in the interactions of the whole proteins [47]. Therefore, the proteins were not allowed to interact by their C-terminal and N-terminal domains along the longitudinal axis.
All of these criteria are meant to compensate for the facts that i) the proteins are truncated at N- and C-termini and ii) the changed degrees of freedom by docking the free cytoplasmic domains. While this situation is far from ideal, there is little alternative until a docking method is developed that allows the anchoring of protein domains at a membrane. I had attempted to limit the center to center distance between the proteins to 45 Å to prevent complexes where the proteins interact along the longitudinal axis. However, this resulted in docking runs where no allowed complex was detected, suggesting that this way of addressing the differing degrees of freedom can be too limiting. Considering the uncertainty introduced by the gaps in the experimentally determined structures and the number of assumptions made to account for the different situations *in silico* and *in vivo*, it is absolutely necessary to validate the computational results experimentally, which was done for the results of this analysis.

8.2.3 The Behavior of the Cytoplasmic Domains Reflects the Behavior of the Ectodomains

Several studies have examined the interactions between the ectodomains of BAK1, BRI1 and BIR3 [44, 25, 45, 47]. For one, the ectodomains of BAK1 and BRI1 only interact when the ligand is present [44, 25]. Correspondingly, our computational results have shown that the cytoplasmic domains of BAK1 and BRI1 can interact *per se* but with a very unfavorable landscape supporting the weak interaction of the cytoplasmic domains of Bojar *et al.* (2014) [123]. As this complex carries the risk of BR signaling in the absence of BR, negative regulators such as BKI1 [26, 27, 123] and BIR3 [29, 30] are required to regulate the interactions between receptor and co-receptor.
More recently, Hohmann and colleagues have demonstrated that the interaction between BAK1 and BIR3 ectodomains is very stable and that the binding site of BIR3 on BAK1 overlaps with the binding site of BRI1 on BAK1 [47]. Therefor, BIR3 and BRI1 compete for the interaction with BAK1 [47]. Finally, as the ectodomains of BRI1 and BAK1 interact only in the presence of the hormonal ligand [25, 44], BRI1 needs to be in a complex with the ligand to compete with BIR3 for the interaction with BAK1 [47].
These observations reflect the behavior we have seen for the cytoplasmic domains of these proteins. Our computational analyses have demonstrated that the interactions of BAK1 and BIR3 cytoplasmic domains is more favorable based on the energetic landscape than the interaction between BAK1 and BRI1 as well as BIR3 and BRI1. In fact, in agree-

ment with the competition for the binding site on the ectodomain of BAK1, the cytoplasmic domains of BRI1 and BIR3 also compete for the binding site on the cytoplasmic domain of BAK1. As this binding site contains both catalytic domain and the activation loop of BAK1, BRI1 has to interact with that domain to facilitate the transphosphorylation events and propagate signal transduction.
Interestingly, Hohmann and colleagues did not observe an interaction between the cytoplasmic domains of BIR2 and BAK1 as well as BRI1 in an isothermal titration calorimentry assay [47]. This result is somewhat surprising as the interaction between BIR2 and BAK1 cytoplasmic domains has been shown before [46]. Furthermore, while this result is for BIR2, this protein shares a high degree of sequence identity with BIR3. Therefore, these results are even more puzzling as the interaction between BIR3 and BAK1 kinase domains has been detected as well [30]. Furthermore, FRET-FLIM measurements have shown that BAK1 and BIR2/3 are in close proximity to each other [46] (also: this thesis p. 63). This has been substantiated by both split ubiquitin system assays [204], which tested the interactions of full length BIR3 with both BAK1 and BRI1 [30]. Furthermore, a bimolecular fluorescence complementation assay using YFP [205] for full length BIR3 and BRI1 expressed in *N. benthamiana* showed that these proteins exist in very close proximity to each other [30]. Additionaly, as no interaction could be observed for BIR3 and BRI1 based on their ectodomains [47], transmembrane and/or cytoplasmic domains likely play a determining role in the observed interactions of the proteins as a whole [46, 30].

8.2.4 Implications of a Trimeric Complex

As final assay of the molecular docking analysis, I tested if a trimeric complex consisting of all three proteins is possible computationally. Here, I docked BRI1 to the complexes computed for BAK1 and BIR3 by both webSDA and ClusPro analysis. As it is currently not possible to compute trimeric complexes using webSDA due to a failure in generating the pqr files, I relied on ClusPro alone for this analysis.
Interestingly, I observed potential complexes for only three of the four docking runs. One docking analysis failed to produce a cluster that passed all criteria for cluster selection. The remaining three potential three complexes all have BRI1 interacting with BAK1 opposite to its binding site with BIR3. This means that the two interactions are likely independent of each other, which fits the experimental observations by Imkampe *et al.* (2017) [30].
The fact that this complex is computationally possible, is not completely unexpected. Different studies have indicated that BAK1-BRI1 hetero-oligomers might exist even when BRs are absent [14, 64, 65]. In particular, Bücherl *et al.* determined that approximately $7\,\%$ of the receptor exists in hetero-oligomers, which is already half of the amount receptor activated during saturated signaling ($15\,\%$) [38]. Nonetheless, there is no signaling activity without the hormone. Consequently, this suggests that BRI1 has to be able to interact with BAK1, while the co-receptor is in complex with BIR3.
The trimeric complexes computed by ClusPro show that it is indeed possible for BAK1 and BRI1 to interact without any risk of signaling activity. For one, the catalytic domain and ac-

tivation loop of BAK1 are part of the interaction surface with BIR3. Second, the activation loop and the catalytic domain of BRI1 are not part of the interaction surface with BAK1. This kind of complex fits to the above mentioned experimental observations.
Furthermore, preformed complexes allow for a fast switch from the inactive state to active signal transduction. A recent study of the interactions between the ectodomains has shown that the interaction between BAK1 and BIR3 is preferred here as well as the no interaction could be observed of the ectodomains of BIR3 and BRI1 [47]. Hohmann and colleagues further demonstrate that BR-bound BRI1 can compete with BIR3 for the interaction with BAK1 [47]. If receptor, co-receptor and negative regulator indeed exist in preformed nanoclusters, the close proximity of all components would allow for an almost immediate transition to active signaling upon ligand binding. However, until this complex can be observed *in planta*, the existence of such a complex is still a matter of discussion.
The existence of preformed receptor complexes is not a foreign concept to signaling pathways. For animals, this phenomenon has been shown to exist for example in bone morphogenetic protein receptor complexes [206] and in epidermal growth factor signaling [207]. In plants, these complexes occur in CLAVATA signaling, which mediates stem cell homeostatis [208].

8.3 Modeling the Fast BR Response

To examine and analyze the temporal dynamics of the fast BR response, I formulated an ODE model using COPASI. Taking into account the information on the cellular compartments and considering the known biochemical reactions, I simulated the BR-induced membrane hyperpolarization and cell wall swelling. Both of these processes are known to precede expansive cell growth [14].
I specifically constructed the model in such a way that the model is first simulated for $24\,\mathrm{h}$ without the hormone. This allows the complex formation of BIR3 with BAK1 and BRI1 and ensures that the resting membrane potential of $-0.121\,\mathrm{mV}$ is described by the model. Due to the model structure, the model reaches an equilibrium state during these simulated $24\,\mathrm{h}$. This is by no means a physiological state [209], as living cells constantly produce and consume energy. Furthermore, proteins are constantly produced and degraded. As neither process is included in the ODE model, the model does not reach a steady state but rather an equilibrium.
Using this model I analyzed the importance of the different model species and parameters to determine those with the greatest impact on the modeling output, the membrane hyperpolarization. This analysis showed that the H^+-ATPases AHA1 and AHA2 have a large impact on the model's response. Here, setting the modeled environment to the meristematic zone, where there is less ATPase, greatly reduces the response (see p. 95). We verified this behavior experimentally, thus affirming the validity of the model.
In order for functional BR signaling to occur, the receptor BRI1 requires the association with the co-receptor BAK1 [23, 24]. Considering the central role of BAK1 in BR signaling,

it is worth mentioning that BAK1 participates in several other signaling pathways. For one, BAK1 regulates an BR-independent pathway mediating cell death [61]. Second, BAK1 is involved in PAMP-triggered immunity, where it interacts with the receptor flagellin-sensitive 2 (FLS2) and elongation factor Tu receptor (EFR) [210]. Treating plants with the ligands for these receptors, greatly reduces the observed level of growth, even if BR is applied exogenously [210]. The cause of this lies in the PAMP-induced production of reactive oxygen species [210], which increases cross-linking of cell wall components [211].
Interestingly, BAK1 is not a limiting factor between the BR-induced and PAMP-induced signaling [63]. In fact, BRI1 and FLS2 mediated signaling pathways exist in different plasma membrane nanodomains [212]. Therefore, BRI1 and FLS2 cannot compete over interaction with BAK1. It also potentially provides some context for why there are different regulators of BAK1 for these signaling pathways: BIR3 regulates BAK1 activity in BR-signaling [30] and BIR2 regulates BAK1 activity in FLS2 signaling [29, 46].
Currently, the model of the fast BR response contains very little information on signal termination. Only one mechanisms for signal termination is included in the model in the form of the slow, inhibitory autophosphorylation of the receptor and the even slower dephosphorylation of that phosphorylation site [79]. However, this yields little information on signal termination. There is experimental evidence of ubiquitination-mediated receptor internalization, however this appears to be largely independent of the ligand [213]. Ubiquitination is therefore more likely a mechanism for controlling the amount of receptor at the plasma membrane [213]. Interestingly, receptor internalization appears to be an important aspect for the genomic respose, as endosomal signaling of BRI1 increases the response of this pathway [214] though it is not a requirement as BRI1 can signal form the plasma membrane [215].
This lack of information is reflected in the uncertainty of the paramters for most dephosphorylation reactions (r_{d3} to r_{d7}) and the inhibitory autophosphorylation (r_{12}). To adress the latter, we have designed longer measurments of the extracellular pH in response to BR stimulation. These measurements will also occur at lower BL concentrations, as $10\,\mathrm{nM}$ is already close to the saturating hormone concentration. However, these experiments will do little in terms of defining the parameters of the dephosphorylation reactions. Here, wash-out experiments would be needed to determine the rate of these reactions.

8.3.1 Assessing the Parameter Space

The complexity of a biological system is often not reflected in the amount of available experimentally determined parameters of kinetic, association and dissociation rates [216]. Therefore, parameters often have to be estimated based on experimental measurements. Still, if there are insufficient data, this can yield more than one parameter set describing the measurements [217].
In the case of the fast BR response, the initial settings in terms of protein concentrations (this thesis and [11]) and the proton leak into the cell (Supplementary Information p. 181) as well as the final output in form of the membrane hyperpolarization [14] are well defined.

There are some experimental measurements for parameters in the signal transduction: The affinity as well as the association rate of the ligand BL to the receptor are well studied and defined [1, 45, 59, 198]. Beyond these data, there exist measurements for the phosphorylation rate of the inhibitor BKI1 [199] and the time-scale of the inhibitory autophosphorylation [79]. Currently, there exists no information on the rate of phosphorylation of receptor and co-receptor in the model. Furthermore, most dephosphorylation rates with the exception of the autoinhibitory phosphorylation of the receptor are completely undefined, which is reflected in the uncertainty of these parameters.
To further limit the allowed parameter space, I used qualitative information to set interval for parameters during parameter estimation. This was the case for the affinity of BIR3 to BAK1 and BRI1, respectively, as I knew the interaction of BIR3 and BAK1 to be the more stable one (this thesis and [30, 46].
While I used as much experimental information as possible to limit the allowed parameter intervals, parameter non-identifiability is still an issue in the ODE model. The reason for this lies in the aforementioned lack of phosphorylation data of the receptor complex and the inactivation of the signaling pathway after removal of the hormone. To address the issue of parameter non-identifiability, I generated a model ensemble with 50 independent parameterizations. If the model behavior and predictions are consistent between parameter sets, it substantiates the modeling results [201], which is the case for the fast BR response model presented in this thesis. However, even a model ensemble does not yield a full picture of the parameter space, but instead represents a sample of the parameters, which can describe the data. Therefore, the experimental validation of the model predictions as done by the experimental collaborators is absolutely necessary to verify the model behavior.

8.3.2 The Role of BIR3 in the ODE Model

The observed overexpression behavior of BIR3 already highlights the regulatory role of BIR3 in BR signaling in general [30]. A secondary role of BIR3 appears to be the stabilization of BAK1 [30]. Therefore, *bir3* mutants show decreased levels of BAK1, which can explain the weak phenotype of these plants [30]. Accordingly, the added expression of BAK1 under the control of the native promotor causes the plants to be slightly more responsive to BR treatment [30]. This last effect is actually reflected in the ODE model of the fast BR response pathway. Here, the *in silico* deletion of *bir3* causes a slight increase in membrane hyperpolarization but the overall behavior still closely resembles the behavior of the wild-type (Fig. 6.14, p. 98).
In fact, a scan of the initial BIR3 concentration shows that the wild-type BIR3 concentration is in a range, where changes in BIR3 expression affect membrane hyperpolarization. This means that plants should be able to adjust the responsiveness to BR stimulation by adjusting BIR3 levels through changes in gene expression or translation rates. This suggests that BIR3 function concerns the fine-tuning of the BR response.

8.3.3 ATPase Levels Control the Response of Fast BR Signaling

The quantification of protein species in the model revealed that H^+-ATPase concentrations increase from the low concentrations in the meristematic zone to the higher concentrations in transition and elongation zones. Combined with the high sensitivity of the membrane potential changes to all parameters concerning ATpase pump activity, this suggests a regulatory role of the ATPase concentration regarding the cellular responsiveness to BR stimulation. This is supported by the model's behavior in the meristematic zone, where the response to BR is notably reduced. Furthermore, the experimental validation of this behavior by both extracellular pH measurements (p. 96) and by measuring the net proton flux at the root surface (p. 97) supports these results.
BR signaling is not limited to inducing cell elongation in the transition and elongation zones. In the meristematic zone, BR regulate cell division of the quiescent center, which is part of the stem cell niche in the root [37]. However, these cells do not react to BR stimulation with cell wall acidification as our experiments have demonstrated (p. 97). This is in agreement with the experimental observations that meristematic cells only elongate at the basal rate [7] as cell expansion is facilitated by the pH-dependent activation of expansins [9, 12]. In consequence, this suggest that the changing H^+-ATPases AHA1 and AHA2 concentrations (see p. 75) are the determining factor in BR-induced cell elongation [2, 17, 21].
Interestingly, the quantification of AHA2-GFP in the root showed columns of cells with higher AHA2 concentrations that start cell elongation earlier than the neighboring columns of cells. These epidermis cells are atrichoblasts and trichoblasts [218]. Trichoblasts are root hair cells, atrichoblasts are non-hair cells. Even in the meristematic zone, atrichoblasts are larger than trichoblasts and the difference remains as the cells elongate [218]. The increased AHA2 amount in atrichoblasts supports the regulatory role of the ATPases regarding BR-induced cell elongation growth [2, 17, 21].

8.3.4 Comparison to Published BR Models

At the time of writing this thesis several models of different aspects of BR signaling have already been published. First, a logic model of the BR response analyzes the qualitative aspects of the signaling pathway [36]. Here, a continuous transformation of the logic based model showed that the system is able to oscillate given the model structure [36]. Second, a steady state model links receptor occupancy to root and hypocotyl elongation by a phenomenological model [39, 40]. Furthermore, a dynamic model of the gene-regulatory pathway considers the spatial aspects of diffusion from the membrane to the nucleus [41]. Last, a small ODE model aided in understanding the interactions of the transcription factors BES1 with brassinosteroid at vascular and organizing center (BRAVO) [37]. Here, the model demonstrated a switch like response to BR stimulation, which provides a mechanism for BR-controlled cell divisions in the quiescent center [37]. As the models presented by van Esse *et al.* [38, 39, 40] and Allen & Ptashnyk [41] are closest in terms of research

question and modeling approach to the models presented in this thesis, both will be examined in more detail below.

Steady State Model This steady state model describes BRI1 response in root and shoot by linking the steady state receptor occupancy with root and shoot elongation [38, 39, 40]. The biochemical model used in this study describes the steady state receptor occupancy defined by the concentration of $[BRI1\ BL]$ (Equation 8.1). Here, the receptor concentration $[BRI1]$, the ligand concentration $[BL]$ and the affinity of the receptor to the ligand K_d.

$$[BRI\ BL] = \frac{K_d + [BRI1_{tot}] + [BL_{tot}] - \sqrt{(K_d + [BRI1_{tot}] + [BL_{tot}])^2 - 4 \cdot [BRI1_{tot}] \cdot [BL_{tot}]}}{2} \tag{8.1}$$

The biochemical model in Equation 8.1 is used in combination with a phenomenological model (Equation 8.2), which describes the root growth depending on the total receptor concentration $BRI1_{tot}$ and the total ligand concentration BL_{tot}. Specifically, root growth $R(BRI1_{tot}, BL_{tot}, t)$ is a combination of the response without BL, which is denoted by $R(0, 0, t)$ and the activating and inhibiting terms of BR signaling.

$$R(BRI1_{tot}, BL_{tot}, t) = R(0, 0, t) + \frac{E_{max}(t) \cdot [BRI1\ BL]}{k_1 + [BRI1\ BL]} \frac{k_2}{k_2 + [BRI1\ BL]} \frac{k_3}{k_3 + [BRI1\ BL]} \tag{8.2}$$

The term $E_{max}(t)$ describes the time-dependent responsiveness of the root elongation to the stimulation with BL, which is an unknown factor. Therefore it regarded as a free parameter that is allowed to change between different time points [38]. In a biological context, $E_{max}(t)$ summarizes aspects such as the age of the seedling, the concentrations of inhibitors and the concentration of the ATPases. One can indeed argue that because $E_{max}(t)$ summarizes so many different physiological effects, it has to be included as a free parameter. It does, however, mean that only the shape of the modeled root length curve is the actual modeling results as the curve can be scaled.
Interestingly, this model is still able to predict root growth in *bri1* loss-of-function mutants and for the weaker ligand 22-homobrassinolide (HBL) [38]. This demonstrates that phenomenological models can yield some insight into complex biochemical processes such as BR-induced root growth. However, it also limits the amount of informational output of the model, as details that can be included in an ODE model, such as the model presented in this thesis, cannot be captured by a phenomenological model.

Dynamic Model of BR-Regulated Gene Expression The dynamic model by Allen & Ptashnyk [41] describes the gene-regulatory pathway with the concentration of unphosphorylated BZR as final output. Here, the signaling pathway is reduced to a few reactions

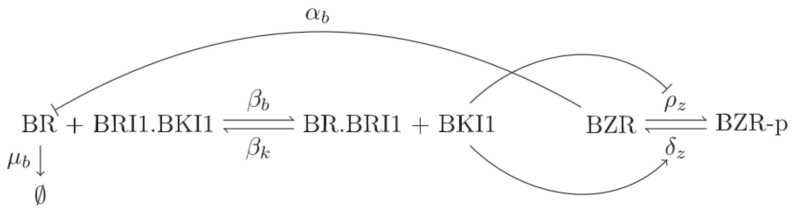

Figure 8.1: Model of BR-regulated gene expression by Allen and Ptashnyk (2017). This model comprises the binding of the ligand BL to the receptor, which releases BKI1 from the complex. The amount of free BKI1 is then taken as output for the signaling pathway that affects BR-regulated gene expression. Figure from [41]

considering ligand synthesis and degradation, ligand binding to the receptor and release of the inhibitor BKI1, ligand dissociation from the receptor complex and binding of the inhibitor (Fig. 8.1). The dephosphorylation and activation of the transcription factor BZR is catalyzed by BKI1 in the model, a stand in for the actual signaling cascade.

The model parameters were, if no experimentally determined parameters were available, fitted to experimental data of relative gene expression. The model, while able to describe the experimental gene expression data, was not tested by generating a model prediction and testing it by additional experimental data. Instead, model validation was seen as parameter estimation to experimental data. This greatly reduces the informative value of the model, as this final test for model quality is missing.

An exploration of the parameter space of the ODE model showed that the system is in principle capable of oscillations [41], which affirms the results of the logic based model [36]. Furthermore, a coupled ODE-PDE model considers the spatial dynamics of BR, the inhibitor BKI1 and phosphorylated BZR along the distance between plasma membrane and nucleus. This model exhibits oscillations with a reduced frequency but increased amplitude, even for parameterizations where the ODE model no longer oscillates [41]. Surprisingly, this model does not comprise receptor internalization [213], which has been shown to increase the response of BR-regulated gene expression [214]. Especially, in the case of the coupled ODE-PDE model, analyzing the spatial distribution of the internalized receptor would have been a highly interesting aspect to the model.

8.4 Root Model

As BRs also induce cell elongation, I expanded the ODE model described in Chapter 6 to include a description of cell elongation. Here, I linked the acidification of the cell wall to cell elongation. This ODE model I then combined with an agent-based representation

of the root tip creating a multi-scale model of the organ. Currently, the multi-scale model is only a simplified and reduced version of the root tip: It comprises only the elongation behavior of an epidermis cell and describes the cell elongation up to a length of 25 µm.
There are several reasons for the latter limitation. While the ODE model is capable of describing the elongation of an epidermis cell from the meristematic zone to the maturation zone, this is beyond the current capabilities of the ABM. In particular, the biomechanical model will need to be adjusted at several points to accommodate the forces generated by the fast elongation rates in the elongation zone and the beginning of maturation zone [7] (see section 8.4.1). Furthermore, a stabilizing framework needs to be provided to maintain the shape of the root during simulations.
Interestingly, agent-based modeling has already been applied to study the regulatory mechanisms of growth in plant roots [219]. In this study, the author tested different regulatory mechanisms with respect to their capability of reproducing the experimentally observed growth behavior [7]. This model model was constructed in VirtualLeaf [108, 109] comprises rules for cell growth, cell division and the cellular transition between the different root zones [7]. An additional example of agent-based models in VirtualLeaf concerns tissue patterning in growth [108].
Unfortunately, VirtualLeaf does not support the integration of detailed intracellular ODE models. This aspect is currently reserved to EPISIM, the agent-based modeling platform used in this thesis [53, 54, 110], and CompuCell3D [220], which uses the BionetSolver to integrate any number of ODE models [221]. However, CompuCell3D uses lattice-based modeling, which models processes such as migration, cell division and cell death as jump-type processes [34].

8.4.1 Biomechanical Model

For this relatively simplistic agent-based model, Erika Tsingos and I adapted an existing center-based biomechanical 2D model implementation in EPISIM to the *A. thaliana* root. However, center-based modeling has the disadvantage that large deviations from a spherical or ellipsoid shape are not sufficiently supported [34]. Considering plant cells have a cuboid shape, where the cell length can exceed the cell width quite drastically, this is an issue. To address this, the definition of the interaction area between ellipsoid cells has already been adjusted to mitigate the effects of cells deviating from a circular shape [110]. Nonetheless, ideally the next step in refining the biomechanical model would be to switch from the center-based model to a vertex-based model, a subclass of deformable cell models that is used for example by the plant-specific agent-based modeling platform VirtualLeaf [108, 109].
Deformable cell models have the advantage that cells are not only defined by their center, width and height but also by the actual surface area of the membrane [34]. Generally, the membrane area is segmented into triangles, for which affecting forces are calculated [34]. Vertex models are a special case, where the cell surface area is instead defined by polygonal tesselation [34]. This not only allows for a more realistic representation of cell

shapes, but also for a more realistic computation of forces between cells. The latter is quite important in thightly packed tissue, which is the point where center-based biomechanical models run into problems [34]. A vertex-based approach further limits the number of cells that can be computed. Center-based biomechanical model can compute up to 10^6 cells reliably in contrast to around 1000 cells in vertex-based modeling approaches [34]. The lower cell number of the vertex-based modeling approach is not problematic as the model of the root tip only comprises a transection along the longitudinal axis. Unfortunately, this biomechanical framework has yet to be implemented into EPISIM at the time of writing this thesis and was not available for modeling. If implementing a vertex-based biomechanical model is not possible, the alternative is to increase the number of simulation steps of the biomechanical model between the simulation steps of the cell behavior model. This will allow the cells to adjust to the repressive forces generated by the cell elongation.
Furthermore, the model is currently lacking a stabilizing framework around the cells of the root tip. Considering the fast elongation rates in the elongation zone [7], the forces between cells can very well push cells apart so strongly that the root shape could potentially deteriorate. Therefore, Erika Tsingos and I plan to define either a layer of dummy cells or a basal lamella around the root tip that prevents the cells from deviating from the shape of the root tip.
Finally, the inclusion of vascular and supporting tissues will also shift the setup of the initial number of cells placed in the simulation space. These cell types have different dimensions [11] and in particular the smaller width of these cell types will shift the initial setup. Also, the number of cells per cell type in each column will vary due to the different cell lengths in the meristematic zone [11]. One way to address this would be to let the biomechanical model reach a steady state before the simulations of the cell behavior model initiate.

8.4.2 Cell Behavior Model

The cell behavior model describes the processes that the cells undergo in each simulation step of the agent-based model. Currently, the processes of cell division, cell elongation and cell death are included.
In plant roots, cells divide in a transverse way so that the new cells are placed along longitudinal axis as illustrated by von Wangenheim *et al.* (2017) [147]. This is in fact represented in the model: The daughter cell is placed slightly above the mother cell to ensure that the root expands along the y-axis. At the moment, only one layer of dividing cells is included in the model. However, experiments show that there are several layers of dividing cells [7, 147]. Adding this to the cell behavior model will also increase the numbers of cells in the initial setup, which has to be coded into the biomechanical model.
Another detail that needs to be integrated into the cell behavior model is the fact that cell division halves the volume of the mother cell. Currently, a mother cell produces a daughter cell of $8\,\mu\mathrm{m}$ length without loosing any of its own volume. It might prove necessary to include a criterion for the minimal cell length of the mother cell, at which cell division is allowed to occur.

Currently, cell division is modeled as a stochastic process (see p. 106). In the simulations of the agent-based model, this can result in a non-uniform distribution of cell division (Fig. 7.15 A and B). In turn, this leads to differing numbers of cells in the individual columns, which would result in very different elongation rates for these cell columns at a longer time-scale [7]. While computational modeling has shown that cell elongation can cope with small and short-term differences in the longitudinal strain rate [219], the behavior of the agent-based model would violate the "Uniform Longitudinal Strain Rule" formulated by the authors of that study [219]. Therefore, a change from a stochastic to a deterministic mechanism is necessary to represent the cell division observed by von Wangenheim *et al.* (2017) [147].
Finally, while the cell behavior model already contains three cell types, this number has to be expanded. Currently, the model comprises columella cells, which only exist to represent the shape of the root cap, one layer of dividing cells, which will have to be greatly adjusted, and the elongating epidermis cell type. In order for the agent-based model to represent an accurate depiction of the *A. thaliana* root, the other cell types for vascular and supporting tissue will have to be included in the model. This means that different initial cell dimensions will have to be defined for each cell type and the submodel for the color code will have to be adjusted.

8.4.3 ODE Model for BR-Induced Cell Elongation

Without my work on the multi-compartment rate laws and especially processes that include the membrane either as compartment or as interaction area, this model would not have been possible. By including growth as a process in the ODE model all compartment volumes change constantly throughout the simulation. This would make the adjustment of parameters, which I describe in chapter 4, very complicated and error prone if not completely unfeasible.
The ODE model currently describes only the elongation behavior of an epidermis cell as this was the cell type with the most data available. In order for the root model to be a realistic representation of the organ, the other cell types forming vascular and supportive tissue have to be included. As these cell types all have different final cell lengths [11], I have to adjust the parameters for cell elongation for each cell type. In the end, this means that there will be one ODE model per cell type that describes the elongation pattern of that particular cell type.
Until then, there are some aspects of the ODE model that need to be revised and considered. The ODE model describing BR-induced cell elongation needs to contain reactions that describe the synthesis of the signaling components. Otherwise, the continued cell elongation would cause the model species to dilute until the signaling pathway is no longer active. For the most part, including protein synthesis is a relatively simple process of producing new proteins proportional to the newly created membrane area and the respective number of $\text{molecules per } \mu m^2$. This description works for the receptor BRI1, the co-receptors BAK1 and BIR3, as well as the negative regulators BKI1 and BIK1.

Only in the case of the ATPases AHA1 and AHA2 as well as the AHA C-terminus, the synthesis of proteins required a more careful description as the expression levels along the root. Here, I used a logistic function to increase the expression levels from the low meristematic concentration to the higher levels in the elongation and maturation zones. Since the position of the cell along the root zones is not described in the ODE model, I used the cell length instead to determine the expression level of AHA1 and AHA2. As I have shown in Fig. 7.7, the actual concentration of the ATPases is not identical to what should be and instead underestimates the concentration of both ATPases and ATPase C-terminus.
This description of the variable levels of AHA1 and AHA2 means that while I have the correct concentration of the proton pumps at the start of the simulations, this is no longer the case once the BR-induced cell elongation begins. As the cell elongates in the model, protein synthesis occurs proportional to the newly created membrane area. It does not compensate for the already existing membrane area with the lower ATPase concentration. This means that the longer a simulation runs, the more the actual concentration in the model deviates from where it should be according to the description of the initial concentration.
While most of the remaining concentration changes are minor, there is one species where the concentration changes dramatically from elongation to maturation zone: The density of the receptor BRI1 changes from $11\,\text{molecules per}\,\mu\text{m}^2$ in the elongation zone to $2\,\text{molecules per}\,\mu\text{m}^2$ in the maturation zone [11]. The inclusion of this fact might make the inhibition of cell elongation by the current cell length obsolete.
Currently, there is no description of cell age or an inhibition of cell elongation due to too quick elongation rates. *In planta*, cell elongation is limited by the cell's capability of producing new cell wall components. Including one of these mechanisms in the model can help to refine the model's response to higher BL concentrations and the lack of any hormone in the model.
To be precise, the currently used dose of $10\,\text{nM}$ BL already shows some inhibitory effect on root growth [11]. The model is not able to represent that and instead shows the normal elongation behavior observed at physiological concentrations around $0.1\,\text{nM}$ to $1\,\text{nM}$ BL. Here, fitting the model to the planned measurements of the extracellular pH at lower BL concentrations can yield a more realistic model behavior.
Also, the model shows no elongation behavior during the first $24\,\text{h}$ of simulation as long as the hormone is absent. However, it is theoretically possible that the basal elongation rate will slowly increase the concentration of AHA1 and AHA2 such that the model will at some point show cell elongation, which is not the case in the actual plant if BR signaling is impaired. A description of cell age or distance from the root tip in terms of cell layers can prevent this from happening.

9 | Conclusions

It was the aim of this thesis to analyze the initiation and regulation of the fast BR response as well as its role in cell elongation by integrative computational modeling. Throughout this thesis, I studied the fast BR response on several different scales. For one, I specified the role of the negative regulator BIR3 by molecular modeling. Secondly, I employed an ODE model of the fast response pathway to study the pathway's behavior in different root zones and determine important model components. Lastly, I combined an agent-based model of the root tip with an ODE model describing the BR-induced cell elongation of an epidermis cell.

In addition to analyzing the fast BR response pathway, I also investigated how changes in cell morphology affect the behavior of ODE models, where different approaches to describing multi-compartment processes have been implemented (Chapter 4, pp. 31). Here, I show that depending on the modeled system it can actually be crucial to include the interaction area between the compartments in the model. In particular, this is the case in the different root zones, where cell size and shape change fundamentally, the model behavior changes a lot depending on the modeling approach.

Using molecular modeling I was able to compute potential complexes between the cytoplasmic domains of the negative regulator BIR3, the receptor BRI1 and the co-receptor BAK1 (Chapter 5, pp. 49). First, I demonstrated that BRI1 and BAK1 can interact based on their cytoplasmic domains alone. While this complex is energetically unfavorable, it carries the risk of unwanted transphosphorylation events occurring. Furthermore, the computational analysis showed that BIR3 can interact with BAK1 and BRI1. Here, the interaction between BIR3 and BAK1 is far more favorable compared to the one between BIR3 and BRI1 as well as between BRI1 and BAK1. As the interaction surface between BIR3 and BAK1 includes the catalytic domain and the activation loop of BAK1, the co-receptor is unable to participate in BR signaling while interacting with BIR3. This sheds light into the phenotype of BIR3 overexpressing *A. thaliana* plants, which resemble *bri1-/-* mutants. Here, the concentration of BIR3 is so high that the addition of the hormone is not enough to induce the interaction bewteen receptor and co-receptor and to overcome the energetically more favorable interaction between BIR3 and BAK1. Finally, the docking analyses revealed that a trimeric complex consisting of all three proteins can exist *per se*. This, in turn, would provide a mechanism for cells to respond almost immediately to BR stimulation as the proteins would only need to change their orientation within the complex.

To model the fast BR response on a cellular scale, I built a model consisting of ODEs in COPASI (Chapter 6, pp. 71). Here, I ensured that the compartimental information was

included correctly, as most proteins involved in the fast BR are located in the plasma membrane and one early response to BRs is the hydration of the cell wall [14]. To account for parameter non-identifiability, I generated a model ensemble of 50 independent model parameterizations. The sensitivity analysis of the membrane potential revealed that the ATPases AHA1 and AHA2 are crucial for the model response to hormone stimulation. In combination with the protein quantification data by Nina Glöckner, this led us to the hypothesis that the cells' responsiveness to BR stimulation is mediated by AHA expression levels. To test this hypothesis, we predicted the signaling response in the meristematic zone, where AHA expression is much lower. The *in silico* predictions showed the model's response is indeed much reduced. We validated this experimentally by MIFE measurements as well as pH measurements by fluorescence microscopy. Last, I validated the model's behavior in a *bir3* deletion mutant, where the behavior resembles the one of the wild-type, which fits the experimental observations.

Finally, I expanded this ODE model to include cell elongation and integrated it into an agent-based representation of the root tip (Chapter 7, pp. 101). This model currently only describes the behavior of one cell type and only models cell elongation up to a cell length of 25 µm. In order for this multi-scale model to be a realistic representation of the root, other cell types have to be included in the simulations. Furthermore, the simulations will have to be extended to comprise the final cell number and to model cell elongation to the final cell length. Once finished, this model will represent a poweful tool for visualizing and studying BR-induced cell elongation *in silico*.

10 | Future Prospects

The computational modeling presented in this thesis has helped in understanding the initiation and regulation of the fast BR response pathway. It has also raised new areas to study.

For one, BRs are not the only hormones that induces cell elongation by activating the H^+ P-type ATPases AHA1 and AHA2. Ladwig *et al.* (2015) discovered that phytosulfokine activate a signaling module in the plasma membrane by *A. thalina* that includes the co-receptor BAK1 as well as the H^+ P-type ATPases AHA1 and AHA2 [71]. This raises the questions of how specificity is achieved between the two signaling pathways and if they might act synergistically.

Here, several modeling approaches might provide useful information: For one, structural modeling could be used to see how the phytosulfokine receptor 1 (PSKR1) cytoplasmic domain can interact with the co-receptor BAK1. Furthermore, an ODE model of this signaling module can provide insight into how the proteins act in this signaling pathway. This model can later be combined with the model of the fast BR response pathway to study the combined response of both pathways.

There is also evidence that both signaling pathways include a cation channel [71]. Cyclic nucleotide gated channel 17 (CNGC17) is hypothesized to form a cation-transporting unit with the ATPases AHA1 and AHA2 [71] and acts downstream of the receptors [71]. This channel will have to be included in the models of these pathways to analyze the specific and synergistic effects of both signaling pathways.

Until then, the ODE model of the fast BR response can still be improved by using long-term pH measurements in response to hormone stimulation. This will provide important information on the less immediate effects of BR stimulation and can give insight into signal termination. Currently, this information is only included by the inhibitory auto-phosphorylation of the receptor BRI1 that occurs on an extremely slow time-scale [79].

For the elongating cell model, this information will also be important as the simulations are much longer for this model. Here, it would also be interesting if cell wall integrity signaling can be integrated. *In planta*, cell wall integrity signaling is intertwined with BR signaling *via* the receptor-like protein 44 (RLP44) [222]. RLP44 presumably activates BR signaling by directly interacting with BAK1 to prevent a loss of cell wall integrity [223].

Furthermore, BR signaling activity has a negative effect on the expression of the receptor BRI1 [82]. This could actually be an important aspect to consider in the elongating cell model as the model transitions from the meristematic zone through the elongation zone to the maturation zone. During this time the receptor concentration changes from 12 and

11 molecules per μm^2 in meristematic and elongation zone to 2 molecules per μm^2 in the maturation zone and the rest of the root [11]. While the effect of the change in expression levels does not impact the short term behavior of the ODE mode, it is important to consider this effect in the ODE model describing BR-induced cell elongation.

Improving the ODE model describing BR-induced cell elongation will also improve the ABM of the root tip, as this model is used to integrate the physiological induction of cell elongation. However, the ODE model currently describes the elongation behavior of only one cell type: an epidermis cell. The other cell types are not yet represented in either the ODE model or the ABM. This means that in order for the multi-scale model of the elongating root tip to be a realistic representation of that organ, the different cell types need to be integrated.

As the ODE model is quite responsive to changes in compartment size and particle numbers, integrating the different cell types requires careful adjustment of the cell elongation parameters. Finally, this means that one ODE model per cell type will be linked to the CBM in the mutli-scale model. There, new cell types will have to be created with specific division rates to account for the different final cell lengths of each cell type. Without specific cell division rates the tissue would grow unevenly, which is not the case in wild-type *A. thaliana* roots, unless it is in response to a stimulus, i.e. a change in root orientation.

Potentially, changing the biomechanical model from a center-based to a vertex-based approach will improve the biomechanical representation of the forces between the cells in the root. Center-based approaches contain a pair-wise description of the forces between cells. This can generate artifacts at high cell densities [34]. Considering the fast elongation rates in the root [7], this can indeed create problems when simulating the quickly elongating root cells. Therefore, Erika Tsingos and I are looking into integrating a vertex-based approach in EPISIM. Vertex-based models are a subclass of deformable cell models [34]. Deformable cell models include a description of the cell boundaries, which can be used to approximate the cell surface [34]. Vertex-based models use polygonal tesselation to describe the cell boundaries, which allows for a more precise description of forces between cells [34].

To ensure that the ABM keeps the shape of the root, either dummy cells or a different kind of boundary needs to be introduced. Otherwise, the forces created by cell elongation and cell division will in the end lead to tissue disorganization due to the strong repulsive forces.

Finally, it might be interesting and worthwhile to build a spatial model of the fast BR response. Bücherl *et al.* (2017) showed that the BRI1 receptor occurs in distinct membrane nano-domains [224]. Especially considering that PSKR1 receptor has a similar function, it would be interesting to find out if these modules occur in the same nano-domains. If that is not the case, this spatial aspect has to be considered in any computational model that considers both signaling pathways.

A different project of the CRC 1101 for specificity encoding in plants built a versatile microscope, that allows for single molecule tracking. Currently, this set-up is being used to determine the diffusional constants of membrane proteins tagged to fluorescent proteins. These measurements allow the distinction between freely diffusing proteins, actively trans-

ported proteins and proteins that are kept in place. It also allows for the distinction of the nano-domains that have been discovered recently [224]. With this information a detailed model consisting of partial differential equations can be built. This could also shed light into the double role of the phosphatase PP2A that inactivates BR signaling on the level of the receptor BRI1 [80, 81] but activates it by promoting the dephosphorylation of the transcription factors BES1/BZR1 that can then diffuse into the nucleus and affect gene-expression [87].

11 | Acknowledgements

While working on my PhD, I have had the opportunity to work with and learn from many people. Most of all, I appreciate the opportunity to work on such an interesting project. I am deeply grateful to my supervisor Prof. Dr. Ursula Kummer for the support, the opportunity to grow and learn. I am also grateful to my second supervisor Prof. Dr. Karin Schumacher, who provided a different perspective to the project and input during the last years. I would also like to thank the other members of my thesis advisory team, Dr. Katrin Hübner and Dr. Sven Sahle, who were always available for discussion and feedback.
This work would not have been possible without the work done by the experimental collaborators at the University of Tübingen. Particularly, Nina Glöckner and Dr. Friederike Wanke in the research group of Prof. Dr. Klaus Harter did a lot of experiments and contributed a large part to this thesis. Furthermore, the support by Klaus Harter was invaluable as he was always willing to discuss new experiments and new topics to address with computational modeling. In addition, this project was supported by Sarina Schulze and Dr. Birgit Kemmerling at the University of Tübingen, who helped by providing information on the negative regulator BIR3.
Furthermore, I thank the Schmeil Foundation (Heidelberg) for their support during my PhD. As this project was part of the CRC1101 for specificity encoding in plants, I thank the German Research Foundation (DFG) for funding. I am also grateful for the support of the Heidelberg Graduate School "Mathematical and Computational Methods for the Sciences".
I have also learned a lot from the discussions with my colleagues. Dr. Anna Feldman-Salit first raised the possibility of using structural modeling to specify the role of the negative regulator. My work on the multi-compartment rate laws together with Pascal Holzheu has advanced my understanding of multi-compartment processes significantly. Erika Tsingos and I have worked in close collaboration during the development of the biomechanical model and will continue to do so to refine the biomechanical description of the root tip.
Finally, for coping with my craziness and stress, I want to thank my partner, my friends and my family for their unwavering support and understanding. Thank you.

12 | Abbreviations

ABM Agent-based model; used to model the emergent behavior of independent cellular agents.

ABPS Adaptive Poisson-Boltzman Server; used to compute the surface electrostatic potential.

AHA1/2 H^+ P-type ATPases.

ANOVA ANalysis of VAriance; statistical method to determine the significance of similar measurements.

B-Factor Measure of how much atoms fluctuate around their average position in an experimentally determined protein structure; values depend on structure resolution and temperature.

BAK1 BRI1-associated kinase; acts as a co-receptor to BRI1 in the fast BR response pathway.

BES1 BRI1-ems-surpressor 1; transcription factor of BR-regulated gene-expression.

BIK1 Botrytis-induced kinase 1; negative regulator of the receptor BRI1.

BIR3 BAK1-interacting receptor 3; inactive kinase that regulates BAK1 activity in BR signaling.

BKI1 BRI1 kinase inhibitor; negative regulator of the receptor BRI1.

BL Brassinolide; biologically most active form of brassinosteroids.

BR Brassinosteroid; plant steroid hormone that regulates several growth and development processes.

BRI1 Brassinosteroid insensitive 1; receptor of BR at the cell surface.

Brz Brassinazole; inhibitor of BR synthesis; needs to be applied for several days to be effective.

BRZ1 Brassinazole-resistant 1; transcription factor of BR-regulated gene-expression.

CBM Cell behavior model; element of an ABM; contains the behavior rules for the cellular agents.

COPASI COmplex PAthway SImulator; software for ODE modeling of biochemical pathways.

EPISIM Agent-based modeling platform developed by Sütterlin *et al.* [53, 54, 110].

FLIM Fluorescence Lifetime Imaging Microscopy

FRET Förster Resonance Energy Transfer.

FRET-FLIM Experimental technique that measures FRET by FLIM.

HPTS 8-Hydroxypyrene-1,3,6-trisulfonic acid trisodium salt; protonated and unprotonated forms of HPTS occur in a pH-dependent manner and can be used to quantify cell wall pH.

IRMSD Interface Root Mean Square Derivation; used by ClusPro to cluster the complexes into up to 30 clusters.

MIFE Microelectrode Ion Flux Estimation; non-invasive technique that measures ion fluxes at the root surface.

MODELLER Software for comparative modeling of protein structures.

ODE Ordinary Differential Equations.

PDB Protein Data Base file; lists all atoms in a protein structure including the position and B-Factor.

PDB2PQR Web server that calculates pqr files based on the pdb file.

PQR File format containing protein residues, their charge and the radius radius.

PROCHECK Software to check protein structure quality based on torsion angles in the amino acid bonds.

QMEAN Qualitative Model Energy ANalysis; scoring method for evaluating the quality of protein structures. Uses the torsion angle over three amino acids, the accessibility to solvent molecules and the interaction potential of Cα atoms.

SBGN Systems Biology Graphical Notation; standard the graphical representation of models.

SBML Systems Biology Markup Language; standard language for the description and annotation of biochemical models.

Bibliography

[1] Steven D Clouse. Brassinosteroid signal transduction: clarifying the pathway from ligand perception to gene expression. *Molecular cell*, 10(5):973–82, nov 2002.

[2] FR Hewitt, T Hough, P O'Neill, JM Sasse, EG Williams, KS Rowan, FR Hewitt, T Hough, P O'Neill, JM Sasse, EG Williams, and KS Rowan. Effect of Brassinolide and other Growth Regulators on the Germination and Growth of Pollen Tubes of Prunus avium using a Multiple Hanging-drop Assay. *Australian Journal of Plant Physiology*, 12(2):201, 1985.

[3] Steven D Clouse, Mark Langford, and Trevor C Mcmorris. A Brassinosteroid-Insensitive Mutant in Arabidopsis thaliana Exhibits Multiple Defects in Growth and Development'. *Plant Physiol*, 11(1):671–678, jul 1996.

[4] Annette Kauschmann, Alison Jessop, Csaba Koncz, Miklos Szekeres, Lotbar Willmitzer, and Thomas Altmann. Genetic evidence for an essential role of brassinosteroids in plant development. *The Plant Journal*, 9(5):701–713, may 1996.

[5] Miklós Szekeres, Kinga Németh, Zsuzsanna Koncz-Kálmán, Jaideep Mathur, Annette Kauschmann, Thomas Altmann, George P Rédei, Ferenc Nagy, Jeff Schell, and Csaba Koncz. Brassinosteroids Rescue the Deficiency of CYP90, a Cytochrome P450, Controlling Cell Elongation and De-etiolation in Arabidopsis. *Cell*, 85(2):171–182, 1996.

[6] Gerard J Bishop and Csaba Koncz. Brassinosteroids and plant steroid hormone signaling. *The Plant cell*, 14 Suppl:S97–S110, 2002.

[7] G T Beemster and T I Baskin. Analysis of cell division and elongation underlying the developmental acceleration of root growth in Arabidopsis thaliana. *Plant physiology*, 116(4):1515–26, apr 1998.

[8] David Rayle and Robert Cleland. Enhancement of Wall Loosening and Elongation by Acid Solutions. *Plant physiology*, 46:250–253, 1970.

[9] Simon Mcqueen-mason, Daniel Durachko, and Daniel Cosgrove. Two Endogenous Proteins That Induce Cell Wall Extension in Plants. *The PLant Cell*, 4(November):1425–1433, 1992.

[10] Olivier Hamant and Jan Traas. The mechanics behind plant development, 2010.

[11] GW van Esse, Adrie H Westphal, Ramya Preethi Surendran, Catherine Albrecht, Boudewijn van Veen, Jan Willem Borst, and Sacco C de Vries. Quantification of the brassinosteroid insensitive1 receptor in planta. *Plant physiology*, 156(4):1691–700, aug 2011.

[12] S J McQueen-Mason and D J Cosgrove. Expansin mode of action on cell walls. Analysis of wall hydrolysis, stress relaxation, and binding. *Plant physiology*, 107(1):87–100, jan 1995.

[13] L Z Wright and D L Rayle. Evidence for a Relationship between H Excretion and Auxin in Shoot Gravitropism. *Plant physiology*, 72(1):99–104, 1983.

[14] Katharina Caesar, Kirstin Elgass, Zhonghua Chen, Peter Huppenberger, Janika Witthöft, Frank Schleifenbaum, Michael R Blatt, Claudia Oecking, and Klaus Harter. A fast brassinolide-regulated response pathway in the plasma membrane of Arabidopsis thaliana. *The Plant journal : for cell and molecular biology*, 66(3):528–40, may 2011.

[15] Janika Witthöft, Katharina Caesar, Kirstin Elgass, Peter Huppenberger, Joachim Kilian, Frank Schleifenbaum, Claudia Oecking, and Klaus Harter. The activation of the Arabidopsis P-ATPase 1 by the brassinosteroid receptor BRI1 is independent of threonine 948 phosphorylation. *Plant Signaling & Behavior*, 6(7):1063–1066, jul 2011.

[16] Janika Witthöft and Klaus Harter. Latest news on Arabidopsis brassinosteroid perception and signaling. *Frontiers in plant science*, 2(October):58, jan 2011.

[17] G. Romani, M. T. Marriè, A. Bonetti, R. Cerana, P. Lado, and E. Marrè. Effects of a brassinosteroid on growth and electrogenic proton extrusion in maize root segments. *Physiologia Plantarum*, 59(4):528–532, dec 1983.

[18] R. Cerana, A. Bonetti, M. T. Marre, G. Romani, P. Lado, and E. Marre. Effects of a brassinosteroid on growth and electrogenic proton extrusion in Azuki bean epicotyls. *Physiologia Plantarum*, 59(1):23–27, sep 1983.

[19] R. Cerana, M. Spelta, A. Bonetti, and P. Lado. On the effects of cholesterol on H+ extrusion and on growth in maize root segments: Comparison with brassinosteroid. *Plant Science*, 38(2):99–105, mar 1985.

[20] N. Bhushan Mandava. Plant-growth promoting brassinosteroids. *Annual Review of Plant Physiology and Plant Molecular Biology*, 39(1):23–52, jun 1988.

[21] Masayuki Katsumi. Interaction of a Brassinosteroid with IAA and GA3 in the Elongation of Cucumber Hypocotyl Sections. *Plant and Cell Physiology*, 26(4):615–625, 1985.

[22] Jianming Li and Joanne Chory. A Putative Leucine-Rich Repeat Receptor Kinase Involved in Brassinosteroid Signal Transduction. *Cell*, 90(5):929–938, 1997.

[23] Jia Li, Jiangqi Wen, Kevin A Lease, Jason T Doke, Frans E Tax, and John C Walker. BAK1, an Arabidopsis LRR Receptor-like Protein Kinase, Interacts with BRI1 and Modulates Brassinosteroid Signaling. *Cell*, 110(2):213–222, 2002.

[24] Kyoung Hee Nam and Jianming Li. BRI1/BAK1, a receptor kinase pair mediating brassinosteroid signaling. *Cell*, 110(2):203–212, 2002.

[25] Yadong Sun, Zhifu Han, Jiao Tang, Zehan Hu, Chengliang Chai, Bin Zhou, and Jijie Chai. Structure reveals that BAK1 as a co-receptor recognizes the BRI1-bound brassinolide. *Cell Research*, 23(11):1326–9, 2013.

[26] Xuelu Wang and Joanne Chory. Brassinosteroids regulate dissociation of BKI1, a negative regulator of BRI1 signaling, from the plasma membrane. *Science (New York, N.Y.)*, 313(5790):1118–1122, aug 2006.

[27] Yvon Jaillais, Michael Hothorn, Youssef Belkhadir, Tsegaye Dabi, Zachary L Nimchuk, Elliot M Meyerowitz, and Joanne Chory. Tyrosine phosphorylation controls brassinosteroid receptor activation by triggering membrane release of its kinase inhibitor. *Genes & development*, 25(3):232–7, feb 2011.

[28] Wenwei Lin, Dongping Lu, Xiquan Gao, Shan Jiang, Xiyu Ma, Zonghua Wang, Tesfaye Mengiste, Ping He, and Libo Shan. Inverse modulation of plant immune and brassinosteroid signaling pathways by the receptor-like cytoplasmic kinase BIK1. *Proceedings of the National Academy of Sciences of the United States of America*, 110(29):12114–9, 2013.

[29] Thierry Halter, Julia Imkampe, Bärbel S Blaum, Thilo Stehle, and Birgit Kemmerling. BIR2 affects complex formation of BAK1 with ligand binding receptors in plant defense. *Plant Signaling & Behavior*, 9(April 2015):1–4, jun 2014.

[30] Julia Imkampe, Thierry Halter, Shuhua Huang, Sarina Schulze, Sara Mazzotta, Nikola Schmidt, Raffaele Manstretta, Sandra Postel, Michael Wierzba, Yong Yang, Walter MAM VanDongen, Mark Stahl, Cyril Zipfel, Michael B. Goshe, Steven Clouse, Sacco C. de Vries, Frans Tax, Xiaofeng Wang, and Birgit Kemmerling. The Arabidopsis Leucine-rich Repeat Receptor Kinase BIR3 Negatively Regulates BAK1 Receptor Complex Formation and Stabilizes BAK1. *The Plant Cell*, page tpc.00376.2017, aug 2017.

[31] Xiaofeng Wang, Uma Kota, Kai He, Kevin Blackburn, Jia Li, Michael B Goshe, Steven C Huber, and Steven D Clouse. Sequential transphosphorylation of the BRI1/BAK1 receptor kinase complex impacts early events in brassinosteroid signaling. *Developmental cell*, 15(2):220–35, aug 2008.

[32] A.A. Kaczor, Damian Bartuzi, T.M. Stępniewski, Dariusz Matosiuk, and Jana Selent. *Protein–protein docking in drug design and discovery*, volume 1762. Humana Press, New York, NY, 2018.

[33] Katrin Hübner, Sven Sahle, and Ursula Kummer. Applications and trends in systems biology in biochemistry. *The FEBS journal*, 278(16):2767–857, aug 2011.

[34] P. Van Liedekerke, M. M. Palm, N. Jagiella, and D. Drasdo. Simulating tissue mechanics with agent-based models: concepts, perspectives and some novel results. *Computational Particle Mechanics*, 2(4):401–444, dec 2015.

[35] Chen Li, Marco Donizelli, Nicolas Rodriguez, Harish Dharuri, Lukas Endler, Vijayalakshmi Chelliah, Lu Li, Enuo He, Arnaud Henry, Melanie I Stefan, Jacky L Snoep, Michael Hucka, Nicolas Le Novère, and Camille Laibe. BioModels Database: An enhanced, curated and annotated resource for published quantitative kinetic models. *BMC Systems Biology*, 4(1):92, jun 2010.

[36] Martial Sankar, Karen S. Osmont, Jakub Rolcik, Bojan Gujas, Danuse Tarkowska, Miroslav Strnad, Ioannis Xenarios, and Christian S. Hardtke. A qualitative continuous model of cellular auxin and brassinosteroid signaling and their crosstalk. *Bioinformatics*, 27(10):1404–1412, may 2011.

[37] Josep Vilarrasa-Blasi, Mary-Paz González-García, David Frigola, Norma Fàbregas, Konstantinos G. Alexiou, Nuria López-Bigas, Susana Rivas, Alain Jauneau, Jan U. Lohmann, Philip N. Benfey, Marta Ibañes, and Ana I. Caño-Delgado. Regulation of Plant Stem Cell Quiescence by a Brassinosteroid Signaling Module. *Developmental Cell*, 30(1):36–47, jul 2014.

[38] G Wilma van Esse, Simon van Mourik, Hans Stigter, Colette a ten Hove, Jaap Molenaar, and Sacco C de Vries. A mathematical model for BRASSINOSTEROID INSENSITIVE1-mediated signaling in root growth and hypocotyl elongation. *Plant physiology*, 160(1):523–32, sep 2012.

[39] G Wilma van Esse, Klaus Harter, and Sacco C de Vries. Computational modelling of the BRI1 receptor system. *Plant, cell & environment*, 36(9):1728–37, sep 2013.

[40] Wilma van Esse, Simon van Mourik, Catherine Albrecht, Jelle van Leeuwen, and Sacco de Vries. A mathematical model for the coreceptors SOMATIC EMBRYOGENESIS RECEPTOR-LIKE KINASE1 and SOMATIC EMBRYOGENESIS RECEPTOR-LIKE KINASE3 in BRASSINOSTEROID INSENSITIVE1-mediated signaling. *Plant physiology*, 163(3):1472–81, nov 2013.

[41] Henry R. Allen and Mariya Ptashnyk. Mathematical modelling and analysis of the brassinosteroid and gibberellin signalling pathways and their interactions. *Journal of Theoretical Biology*, 432:109–131, nov 2017.

[42] Ji She, Zhifu Han, Tae-Wuk Kim, Jinjing Wang, Wei Cheng, Junbiao Chang, Shuai Shi, Jiawei Wang, Maojun Yang, Zhi-Yong Wang, and Jijie Chai. Structural insight into brassinosteroid perception by BRI1. *Nature*, 474(7352):472–6, jun 2011.

[43] Michael Hothorn, Youssef Belkhadir, Marlene Dreux, Tsegaye Dabi, Joseph. P. Noel, Ian A. Wilson, and Joanne Chory. Structural basis of steroid hormone perception by the receptor kinase BRI1. *Nature*, 474(7352):467–472, jun 2011.

[44] Julia Santiago, Christine Henzler, and Michael Hothorn. Molecular mechanism for plant steroid receptor activation by somatic embryogenesis co-receptor kinases. *Science (New York, N.Y.)*, 341(2013):889–92, 2013.

[45] Ulrich Hohmann, Julia Santiago, Joël Nicolet, Vilde Olsson, Fabio M Spiga, Ludwig A. Hothorn, Melinka A Butenko, and Michael Hothorn. Mechanistic basis for the activation of plant membrane receptor kinases by SERK-family coreceptors. *Proceedings of the National Academy of Sciences*, 115(13):201714972, mar 2018.

[46] Thierry Halter, Julia Imkampe, Sara Mazzotta, Michael Wierzba, Sandra Postel, Christoph Bücherl, Christian Kiefer, Mark Stahl, Delphine Chinchilla, Xiaofeng Wang, Thorsten Nürnberger, Cyril Zipfel, Steven Clouse, Jan Willem Borst, Sjef Boeren, Sacco C de Vries, Frans Tax, and Birgit Kemmerling. The leucine-rich repeat receptor kinase BIR2 is a negative regulator of BAK1 in plant immunity. *Current biology : CB*, 24(2):134–43, jan 2014.

[47] Ulrich Hohmann, Joël Nicolet, Andrea Moretti, Ludwig A. Hothorn, and Michael Hothorn. The SERK3 elongated allele defines a role for BIR ectodomains in brassinosteroid signalling, jun 2018.

[48] Xiaofeng Yu, Michael Martinez, Annika L Gable, Jonathan C Fuller, Neil J Bruce, Stefan Richter, and Rebecca C Wade. webSDA: a web server to simulate macromolecular diffusional association. *Nucleic acids research*, 43(W1):W220–4, jul 2015.

[49] Stephen R Comeau, David W Gatchell, Sandor Vajda, and Carlos J Camacho. ClusPro: An automated docking and discrimination method for the prediction of protein complexes. *Bioinformatics*, 20(1):45–50, 2004.

[50] Dima Kozakov, Ryan Brenke, Stephen R Comeau, and Sandor Vajda. PIPER: An FFT-based protein docking program with pairwise potentials. *Proteins: Structure, Function and Genetics*, 65(2):392–406, 2006.

[51] Dima Kozakov, Dmitri Beglov, Tanggis Bohnuud, Scott E Mottarella, Bing Xia, David R Hall, and Sandor Vajda. How good is automated protein docking? *Proteins: Structure, Function and Bioinformatics*, 81(12):2159–2166, 2013.

[52] Dima Kozakov, David R Hall, Bing Xia, Kathryn A Porter, Dzmitry Padhorny, Christine Yueh, Dmitri Beglov, and Sandor Vajda. The ClusPro web server for protein-protein docking. *Nature Protocols*, 12(2):255–278, 2017.

[53] Thomas Sütterlin, Simone Huber, Hartmut Dickhaus, and Niels Grabe. Modeling multi-cellular behavior in epidermal tissue homeostasis via finite state machines in multi-agent systems. *Bioinformatics*, 25(16):2057–2063, aug 2009.

[54] Thomas Sütterlin, Christoph Kolb, Hartmut Dickhaus, Dirk Jäger, and Niels Grabe. Bridging the scales: Semantic integration of quantitative SBML in graphical multi-cellular models and simulations with EPISIM and COPASI. *Bioinformatics*, 29(2):223–229, jan 2013.

[55] Cang-Jin Yang, Chi Zhang, Yang-Ning Lu, Jia-Qi Jin, and Xue-Lu Wang. The mechanisms of brassinosteroids' action: from signal transduction to plant development. *Molecular plant*, 4(4):588–600, jul 2011.

[56] Steven D Clouse. Brassinosteroid signal transduction: from receptor kinase activation to transcriptional networks regulating plant development. *The Plant cell*, 23(4):1219–30, apr 2011.

[57] Ana Caño-Delgado, Yanhai Yin, Cong Yu, Dionne Vafeados, Santiago Mora-García, Jin-Chen Cheng, Kyoung Hee Nam, Jianming Li, and Joanne Chory. BRL1 and BRL3 are novel brassinosteroid receptors that function in vascular differentiation in Arabidopsis. *Development (Cambridge, England)*, 131(21):5341–51, nov 2004.

[58] Norma Fàbregas, Na Li, Sjef Boeren, Tara E Nash, Michael B Goshe, Steven D Clouse, Sacco de Vries, and Ana I Caño-Delgado. The brassinosteroid insensitive1-like3 signalosome complex regulates Arabidopsis root development. *The Plant cell*, 25(9):3377–88, sep 2013.

[59] Toshinori Kinoshita, A Caño-Delgado, and Hideharu Seto. Binding of brassinosteroids to the extracellular domain of plant receptor kinase BRI1. *Nature*, 433(13):167–171, 2005.

[60] Yvon Jaillais, Youssef Belkhadir, Emilia Balsemão-Pires, Jeffery L Dangl, and Joanne Chory. Extracellular leucine-rich repeats as a platform for receptor/coreceptor complex formation. *Proceedings of the National Academy of Sciences of the United States of America*, 108(20):8503–7, may 2011.

[61] Kai He, Xiaoping Gou, Tong Yuan, Honghui Lin, Tadao Asami, Shigeo Yoshida, Scott D Russell, and Jia Li. BAK1 and BKK1 Regulate Brassinosteroid-Dependent Growth and Brassinosteroid-Independent Cell-Death Pathways. *Current Biology*, 17(13):1109–1115, jul 2007.

[62] Thomas W H Liebrand, Harrold A van den Burg, and Matthieu H A J Joosten. Two for all: Receptor-associated kinases SOBIR1 and BAK1. *Trends in Plant Science*, 19(2):123–132, feb 2014.

[63] Catherine Albrecht, Freddy Boutrot, Cécile Segonzac, Benjamin Schwessinger, Selena Gimenez-Ibanez, Delphine Chinchilla, John P Rathjen, Sacco C de Vries, and Cyril Zipfel. Brassinosteroids inhibit pathogen-associated molecular pattern-triggered immune signaling independent of the receptor kinase BAK1. *Proceedings of the National Academy of Sciences of the United States of America*, 109(1):303–8, jan 2012.

[64] Christoph A Bücherl, G Wilma van Esse, Alex Kruis, Jeroen Luchtenberg, Adrie H Westphal, José Aker, Arie van Hoek, Catherine Albrecht, Jan Willem Borst, Sacco C de Vries, G Wilma Van Esse, Alex Kruis, Jeroen Luchtenberg, Adrie H Westphal, José Aker, Arie Van Hoek, Catherine Albrecht, Jan Willem Borst, Sacco C De Vries, G W E, and S C V. Visualization of BRI1 and BAK1 (SERK3) Membrane Receptor Heterooligomers during Brassinosteroid Signaling. *Plant physiology*, 162(August):1911–1925, aug 2013.

[65] Stefan J. Hutten, Danny S. Hamers, Marije Aan Den Toorn, Wilma Van Esse, Antsje Nolles, Christoph A. B??cherl, Sacco C. De Vries, Johannes Hohlbein, and Jan Willem Borst. Visualization of BRI1 and SERK3/BAK1 nanoclusters in Arabidopsis roots. *PLoS ONE*, 12(1):e0169905, jan 2017.

[66] Beilei Lei, Jiyuan Liu, and Xiaojun Yao. Unveiling the molecular mechanism of brassinosteroids: Insights from structure-based molecular modeling studies. *Steroids*, 104:111–117, 2015.

[67] Xuelu Wang, Xiaoqing Li, Jill Meisenhelder, Tony Hunter, Shigeo Yoshida, Tadao Asami, and Joanne Chory. Autoregulation and homodimerization are involved in the activation of the plant steroid receptor BRI1. *Developmental Cell*, 8:855–865, 2005.

[68] Li-Ling Lin, Chia-Lang Hsu, Chia-Wei Hu, Shiao-Yun Ko, Hsu-Liang Hsieh, Hsuan-Cheng Huang, and Hsueh-Fen Juan. Integrating Phosphoproteomics and Bioinformatics to Study Brassinosteroid-Regulated Phosphorylation Dynamics in Arabidopsis. *BMC Genomics*, 16(1):533, 2015.

[69] Yukari Amano, Hiroko Tsubouchi, Hidefumi Shinohara, Mari Ogawa, and Yoshikatsu Matsubayashi. Tyrosine-sulfated glycopeptide involved in cellular proliferation and expansion in Arabidopsis. *Proceedings of the National Academy of Sciences*, 104(46):18333–18338, nov 2007.

[70] Anja T Fuglsang, Astrid Kristensen, Tracey A Cuin, Waltraud X Schulze, Jörgen Persson, Kristina H Thuesen, Cecilie K Ytting, Christian B Oehlenschlæger, Khalid Mahmood, Teis E Sondergaard, Sergey Shabala, and Michael G Palmgren. Receptor kinase-mediated control of primary active proton pumping at the plasma membrane. *The Plant journal : for cell and molecular biology*, 80(6):951–64, dec 2014.

[71] Friederike Ladwig, Renate I. Dahlke, Nils Stührwohldt, Jens Hartmann, Klaus Harter, and Margret Sauter. Phytosulfokine Regulates Growth in Arabidopsis through a Response Module at the Plasma Membrane That Includes CYCLIC NUCLEOTIDE-GATED CHANNEL17, H + -ATPase, and BAK1. *The Plant Cell*, 27(6):1718–1729, jun 2015.

[72] Michael G. Palmgren, Marianne Sommarin, Ramon Serrano, and Christer Larsson. Identification of an autoinhibitory domain in the C-terminal region of the plant plasma membrane H+-ATPase. *Journal of Biological Chemistry*, 266(30):20470–20475, 1991.

[73] B Regenberg, J M Villalba, F C Lanfermeijer, and M G Palmgren. C-terminal deletion analysis of plant plasma membrane H(+)-ATPase: yeast as a model system for solute transport across the plant plasma membrane. *The Plant cell*, 7(10):1655–1666, oct 1995.

[74] L Baekgaard, Anja T. Fuglsang, and Michael G. Palmgren. Regulation of plant plasma membrane H+- and Ca2+-ATPases by terminal domains. *J Bioenerg Biomembr*, 37(6):369–374, dec 2005.

[75] A T Fuglsang, S Visconti, K Drumm, T Jahn, A Stensballe, B Mattei, O N Jensen, P Aducci, and M G Palmgren. Binding of 14-3-3 protein to the plasma membrane H(+)-ATPase AHA2 involves the three C-terminal residues Tyr(946)-Thr-Val and requires phosphorylation of Thr(947). *The Journal of biological chemistry*, 274(51):36774–80, dec 1999.

[76] Fredrik Svennelid, Anne Olsson, Markus Piotrowski, Magnus Rosenquist, Cristian Ottman, Christer Larsson, Claudia Oecking, and Marianne Sommarin. Phosphorylation of Thr-948 at the C Terminus of the Plasma Membrane H + -ATPase Creates a Binding Site for the Regulatory 14-3-3 Protein. *The Plant Cell*, 11(12):2379, dec 1999.

[77] Claudia Oecking, Markus Piotrowski, Jens Hagemeier, and Klaus Hagemann. Topology and target interaction of the fusicoccin-binding 14-3-3 homologs of Commelina communis. *The Plant Journal*, 12(2):441–453, aug 1997.

[78] M Piotrowski, P Morsomme, M Boutry, and C Oecking. Complementation of the Saccharomyces cerevisiae plasma membrane H+-ATPase by a plant H+-ATPase generates a highly abundant fusicoccin binding site. *The Journal of biological chemistry*, 273(45):30018–23, nov 1998.

[79] Man-Ho Oh, Xiaofeng Wang, Steven D Clouse, and Steven C Huber. Deactivation of the Arabidopsis BRASSINOSTEROID INSENSITIVE 1 (BRI1) receptor kinase by autophosphorylation within the glycine-rich loop. *Proceedings of the National Academy of Sciences of the United States of America*, 109(1):327–32, jan 2012.

[80] Guang Wu, Xiuling Wang, Xianbin Li, Yuji Kamiya, Marisa S Otegui, and Joanne Chory. Methylation of a phosphatase specifies dephosphorylation and degradation of activated brassinosteroid receptors. *Science Signaling*, 4(172):ra29, may 2011.

[81] Simone Di Rubbo, Niloufer G Irani, and Eugenia Russinova. PP2A phosphatases: the "on-off" regulatory switches of brassinosteroid signaling. *Science signaling*, 4(172):pe25, jan 2011.

[82] Carsten Müssig, Sabine Fischer, and Thomas Altmann. Brassinosteroid-regulated gene expression. *Plant physiology*, 129(3):1241–51, jul 2002.

[83] Wenqiang Tang, Tae Wuk Kim, Juan A Oses-Prieto, Yu Sun, Zhiping Deng, Shengwei Zhu, Ruiju Wang, Alma L Burlingame, and Zhi Yong Wang. BSKs mediate signal transduction from the receptor kinase BRI1 in Arabidopsis. *Science*, 321(5888):557–560, jul 2008.

[84] Santiago Mora-García, Grégory Vert, Yanhai Yin, Ana Caño-Delgado, Hyeonsook Cheong, and Joanne Chory. Nuclear protein phosphatases with Kelch-repeat domains modulate the response to brassinosteroids in Arabidopsis. *Genes and Development*, 18(4):448–460, feb 2004.

[85] J Li, K H Nam, D Vafeados, and J Chory. BIN2, a new brassinosteroid-insensitive locus in Arabidopsis. *Plant physiology*, 127(1):14–22, sep 2001.

[86] Tae-Wuk Wuk Kim, Shenheng Guan, Yu Ying Sun, Zhiping Deng, Wenqiang Tang, Jian-Xiu Xiu Shang, Yu Ying Sun, Alma L. Burlingame, and Zhi-Yong Yong Wang. Brassinosteroid signal transduction from cell-surface receptor kinases to nuclear transcription factors. *Nature cell biology*, 11(10):1254–60, oct 2009.

[87] Wenqiang Tang, Min Yuan, Ruiju Wang, Yihong Yang, Chunming Wang, Juan A Oses-Prieto, Tae Wuk Kim, Hong Wei Zhou, Zhiping Deng, Srinivas S Gampala, Joshua M Gendron, Else M Jonassen, Cathrine Lillo, Alison DeLong, Alma L Burlingame, Ying Sun, and Zhi Yong Wang. PP2A activates brassinosteroid-responsive gene expression and plant growth by dephosphorylating BZR1. *Nature Cell Biology*, 13(2):124–131, feb 2011.

[88] Teva Vernoux, Géraldine Brunoud, Etienne Farcot, Valérie Morin, Hilde Van den Daele, Jonathan Legrand, Marina Oliva, Pradeep Das, Antoine Larrieu, Darren Wells, Yann Guédon, Lynne Armitage, Franck Picard, Soazig Guyomarc'h, Coralie Cellier, Geraint Parry, Rachil Koumproglou, John H Doonan, Mark Estelle, Christophe Godin, Stefan Kepinski, Malcolm Bennett, Lieven De Veylder, and Jan Traas. The auxin signalling network translates dynamic input into robust patterning at the shoot apex. *Molecular systems biology*, 7(508):508, jan 2011.

[89] Leah R Band, Darren M Wells, John A Fozard, Teodor Ghetiu, Andrew P French, Michael P Pound, Michael H Wilson, Lei Yu, Wenda Li, Hussein I Hijazi, Jaesung Oh, Simon P Pearce, Miguel A Perez-Amador, Jeonga Yun, Eric Kramer, Jose M Alonso, Christophe Godin, Teva Vernoux, T Charlie Hodgman, Tony P Pridmore, Ranjan Swarup, John R King, and Malcolm J Bennett. Systems analysis of auxin transport in the Arabidopsis root apex. *The Plant cell*, 26(3):862–75, mar 2014.

[90] Nicolas Guex and Manuel C. Peitsch. SWISS-MODEL and the Swiss-PdbViewer: An environment for comparative protein modeling. *Electrophoresis*, 18(15):2714–2723, 1997.

[91] Benjamin Webb and Andrej Sali. Comparative Protein Structure Modeling Using MODELLER. *Current Protocols in Bioinformatics*, 47(5.6):5.6.1–5.6.32, sep 2014.

[92] Burkhard Rost. Twilight zone of protein sequence alignments. *Protein Engineering, Design and Selection*, 12(2):85–94, feb 1999.

[93] G. N. Ramachandran, C. Ramakrishnan, and V. Sasisekharan. Stereochemistry of polypeptide chain configurations, jul 1963.

[94] C Ramakrishnan and G. N. Ramachandran. Stereochemical Criteria for Polypeptide and Protein Chain Conformations: II. Allowed Conformations for a Pair of Peptide Units. *Biophysical Journal*, 5:909–933, nov 1965.

[95] R. A. Laskowski, M. W. MacArthur, D. S. Moss, and J. M. Thornton. PROCHECK: a program to check the stereochemical quality of protein structures. *Journal of Applied Crystallography*, 26(2):283–291, apr 1993.

[96] RomanA. Laskowski, J.AntoonC. Rullmann, MalcolmW. MacArthur, Robert Kaptein, and JanetM. Thornton. AQUA and PROCHECK-NMR: Programs for checking the quality of protein structures solved by NMR. *Journal of Biomolecular NMR*, 8(4), dec 1996.

[97] Pascal Benkert, Silvio C. E. Tosatto, and Dietmar Schomburg. QMEAN: A comprehensive scoring function for model quality assessment. *Proteins: Structure, Function, and Bioinformatics*, 71(1):261–277, apr 2008.

[98] Pascal Benkert, Marco Biasini, and Torsten Schwede. Toward the estimation of the absolute quality of individual protein structure models. *Bioinformatics*, 27(3):343–350, feb 2011.

[99] Domantas Motiejunas, Razif Gabdoulline, Ting Wang, Anna Feldman-Salit, Tim Johann, Peter J. Winn, and Rebecca C. Wade. Protein-protein docking by simulating the process of association subject to biochemical constraints. *Proteins: Structure, Function and Genetics*, 71(4):1955–1969, jan 2008.

[100] Ayako Yachie-Kinoshita, Taiko Nishino, Hanae Shimo, Makoto Suematsu, and Masaru Tomita. A Metabolic Model of Human Erythrocytes: Practical Application of the E-Cell Simulation Environment. *Journal of Biomedicine and Biotechnology*, 2010:1–14, 2010.

[101] Dirk Görlich, Michael J Seewald, and Katharina Ribbeck. Characterization of Ran-driven cargo transport and the RanGTPase system by kinetic measurements and computer simulation. *The EMBO journal*, 22(5):1088–100, mar 2003.

[102] Matthew P. Edgington and Marcus J. Tindall. Mathematical Analysis of the Escherichia coli Chemotaxis Signalling Pathway. *Bulletin of Mathematical Biology*, 80(4):758–787, apr 2018.

[103] Jennifer Levering, Ursula Kummer, Konrad Becker, and Sven Sahle. Glycolytic oscillations in a model of a lactic acid bacterium metabolism. *Biophysical Chemistry*, 172:53–60, feb 2013.

[104] Stefan Hoops, Sven Sahle, Ralph Gauges, Christine Lee, Jürgen Pahle, Natalia Simus, Mudita Singhal, Liang Xu, Pedro Mendes, and Ursula Kummer. COPASI–a COmplex PAthway SImulator. *Bioinformatics (Oxford, England)*, 22(24):3067–74, dec 2006.

[105] Wolfram Liebermeister and Edda Klipp. Bringing metabolic networks to life: Convenience rate law and thermodynamic constraints. *Theoretical Biology and Medical Modelling*, 3:41, dec 2006.

[106] Jan-Hendrik S. Hofmeyr. SBML and rate laws for multi-compartment kinetic modelling. personal communication.

[107] M. Hucka, A. Finney, H. M. Sauro, H. Bolouri, J. C. Doyle, H. Kitano, A. P. Arkin, B. J. Bornstein, D. Bray, A. Cornish-Bowden, A. A. Cuellar, S. Dronov, E. D. Gilles, M. Ginkel, V. Gor, I. I. Goryanin, W. J. Hedley, T. C. Hodgman, J. H. Hofmeyr, P. J. Hunter, N. S. Juty, J. L. Kasberger, A. Kremling, U. Kummer, N. Le Novère, L. M. Loew, D. Lucio, P. Mendes, E. Minch, E. D. Mjolsness, Y. Nakayama, M. R. Nelson, P. F. Nielsen, T. Sakurada, J. C. Schaff, B. E. Shapiro, T. S. Shimizu, H. D. Spence, J. Stelling, K. Takahashi, M. Tomita, J. Wagner, and J. Wang. The systems biology markup language (SBML): A medium for representation and exchange of biochemical network models. *Bioinformatics*, 19(4):524–531, mar 2003.

[108] R. M. H. Merks, M. Guravage, D. Inze, and G. T. S. Beemster. VirtualLeaf: An Open-Source Framework for Cell-Based Modeling of Plant Tissue Growth and Development. *PLANT PHYSIOLOGY*, 155(2):656–666, feb 2011.

[109] Roeland M. H. Merks and Michael A. Guravage. Building simulation models of developing plant organs using VirtualLeaf. *Methods in molecular biology (Clifton, N.J.)*, 959:333–352, 2013.

[110] Thomas Sütterlin, Erika Tsingos, Jalil Bensaci, Georgios N. Stamatas, and Niels Grabe. A 3D self-organizing multicellular epidermis model of barrier formation and hydration with realistic cell morphology based on EPISIM. *Scientific Reports*, 7(43472):43472, mar 2017.

[111] Elke Barbez, Kai Dünser, Angelika Gaidora, Thomas Lendl, and Wolfgang Busch. Auxin steers root cell expansion via apoplastic pH regulation in Arabidopsis thaliana. *Proceedings of the National Academy of Sciences*, 114(24):E4884–E4893, jun 2017.

[112] H. M. Berman, John Westbrook, Zukang Feng, Gary Gilliland, T. N. Bhat, Helge Weissig, Ilya N. Shindyalov, and Philip E. Bourne. The protein data bank. *Nucleic acids research*, 28(1):235–242, jan 2000.

[113] Peter W. Rose, Andreas Prlić, Ali Altunkaya, Chunxiao Bi, Anthony R. Bradley, Cole H. Christie, Luigi Di Costanzo, Jose M. Duarte, Shuchismita Dutta, Zukang Feng, Rachel Kramer Green, David S. Goodsell, Brian Hudson, Tara Kalro, Robert

Lowe, Ezra Peisach, Christopher Randle, Alexander S. Rose, Chenghua Shao, Yi Ping Tao, Yana Valasatava, Maria Voigt, John D. Westbrook, Jesse Woo, Huangwang Yang, Jasmine Y. Young, Christine Zardecki, Helen M. Berman, and Stephen K. Burley. The RCSB protein data bank: Integrative view of protein, gene and 3D structural information. *Nucleic Acids Research*, 45(D1):D271–D281, jan 2017.

[114] Eric F. Pettersen, Thomas D. Goddard, Conrad C. Huang, Gregory S. Couch, Daniel M. Greenblatt, Elaine C. Meng, and Thomas E. Ferrin. UCSF Chimera - A visualization system for exploratory research and analysis. *Journal of Computational Chemistry*, 25(13):1605–1612, oct 2004.

[115] Elaine C Meng, Eric F Pettersen, Gregory S Couch, Conrad C Huang, and Thomas E Ferrin. Tools for integrated sequence-structure analysis with UCSF Chimera. *BMC Bioinformatics*, 7(1):339, jul 2006.

[116] S Henikoff and J G Henikoff. Amino acid substitution matrices from protein blocks. *Proceedings of the National Academy of Sciences of the United States of America*, 89(22):10915–9, nov 1992.

[117] Bertil Halle. Flexibility and packing in proteins. *Proceedings of the National Academy of Sciences of the United States of America*, 99(3):1274–1279, feb 2002.

[118] Oliviero Carugo. How large B-factors can be in protein crystal structures. *BMC Bioinformatics*, 19(1):61, feb 2018.

[119] Fabian Sievers, Andreas Wilm, David Dineen, Toby J Gibson, Kevin Karplus, Weizhong Li, Rodrigo Lopez, Hamish McWilliam, Michael Remmert, Johannes Söding, Julie D Thompson, and Desmond G Higgins. Fast, scalable generation of high-quality protein multiple sequence alignments using Clustal Omega. *Molecular systems biology*, 7(1):539, oct 2011.

[120] Hamish McWilliam, Weizhong Li, Mahmut Uludag, Silvano Squizzato, Young Mi Park, Nicola Buso, Andrew Peter Cowley, and Rodrigo Lopez. Analysis Tool Web Services from the EMBL-EBI. *Nucleic acids research*, 41(Web Server issue):W597–600, jul 2013.

[121] Weizhong Li, Andrew Cowley, Mahmut Uludag, Tamer Gur, Hamish McWilliam, Silvano Squizzato, Young Mi Park, Nicola Buso, and Rodrigo Lopez. The EMBL-EBI bioinformatics web and programmatic tools framework. *Nucleic acids research*, 43(W1):W580–4, jul 2015.

[122] Bärbel S. Blaum, Sara Mazzotta, Erik R. Nöldeke, Thierry Halter, Johannes Madlung, Birgit Kemmerling, and Thilo Stehle. Structure of the pseudokinase domain of BIR2, a regulator of BAK1-mediated immune signaling in Arabidopsis. *Journal of Structural Biology*, 186:112–121, 2014.

[123] Daniel Bojar, Jacobo Martinez, Julia Santiago, Vladimir Rybin, Richard Bayliss, and Michael Hothorn. Crystal structures of the phosphorylated BRI1 kinase domain and implications for brassinosteroid signal initiation. *Plant Journal*, 78(1):31–43, apr 2014.

[124] Todd J Dolinsky, Jens E Nielsen, J Andrew McCammon, and Nathan A Baker. PDB2PQR: An automated pipeline for the setup of Poisson-Boltzmann electrostatics calculations. *Nucleic Acids Research*, 32(WEB SERVER ISS.):W665–7, jul 2004.

[125] N. A. Baker, D. Sept, S. Joseph, M. J. Holst, and J. A. McCammon. Electrostatics of nanosystems: Application to microtubules and the ribosome. *Proceedings of the National Academy of Sciences*, 98(18):10037–10041, aug 2001.

[126] Michael Martinez, Neil J. Bruce, Julia Romanowska, Daria B. Kokh, Musa Ozboyaci, Xiaofeng Yu, Mehmet Ali Öztürk, Stefan Richter, and Rebecca C. Wade. SDA 7: A modular and parallel implementation of the simulation of diffusional association software. *Journal of Computational Chemistry*, 36(21):1631–1645, aug 2015.

[127] Razif R. Gabdoulline and Rebecca C. Wade. Brownian Dynamics Simulation of Protein–Protein Diffusional Encounter. *Methods*, 14(3):329–341, mar 1998.

[128] R.R. Gabdoulline and R.C. Wade. Simulation of the diffusional association of barnase and barstar. *Biophysical Journal*, 72(5):1917–1929, may 1997.

[129] R. R. Gabdoulline and R. C. Wade. Effective Charges for Macromolecules in Solvent. *The Journal of Physical Chemistry*, 100(9):3868–3878, jan 1996.

[130] Adrian H Elcock, Razif R Gabdoulline, Rebecca C Wade, and J.Andrew McCammon. Computer simulation of protein-protein association kinetics: acetylcholinesterase-fasciculin. *Journal of Molecular Biology*, 291(1):149–162, sep 1999.

[131] Razif R. Gabdoulline and Rebecca C. Wade. On the Contributions of Diffusion and Thermal Activation to Electron Transfer between Phormidium laminosum Plastocyanin and Cytochrome f : Brownian Dynamics Simulations with Explicit Modeling of Nonpolar Desolvation Interactions and Electron. *Journal of the American Chemical Society*, 131(26):9230–9238, jul 2009.

[132] Stephen R Comeau, David W Gatchell, Sandor Vajda, and Carlos J Camacho. ClusPro: a fully automated algorithm for protein-protein docking. *Nucleic Acids Research*, 32(Web Server):W96–W99, jul 2004.

[133] Schrödinger, LLC. The PyMOL molecular graphics system, version 1.8. November 2015.

[134] Mansour Karimi, Dirk Inzé, and Ann Depicker. GATEWAY vectors for Agrobacterium-mediated plant transformation. *Trends in plant science*, 7(5):193–5, may 2002.

[135] A. Bleckmann, S. Weidtkamp-Peters, C. A.M. Seidel, and R. Simon. Stem Cell Signaling in Arabidopsis Requires CRN to Localize CLV2 to the Plasma Membrane. *PLANT PHYSIOLOGY*, 152(1):166–176, jan 2010.

[136] R. Eberhart and J. Kennedy. A new optimizer using particle swarm theory. In *MHS'95. Proceedings of the Sixth International Symposium on Micro Machine and Human Science*, pages 39–43. IEEE, 1995.

[137] Robert Hooke and T A Jeeves. "Direct Search" Solution of Numerical and Statistical Problems*. *Journal of the ACM*, 8(2):212–229, 1961.

[138] Thomas Bäck and Hans-Paul Schwefel. An Overview of Evolutionary Algorithms for Parameter Optimization. *Evolutionary Computation*, 1(1):1–23, mar 1993.

[139] T Bäck, D B Fogel, and Z Michalewicz. Handbook of Evolutionary Computation. *Evolutionary Computation*, 2:1–11, jan 1997.

[140] Zbigniew Michalewicz. Evolution strategies and other methods. In *Genetic algorithms+ data structures= evolution programs*, pages 159–177. Springer Berlin Heidelberg, Berlin, Heidelberg, 1996.

[141] Melanie Mitchell. *An introduction to genetic algorithms*. MIT Press, Boston, 1998.

[142] Linda Petzold. Automatic Selection of Methods for Solving Stiff and Nonstiff Systems of Ordinary Differential Equations. *SIAM Journal on Scientific and Statistical Computing*, 4(1):136–148, mar 1983.

[143] R Development Core Team. *R: A Language and Environment for Statistical Computing*. R Foundation for Statistical Computing, Vienna, Austria, 2008. ISBN 3-900051-07-0.

[144] Caroline A Schneider, Wayne S Rasband, and Kevin W Eliceiri. NIH Image to ImageJ: 25 years of image analysis. *Nature methods*, 9(7):671–5, jul 2012.

[145] Pedro Silva, Reiaz Ul-Rehman, Cláudia Rato, Gian-Pietro Di Sansebastiano, and Rui Malhó. Asymmetric localization of Arabidopsis SYP124 syntaxin at the pollen tube apical and sub-apical zones is involved in tip growth. *BMC Plant Biology*, 10(1):179, aug 2010.

[146] Kisten Sisse Krag Gjetting, Cecilie Karkov Ytting, Alexander Schulz, and Anja Thoe Fuglsang. Live imaging of intra-and extracellular pH in plants using pHusion, a novel genetically encoded biosensor. *Journal of Experimental Botany*, 63(8):3207–3218, may 2012.

[147] Daniel von Wangenheim, Robert Hauschild, Matyáš Fendrych, Vanessa Barone, Eva Benková, and Jiří Friml. Live tracking of moving samples in confocal microscopy for vertically grown roots. *eLife*, 6:e26792, jun 2017.

[148] Thomas Maiwald and Jens Timmer. Dynamical modeling and multi-experiment fitting with PottersWheel. *Bioinformatics*, 24(18):2037–2043, sep 2008.

[149] Susana R Neves, Panayiotis Tsokas, Anamika Sarkar, Elizabeth A Grace, Padmini Rangamani, Stephen M Taubenfeld, Cristina M Alberini, James C Schaff, Robert D Blitzer, Ion I Moraru, and Ravi Iyengar. Cell shape and negative links in regulatory motifs together control spatial information flow in signaling networks. *Cell*, 133(4):666–80, may 2008.

[150] G C Brown and B N Kholodenko. Spatial gradients of cellular phospho-proteins. *FEBS letters*, 457(3):452–4, sep 1999.

[151] Madeleine L Craske, Marc Fivaz, Nizar N Batada, and Tobias Meyer. Spines and neurite branches function as geometric attractors that enhance protein kinase C action. *The Journal of cell biology*, 170(7):1147–58, sep 2005.

[152] Matthew David Onsum, Kit Wong, Paul Herzmark, Henry R Bourne, and Adam Paul Arkin. Morphology matters in immune cell chemotaxis: Membrane asymmetry affects amplification. *Physical Biology*, 3(3):190–199, sep 2006.

[153] Ian C. Schneider, Elizabeth M. Parrish, and Jason M. Haugh. Spatial analysis of 3' phosphoinositide signaling in living fibroblasts, III: Influence of cell morphology and morphological polarity. *Biophysical Journal*, 89(2):1420–1430, aug 2005.

[154] Charles C. Fink, Boris Slepchenko, Ion I. Moraru, James Watras, James C. Schaff, and Leslie M. Loew. An image-based model of calcium waves in differentiated neuroblastoma cells. *Biophysical Journal*, 79(1):163–183, jul 2000.

[155] Jason Meyers, Jennifer Craig, and David J Odde. Potential for control of signaling pathways via cell size and shape. *Current biology : CB*, 16(17):1685–93, sep 2006.

[156] Narat J. Eungdamrong and Ravi Iyengar. Compartment-Specific Feedback Loop and Regulated Trafficking Can Result in Sustained Activation of Ras at the Golgi. *Biophysical Journal*, 92(3):808–815, feb 2007.

[157] Nicholas Hernjak, Boris M Slepchenko, Kathleen Fernald, Charles C Fink, Dale Fortin, Ion I Moraru, James Watras, and Leslie M Loew. Modeling and analysis of calcium signaling events leading to long-term depression in cerebellar Purkinje cells. *Biophysical journal*, 89(6):3790–806, dec 2005.

[158] Björn H Junker, Christian Klukas, and Falk Schreiber. VANTED: A system for advanced data analysis and visualization in the context of biological networks. *BMC Bioinformatics*, 7(1):109, 2006.

[159] Nicolas Le Novère, Michael Hucka, Huaiyu Mi, Stuart Moodie, Falk Schreiber, Anatoly Sorokin, Emek Demir, Katja Wegner, Mirit I Aladjem, Sarala M Wimalaratne,

Frank T Bergman, Ralph Gauges, Peter Ghazal, Hideya Kawaji, Lu Li, Yukiko Matsuoka, Alice Villéger, Sarah E Boyd, Laurence Calzone, Melanie Courtot, Ugur Dogrusoz, Tom C Freeman, Akira Funahashi, Samik Ghosh, Akiya Jouraku, Sohyoung Kim, Fedor Kolpakov, Augustin Luna, Sven Sahle, Esther Schmidt, Steven Watterson, Guanming Wu, Igor Goryanin, Douglas B Kell, Chris Sander, Herbert Sauro, Jacky L Snoep, Kurt Kohn, and Hiroaki Kitano. The Systems Biology Graphical Notation. *Nature Biotechnology*, 27(8):735–741, aug 2009.

[160] M. Geisler, B. Wang, and J. Zhu. Auxin transport during root gravitropism: Transporters and techniques, jan 2014.

[161] L Taiz. The plant vacuole. *Journal of Experimental Biology*, 172(6):113–122, 1992.

[162] Boris N Kholodenko, Oleg V Demin, Gisela Moehren, and Jan B Hoek. Quantification of short term signaling by the epidermal growth factor receptor. *Journal of Biological Chemistry*, 274(42):30169–30181, oct 1999.

[163] K S Brown, C C Hill, G A Calero, C R Myers, K H Lee, J P Sethna, and R A Cerione. The statistical mechanics of complex signaling networks: Nerve growth factor signaling. *Physical Biology*, 1(3):184–195, oct 2004.

[164] Leonid E Fridlyand, Natalia Tamarina, and Louis H Philipson. Modeling of Ca2+ flux in pancreatic beta-cells: role of the plasma membrane and intracellular stores. *American journal of physiology. Endocrinology and metabolism*, 285(1):E138–54, jul 2003.

[165] Alan Bush, Gustavo Vasen, Andreas Constantinou, Paula Dunayevich, Inés Lucía Patop, Matías Blaustein, and Alejandro Colman-Lerner. Yeast GPCR signaling reflects the fraction of occupied receptors, not the number. *Molecular systems biology*, 12(12):898, dec 2016.

[166] James Schaff, Charles C Fink, Boris Slepchenko, John H Carson, and Leslie M Loew. A general computational framework for modeling cellular structure and function. *Biophysical Journal*, 73(3):1135–1146, sep 1997.

[167] A Goldbeter. A model for circadian oscillations in the Drosophila period protein (PER). *Proceedings. Biological sciences*, 261(1362):319–24, sep 1995.

[168] Birgit Schoeberl, Claudia Eichler-Jonsson, Ernst Dieter Gilles, and Gertraud Müller. Computational modeling of the dynamics of the MAP kinase cascade activated by surface and internalized EGF receptors. *Nature biotechnology*, 20(4):370–5, apr 2002.

[169] Wayne G Fisher, Pei-Chi Yang, Ram K Medikonduri, and M Saleet Jafri. NFAT and NFkappaB activation in T lymphocytes: a model of differential activation of gene expression. *Annals of biomedical engineering*, 34(11):1712–28, nov 2006.

[170] Narat J Eungdamrong and Ravi Iyengar. Compartment-specific feedback loop and regulated trafficking can result in sustained activation of Ras at the Golgi. *Biophysical journal*, 92(3):808–15, feb 2007.

[171] Bernhard Schmierer, Alexander L Tournier, Paul A Bates, and Caroline S Hill. Mathematical modeling identifies Smad nucleocytoplasmic shuttling as a dynamic signal-interpreting system. *Proceedings of the National Academy of Sciences of the United States of America*, 105(18):6608–13, may 2008.

[172] Takashi Nakakuki, Marc R Birtwistle, Yuko Saeki, Noriko Yumoto, Kaori Ide, Takeshi Nagashima, Lutz Brusch, Babatunde A Ogunnaike, Mariko Okada-Hatakeyama, and Boris N Kholodenko. Ligand-specific c-Fos expression emerges from the spatiotemporal control of ErbB network dynamics. *Cell*, 141(5):884–96, may 2010.

[173] Zhike Zi, Zipei Feng, Douglas A Chapnick, Markus Dahl, Difan Deng, Edda Klipp, Aristidis Moustakas, and Xuedong Liu. Quantitative analysis of transient and sustained transforming growth factor-β signaling dynamics. *Molecular systems biology*, 7(1):492, may 2011.

[174] Garrett Jenkinson and John Goutsias. Thermodynamically consistent model calibration in chemical kinetics. *BMC systems biology*, 5(1):64, may 2011.

[175] Monica Schliemann, Eric Bullinger, Steffen Borchers, Frank Allgöwer, Rolf Findeisen, and Peter Scheurich. Heterogeneity reduces sensitivity of cell death for TNF-stimuli. *BMC systems biology*, 5(1):204, dec 2011.

[176] Graham R Smith and Daryl P Shanley. Computational modelling of the regulation of Insulin signalling by oxidative stress. *BMC systems biology*, 7(1):41, may 2013.

[177] Karen van Eunen, Sereh M J Simons, Albert Gerding, Aycha Bleeker, Gijs den Besten, Catharina M L Touw, Sander M Houten, Bert K Groen, Klaas Krab, Dirk-Jan Reijngoud, and Barbara M Bakker. Biochemical competition makes fatty-acid β-oxidation vulnerable to substrate overload. *PLoS computational biology*, 9(8):e1003186, aug 2013.

[178] Soheil Rastgou Talemi, Therese Jacobson, Vijay Garla, Clara Navarrete, Annemarie Wagner, Markus J Tamás, and Jörg Schaber. Mathematical modelling of arsenic transport, distribution and detoxification processes in yeast. *Molecular microbiology*, 92(6):1343–56, jun 2014.

[179] Veronika Reiterer, Dirk Fey, Walter Kolch, Boris N Kholodenko, and Hesso Farhan. Pseudophosphatase STYX modulates cell-fate decisions and cell migration by spatiotemporal regulation of ERK1/2. *Proceedings of the National Academy of Sciences of the United States of America*, 110(31):E2934–43, jul 2013.

[180] Ayse Koca Caydasi, Maiko Lohel, Gerd Grünert, Peter Dittrich, Gislene Pereira, and Bashar Ibrahim. A dynamical model of the spindle position checkpoint. *Molecular systems biology*, 8:582, may 2012.

[181] Paul Jorgensen, Nicholas P Edgington, Brandt L Schneider, Ivan Rupes, Mike Tyers, and Bruce Futcher. The Size of the Nucleus Increases as Yeast Cells Grow. *Molecular Biology of the Cell*, 18(9):3523–3532, sep 2007.

[182] Jörg Urban, Alexandre Soulard, Alexandre Huber, Soyeon Lippman, Debdyuti Mukhopadhyay, Olivier Deloche, Valeria Wanke, Dorothea Anrather, Gustav Ammerer, Howard Riezman, James R. Broach, Claudio De Virgilio, Michael N. Hall, and Robbie Loewith. Sch9 Is a Major Target of TORC1 in Saccharomyces cerevisiae. *Molecular Cell*, 26(5):663–674, jun 2007.

[183] Christopher Grefen. The split-ubiquitin system for the analysis of three-component interactions. *Methods in Molecular Biology*, 1062:659–678, 2014.

[184] Liming Yan, Yuanyuan Ma, Dan Liu, Xiaochao Wei, Yuna Sun, Xiaoyue Chen, Huadong Zhao, Jingwen Zhou, Zhiyong Wang, Wenqing Shui, and Zhiyong Lou. Structural basis for the impact of phosphorylation on the activation of plant receptor-like kinase BAK1. *Cell research*, 22(8):1304–8, aug 2012.

[185] Wei Cheng, Kathy R. Munkvold, Haishan Gao, Johannes Mathieu, Simon Schwizer, Sha Wang, Yong Bin Yan, Jinjing Wang, Gregory B. Martin, and Jijie Chai. Structural analysis of pseudomonas syringae AvrPtoB bound to host BAK1 reveals two similar kinase-interacting domains in a type III effector. *Cell Host and Microbe*, 10(6):616–626, dec 2011.

[186] Vera Göhre, Thomas Spallek, Heidrun Häweker, Sophia Mersmann, Tobias Mentzel, Thomas Boller, Marta de Torres, John W. Mansfield, and Silke Robatzek. Plant Pattern-Recognition Receptor FLS2 Is Directed for Degradation by the Bacterial Ubiquitin Ligase AvrPtoB. *Current Biology*, 18(23):1824–1832, dec 2008.

[187] Xiaofeng Wang, Michael B Goshe, Erik J Soderblom, Brett S Phinney, Jason A Kuchar, Jia Li, Tadao Asami, Shigeo Yoshida, Steven C Huber, and Steven D Clouse. Identification and Functional Analysis of in Vivo Phosphorylation Sites of the Arabidopsis BRASSINOSTEROID-INSENSITIVE1 Receptor Kinase. *The Plant cell*, 17(June):1685–1703, 2005.

[188] Hye Sup Yun, Young Hee Bae, Yun Ji Lee, Soo Chul Chang, Seong Ki Kim, Jianming Li, and Kyoung Hee Nam. Analysis of phosphorylation of the BRI1/BAK1 complex in arabidopsis reveals amino acid residues critical for receptor formation and activation of BR signaling. *Molecules and Cells*, 27(2):183–190, feb 2009.

[189] Wenfei Wang, Ming Yi Bai, and Zhi Yong Wang. The brassinosteroid signaling network-a paradigm of signal integration. *Current Opinion in Plant Biology*, 21:147–153, 2014.

[190] D. M. Friedrichsen. Brassinosteroid-Insensitive-1 Is a Ubiquitously Expressed Leucine-Rich Repeat Receptor Serine/Threonine Kinase. *PLANT PHYSIOLOGY*, 123(4):1247–1256, aug 2000.

[191] Gwo-Yu Chuang, Dima Kozakov, Ryan Brenke, Stephen R. Comeau, and Sandor Vajda. DARS (Decoys As the Reference State) Potentials for Protein-Protein Docking. *Biophysical Journal*, 95(9):4217–4227, nov 2008.

[192] Ulrich Hohmann, Kelvin Lau, and Michael Hothorn. The Structural Basis of Ligand Perception and Signal Activation by Receptor Kinases. *Annu. Rev. Plant Biol*, 68(9):1–928, 2017.

[193] The UniProt Consortium. UniProt: the universal protein knowledgebase. *Nucleic Acids Research*, 45(D1):D158–D169, jan 2017.

[194] Janna Hastings, Gareth Owen, Adriano Dekker, Marcus Ennis, Namrata Kale, Venkatesh Muthukrishnan, Steve Turner, Neil Swainston, Pedro Mendes, and Christoph Steinbeck. ChEBI in 2016: Improved services and an expanding collection of metabolites. *Nucleic Acids Research*, 44(D1):D1214–D1219, jan 2016.

[195] Debbie Winter, Ben Vinegar, Hardeep Nahal, Ron Ammar, Greg V. Wilson, and Nicholas J. Provart. An "electronic fluorescent pictograph" Browser for exploring and analyzing large-scale biological data sets. *PLoS ONE*, 2(8):e718, aug 2007.

[196] Amie Caroline Scott and N S Allen. Changes in cytosolic pH within Arabidopsis root columella cells play a key role in the early signaling pathway for root gravitropism. *Plant physiology*, 121(4):1291–1298, 1999.

[197] Yu Luo, Stefan Scholl, Anett Doering, Yi Zhang, Niloufer G. Irani, Simone Di Rubbo, Lutz Neumetzler, Praveen Krishnamoorthy, Isabelle Van Houtte, Evelien Mylle, Volker Bischoff, Samantha Vernhettes, Johan Winne, Jiří Friml, York-Dieter Stierhof, Karin Schumacher, Staffan Persson, and Eugenia Russinova. V-ATPase activity in the TGN/EE is required for exocytosis and recycling in Arabidopsis. *Nature Plants*, 1(7):15094, jul 2015.

[198] Zhi-yong Wang, Hideharu Seto, Shozo Fujioka, Shigeo Yoshida, and Joanne Chory. BRI1 is a critical component of a plasma-membrane receptor for plant steroids. *Nature*, 410(MARCH):380–383, 2001.

[199] Jie Wang, Jianjun Jiang, Jue Wang, Lei Chen, Shi-long Fan, Jia-wei Wu, Xuelu Wang, and Zhi-xin Wang. Structural insights into the negative regulation of BRI1 signaling by BRI1-interacting protein BKI1. *Cell research*, 24(11):1–14, 2014.

[200] P. J. White, B. Biskup, J. T. M. Elzenga, U. Homann, G. Thiel, F. Wissing, and F. J. M. Maathuis. Advanced patch-clamp techniques and single-channel analysis. *Journal of Experimental Botany*, 50(Special):1037–1054, jun 1999.

[201] Deyan Luan, Fania Szlam, Kenichi A. Tanaka, Philip S. Barie, and Jeffrey D. Varner. Ensembles of uncertain mathematical models can identify network response to therapeutic interventions. *Molecular BioSystems*, 6(11):2272–2286, nov 2010.

[202] Dorota Focht, Tristan I. Croll, Bjorn P. Pedersen, and Poul Nissen. Improved model of proton pump crystal structure obtained by interactive molecular dynamics flexible fitting expands the mechanistic model for proton translocation in P-type ATPases. *Frontiers in Physiology*, 8(APR):202, apr 2017.

[203] Daniel J Cosgrove. Growth of the plant cell wall. *Nature reviews. Molecular cell biology*, 6(11):850–61, nov 2005.

[204] Christopher Grefen, Petr Obrdlik, and Klaus Harter. The determination of protein-protein interactions by the mating-based split-ubiquitin system (mbSUS). *Methods in Molecular Biology*, 479:217–233, 2009.

[205] Christopher Grefen, Naomi Donald, Kenji Hashimoto, Jörg Kudla, Karin Schumacher, and Michael R. Blatt. A ubiquitin-10 promoter-based vector set for fluorescent protein tagging facilitates temporal stability and native protein distribution in transient and stable expression studies. *Plant Journal*, 64(2):355–365, oct 2010.

[206] Lilach Gilboa, Anja Nohe, Tanja Geissendörfer, Walter Sebald, Yoav I. Henis, and Petra Knaus. Bone Morphogenetic Protein Receptor Complexes on the Surface of Live Cells: A New Oligomerization Mode for Serine/Threonine Kinase Receptors. *Molecular Biology of the Cell*, 11(3):1023–1035, mar 2000.

[207] Takanori Moriki, Hiroko Maruyama, and Ichi N Maruyama. Activation of preformed EGF receptor dimers by ligand-induced rotation of the transmembrane domain. *Journal of Molecular Biology*, 311(5):1011–1026, aug 2001.

[208] Marc Somssich, Qijun Ma, Stefanie Weidtkamp-Peters, Yvonne Stahl, Suren Felekyan, Andrea Bleckmann, Claus A M Seidel, and Rüdiger Simon. Real-time dynamics of peptide ligand-dependent receptor complex formation in planta. *Science Signaling*, 8(388):ra76, aug 2015.

[209] Alan C. Burton. The properties of the steady state compared to those of equilibrium as shown in characteristic biological behavior. *Journal of Cellular and Comparative Physiology*, 3(3):327–349, dec 1939.

[210] Delphine Chinchilla, Cyril Zipfel, Silke Robatzek, Birgit Kemmerling, Thorsten Nürnberger, Jonathan D. G. Jones, Georg Felix, and Thomas Boller. A flagellin-induced complex of the receptor FLS2 and BAK1 initiates plant defence. *Nature*, 448(7152):497–500, jul 2007.

[211] Maurice Tronchet, Claudine Balagué, Thomas Kroj, Lise Jouanin, and Dominique Roby. Cinnamyl alcohol dehydrogenases-C and D, key enzymes in lignin biosynthesis, play an essential role in disease resistance in Arabidopsis. *Molecular plant pathology*, 11(1):83–92, jan 2010.

[212] Christoph A. Bücherl, Iris Katharina Jarsch, Christian Schudoma, Silke Robatzek, Daniel Maclean, Thomas Ott, Cyril Zipfel, Plant Genome, Seoul National, and Cell

Biology. Plant immune and growth receptors share common signalling components but localise to distinct plasma membrane nanodomains. *eLife*, 6:e25114, mar 2017.

[213] Sara Martins, Esther M. N. Dohmann, Anne Cayrel, Alexander Johnson, Wolfgang Fischer, Florence Pojer, Béatrice Satiat-Jeunemaître, Yvon Jaillais, Joanne Chory, Niko Geldner, and Grégory Vert. Internalization and vacuolar targeting of the brassinosteroid hormone receptor BRI1 are regulated by ubiquitination. *Nature Communications*, 6(1):6151, dec 2015.

[214] Niko Geldner, Derek L Hyman, Xuelu Wang, Karin Schumacher, and Joanne Chory. Endosomal signaling of plant steroid receptor kinase BRI1. *Genes & development*, 21(13):1598–602, jul 2007.

[215] NG Irani, Simone Di Rubbo, and Evelien Mylle. Fluorescent castasterone reveals BRI1 signaling from the plasma membrane. *Nature chemical . . .* , 8(JUNE), 2012.

[216] James E. Bailey. Complex biology with no parameters, jun 2001.

[217] I Swameye, T G Muller, J Timmer, O Sandra, and U Klingmuller. Identification of nucleocytoplasmic cycling as a remote sensor in cellular signaling by databased modeling. *Proceedings of the National Academy of Sciences of the United States of America*, 100(3):1028–33, feb 2003.

[218] Christian Löfke, Kai Dünser, and Jürgen Kleine-Vehn. Epidermal patterning genes impose non-cell autonomous cell size determination and have additional roles in root meristem size control. *Journal of Integrative Plant Biology*, 55(9):864–875, sep 2013.

[219] Dirk De Vos, Kris Vissenberg, Jan Broeckhove, and Gerrit T S Beemster. Putting Theory to the Test: Which Regulatory Mechanisms Can Drive Realistic Growth of a Root? *PLoS Computational Biology*, 10(10):e1003910, oct 2014.

[220] Maciej H. Swat, Gilberto L. Thomas, Julio M. Belmonte, Abbas Shirinifard, Dimitrij Hmeljak, and James A. Glazier. Multi-Scale Modeling of Tissues Using CompuCell3D. *Methods in Cell Biology*, 110:325–366, jan 2012.

[221] Vivi Andasari, Ryan T. Roper, Maciej H. Swat, and Mark A. J. Chaplain. Integrating Intracellular Dynamics Using CompuCell3D and Bionetsolver: Applications to Multiscale Modelling of Cancer Cell Growth and Invasion. *PLoS ONE*, 7(3):e33726, mar 2012.

[222] Sebastian Wolf, Dieuwertje van der Does, Friederike Ladwig, Carsten Sticht, Andreas Kolbeck, Ann-Kathrin Schürholz, Sebastian Augustin, Nana Keinath, Thomas Rausch, Steffen Greiner, Karin Schumacher, Klaus Harter, Cyril Zipfel, and Herman Höfte. A receptor-like protein mediates the response to pectin modification by activating brassinosteroid signaling. *Proceedings of the National Academy of Sciences*, 111(42):15261–15266, oct 2014.

[223] Sebastian Wolf and Steffen Greiner. Growth control by cell wall pectins. *Protoplasma*, 249 Suppl:S169–75, jun 2012.

[224] Christoph A Bücherl, Iris K Jarsch, Christian Schudoma, Cécile Segonzac, Malick Mbengue, Silke Robatzek, Daniel MacLean, Thomas Ott, and Cyril Zipfel. Plant immune and growth receptors share common signalling components but localise to distinct plasma membrane nanodomains. *eLife*, 6, 2017.

A | Multi-Compartment Rate Laws

A.1 Model Parameters

A.1.1 Toy Models

Table A.1: Kinetic parameters and the scaling factors of the transport model in the different modeling approaches. Shown are the permeability parameters k_1 and k_{-1}, their values and the included scaling factor for the meristematic epidermis cell.

	Parameter	Value	Units	Scaling Factor
multi-compartment, with membrane	k_1	0.0001	$\mathrm{dm\,s^{-1}}$	
	k_{-1}	0.0001	$\mathrm{dm\,s^{-1}}$	
multi-compartment, w/o membrane	k_1	$7.67 \cdot 10^{-12}$	$\mathrm{dm^3\,s^{-1}}$	$area$
	k_{-1}	$7.67 \cdot 10^{-12}$	$\mathrm{dm^3\,s^{-1}}$	$area$
one compartment	k_1	25.3165	$\mathrm{s^{-1}}$	$\frac{area}{V_1}$
	k_{-1}	8.75574	$\mathrm{s^{-1}}$	$\frac{area}{V_2}$

Table A.2: Area of the membrane surface during vertical and horizontal transport. Listed are the interaction area for horizontal and vertical transport in the different root zones.

Root Zone	Direction of Transport	Interaction Area
meristematic	vertical	$1.9208 \times 10^{-8}\,\mathrm{dm^2}$
	horizontal	$1.5876 \times 10^{-8}\,\mathrm{dm^2}$
elongation	vertical	$4.3803 \times 10^{-8}\,\mathrm{dm^2}$
	horizontal	$2.22 \times 10^{-7}\,\mathrm{dm^2}$
maturation	vertical	$5.0562 \times 10^{-8}\,\mathrm{dm^2}$
	horizontal	$7.3617 \times 10^{-7}\,\mathrm{dm^2}$

Table A.3: Parameter overview of the receptor toy model. All parameters were chosen such that the behavior in the meristematic zone was identical for all modeling approaches.

	Parameter	Value	Units	Scaling Factor
without	k_1	$7.67 \cdot 10^{-10}$	$\mathrm{dm}^5\,\mathrm{mol}^{-1}\,\mathrm{s}^{-1}$	$area$
area-scaling	k_{-1}	$7.67 \cdot 10^{-10}$	$\mathrm{dm}^2\,\mathrm{s}^{-1}$	$area$
	k_2	$7.67 \cdot 10^{-9}$	$\mathrm{dm}^2\,\mathrm{s}^{-1}$	$area$
	k_3	0.01	s^{-1}	
with	k_1	0.01	$\mathrm{dm}^3\,\mathrm{mol}^{-1}\,\mathrm{s}^{-1}$	
area-scaling	k_{-1}	0.01	s^{-1}	
	k_2	0.1	s^{-1}	
	k_3	0.01	s^{-1}	
one	k_1	2531.65	$\mathrm{dm}^3\,\mathrm{mol}^{-1}\,\mathrm{s}^{-1}$	$\frac{area}{V_{cell\,wall}}$
compartment	k_{-1}	905.549	s^{-1}	$\frac{area}{V_{cell}}$
	k_2	0.1	s^{-1}	
	k_3	0.01	s^{-1}	

A.1.2 RanGTP Transport Model

Compartment Sizes

Table A.4: Compartment sizes of the RanGTP model. The surface area of the nuclear envelope was approximated by assuming a spherical shape of the nucleus.

Model Version	Nuclear Volume	Cytosolic Volume	Nuclear Area
original	$1.2 \times 10^{-11}\,\mathrm{dm}^3$	$1.8 \times 10^{-11}\,\mathrm{dm}^3$	$2.53 \times 10^{-7}\,\mathrm{dm}^2$
wild type	$1.73 \times 10^{-15}\,\mathrm{dm}^3$	$2.6 \times 10^{-14}\,\mathrm{dm}^3$	$6.94\,\mathrm{dm}^2$
sch9-/-	$2.91 \times 10^{-15}\,\mathrm{dm}^3$	$4.18\,\mathrm{dm}^3$	$9.86 \times 10^{-10}\,\mathrm{dm}^2$

A.2 Additional Plots

A.2.1 Receptor Toy Model

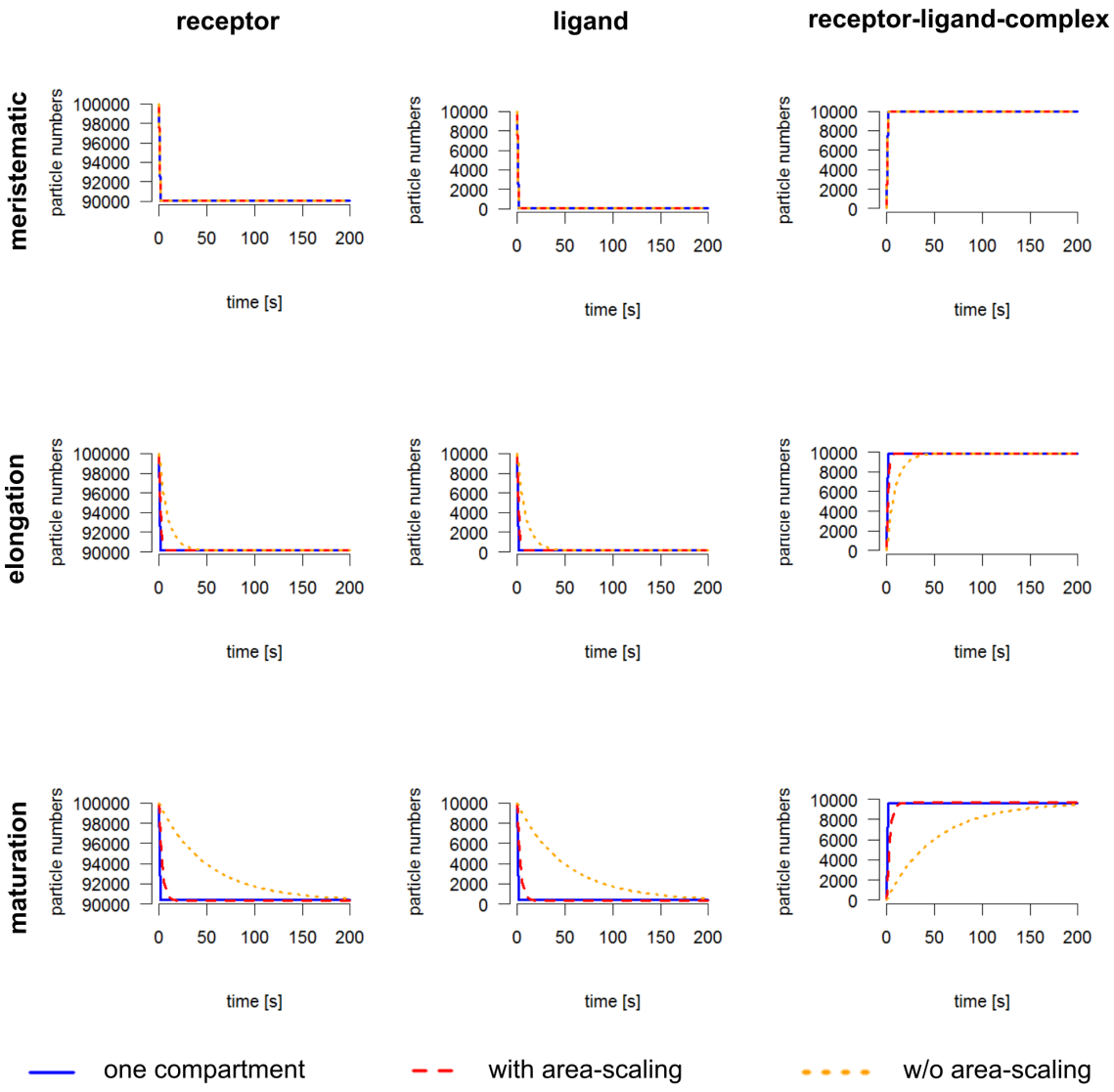

Figure A.1: Simulated time-course behavior of the other species in the receptor model. The figure summarizes the time-course simulations of the receptor, the ligand and the receptor-ligand-complex for the respective root zone. The one compartment model is indicated in blue, the multi-compartment model with area scaling is indicated in red and the multi-compartment model without area-scaling is shown in yellow.

A.3 Files

The COPASI model files used in this chapter are included in the attached CD. Here, I list and describe the included files.

Toy Models

	Model File	Included Parameter Sets
transport model	transport.cps	meristematic zone, whole cell
		elongation zone, whole cell
		maturation zone, whole cell
	transport_cells.cps	meristematic zone, horizontal transport
		meristematic zone, vertical transport
		elongation zone, horizontal transport
		elongation zone, vertical transport
		maturation zone, horizontal transport
		maturation zone, vertical transport
receptor model	receptor.cps	meristemtatic zone
		elongation zone
		maturation zone

Example Model

	File	Included Parameter Sets
volume-scaling	BIOMD0000000192.cps	original_model
		wild-type, original parameters
		wild type, corrected parameters
		sch9 mutant, original parameters
		sch9 mutant, unadjusted parameters
		sch9 mutant, corrected parameters
area-scaling	BIOMD0000000192_area.cps	original_behavior
		wild type
		sch9 mutant

B | Structural Modeling

B.1 Comparative Modeling

B.1.1 Sequence Alignments

Code for Sequence Alignment

The basic code was kindly provided by Dr. Anna Feldman-Salit and adapted to the specific proteins by me.

```
env = environ()
env.io.atom_files_directory = [r'file␣path']

#----------------------------------#
# Alignment files preparation    #
#----------------------------------#

aln = alignment(env)
mdl = model(env)

# Load the template structure
code = 'template'
mdl.read(file=code, model_segment=('FIRST:@', 'END:'))
aln.append_model(mdl, align_codes=code, atom_files=code)

# Load the amino acid sequence
aln.append(file='target.ali', align_codes='target')

# Align sequences
aln.malign(gap_penalties_1d = (-500, -300))
aln.write(file='target-template.ali', alignment_format='PIR')
aln.write(file='target-template.pap', alignment_format='PAP')
```

```
position          870       880       890       900       910       920
5lpw            KPLRKLTFADLLQATNGFHNDSLIGSGGFGDVYKAILKDGSAVAIKKLIHVSGQGDREFMAEM
BRI1            KPLRKLTFADLLQATNGFHNDSLIGSGGFGDVYKAILKDGSAVAIKKLIHVSGQGDREFMAEM
conserved       ************************************************************

position       930       940       950       960       970       980       990
5lpw            ETIGKIKHRNLVPLLGYCKVGDERLLVYEFMKYGSLEDVLHDP---GVKLNWSTRRKIAIGSA
BRI1            ETIGKIKHRNLVPLLGYCKVGDERLLVYEFMKYGSLEDVLHDPKKAGVKLNWSTRRKIAIGSA
conserved       ********************************************___*****************

position            1000      1010      1020      1030      1040      1050
5lpw            RGLAFLHHNCSPHIIHRDMKSSNVLLDENLEARVSDFGMARLMSAMDTHLSVSTLAGTPGYVP
BRI1            RGLAFLHHNCSPHIIHRDMKSSNVLLDENLEARVSDFGMARLMSAMDTHLSVSTLAGTPGYVP
conserved       ************************************************************

position          1060      1070      1080      1090      1100      1110
5lpw            PEYYQSFRCSTKGDVYSYGVVLLELLTGKRPT---------LVGWVKQHAKLRISDVFDPELM
BRI1            PEYYQSFRCSTKGDVYSYGVVLLELLTGKRPTDSPDFGDNNLVGWVKQHAKLRISDVFDPELM
conserved       *********************************_________**********************

position       1120      1130      1140      1150      1160
5lpw            KEDPALEIELLQHLKVAVACLDDRAWRRPTMVQVMAMFKEIQA
BRI1            KEDPALEIELLQHLKVAVACLDDRAWRRPTMVQVMAMFKEIQA
conserved       *******************************************
```

Figure B.1: Sequence alignment of the structurally resolved residues in 5lpw and the amino acid sequence of BRI1. This sequence alignment was generated using Modeller [91].

```
BAK1 (3tl8)  -------------RRKKPQDHFFDVPAEEDPEVHLGQLKRFSLRELQVASDNFSNKNILG   47
BRI1 (5lpw)  ------------------------E-----------KPLRKLAFADLLQATNGFHNDSLIG   26
BIR2 (4l68)  GSHMGSGLAQRLRSHKLTQVSLFQ-----------KPLVKVKLGDLMAATNNFNSENIIV   49
BIR3         ------DWIGLLRSHKLVQVTLFQ-----------KPIVKIKLGDLMAATNNFSSGNIDV   43
                                   :             : :. : :*  *::.* . .:

BAK1 (3tl8)  RGGFGKVYKGRLADGTLVAVKRLKEERTQGGELQFQTEVEMISMAVHRNLLRLRGFCMTP   107
BRI1 (5lpw)  SGGFGDVYKAILKDGSAVAIKKLIHVSG-QGDREFMAEMETIGKIKHRNLVPLLGYCKVG   85
BIR2 (4l68)  STRTGTTYKALLPDGSALAVKHLS-TCK-LGEREFRYEMNQLWELRHSNLAPLLGFCVVE   107
BIR3         SSRTGVSYKADLPDGSALAVKRLS-ACG-FGEKQFRSEMNKLGELRHPNLVPLLGYCVVE   101
                 *  **. * **: :*:*:*       *: :*  *:: :    * **  * *:* .

BAK1 (3tl8)  TERLLVYPYMANGSVASCLRERPESQPPLDWPKRQRIALGSARGLAYLHDHCDPKIIHRD   167
BRI1 (5lpw)  DERLLVYEFMKYGSLEDVLHDPKKAGVKLNWSTRRKIAIGSARGLAFLHHNCSPHIIHRD   145
BIR2 (4l68)  EEKFLVYKYMSNGTLHSLLDSN---RGELDWSTRFRIGLGAARGLAWLHHGCRPPILHQN   164
BIR3         DERLLVYKHMVNGTLFSQLHNGGLCDAVLDWPTRRAIGVGAAKGLAWLHHGCQPPYLHQF   161
              *::*** .*  *:: . * .       *:* .*  *.:*:*:***:**. * *  :*:

BAK1 (3tl8)  VKAANILLDEEFEAVVGDFGLAKLMDYKDTHVTT---AVRGTIGHIAPEYLSTGKSSEKT   224
BRI1 (5lpw)  MKSSNVLLDENLEARVSDFGMARLMSAMDTHLSV--STLAGTPGYVPPEYYQSFRCSTKG   203
BIR2 (4l68)  ICSSVILIDEDFDARIIDSGLARLMVPSDNNESSFMTGDLGEFGYVAPEYSTTMLASLKG   224
BIR3         ISSNVILLDDDFDARITDYGLAKLVGSRDSNDSSFNNGDLGELGYVAPEYSSTMVASLKG   221
             : :  :*:*::::* : * *:*:*:   *.: :       *  *:: ***  :  .* *

BAK1 (3tl8)  DVFGYGVMLLELITGQRAFDLARLANDDDVMLLDWVKGLLKEKKLEALVDVDLQG--NYK   282
BRI1 (5lpw)  DVYSYGVVLLELLTGKRPTDSPDFG---DNNLVGWVKQHAK-LRISDVFDPELMKEDPAL   259
BIR2 (4l68)  DVYGLGVVLLELATGLKAV----GGEGFKGSLVDWVKQLESSGRIAETFDENIRG--KGH   278
BIR3         DVYGFGIVLLELVTGQKPLSVINGVEGFKGSLVDWVSQYLGTGRSKDAIDRSICD--KGH   279
             **:. *::**** ** :           .  *:.**.      :    .* .:

BAK1 (3tl8)  DEEVEQLIQVALLCTQSSPMERPKMSEVVRMLEGDGLAERWEEWQKEEMFRQDFNYPTHL   342
BRI1 (5lpw)  EIELLQHLKVAVACLDDRAWRRPTMVQVMAMFKEIQA----------------------   296
BIR2 (4l68)  DEEISKFVEIALNCVSSRPKERWSMFQAYQSLKAIAEKQGYSFSEQDDDFPLIFDTQENE   338
BIR3         DEEILQFLKIACSCVVSRPKERPTMIQVYESLKNMADKHGV--SEHYDEFPLVFNKQ*--   334
             : *: : :::*  *  .   .* .* :.   ::

BAK1 (3tl8)  E-     343
BRI1 (5lpw)  --     296
BIR2 (4l68)  KV     340
BIR3         --     334
```

Figure B.2: Multiple sequence alignment of the cytoplasmic domains of BIR2, BIR3, BAK1 and BRI1. The sequence alignment was generated using the alignment tool Clustal Omega of the European Bioinformatics Institute [119, 120, 121]

B.1.2 Comparative Modeling

The code listed here was used to generate the structure for BIR3 and to fill the gaps in the structure of BRI1 using Modeller [91].

Comparative Modeling

The basic code was kindly provided by Dr. Anna Feldman-Salit and adapted to the specific proteins by me.

```
#!/bin/sh -v

# Homology modelling by the automodel class

#from modeller import *
# Load standard Modeller classes
from modeller.automodel import *    # Load the automodel class

log.verbose()    # request verbose output
env = environ()  # create a new MODELLER environment to build this model in

# directories for input atom files

env.io.atom_files_directory = [r'file path']

#env.io.atom_files_directory = [r'.']
# Read in HETATM records from template PDBs

# env.io.hetatm = True

#-----------------
# MOLECULE 1
#-----------------

a = automodel(env,
              alnfile  = 'target_template.ali',   # alignment filename
              knowns   = 'template',              # codes_templates
              sequence = 'target')                # code of the target
a.starting_model= 1                           # index of the first model
a.ending_model  = 1                           # index of the last model
# (determines how many models to calculate)

# do the actual homology modelling
a.make()
```

B.2 Simulaiton of Diffusional Association

B.2.1 ClusPro Constraints

The JSON constraints were used to limit the maximal distance between protein centers to 45 Å and thereby reproducing the settings of the webSDA computations.

BRI1 and BAK1

{"required":1,"groups":[{"required":1,"restraints":[{"type":"residue",

"dmax":45,"dmin":30,"rec_chain":"A","rec_resid":"149",

"lig_chain":"A","lig_resid":"418"}]}]}

C | ODE Modeling

C.1 Additional Experimental Data

C.1.1 Western Blot Data

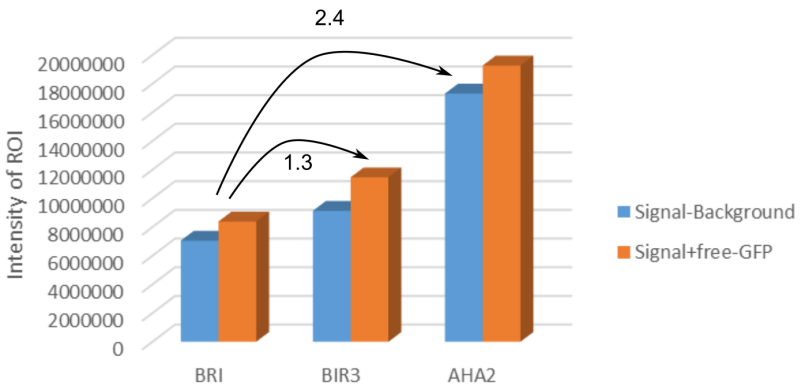

Figure C.1: Exemplary Western Blot result of the protein quantification in *A.thaliana* roots. The negative regulator BIR3 and the ATPase AHA2 were quantified in relation to BRI1. The figure was kindly provided by Nina Glöckner.

C.1.2 Calculations of the Proton Leak Rate

The boundaries for the proton leak reaction were calculated based on the experimental measurements by Dr. Stefan Scholl. Based on Figure C.2 B, the proton leak is at least from pH 5.5 to 7.0 and at most from pH 5.34 to 7.7. This translates to a difference in proton concentration ΔH^+_{out} between $3.06\,10^{-6}\,mol\,h^{-1}$ and $4.55\,10^{-6}\,mol\,h^{-1}$. The amount of protons transported per second can now be calculated by:

$$transport[mol\,s^{-1}] = \Delta H^+_{out} \cdot V_{cell\,wall}[dm^3] \cdot \frac{1}{3600} \tag{C.1}$$

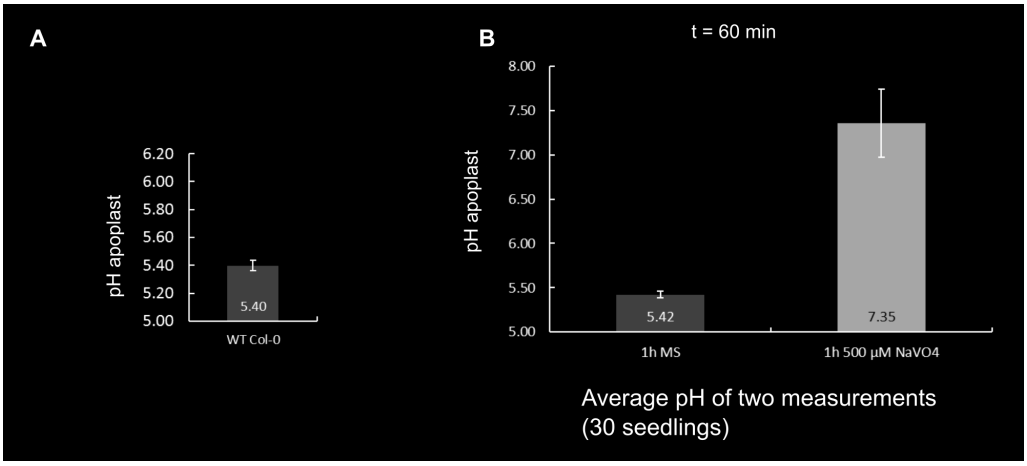

Figure C.2: Measurement of apoplast pH. A: Average pH of the apoplast in the elongation zone. **B:** The plants were treated with $500\,\mu m$ ortho-vanadate and measurements were taken by fluorescence microscopy. The apoplast pH was measured in comparison to plants treated with pure medium as control. Figures are courtesy of Dr. Stefan Scholl.

The last factor is multiplied to scale from hours to seconds. Based on the rate law used to describe the proton leak, it is now possible to estimate the rate for this reaction:

$$area \cdot k \cdot ([H^+_{out}] - [H^+_{in}]) = transport[mol\,s^{-1}] \tag{C.2}$$

$$k = \frac{transport[mol\,s^{-1}]}{area \cdot ([H^+_{out}] - [H^+_{in}])} \tag{C.3}$$

Based on the intracellular pH of 7.2, the average extracellular pH in the elongation zone of 5.4 C.2 A and the cell surface, the rate can now be calculated:

$$k = \frac{transport[mol\,s^{-1}]}{(10^{-5.4}[mol\,dm^{-3}] - 10^{-7.2}[mol\,dm^{-3}]) \cdot area} \tag{C.4}$$

$$k = \frac{transport[mol\,s^{-1}] \cdot 10^9}{0.0021\,nmol\,dm^{-1}} \tag{C.5}$$

$$k = \frac{transport[nmol\,s^{-1}]}{0.0021\,nmol\,dm^{-1}} \tag{C.6}$$

Based on these calculations k has a value between $0.84\,10^{-9}\,dm\,s^{-1}$ and $1.25\,10^{-9}\,dm\,s^{-1}$. I used these values as boundaries for the proton leak reaction during parameter estimation.

C.2 Compartment Sizes

Cell Wall Volume

$$V_{cell\,wall}(t) = A_{cell\,surface} \cdot cell\,wall\,thickness(t)$$

C.3 Ordinary Differential Equations

BRI1

$$\begin{aligned}\frac{d([BRI1] \cdot A_{cell\,surface})}{dt} =& - A_{cell\,surface} \cdot (k_{on} \cdot stimulation \cdot [BL] \cdot [BRI1] - k_{off} \cdot [BRI1\,BL]) \\ &+ A_{cell\,surface} \cdot k_{off} \cdot [BRI1p\,BL] \\ &- A_{cell\,surface} \cdot (k \cdot [BRI1] \cdot [BIR3] - k \cdot K_D \cdot [BIR3\,BRI1]) \\ &+ A_{cell\,surface} \cdot k_{off2} \cdot [BAK1\,BRI1p\,BL] \\ &+ A_{cell\,surface} \cdot k_{off2} \cdot [BAK1p\,BRI1pp\,BL] \\ &+ A_{cell\,surface} \cdot k_{off3} \cdot [BAK1p\,BRI1pppS891\,BL]\end{aligned}$$

BL

$$\begin{aligned}\frac{d([BL] \cdot V_{cell\,wall})}{dt} =& - A_{cell\,surface} \cdot (k_{on} \cdot stimulation \cdot [BL] \cdot [BRI1] - k_{off} \cdot [BRI1\,BL]) \\ &+ A_{cell\,surface} \cdot k_{off} \cdot [BRI1p\,BL] \\ &+ A_{cell\,surface} \cdot k_{off2} \cdot [BAK1\,BRI1p\,BL] \\ &+ A_{cell\,surface} \cdot k_{off2} \cdot [BAK1p\,BRI1pp\,BL] \\ &+ A_{cell\,surface} \cdot k_{off3} \cdot [BAK1p\,BRI1pppS891\,BL] \\ &+ V_{cell\,wall} \cdot stimulation \cdot flux \cdot dose_{BL} \\ &- V_{cell\,wall} \cdot k \cdot [BL]\end{aligned}$$

BKI1

$$\begin{aligned}\frac{d([BKI1] \cdot A_{cell\,surface})}{dt} =& - A_{cell\,surface} \cdot k \cdot [BRI1\,BL] \\ &\cdot \frac{[BKI1]}{(K_{i,BKI1} + [BKI1] \cdot (1 + \frac{[BKI1]}{K_{i,BKI1}}) \cdot (1 + \frac{[BIK1]}{K_{i,BIK1}}) \cdot (1 + \frac{[BRI1\,CT]}{K_{i,BRI1\,CT}})} \\ &+ A_{cell\,surface} \cdot k \cdot [BKI1pY211]\end{aligned}$$

BKI1pY211

$$\begin{aligned}\frac{d([BKI1]\cdot A_{cell\,surface})}{dt} =& + A_{cell\,surface}\cdot k\cdot [BRI1\,BL] \\ & \cdot \frac{[BKI1]}{(K_{i,BKI1}+[BKI1]\cdot(1+\frac{[BKI1]}{K_{i,BKI1}})\cdot(1+\frac{[BIK1]}{K_{i,BIK1}})\cdot(1+\frac{[BRI1\,CT]}{K_{i,BRI1\,CT}})} \\ & - A_{cell\,surface}\cdot k\cdot [BKI1pY211]\end{aligned}$$

BKI1

$$\begin{aligned}\frac{d([BKI1]\cdot A_{cell\,surface})}{dt} =& - A_{cell\,surface}\cdot k\cdot [BRI1\,BL] \\ & \cdot \frac{[BKI1]}{(K_{i,BKI1}+[BKI1]\cdot(1+\frac{[BKI1]}{K_{i,BKI1}})\cdot(1+\frac{[BIK1]}{K_{i,BIK1}})\cdot(1+\frac{[BRI1\,CT]}{K_{i,BRI1\,CT}})} \\ & + A_{cell\,surface}\cdot k\cdot [BKI1pY211]\end{aligned}$$

AHA C-terminus P

$$\begin{aligned}\frac{d([AHA\,CTp]\cdot A_{cell\,surface})}{dt} =& - A_{cell\,surface}\cdot k\cdot [AHA\,CTp] \\ & + A_{cell\,surface}\cdot k\cdot [BAK1p\,BRI1pp\,BL]\cdot\frac{[AHA\,CT]}{[AHA\,CT]+K}\end{aligned}$$

AHA C-terminus

$$\begin{aligned}\frac{d([AHA\,CTp]\cdot A_{cell\,surface})}{dt} =& + A_{cell\,surface}\cdot k\cdot [AHA\,CTp] \\ & - A_{cell\,surface}\cdot k\cdot [BAK1p\,BRI1pp\,BL]\cdot\frac{[AHA\,CT]}{[AHA\,CT]+K}\end{aligned}$$

BAK1

$$\begin{aligned}\frac{d([BAK1]\cdot A_{cell\,surface})}{dt} =& - A_{cell\,surface}\cdot (k\cdot [BAK1]\cdot [BIR3] - k\cdot K_D\cdot [BIR3\,BAK1]) \\ & - A_{cell\,surface}\cdot (k\cdot [BAK1]\cdot [BRI1p\,BL] - k\cdot K_D\cdot [BAK1\,BRI1p\,BL]) \\ & + A_{cell\,surface}\cdot k_{off2}\cdot [BAK1\,BRI1p\,BL] \\ & + A_{cell\,surface}\cdot k_{off2}\cdot [BAK1p\,BRI1pp\,BL] \\ & + A_{cell\,surface}\cdot k_{off3}\cdot [BAK1p\,BRI1pppS891\,BL]\end{aligned}$$

BAK1 BRI1p BL

$$\begin{aligned}\frac{d([BAK1\,BRI1p\,BL]\cdot A_{cell\,surface})}{dt} =& + A_{cell\,surface}\cdot(k\cdot[BRI1p\,BL]\cdot[BAK1]\\ & - k_{off}\cdot[BAK1\,BRI1p\,BL])\\ & - A_{cell\,surface}\cdot k_{off2}\cdot[BAK1\,BRI1p\,BL]\\ & - A_{cell\,surface}\cdot k\cdot[BAK1\,BRI1p\,BL]\end{aligned}$$

BAK1p BRI1pp BL

$$\begin{aligned}\frac{d([BAK1p\,BRI1pp\,BL]\cdot A_{cell\,surface})}{dt} =& + A_{cell\,surface}\cdot k\cdot[BAK1\,BRI1p\,BL]\\ & - A_{cell\,surface}\cdot k_{off2}\cdot[BAK1p\,BRI1pp\,BL]\\ & - A_{cell\,surface}\cdot k\cdot[BAK1p\,BRI1pp\,BL]\end{aligned}$$

BAK1p BRI1pppS891 BL

$$\begin{aligned}\frac{d([BAK1p\,BRI1pppS891\,BL]\cdot A_{cell\,surface})}{dt} =& + A_{cell\,surface}\cdot k\cdot[BAK1p\,BRI1pp\,BL]\\ & - A_{cell\,surface}\cdot k_{off3}\cdot[BAK1p\,BRI1pppS891\,BL]\end{aligned}$$

BIK1

$$\begin{aligned}\frac{d([BIK1]\cdot A_{cell\,surface})}{dt} =& - A_{cell\,surface}\cdot k\cdot[BRI1\,BL]\\ & \cdot\frac{[BIK1]}{(K_{i,BIK1}+[BIK1]\cdot(1+\frac{[BKI1]}{K_{i,BKI1}})\cdot(1+\frac{[BIK1]}{K_{i,BIK1}})\cdot(1+\frac{[BRI1\,CT]}{K_{i,BRI1\,CT}})}\\ & + A_{cell\,surface}\cdot k\cdot[BIK1p]\end{aligned}$$

BIK1p

$$\begin{aligned}\frac{d([BIK1p]\cdot A_{cell\,surface})}{dt} =& + A_{cell\,surface}\cdot k\cdot[BRI1\,BL]\\ & \cdot\frac{[BIK1]}{(K_{i,BIK1}+[BIK1]\cdot(1+\frac{[BKI1]}{K_{i,BKI1}})\cdot(1+\frac{[BIK1]}{K_{i,BIK1}})\cdot(1+\frac{[BRI1\,CT]}{K_{i,BRI1\,CT}})}\\ & - A_{cell\,surface}\cdot k\cdot[BIK1p]\end{aligned}$$

BRI1 BL

$$\begin{aligned}\frac{d([BRI1\,BL]\cdot A_{cell\,surface})}{dt} =& - A_{cell\,surface}\cdot k\cdot[BRI1\,BL]\\ &\cdot\frac{[1]}{(1+\frac{[BKI1]}{K_{i,BKI1}})\cdot(1+\frac{[BIK1]}{K_{i,BIK1}})\cdot(1+\frac{[BRI1\,CT]}{K_{i,BRI1\,CT}})}\\ &+ A_{cell\,surface}\cdot(k\cdot stimulation\cdot[BL]\cdot[BRI1]-k_{off}\cdot[BRI1\,BL])\end{aligned}$$

BRI1p BL

$$\begin{aligned}\frac{d([BRI1p\,BL]\cdot A_{cell\,surface})}{dt} =& + A_{cell\,surface}\cdot k\cdot[BRI1\,BL]\\ &\cdot\frac{[1]}{(1+\frac{[BKI1]}{K_{i,BKI1}})\cdot(1+\frac{[BIK1]}{K_{i,BIK1}})\cdot(1+\frac{[BRI1\,CT]}{K_{i,BRI1\,CT}})}\\ &-_{cell\,surface}\cdot(k\cdot[BAK1]\cdot[BRI1p\,BL]-koff\cdot[BAK1\,BRI1p\,BL])\\ &- A_{cell\,surface}\cdot k_{off}\cdot[BRI1p\,BL]\end{aligned}$$

BIR3

$$\begin{aligned}\frac{d([BIR3]\cdot A_{cell\,surface})}{dt} =& - A_{cell\,surface}\cdot(k\cdot[BIR3]\cdot[BAK1]-k\cdot K_D\cdot[BIR3\,BAK1])\\ &- A_{cell\,surface}\cdot(k\cdot[BIR3]\cdot[BRI1]-k\cdot K_D\cdot[BIR3\,BRI1])\end{aligned}$$

BIR3 BAK1

$$\frac{d([BIR3]\cdot A_{cell\,surface})}{dt} = - A_{cell\,surface}\cdot(k\cdot[BIR3]\cdot[BAK1]-k\cdot K_D\cdot[BIR3\,BAK1])$$

BIR3 BRI1

$$\frac{d([BIR3]\cdot A_{cell\,surface})}{dt} = - A_{cell\,surface}\cdot(k\cdot[BIR3]\cdot[BRI1]-k\cdot K_D\cdot[BIR3\,BRI1])$$

Extracellular Proton Concentration

$$\frac{d([H^+_{out}] \cdot V_{cell\,wall})}{dt} = + A_{cell\,surface} \cdot k \cdot [AHA] \cdot [H^+_{in}] \cdot \frac{[AHA]}{[AHA] + Inhibition_{AHACT} \cdot [AHACT]} - A_{cell\,surface} \cdot k \cdot ([H^+_{out}] - [H^+_{in}])$$

C.4 Data used for Parameter Estimation

C.4.1 Dose Response Data

This data file comprises the data of the resting membrane potential in absence of the hormone as well as the dose-response data of the membrane potential in response to BL stimulation. The stimulation with BL occurs after $1\,d = 86400\,s$. The respective dose of BL has the units of nM. The corresponding membrane potential value is listed in the column called E_m. The BRI1 expression factor is also listed.

BL	BRI1	Time	Em
0	1	10000	−0.121
0	1	20000	−0.121
0	1	30000	−0.121
0	1	50000	−0.121
0	1	0	−0.121
0	1	5000	−0.121
0	1	40000	−0.121
0	1	86400	−0.121
0	1	0	−0.121
0	1	15000	−0.121
0	1	20000	−0.121
0	1	86400	−0.121
10	1	86400	−0.121
10	1	87000	−0.1236
10	1	87600	−0.1262
10	1	88200	−0.1288
10	1	86400	−0.121
10	1	87000	−0.1246
10	1	87600	−0.1282
10	1	88200	−0.1318
10	1	86400	−0.121
10	1	87000	−0.1256
10	1	87600	−0.1302

10	1	88200	-0.1348
50	1	86400	-0.121
50	1	87000	-0.124
50	1	87600	-0.127
50	1	88200	-0.1298
50	1	86400	-0.121
50	1	87000	-0.1245
50	1	87600	-0.1281
50	1	88200	-0.1316
50	1	86400	-0.121
50	1	87000	-0.1251
50	1	87600	-0.1293
50	1	88200	-0.1334
100	1	86400	-0.121
100	1	87000	-0.1251
100	1	87600	-0.1292
100	1	88200	-0.1333
100	1	86400	-0.121
100	1	87000	-0.1264
100	1	87600	-0.1318
100	1	88200	-0.1374
100	1	86400	-0.121
100	1	87000	-0.1277
100	1	87600	-0.1344
100	1	88200	-0.1411

C.4.2 Overexpression Data

This data file comprises the reconstructed response based on the overexpression phenotype of BIR3 and BIR3&BRI1 overexpressing plants. The basic set up is identical to the dose response data above. The overexpression factors of BRI1 and BIR3 are listed in the columns called $BRI1$ and $BIR3$, respectively.

BL	Time	BRI1	BIR3	Em
10	86400	1	100	-0.121
10	87600	1	100	-0.121
10	86400	130	100	-0.121
10	87600	130	100	-0.128

C.5 Boundaries of Parameter Estimation

Reaction	Parameter	Lower Bound	Upper Bound	Reference
r_{01}	k	10^{-6}	10^{6}	
r_{02}	k	$8.4 \cdot 10^{-10}$	$1.25 \cdot 10^{-9}$	Dr. Stefan Scholl
r_{03}	k	1	10^{6}	
r_{04}	k	1	10^{6}	
r_{07}	k_{cat}	0.0097	97	estimated within a 2 orders of magnitude of [199]
r_{08}	k_1	10^{-6}	10^{6}	
r_{09}	k_1	10^{-6}	10^{6}	
r_{10}	k_1	10^{-6}	10^{6}	
r_{11}	K	0.003	10^{6}	
r_{11}	k	10^{-6}	10	
r_{12}	k_1	10^{-4}	10^{-4}	approx. by [79]
r_{d4}	k	10^{-12}	10^{-8}	approx. by [79]
r_{d5}	k	10^{-12}	10^{-4}	
r_{d6}	k_1	10^{-12}	10^{-4}	
r_{d7}	k_1	10^{-12}	10^{-4}	
$BKI1$	K_i	10^{-6}	10^{-3}	
$BIK1$	K_i	10^{-6}	10^{-3}	
$BRI1\,CT$	K_i	10^{-6}	10^{-3}	
$BAK1$	K_D	10^{-8}	10^{-2}	
BL	K_D	7	55	[1, 45, 59, 198]
$BL\,BRI1\,BAK1$	k_{off}	10^{-6}	0.0105	[45]
$AHACT$	$inhibition$	1	6.7	[73]
$BIR3\,BAK1$	K_d	10^{-8}	10^{-4}	estimated acc. to [30]
$BIR3\,BAK1$	K_d	10^{-3}	1	estimated acc. to [30]

C.5.1 Exemplary Parameter Set

Table C.1: Exemplary parameter set of the ODE model of the fast BR response. The remaining 49 parameter sets are included on the attached CD.

Reaction	Parameter	Value
r_{01}	k	0.000 588 774 $\mathrm{dm^3\,nmol^{-1}\,s^{-1}}$
r_{02}	k	$1.25 \times 10^{-9}\,\mathrm{dm\,s^{-1}}$
r_{03}	k	993 351 $\mathrm{dm^2\,nmol^{-1}\,s^{-1}}$
r_{04}	k	1 $\mathrm{dm^2\,nmol^{-1}\,s^{-1}}$
r_{07}	k_{cat}	10.9191 $\mathrm{s^{-1}}$
r_{08}	k_1	948 636 $\mathrm{s^{-1}}$
r_{09}	k_1	92.073 $\mathrm{dm^2\,nmol^{-1}\,s^{-1}}$
r_{10}	k_1	140 940 $\mathrm{s^{-1}}$
r_{11}	K	0.004 489 36 $\mathrm{nmol\,dm^{-2}}$
r_{11}	k	9.999 78 $\mathrm{s^{-1}}$
r_{12}	k_1	0.000 099 999 6 $\mathrm{s^{-1}}$
r_{d4}	k	$9.22 \times 10^{-9}\,\mathrm{s^{-1}}$
r_{d5}	k	$7.227\,69 \times 10^{-5}\,\mathrm{dm\,s^{-1}}$
r_{d6}	k_1	$9.996\,32 \times 10^{-5}\,\mathrm{s^{-1}}$
r_{d7}	k_1	$9.999\,99 \times 10^{-5}\,\mathrm{s^{-1}}$
$BKI1$	K_i	0.000 205 491 $\mathrm{nmol\,dm^{-2}}$
$BIK1$	K_i	0.000 158 267 $\mathrm{nmol\,dm^{-2}}$
$BRI1\,CT$		0.000 967 652 $\mathrm{nmol\,dm^{-2}}$
$BAK1$	K_D	0.001 208 56 $\mathrm{nmol\,dm^{-2}}$
BL	K_D	55 nM
$BL\,BRI1\,BAK1$	k_{off}	0.0105 $\mathrm{s^{-1}}$
$AHACT$	$inhibition$	1.715 22
$BIR3\,BAK1$	K_d	0.000 018 252 $\mathrm{nmol\,dm^{-2}}$
$BIR3\,BAK1$	K_d	0.001 121 22 $\mathrm{nmol\,dm^{-2}}$

C.6 Additional Plots

C.6.1 BIR3 and BRI1 Overexpression Model

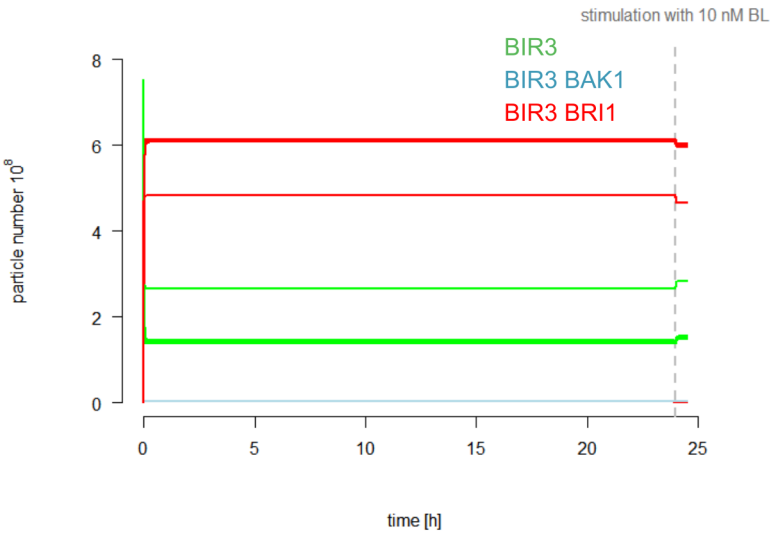

Figure C.3: Time-course simulation of the BIR3&BRI1 overexpressing model befor stimulation with BL. The time-course includes the 24 h before the addition of the hormone. $BIR3$ is indicated in green; $BIR3\,BRI1$ is indicated in red; $BIR3\,BAK1$ is indicated in blue. The behavior of all 50 model parameterizations was plotted.

C.7 Files

The ODE models were built in COPASI version 184, which supports 2-dimensional compartments. Opening this model in an older version of COPASI will result in the 2D compartment to be interpreted as a 3D compartment.

	File Name	Description
Model	1-50.cps	Model of the fast brassinosteroid response pathway that was used for the simulations in this thesis. The following parameter sets were included per model: elongation zone (wild-type), elongation zone (bir3 deletion) and meristematic zone (wild-type).
Data	data_2.txt	Experimental data used for parameter estimation. Includes dose response data on the membrane hyperpolarization [14].
	overexpression.txt	Qualitative experimental data of BIR3 and BIR3 & BRI1 overexpression plants and their response to stimulation with brassinosteroids.
	overview_fits.xlsx	Contains the overview of the parameter estimation results. This comprises all 50 parameter sets, the sensitivities in the elongation zone and meristematic zone, the dose response data for 10, 50 and 100 nM BL and the fitted behavior of the BIR3 and BIR3&BRI1 overexpression at 10 nM BL.

D | Root Model

D.1 Changes of the Biomechanical Model Code

D.1.1 Initial Settings

```
int cellrows = 14;
int cellcols = 14;

// Distances for placing cells
double xdelta = (2*rootrad)/cellcols;
double ydelta = (rootdome + rootrad)/(cellrows);

// Create cells at predefined positions

int sub = (cellcols/2) - 1; // Used to make narrowing tip

for (int row = 0; row < cellrows; row+=1 ) {

    for (int col = sub; col < cellcols-sub; col+=1) {

        Double2D newPos;
        UniversalCell newcell = new UniversalCell(null, null, true);
        RootTipCenterBased2DModel mechModel = ((RootTipCenterBased2DModel)
            newcell.getEpisimBioMechanicalModelObject());

        newPos = new Double2D(xstart + xdelta*col, ystart + ydelta*row);
        mechModel.setCellWidth(CELL_WIDTH);
        mechModel.setCellHeight(CELL_HEIGHT);
        mechModel.setStandardCellWidth(CELL_WIDTH);
        mechModel.setStandardCellHeight(CELL_HEIGHT);

        mechModel.setCellLocationInCellField(newPos);

        standardCellEnsemble.add(newcell);
    }

    if (sub > 0) {
         sub -= 1;

}

        //RootTipCenterBased2DModel.setDummyCellSize(CELL_WIDTH);
        //initializeBiomechanics(standardCellEnsemble);
        return standardCellEnsemble;
}
```

D.1.2 Directional bias of cell division

```
if(cell != null && cell.getMotherCell() != null)
{
    double cellWidth = 0;
    double cellHeight = 0;

    if(cell.getMotherCell().getEpisimBioMechanicalModelObject()
            instanceof RootTipCenterBased2DModel)
    {
        EpisimModelConnector motherCellConnector =((RootTipCenterBased2DModel)
            cell.getMotherCell().getEpisimBioMechanicalModelObject()).getEpisimModelConnector();

        // Default division bias value
        double deltaX = TissueController.getInstance()
            .getActEpidermalTissue().random.nextDouble()*0.005-0.0025;
        double deltaY = TissueController.getInstance()
            .getActEpidermalTissue().random.nextDouble()*0.005-0.0025;

        if(motherCellConnector instanceof RootTipEpisimCenterBasedMC)
        {
            cellWidth = ((RootTipEpisimCenterBasedMC)motherCellConnector).getWidth();
            cellHeight = ((RootTipEpisimCenterBasedMC)motherCellConnector).getHeight();
            setCellWidth(cellWidth);
            setCellHeight(cellHeight);
            cellEllipseObject.setMajorAxisAndMinorAxis(((RootTipEpisimCenterBasedMC)motherCellConnector)
                .getWidth(), ((RootTipEpisimCenterBasedMC)motherCellConnector).getHeight());

            deltaX = ((RootTipEpisimCenterBasedMC)motherCellConnector).getBiasX();
            deltaY = ((RootTipEpisimCenterBasedMC)motherCellConnector).getBiasY();

            Double2D oldLoc = cellField.getObjectLocation(cell.getMotherCell());

            // Calculation of initial daughter cell location after cell division
            if(oldLoc != null)
            {
                // Place newly-generated cell on mother cell location + division bias
                if(oldLoc != null){
                    Double2D newloc = new Double2D(oldLoc.x + deltaX, oldLoc.y + deltaY);
                    cellLocation    = newloc;
                    cellField.setObjectLocation(cell, newloc);
                    SimulationDisplayProperties props = ((RootTipCenterBased2DModel)cell.getMotherCell()
                        .getEpisimBioMechanicalModelObject()).getCellEllipseObject()
                        .getLastSimulationDisplayProps();
                    this.setLastSimulationDisplayPropsForNewCellEllipse(props, cellLocation);
                }
            }
        }
    }
}
```

D.2 Changed Definitions and ODEs

Cell Wall Volume

$$V_{cell\,wall}(t) = A_{cell\,surface}(t) \cdot cell\,wall\,thickness(t)$$

Cytoplasm Volume

$$V_{cytoplasm}(t) = cell\,width \cdot cell\,width \cdot cell\,length(t) \cdot 0.35$$

Cell Surface Area

$$A_{cell\,surface}(t) = 2 \cdot cell\,width^2 + 4 \cdot cell\,width \cdot cell\,length(t)$$

BRI1

$$\begin{aligned}\frac{(d[BRI1] \cdot A_{cell\,surface})}{dt} =& - A_{cell\,surface} \cdot (k_{on} \cdot stimulation \cdot [BL] \cdot [BRI1] - k_{off} \cdot [BRI1\,BL]) \\ &+ A_{cell\,surface} \cdot k_{off} \cdot [BRI1p\,BL] \\ &- A_{cell\,surface} \cdot (k \cdot [BRI1] \cdot [BIR3] - k \cdot K_D \cdot [BIR3\,BRI1]) \\ &+ A_{cell\,surface} \cdot k_{off2} \cdot [BAK1\,BRI1p\,BL] \\ &+ A_{cell\,surface} \cdot k_{off2} \cdot [BAK1p\,BRI1pp\,BL] \\ &+ A_{cell\,surface} \cdot k_{off3} \cdot [BAK1p\,BRI1pppS891\,BL] \\ &+ A_{cell\,surface} \cdot (scaling\,factor\,for\,protein\,synthesis \cdot 11)\end{aligned}$$

BKI1

$$\begin{aligned}\frac{d([BKI1] \cdot A_{cell\,surface})}{dt} =& - A_{cell\,surface} \cdot k \cdot [BRI1\,BL] \\ &\cdot \frac{[BKI1]}{(K_{i,BKI1} + [BKI1] \cdot (1 + \frac{[BKI1]}{K_{i,BKI1}}) \cdot (1 + \frac{[BIK1]}{K_{i,BIK1}}) \cdot (1 + \frac{[BRI1\,CT]}{K_{i,BRI1\,CT}})} \\ &+ A_{cell\,surface} \cdot k \cdot [BKI1pY211] \\ &+ A_{cell\,surface} \cdot scaling\,factor\,for\,protein\,synthesis \cdot 13.2\end{aligned}$$

BKI1

$$\begin{aligned}\frac{d([BKI1] \cdot A_{cell\,surface})}{dt} =& - A_{cell\,surface} \cdot k \cdot [BRI1\,BL] \\ &\cdot \frac{[BKI1]}{(K_{i,BKI1} + [BKI1] \cdot (1 + \frac{[BKI1]}{K_{i,BKI1}}) \cdot (1 + \frac{[BIK1]}{K_{i,BIK1}}) \cdot (1 + \frac{[BRI1\,CT]}{K_{i,BRI1\,CT}})} \\ &+ A_{cell\,surface} \cdot k \cdot [BKI1pY211] \\ &+ A_{cell\,surface} \cdot scaling\,factor\,for\,protein\,synthesis \cdot 13.2\end{aligned}$$

AHA C-terminus

$$\begin{aligned}\frac{d([AHACTp]\cdot A_{cell\,surface})}{dt} = &+ A_{cell\,surface}\cdot k\cdot [AHACTp]\\ &- A_{cell\,surface}\cdot [BAK1p\,BRI1pp\,BL]\cdot \frac{[AHACT]}{[AHACT]+K}\\ &+ A_{cell\,surface}\cdot scaling\,factor\,for\,protein\,synthesis\\ &\cdot translation\,rate\,AHA\end{aligned}$$

BIR3

$$\begin{aligned}\frac{d([BIR3]\cdot A_{cell\,surface})}{dt} = &- A_{cell\,surface}\cdot (k\cdot [BIR3]\cdot [BAK1] - k\cdot K_{D,BIR3,BAK1}\cdot [BIR3\,BAK1])\\ &- A_{cell\,surface}\cdot (k\cdot [BIR3]\cdot [BRI1] - k\cdot K_{D,BIR3,BRI1}\cdot [BIR3\,BRI1])\\ &+ A_{cell\,surface}\cdot scaling\,factor\,for\,protein\,synthesis\cdot stoichiometry\,BIR3)\end{aligned}$$

BAK1

$$\begin{aligned}\frac{d([BAK1]\cdot A_{cell\,surface})}{dt} = &- A_{cell\,surface}\cdot (k\cdot [BAK1]\cdot [BIR3] - k\cdot K_D\cdot [BIR3\,BAK1])\\ &- A_{cell\,surface}\cdot (k\cdot [BAK1]\cdot [BRI1p\,BL] - k\cdot K_D\cdot [BAK1\,BRI1p\,BL])\\ &+ A_{cell\,surface}\cdot k_{off2}\cdot [BAK1\,BRI1p\,BL]\\ &+ A_{cell\,surface}\cdot k_{off2}\cdot [BAK1p\,BRI1pp\,BL]\\ &+ A_{cell\,surface}\cdot k_{off3}\cdot [BAK1p\,BRI1pppS891\,BL]\\ &+ A_{cell\,surface}\cdot (scaling\,factor\,for\,protein\,synthesis\cdot 5)\end{aligned}$$

AHA

$$\begin{aligned}\frac{d([AHA]\cdot A_{cell\,surface})}{dt} = &+ A_{cell\,surface}\cdot scaling\,factor\,for\,protein\,synthesis\\ &\cdot translation\,rate\,AHA\end{aligned}$$

Intracellular Proton Concentration

$$\begin{aligned}\frac{d([H^+_{in}]\cdot V_{cytoplasm})}{dt} = &- V_{cytoplasm}\cdot (k\cdot [H^+_{in}])\\ &+ V_{cytoplasm}\cdot flux_{[H^+_{in}]}\\ &+ A_{cell\,surface}\cdot k([H^+_{out}] - [H^+_{in}])\\ &- A_{cell\,surface}\cdot k\cdot [AHA]\cdot [H^+_{in}]\cdot \frac{[AHA]}{[AHA] + Inhibition_{AHACT}\cdot [AHACT]}\end{aligned}$$

Cell Wall Instability

$$cell\,wall\,instability = 5 \cdot 10^{-4} \cdot stimulation \cdot \left(\frac{1}{1 + e^{-0.0005 \cdot ([H_{out}] - 2 \cdot proton\,readout)}} - \frac{1}{1 + e^{-5{,}000{,}000 \cdot (cell\,wall\,thickness - 6.525\,10^{-6})}} \right)$$

Ratio AHA2:BRI1

$$ratio\,AHA2 : BRI1 = \frac{1}{1 + e^{-8800 \cdot (cell\,length - 0.00016}} \cdot 0.9$$

D.3 Parameter Values

Table D.1: Parameter values of the elongating cell ODE model.

Reaction	Parameter	Value
r_{01}	k	0.000 548 910 372 1 $dm^3\,nmol^{-1}\,s^{-1}$
r_{02}	k	$1.148\,676\,594 \times 10^{-9}\,dm\,s^{-1}$
r_{03}	k	123 351.7945 $dm^2\,nmol^{-1}\,s^{-1}$
r_{04}	k	468 708.5154 $dm^2\,nmol^{-1}\,s^{-1}$
r_{07}	k_{cat}	96.120 317 53 s^{-1}
r_{08}	k_1	3436.810 685 s^{-1}
r_{09}	k_1	2272.103 802 $dm^2\,nmol^{-1}\,s^{-1}$
r_{10}	k_1	2727.083 532 s^{-1}
r_{11}	K	$9.520\,865\,887 \times 10^{-5}\,nmol\,dm^{-2}$
r_{11}	k	0.949 557 063 4 s^{-1}
r_{12}	k_1	$1.189\,518\,838 \times 10^{-5}\,s^{-1}$
r_{d4}	k	$4.290\,023\,087 \times 10^{-9}\,s^{-1}$
r_{d5}	k	$2.993\,625\,519 \times 10^{-12}\,dm\,s^{-1}$
r_{d6}	k_1	$3.967\,025\,12 \times 10^{-8}\,s^{-1}$
r_{d7}	k_1	0.0001 s^{-1}
$BKI1$	K_i	0.000 944 475 075 4 $nmol\,dm^{-2}$
$BIK1$	K_i	0.000 715 067 125 7 $nmol\,dm^{-2}$
$BRI1\,CT$		0.000 554 752 860 4 $nmol\,dm^{-2}$
$BAK1$	K_D	0.032 343 459 42 $nmol\,dm^{-2}$
BL	K_D	55 nM
$BL\,BRI1\,BAK1$	k_{off}	0.0105 s^{-1}
$AHA\,CT$	$inhibition$	1.741 070 029
$BIR3\,BAK1$	K_d	$4.353\,077\,802 \times 10^{-7}\,nmol\,dm^{-2}$
$BIR3\,BAK1$	K_d	0.016 472 518 26 $nmol\,dm^{-2}$

D.4 Files

The ODE models were built in COPASI version 184, which supports 2-dimensional compartments. Opening this model in an older version of COPASI will result in the 2D compartment to be interpreted as a 3D compartment. Furthermore, earlier versions of COPASI are unable to export the SBML file of the model correctly. Instead of the change in cell length, the actual cell length is exported, which results in completely changed model behavior.

	File Name	Description
Agent-Based Model	Root_transection_with_SBML.zip	Export of the agent-based model including all model parameters, cell behavior submodels, imported SBML file containing the COPASI ODE model of the fast BR response.
Biomechanical Model	biomechanics_root.jar	Contains the biomechanical information on the interaction between cells as well as the initial settings for the simulations. Is part of the EPISIM simulator but also has to be compiled and linked to the cell behavior model in the EPISIM simulator. Changes in the biomechanical model require a newly compiled version of the EPISIM simulator and reestablishing the link to the cell behavior model within the EPISIM modeller.
COPASI Models	thesis_02_07_2018.cps	ODE model of the BR-induced cell elongation.
	thesis_02_07_2018_rescue.cps	model version used to simulate the rescue experiment with BL application 12 h after allowing cell elongation to occur
	thesis_02_07_2018_episim.cps	model version updated to the point where BL stimulation is triggered by an event in the regular ODE model